



The University of
Nottingham

**Proton Conductivity Studies in
Metal-Organic Frameworks**

Simona Pili

**Thesis submitted to the University of Nottingham for
the degree of Doctor of Philosophy**

(August 2015)

Declaration

Except where specific reference is made to other sources, the work presented in this report is the original work of the author. It has not been submitted in whole or in part for any other degree.

Signed:

Simona Pili

Date:

Abstract

This Thesis describes the synthesis and characterisation of novel metal-organic frameworks designed for proton conductivity applications. A new system for impedance measurements was constructed and tested, and the proton conductivity of a variety of MOFs was studied. Additionally, the effect of ligands with phosphonate functional groups, the strategic choice of metal ions and the use of proton carrier guests loaded in the pores of MOFs to obtain conducting materials was investigated.

Chapter 1 introduces the current challenges in energy sustainability and endorses fuel cells as an alternative energy source. A careful description of the proton exchange membrane (PEM), key component of fuel cells, with emphasis on the materials currently used in industry is discussed. The need to overcome the limitations of PEMs under the working conditions and understanding the molecular mechanism of proton conduction is crucial for the design of new materials with improved proton conductivity properties. Recently, metal-organic frameworks (MOFs) have been pointed as alternative candidates for proton conduction application. Their crystalline nature combined with the possibility to design their structures by choosing opportune functional groups and proton-carrier guests make them promising candidates as proton conducting materials.

Chapter 2 presents a brief introduction of Electrochemical Impedance Spectroscopy (EIS), the main technique used to evaluate the proton conductivity of the MOFs in Chapters 3, 4 and 5. An overview of the physical basis of EIS and the data analysis strategies are discussed. In the second part of Chapter 2 the newly designed experimental set up employed to measure the proton conductivity of MOFs is described with emphasis on the design of the conductivity cell, control of

temperature and relative humidity, and sample preparation. The calibration of the experimental set up was performed using imidazole, a readily available linker with known conductivity.

In Chapter 3 the synthesis and structural characterisation of two new isostructural phosphonate-based MOFs, $[\text{Ni}_3(\text{H}_3\text{L}^1)_2(\text{H}_2\text{O})_{10.5}(\text{DMF})_3]$ and $[\text{Co}_3(\text{H}_3\text{L}^1)_2(\text{H}_2\text{O})_{10.4}(\text{DMF})_3]$ ($\text{H}_6\text{L}^1 =$ benzene-1,3,5-*p*-phenylphosphonic acid), denoted as NOTT-500(Ni) and NOTT-500(Co), are described. X-ray structural analysis revealed that these materials have acidic phosphonate groups (P-OH) and water molecules coordinated to the metal ions (M-OH₂) organised in an efficient proton-hopping pathway. TGA, VT-PXRD and solid-state UV-visible analyses showed a reversible structural phase transition associated with a marked change in colour upon dehydration-hydration of NOTT-500(Ni, Co). Proton conductivity measurements were performed exhibiting values of $1.11(03) \times 10^{-4} \text{ S cm}^{-1}$ and $4.42(06) \times 10^{-5} \text{ S cm}^{-1}$ for NOTT-500(Ni) and NOTT-500(Co) respectively, at 99 % RH and 25 °C. The activation energy of the proton transfer process for NOTT-500(Ni) was determined over the temperature range of 18-31 °C at 99 % RH, giving a value of 0.46 eV which indicates the proton conduction occurs through the combination of the Grotthuss and Vehicle mechanisms. Quasi-elastic neutron scattering (QENS) experiments on NOTT-500(Ni) under anhydrous conditions (0 % RH) suggested that the proton transfer in the hopping pathway (regulated by the Grotthuss mechanism) is well described by a “Spherical free diffusion” model, with an activation energy of 0.076 eV.

Chapter 4 introduces two novel approaches to enhance the proton conductivity of a new family of lanthanide MOFs, $[\text{M}(\text{HL}^2)]$ ($\text{H}_4\text{L}^2 =$ biphenyl-4,4'-diphosphonic acid;

M = La, Ce, Nd, Sm, Gd, Ho). The first method aims to increase the concentration of protons in a fixed volume of MOF by using the shorter version of the organic ligand, benzene-1,4-diphosphonic acid, H_4L^3 , with subsequent improvement of the proton conductivity properties in $[M(HL^3)]$ (M = La, Ce, Nd, Sm, Gd, Ho). The second method to achieve better proton conductivity was carried out by substituting 3+ metal ions, Ln(III), with a 2+ metal, Ba(II), leading to the synthesis of an isostructural complex $[Ba(H_2L^2)]$ with increased number of protons in comparison with $[M(HL^2)]$. The proton conductivities of $[M(HL^3)]$ (10^{-4} S cm^{-1}) and $[Ba(H_2L^2)]$ (10^{-5} S cm^{-1}) exhibited a significant increase when compared with $[M(HL^2)]$ (10^{-6} S cm^{-1}) at 25 °C and 99 % RH. Extensive impedance studies at different temperatures and relative humidities were performed together with full characterisation of all the materials presented in this Chapter.

Chapter 5 describes a preliminary study of two new complexes synthesised through postsynthetic modification of the well-known MOF, NOTT-300(Al). The addition of imidazole (a proton carrier) into the 1D channels was performed using two different approaches; the vapour diffusion (d) and solvation methods (s). Impedance studies of the post-synthetically modified complexes, Im@NOTT-300(Al)-(d) and Im@NOTT-300(Al)-(s), both with formula $\{Al_2(OH)_2(C_{16}O_8H_6)(Al_2O_3)(CH_4O)_2(C_3N_2H_4)_{0.61}\}_\infty$, were investigated. The experimental results showed that at 20 °C and 99 % RH the proton conductivity of Im@NOTT-300(Al)-(d) ($2.39(11) \times 10^{-5}$ S cm^{-1}) and Im@NOTT-300(Al)-(s) ($1.37(13) \times 10^{-5}$ S cm^{-1}) is two orders of magnitude higher compared with NOTT-300(Al) ($1.08(10) \times 10^{-7}$ S cm^{-1}). These preliminary studies suggested the postsynthetic modification of porous MOFs with proton-carrier guest molecules is a promising direction for further research in this area.

In Chapter 6 is summarised the work presented in this thesis.

List of publications

1. S. Pili, S. Yang, C. G. Morris, V. Garcia-Sakai, T. L. Easun, S. P. Argent, M. Li, W. Lewis, M. R. Warren, C. Murray, C. C. Tang, M. Schröder, “Proton conduction in two phosphonate-based metal-organic frameworks by intrinsic Spherical free diffusion” Manuscript in preparation.
2. S. Pili, S. Yang, I. DaSilva, M. Li, C. Murray, C. C. Tang, M. Schröder, “New strategies to enhance proton conductivity in a new family of lanthanide MOFs” Manuscript in preparation.

Acknowledgments

I would like to thank all the people that have contributed in some way to this work. First of all I wish to thank my supervisor Prof. Martin Schröder for giving me the opportunity to work in his group and for the guidance and support he has demonstrated through the course of my PhD.

Dr Sihai Yang deserves special thanks for training me at the start of my PhD and for his constant expertise and support, his help was essential for the success of my research. A great acknowledgment also goes to Dr Timothy Easun for his extensive advices, enlightening discussions and not less important, his English lessons.

Many thanks to Dr William Lewis and Dr Stephen Argent for their help with the crystallographic analysis.

Particular thanks to Dr Sihai Yang and Dr Stephen Argent for their considerable input in solving the structures of NOTT-500(Ni, Co).

Thanks to Chris Morris for indexing the PXRD data reported in Chapter 3 and determining the space group of the new crystallographic phases of NOTT-500(Ni, Co).

Thanks to Dr Ivan DaSilva for indexing the PXRD patterns and solving the structures of $[M(HL^2)]$, $[M(HL^3)]$ and $[Ba(H_2L^2)]$ reported in Chapter 4.

Thanks to Dr Chiu Tang (Beamline I11) and Dr Mark Warren (Beamline I19) in Diamond Light Source and Dr Victoria Garcia-Sakai (from IRIS) in ISIS Rutherford Appleton Laboratory for their assistance during the collection and analysis of the data.

Many thanks to Dr Ming Li for useful discussions about the proton conductivity project.

I would also like to acknowledge my project students Eleonora Conca and George Pitt for their valuable contribution to the work presented in this Thesis. Thanks to Peter Rought for his help during the testing of the conductivity cell.

Thanks also to all the technical staff of the School of Chemistry, especially Mark Guyler and Mel who build the conductivity cells, fixed them in several occasions and made my research possible.

Special thanks to Prof. Martin Schröder, Dr Timothy Easun, Dr Stephen Argent, Dr Sihai Yang, Will Trenholme, Jenny Eyley and Rossella Mascia for spending time proof-reading this thesis.

Many thanks to all the people in the Inorganic Department, in particular the Schröder group, past and present, for the extraordinary collaborative environment they established. Thanks to my friends and colleagues in the office, Will, Martyn, Ruth, Sav, Chris, Jenny, Nevo, Florian, Harry, Bahar, Nada, Carlo, Cristina, Jian, Yong, Shan, Luck, Thien, Pete, Andrea, Irina, Maggie and everyone else in the group for the good time in Nottingham during the past four years.

Thanks to Rossella for her support and patience in the house during the thesis writing period, friendship and support.

Another lot of thanks go to all my friends back home that despite the distance have always been close to me. Special thanks to Debby, Locci, Mely, Ale, Noe, Ghiane, Eli, Michi, Ricki e Ila.

Finally I would like to acknowledge my cousins, family and parents, without their love and support during my time here I could not have manage this incredible feat and I wish to dedicate this Thesis to my Mum and Dad. Grazie.

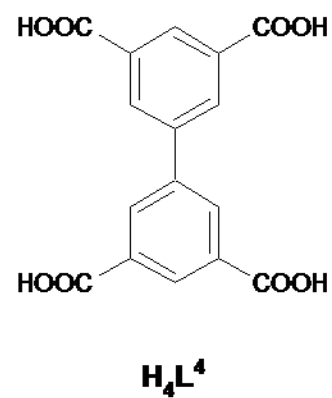
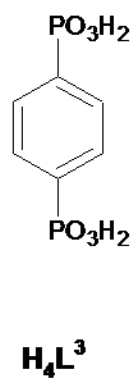
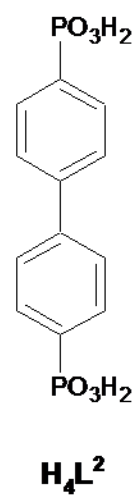
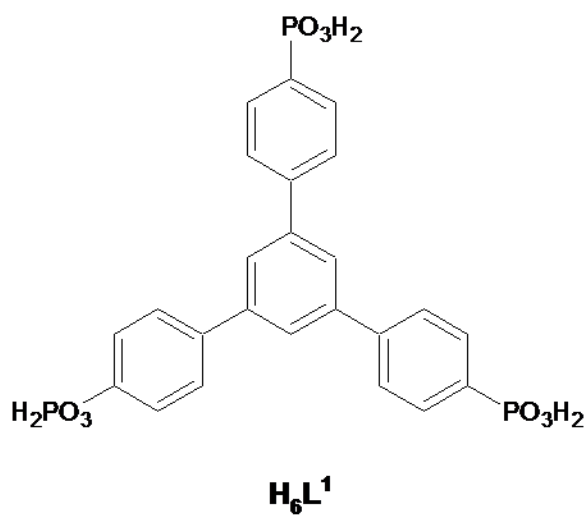
Abbreviations

A	Ampere or Area, according to text
Å	Angstrom
AC	Alternating current
AFC	Alkaline fuel cell
ATR	Attenuated total reflectance
C	Celsius or Capacitor, according to text
CH ₃ CN	Acetonitrile
CHN	Elemental analysis
CP	Coordination polymer
CPE	Constant phase element
Γ	Half width half maximum
d	Doublet (NMR)
(d)	Vapour diffusion method
3D	Three dimensional
°	Degree
DC	Direct current
DCM	Dichloromethane
DMF	Dimethylformamide
DMSO	Dimethylsulfoxide
DOF	Department of Defence
E	Potential
E _a	Activation energy
ΔE _{res}	Energy resolution
ECR	Energy Research Corporation
EIS	Electrochemical Impedance Spectroscopy
EISF	Elastic incoherent structure factor
EU	European Union
eV	Electron volt
EW	Equivalent weight
φ	Phase
FC	Fuel cell
G8	The group of eight

GDL	Gas diffusion layer
GE	General electric
HR-PXRD	High resolution powder X-ray diffraction
HT-PXRD	High temperature powder X-ray diffraction
HWHM	Half width half maximum
Im	Imidazole
IR	Infrared
j	Bessel function
K	Kelvin
K_B	Boltzmann's constant
L	Ligand or Inductor, according to text
l	Thickness
M	Metal
(m)	Medium
m	Slope
MCFC	Molten carbonate fuel cell
MEA	Membrane electrode assembly
MeOH	Methanol
MIL	Material of Institute Lavoisier
MMM	Mixed matrix membrane
MOF	Metal-organic framework
mp	Melting point
m/z	Mass : Charge ratio
n.a.	Non available
NMR	Nuclear Magnetic Resonance
p	Immobile fraction
PAFC	Phosphonic acid fuel cell
PEM	Proton exchange membrane
PEM-FC	Proton exchange membrane fuel cell
ppm	Part per million
PTFE	Polytetrafluoroethylene
PXRD	Powder X-ray diffraction
Q	Scattering vector
QENS	Quasi-elastic neutron scattering

QPE	Constant phase element
R	Resistance
r	Distance
% RH	Relative humidity
RT	Room temperature
s	Singlet (NMR) or Seconds, according to context
S	Siemens
(s)	Solvation method or strong, according to text
σ	Proton conductivity
σ_{inc}	Incoherent scattering cross section
SCP	Surface coordination polymer
SOFC	Solid oxide fuel cell
t	Triplet (NMR)
τ	Single time constant
Temp.	Temperature
TGA	Thermogravimetric analysis
US	United States
UV-Vis	Ultraviolet-visible
V	Volt
VT-PXRD	Variable temperature powder X-ray diffraction
Z	Impedance
Z'	Real impedance
Z''	Imaginary impedance
(w)	Weak
Ω	Ohm
ω	frequency

List of ligands



Contents Page

Title Page

Declaration.....	i
Abstract.....	ii
List of publications.....	v
Acknowledgements.....	vi
Abbreviations.....	viii
List of ligands.....	xi
Contents page.....	xii
1. Introduction.....	1
2. Electrochemical Impedance Spectroscopy: Experimental design.....	41
3. Proton conduction in two phosphonate-based metal-organic frameworks mediated by intrinsic “spherical free diffusion”.....	79
4. New strategies to enhance proton conductivity in a family of lanthanide MOFs.....	151
5. Post synthetic modification of NOTT-300(Al) and proton conductivity studies.....	255
6. Conclusions and future perspectives.....	287
Experimental details and conditions.....	293

Chapter 1

Introduction

List of Contents

1.1 Energy in the 21 st century.....	1
1.2 Fuel cells.....	2
1.2.1 Historical background.....	3
1.2.2 Fuel cell description.....	4
1.2.3 Applications of fuel cells	5
1.3 PEM fuel cells	7
1.3.1 Nafion as PEM in fuel cells	10
1.3.2 Desired properties and problems with current PEMs	13
1.4 Metal-organic frameworks for proton conducting applications in PEM-FCs..	14
1.4.1 Metal-organic frameworks.....	14
1.4.2 MOFs as proton conducting materials	16
1.4.3 Types of proton conducting MOFs.....	16
1.4.4 Conclusions and future perspectives.....	27
1.5 The scope of this Thesis	28
1.6 References	30

1.1 Energy in the 21st century

Energy is an essential part of today's society and modern industrialised economy. Considerable economic and population growth are expected during the 21st century on a worldwide scale.^{1,2} Consequently, statistical data of US Energy Information Administration (EIA) and the International Energy Agency (IEA), state that the global primary energy consumption, including transportation, industry, residential and commercial is estimated to exponentially increase (Figure 1.1).^{3,4}

In current global energy consumption, fossil fuels (oil, gas and coal) account for about 86 % of the energy demand.^{3,5} Even though the world energy system is predicted to rely on fossil fuels for the next few decades, their availability is ultimately limited.^{3,6} In addition, the uneven distribution of fossil fuels reserves and their depletion are contributing to make the fossil fuel-based economy unsustainable.^{1,5} Moreover, the production of energy by burning fossil fuels is responsible for emission of carbon dioxide and pollutants in air.^{2,3,7-9} Along with the increased energy consumption and the reduced availability of the world's fossil fuels, environmental policies demand reduction in polluting gas emission which seriously impacts the climate change. EU and G8 leaders declared in 2009 that CO₂ emissions must be cut by at least 80 % (from 1990 levels) by 2050 in order for atmospheric CO₂ to stabilise at 450 parts per million (ppm) and keep global warming below 2 °C.¹¹ This leads to a compelling need to expand the contribution of efficient and renewable energy sources as an alternative to fossil fuel combustion.⁵ The energy transition initiative currently aims to use 20 % of power from renewable resources by 2020, 50 % by 2050 and 100 % by 2100.^{3,10}

To be a viable and competitive energy source, emerging energy technologies must not produce carbon dioxide emissions nor contribute to climate change.^{9,12} One of the

solutions to impede the energy crisis is to move towards a global hydrogen economy. Research has been focused on development and deployment of hydrogen and fuel cell technologies as a potential energy solution for the 21st century.⁵

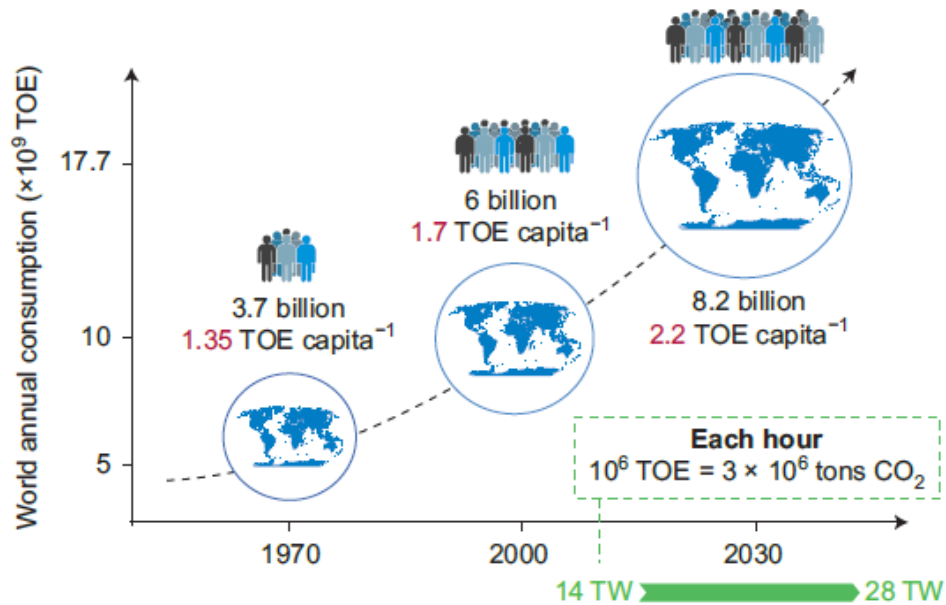


Figure 1.1. Past, present and forecast of the world’s energy needs. TOE = ton of oil equivalent.⁴

1.2 Fuel cells

Fuel cells are efficient and non-polluting power sources.^{12–14} Unlike internal combustion engines, they utilise clean fuels such as hydrocarbons, alcohols and most importantly hydrogen, to produce energy.

A fuel cell is an electrochemical device operating at various temperatures (from 50 °C up to 1000 °C) that transforms the chemical energy of a fuel (such as hydrogen, methanol and natural gas) and an oxidant (dioxygen from air) into water, heat and electricity in the presence of a catalyst.^{13,15} A fuel cell is similar to a battery such that it consists of a pair of electrodes and an electrolyte; it generates electricity from an

electrochemical reaction and heat as by-product. However, a battery holds a closed store of energy within it and once this is depleted the battery must be discarded or recharged. Unlike a battery, the species consumed during the electrochemical reaction are continuously replenished in the fuel cell so that there is never a need to recharge the cell.¹⁶

Fuel cells powered by hydrogen from abundant and renewable sources are an ideal solution for non-polluting energy production. Extensive research and development of this technology over the past fifteen years has delivered vehicles, small devices and stationary plants with impressive performances and negligible-levels of emission of greenhouse gases in the environment.^{17,18}

1.2.1 Historical background

Fuel cells are one of the oldest electrical energy conversion technologies known to man.^{19,20} Their invention is attributed to Sir William Robert Grove and dates back more than 150 years (Figure 1.2).¹⁴ However, until the first half of the 20th century, the widespread and inexpensive availability of fossil fuels limited the demand in developing fuel cells for energy production.¹⁴ Considerable attention on fuel cells as energy-generators was shown in the 1960s by NASA which use them in space missions.^{20,21} Starting from the 1970s, concerns over air pollution and energy availability focussed the US and Europe on pursuing environmental-friendly politics. Many national governments and large companies such as General Motors and Shell, started to invest in renewable energy sources, including fuel cells. During the 1990s, increased use of electricity intensified the demand for efficient electrical energy conversion systems. Fuel cells were initially introduced as small power generators and soon developed further for both transport applications and megawatt-scale

centralised plants.^{14,19} At the beginning of the 21st century increment of the world's population, raised energy demands, and serious environmental concerns became driving forces for worldwide investment in clean power generation systems.^{14,22}

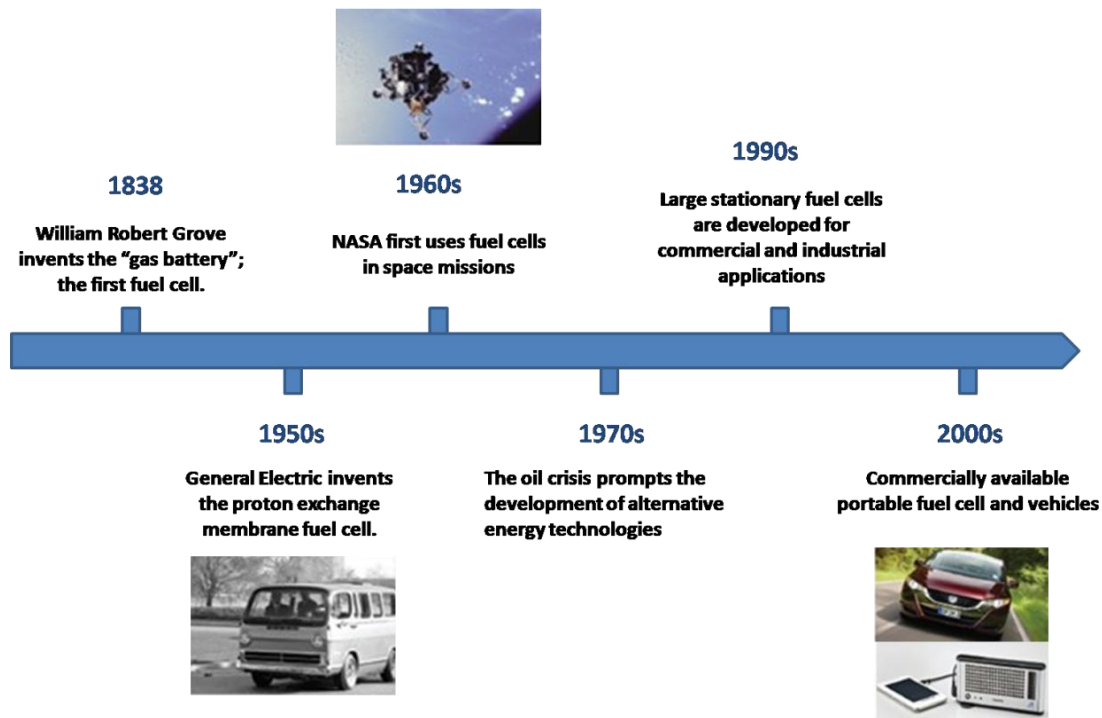


Figure 1.2. Schematic representation of the fuel cells history; from their invention until 2000s.

1.2.2 Fuel cell description

A fuel cell is a device that produces electricity from a chemical reaction: it consists of two electrodes, one positive (cathode) and one negative (anode), which are separated by an electrolyte (Figure 1.3).⁵ The electrolyte carries electrically-charged particles between the electrodes whilst a catalyst is used to facilitate the reactions at the electrodes. The ability of the electrolyte to allow the selective migration of protons is a key factor in the working efficiency of the fuel cell. The basic working process of a hydrogen fuel cell to produce electrical current consists of feeding H₂ to

the anode and oxygen to the cathode. The hydrogen is catalytically oxidised at the anode into protons and electrons (Reaction 1). The electrons pass through an external circuit producing a flow of electricity, while the protons selectively migrate to the cathode through the electrolyte. At the cathode oxygen is combined with electrons and protons and is reduced to water (Reaction 2). The overall reaction is summarised in Reaction 3. The heat produced during the process can be harnessed resulting in efficient use of fuel and the absence of undesirable waste products.

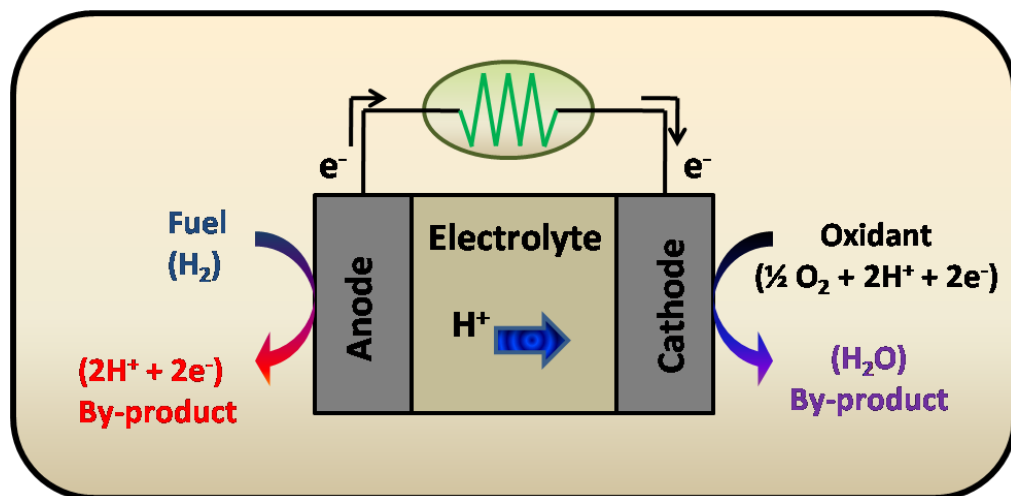
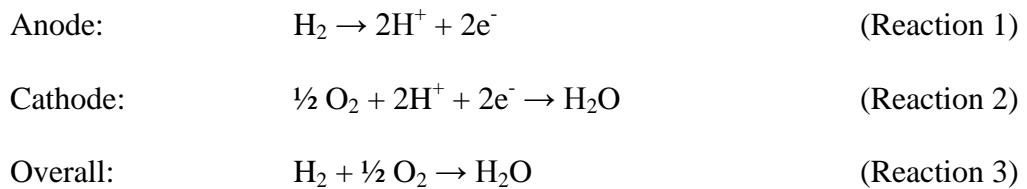


Figure 1.3. Scheme of a proton conducting hydrogen fuel cell; representation of the main components and operating principle.

1.2.3 Applications of fuel cells

During the last decade, the set of challenges facing renewable and clean energy production have created commercial opportunities for fuel cells (Figure 1.4).

Efficient and cheaper fuel cell technologies have been exploited by automakers and manufactures in a broad range of applications, from portable and stationary power to transportation.²²⁻²⁴

Portable fuel cells have been exploited for military and civilian applications; personal electronic devices of different sizes such as MP3 players, cameras, laptops and radios have been designed.¹⁶ Stationary fuel cells are suitable for on-site power generation to provide electricity. Fuel cell systems can be directly connected to a building to provide both power and heat with cogeneration efficiencies of 80 %.¹⁶ Stationary fuel cells are currently used in hospitals, nursing homes, hotels, office buildings, schools, and utility power plants providing primary or backup power.²² Currently, most fuel cell based power plants are produced and reside in the United States owing to the active support of the Department of Defence (DOF) and the Energy Research Corporation (ECR). Similarly, the South Korean government has built 300 operating plants since 2012. The European Commission has endorsed the concept of a Hydrogen and Fuel Cell Technology Platform (with the expenditure of € 2.8 billion over a period of 10 years) in order to reduce CO₂ emission of 60 % by 2015.²²

Transportation constitutes the primary target market for both fuel cells and hydrogen.^{14,16} Fuel cells for transportation have the potential to reduce automotive CO₂ emissions. Moreover, fuel cell technology offers lower maintenance costs, high reliability, silent operation, faster fuelling and uninterrupted power.²² Major automobile manufacturers, Toyota, Honda, and Nissan are planning to commercially produce fuel cell cars in the future.

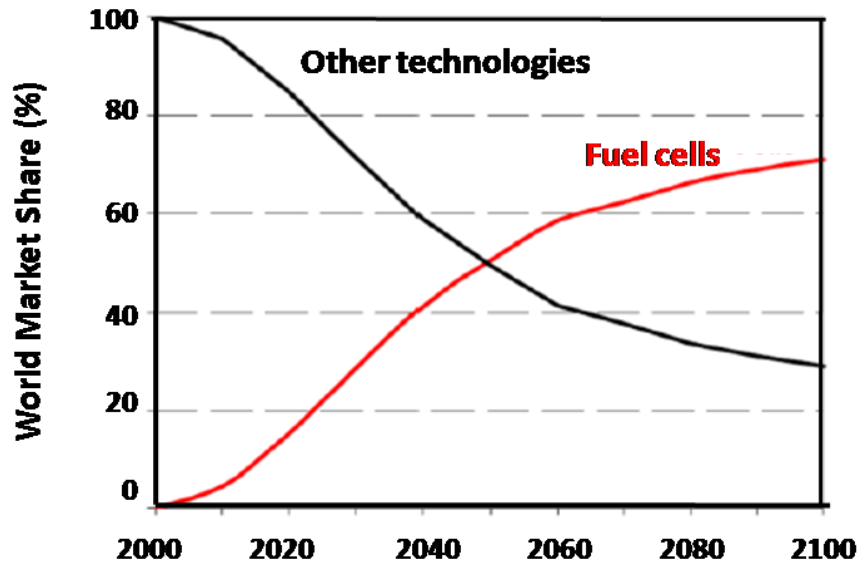


Figure 1.4. Projected world market share of fuel cells in the 21st century.²²

Despite recent developments, fuel cell technology is just entering the first stages of commercialisation and intensive research focuses on depressing the costs while improving their performance and durability.^{13,17,22}

1.3 PEM fuel cells

Fuel cells are classified according to the type of electrolyte employed; currently the main electrolytes are alkali, molten carbonate, phosphoric acid, solid oxide and proton exchange membrane. The first three are liquid while the remaining two are solid electrolytes. The type of the electrolyte chosen constrains the design of the fuel cell, the materials used for its construction and the type of catalyst employed.²⁵ The efficiency of the fuel cell and its operational temperature range are dependent on the electrolyte chosen. Alkaline (AFC), phosphonic acid (PAFC) and proton exchange membrane (PEM-FC) fuel cells operate at temperatures between 80 °C (PEM-FC) and 250 °C (AFC, PAFC) with conversion energy efficiency of 60-80 %.^{14,25-31} These fuel cells use platinum as a catalyst which is expensive and extremely

sensitive to CO and CO₂ poisoning. Such gases are found as impurities in hydrogen-rich gaseous fuel produced by reforming of natural gas, methanol or gasoline, making necessary the presence of an additional reactor to reduce their amount in the fuel before it is used to fill the cell.^{14,30–33} Molten carbonate (MCFC) and solid oxide fuel cell (SOFCs) work at high temperatures (650-1000 °C) which allow the use of non-precious metals as the catalyst and avoid CO₂ poisoning.^{25,27,34–38} However, the working conditions reduce the durability of these fuel cells representing their major limitation.^{38,39}

Among the established fuel cell designs, those based upon polymer electrolyte membrane (PEM) with hydrogen fuel are promising candidates as power sources in the automotive and portable industry.¹⁸ PEM-FCs operate at low temperatures (80 °C), offer high efficiency (60%), and minimal environmental impact.⁴⁰

PEM-FC technology has been well established since early 1960s and successfully developed as electrical power sources for military, space craft and submarine applications.^{13,41,42} From the 1980s, PEM-FC technology was particularly exploited in portable and vehicular applications.¹³ During the last decade they have been employed for a variety of purposes such as mobile phones, laptops, cars, buses, boats, houses, stationary plants and the space shuttle orbiter.^{1,13,41}

Membrane electrode assembly, MEA:

The essential component of PEM-FCs is the membrane electrode assembly (MEA), which consists of the membrane, the catalyst layer and the gas diffusion layers (GDLs) (Figure 1.5). The polymer electrolyte membrane (or proton exchange membrane), PEM, is the key component of PEM-FC technology which conducts protons from the anode to the cathode whilst blocking electrons and other substances

which would disrupt the chemical reaction.⁴⁰ PEMs made of polyperfluorosulfonic acid are well-known for their high chemical inertness, good thermal stability, reasonable mechanical strength and excellent proton conductivity when highly hydrated.⁴³ Layers of platinum-based catalyst are applied at each side of the membrane. On the anode side, the catalyst enables H_2 to be split into protons and electrons; on the cathode side it promotes the oxygen reduction into water (Reaction 1 and 2, Section 1.2.2). Conventional catalyst layers consist of nanometer-sized particles of platinum or platinum alloy dispersed on a carbon support. To facilitate the transport of reactants and remove the water produced during the reaction, gas diffusion layers (GDLs) are applied outside the catalyst layer. A typical GDL is composed of a sheet of porous carbon paper coated with hydrophobic polytetrafluoroethylene (PTFE), which prevents excessive water build-up. When individual PEM-FCs are assembled into fuel cell stacks, bipolar plates providing channels for the gaseous fuel and air, are used.

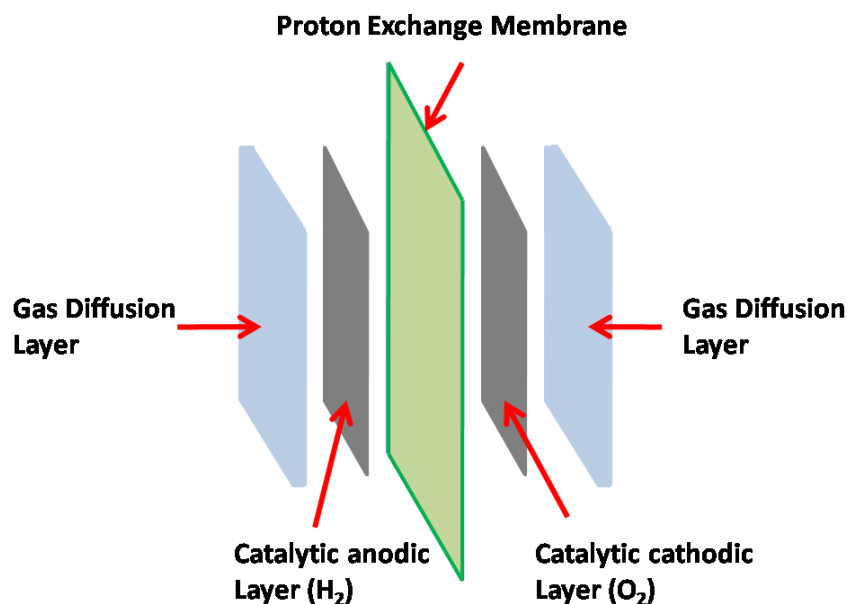


Figure 1.5. Schematic representation of the membrane electrode assembly (MEA) and its components; the membrane, the catalyst and the gas diffusion layers.

1.3.1 Nafion as PEM in fuel cells

PEM-FC technology was developed by Thomas Grubb and co-workers at the US General Electric Company (GE) in the 1950s.²⁷ Sulfonated polystyrene membranes were initially used as electrolyte. In the 1970s DuPont Inc developed Nafion, which is currently the best performing solid polymeric electrolyte in H₂/O₂ fuel cells operating in the temperature range between 50–90 °C and became the most extensively studied PEM.^{18,27,42-44}

Nafion is a perfluorinated copolymer with ionic side chains (Figure 1.6).⁴⁵ It consists of a hydrophobic perfluorinated polyethylene backbone, essential for the structural integrity of the membrane, and highly hydrophilic side chains of sulfonic acid terminated with perfluoro vinyl ether pendant within which ionic transport occurs.^{1,40,46} By varying x, y and z the structure and properties of Nafion also change. Typical values of x and y are 7 and 1, respectively; z (typically 1) can be varied to control the length of the side-chain.¹ Nafion membranes are described by the thickness and equivalent weight (EW), (weight of polymer per mole of sulphonate). Thus, Nafion 115 denotes for 1100 g EW and thickness of 0.005 inch (127 μm).

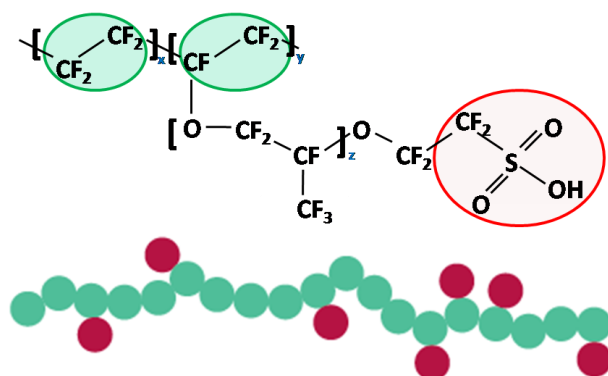


Figure 1.6. Representation of the molecular structure of Nafion; a fluorine-containing copolymer with aperiodic placement of sulphonate functionalities (red circles) along its contour.⁴⁵

Despite the wide attention paid by industry and the considerable research undertaken, the hierarchical structure of Nafion membranes and the mechanism of cation exchange during fuel cell operation remain poorly understood.¹⁸

Numerous studies to characterise the structure and model the mechanism of the electrochemical reactions have been performed. For this purpose, analytic techniques including nuclear magnetic resonance (NMR), infrared (IR) spectroscopy, AC impedance spectroscopy and quasi elastic neutron scattering (QENS), have been used.^{1,45}

Numerous studies demonstrate that Nafion membranes exhibit a bicontinuous nanostructure involving a hydrophobic matrix supporting ionic domains that swell on hydration. The distribution of the two phases from the nanoscale to the microscale has been subject of much debate. The morphology of Nafion membranes is known to change with hydration level, processing conditions and thermal history. As yet, there is no consensus on its mesoscopic structure, dependence on the fabrication process, thermal history and ageing properties. The characterisation problems are primarily a result of the lack of long-range structural order in Nafion.^{1,18}

Proton conduction and operating conditions of Nafion:

Nafion is currently the best hydrocarbonated ionic polymer PEM used for industrial applications.^{18,46} Nafion is an excellent proton conductor ($\sim 10^{-2}$ S cm⁻¹) at high relative humidities (> 98 %) and at temperatures below 80 °C.⁴⁴ It is chemically and electrochemically stable in acidic and oxidising environments. Moreover, it has low permeability to gaseous reactants and excellent mechanical properties including flexibility, ductibility and water-swelling capacity.

The presence of water is essential for Nafion to act as a proton conductor; thus it needs to be equilibrated with 100 % relative humidity (RH) vapour or with liquid

water prior to its use.^{47,48} The proton transport occurs through water-swollen in hydrophilic channels that form as a result of nano-phase separation of the hydrophilic and hydrophobic segments of the polymer. Proton conduction occurs via a combination of a Grotthuss, Vehicular and Surface mechanisms (Figure 1.7). In the Vehicular mechanism the water molecules act as shuttles along the channels and the protons move as a water-solvated species (e.g., H_5O_2^+ , H_9O_4^+ , etc.). In the Grotthuss mechanism the transport of protons occurs via the “hopping” of protons from one water molecule to the next by the formation and breaking of O-H bonds. Water molecules also promote the dissociation of the protons from the sulphonic acid groups and facilitate proton transfer through the membrane; this is known as surface transport.^{1,46}

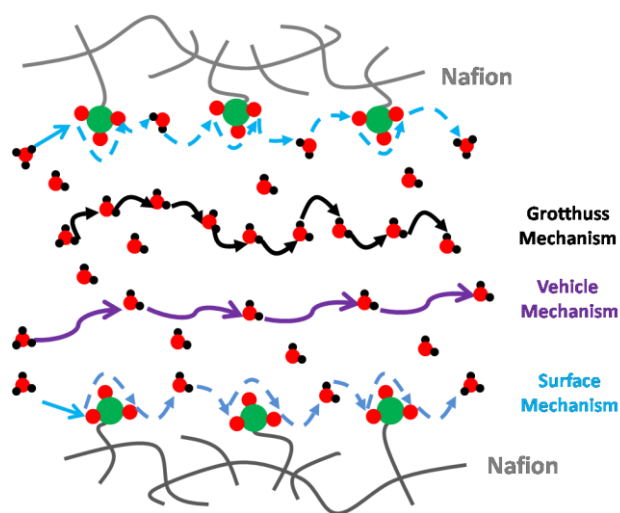


Figure 1.7. Schematic illustration of the proton conduction mechanisms in Nafion under hydrated conditions; Grotthuss, Vehicular and Surface mechanisms. Oxygen (*red*), hydrogen (*black*), sulphur (*green*).⁴⁴

The need for hydrated conditions to exploit the proton conduction properties of Nafion constrains the working temperature range of PEM fuel cells. The use of elevated temperatures leads to evaporation of water from the membrane causing a

dramatic decrease in hydration level and consequent reduction of the proton conductivity by several orders of magnitude.^{46,49} The upper limit of the working temperature arises mainly from the difficulty in maintaining a sufficiently high hydration level at higher temperatures.⁴³ For practical applications, maintaining the membrane under humid conditions requires additional humidification systems to manage water distribution thus increasing the manufacturing costs and the complexity of the system.^{46,47}

1.3.2 Desired properties and problems with current PEMs

Hydrated perfluorosulfonic polymers show excellent performance in PEM-FCs operating at moderate temperatures (< 90 °C) and high relative humidity (100 % RH) with pure hydrogen as a fuel. PEMs able to operate in absence of water above 120 °C will bring revolutionary advances in PEM-FC designs for large consumer markets.^{13,46}

The main limitations of the current membranes concern the risk of poisoning the expensive platinum catalyst by CO₂ and CO, the grade of hydrogen-fuel and water management. High temperatures improve the catalyst tolerance of the residual CO present in the hydrogen stream.^{41,49} At 80 °C the CO tolerance is about 10-20 ppm; increasing the temperature to 130 °C the CO tolerance dramatically increases to 1000 ppm and up to 30000 ppm at 200 °C.⁴⁷ CO impurities are often found in hydrogen-rich gaseous fuel produced by reforming of natural gas, methanol or gasoline. These fuels are much cheaper compared to high purity hydrogen, typically required in PEM fuel cells, which negatively impacts the costs and the commercialisation of these technologies. In addition to increasing the CO tolerance, high working temperatures can enhance the kinetics of the electrochemical reactions at the anode and cathode

resulting in a more efficient energy conversion.⁴⁶ At temperatures above 120 °C, flooding of the catalyst layers can be avoided owing to the elimination of liquid water. The waste heat due to high temperature running may be recovered and it may be feasible to use non-precious metal catalysts.¹

1.4 Metal-organic frameworks for proton conducting applications in PEM-FCs

As has been discussed, PEM fuel cells represent an appealing option as alternative energy systems.⁵⁰ The design of new electrolyte materials to tackle current technical limitations is critical to increase the efficacy of PEM-FCs and has recently garnered great attention in the fuel cell technology. Among the requirements for better electrolytes, the new materials need to possess high conductivity ($> 10^{-2}$ S cm⁻¹) to facilitate the transport of protons between electrodes, good thermal and chemical stability at the operating conditions (variable temperature and variable % RH), membrane processability and low costs.⁵¹ Rational design of novel conducting materials is of fundamental importance to obtain a molecular-level understanding of the chemistry and mechanism of the proton migration and water molecules under the working conditions.¹ Recently metal-organic frameworks (MOFs) have been investigated as potential candidates for proton conducting applications thanks to their high crystallinity (allowing structural insight into the proton-conduction pathway and mechanism), designable and modular nature, chemically functionalisable pores and thermal and chemical stability.

1.4.1 Metal-organic frameworks

MOFs are crystalline porous materials formed by the self-assembly of metal cations and bridging organic linkers that extend into usually three dimensional networks.

MOFs have subclass of coordination polymers (CPs) and zeolite chemistries. Coordination polymers date back to the 1960s; however, the interest in these materials started to grow from the early 1990s with pioneering work of Hoskins and Robson.⁵²⁻⁵⁵ For the first time they designed and synthesised a coordination polymer with premeditated structure, the diamond-like $\{\text{Cu(I)}[\text{C}(\text{C}_6\text{H}_4\cdot\text{CN})_4]^+[\text{BF}_4]^-$ network. The term MOFs was popularised in 1995 by Yaghi *et al.* in reference to three-dimensional porous coordination networks.⁵⁶

MOFs consist of metal ions and functionalised organic linkers; the arrangement of appropriate components can lead to the formation of highly porous materials with high internal surface areas and large pore volumes.⁵⁷ The designability of their structures and the availability of a great variety of metals and organic ligands offer the chance to synthesise a vast range of frameworks with desired structures for a large number of potential applications. Since the early 1990s, most research on MOFs has typically focused on exploiting high surface areas and pore volumes for applications in gas storage⁵⁸⁻⁶⁵, gas separation⁶⁶, catalysis⁶⁷ and magnetism.⁶⁸

MOFs typically form in solution *via* self-assembly from metal salt and organic ligand; self-assembly requires reversible bond formation in which components, either separate or linked, spontaneously form low energy ordered structures.⁶⁹ The majority of MOFs are synthesised by solvothermal or hydrothermal methods in which the reactions are carried out in organic solvents or water at high temperatures in a closed vessel under autogenous pressure. The framework structure of a MOF not only depends on the metal and organic building blocks but also many additional factors such as solvent, temperature, reactant concentration, pH, reaction time and pressure.⁷⁰

1.4.2 MOFs as proton conducting materials

As a new type of functional material, MOFs are good candidates to overcome the limitations of currently used proton conducting materials in PEM fuel cells. The exceptionally high crystallinity and modular nature of MOFs allow elucidation of structural information about the conductivity mechanism and enable direct visualisation of proton conduction pathways by diffraction methods, which is not possible in polymer-based electrolytes due to a lack of long-range order.^{71–80} MOFs can be functionalised at specific positions through the selection of the metal node and organic linker. This can allow for the incorporation of acidic protons within the framework, resulting in efficient proton-hopping pathways. Other properties of MOFs that make them an attractive replacement for currently used PEMs include the high thermal stability of these materials. This would enable fuel cells to be run at much higher temperatures making process more energy efficient.

The first attempt to study a proton-conducting coordination polymer (CP) was reported by Kanda *at al.* in the late 1970s with a two dimensional network, [*N,N'*-bis(2-hydroxyethyl)dithiooxamido] Cu(II), [(HOC₂H₄)₂(dtoa)Cu].^{50,81,82} However, this field received little further attention until 2009, when more research began to investigate CPs and MOFs as proton conducting materials. The potential for use of MOFs as proton conductors has not been as widely explored as their potential for gas storage and gas separation applications; although increasing interest has been shown during the past three years.⁵⁰

1.4.3 Types of proton conducting MOFs

Proton conducting MOFs can be divided into two main types; water-mediated proton conducting MOFs and anhydrous proton conducting MOFs.^{50,51} In the water-mediated

materials transport of protons relies on both hydrogen bonding functional groups on the framework and water-solvent molecules. These materials work at low temperatures (20-80 °C) with proton conductivity ranging between 10^{-2} S cm⁻¹ and 10^{-8} S cm⁻¹. Anhydrous proton conducting MOFs are characterised by water-free proton conduction pathways and operate at temperatures above 100 °C with proton conductivity ranging between 10^{-2} S cm⁻¹ to 10^{-6} S cm⁻¹.⁵⁰

Proton-transport in solids occurs through two general mechanisms. In the Vehicle mechanism the charge is transported by self-diffusion of protogenic species (e.g. H₂O) which can be present within the framework or loaded into the solid. The Grotthuss (or proton-hopping) mechanism involves the conduction of protons from site to site within a hydrogen-bonded network.⁸³⁻⁸⁷ These processes can primarily be identified by the activation energies (E_a) obtained through AC impedance measurements (Chapter 2). The Vehicle mechanism generally requires a large energy contribution to transport the proton-carriers, of the order $E_a > 0.4$ eV; while the Grotthuss mechanism typically requires a smaller contribution of $E_a < 0.4$ eV. In different MOFs, the proton transport has been previously described through both the Vehicle mechanism and the Grotthuss mechanism.^{72,78,79,88} Examples of proton conductivity mechanisms simultaneously regulated by both vehicle and Grotthuss mechanism have also been discussed.^{80,89-91}

Water-mediated proton conducting MOFs:

The water-mediated proton conduction of MOFs occurs at low temperatures (below 80 °C) and relies on the presence of water molecules which play a key role in the migration of protons through the hydrogen-bonding networks.⁵⁰ These materials need both a proton-carrier (H₃O⁺ or H⁺) and an efficient proton-conducting pathway

obtained by using ligands with specific functional groups or by doping MOFs with proton-carriers.

The majority of MOFs and CPs investigated so far as proton conductors belong to the water-mediated category (Table 1.1). Most of this research started to develop in 2009 and has grown quickly owing to the significant contributions of H. Kitagawa, Shimizu, Banerjee and Cabeza. Up till now use of ligands with specific functional groups is one of the most common strategies.

In 2010 Shimizu *et al.* studied the proton conductivity of a MOF with a phosphonate-based ligand, $Zn_2(btp)(H_2O)_2 \cdot 2H_2O$ ($btp = 1,3,5$ -benzenetriphosphonate), which was found to have a proton conductivity (σ) of $3.5 \times 10^{-5} \text{ S cm}^{-1}$ at $25 \text{ }^\circ\text{C}$ and 98 % RH with E_a of 0.17 eV.⁷⁸ In the following years Cabeza and co-workers showed particular interest in phosphonate-based MOFs as proton conductors reporting examples with σ between $10^{-5} \text{ S cm}^{-1}$ and $10^{-4} \text{ S cm}^{-1}$. Pursuing the idea of using ligands with strong acidic groups, in 2014 H. Kitagawa *et al.* reported a MOF, $[Zn(5\text{-sipH})(bpy)] \cdot DMF \cdot 2H_2O$ ($5\text{-sipH}_3 = 5\text{-sulfoisophthalic acid}$; $bpy = 4,4'$ -bipyridine), which showed conductivity of $3.9 \times 10^{-4} \text{ S cm}^{-1}$ at $25 \text{ }^\circ\text{C}$ and 60 % RH (Figure 1.8).⁹²

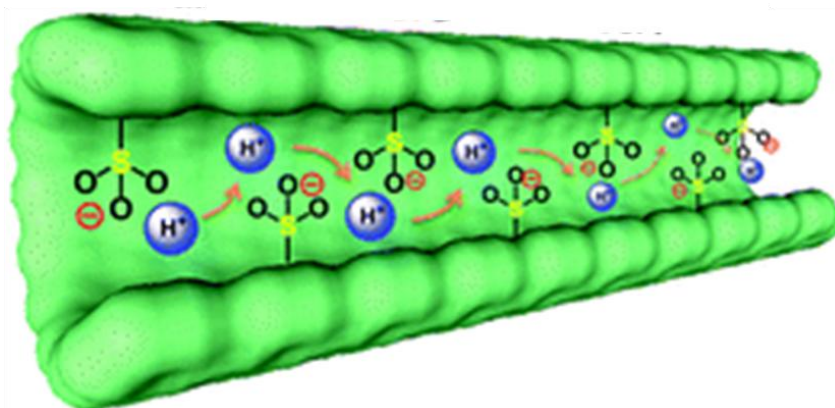


Figure 1.8. Schematic representation of $[Zn(5\text{-sipH})(bpy)] \cdot DMF \cdot 2H_2O$ decorated with non-coordinated sulfonic acid groups to facilitate proton transport.⁹²

H. Kitagawa *et al.* reported the proton conductivity of a widely studied MOF, MIL-53(M) (MIL = Material of Institut Lavoisier; M = trivalent metal ion, also designed as M(OH)(bdc) ($H_2bdc = 1,4\text{-benzenedicarboxylic acid}$), functionalised with various functional groups.⁹³ MIL-53(M) consists of infinite chains of corner-sharing $MO_4(OH)_2$ octahedra interconnected by dicarboxylate groups and has one-dimensional diamond-shaped channels (Figure 1.9). An interesting feature of MIL-53 is its high flexibility which allows the functionalisation of the ligand to exploit the relation between functional groups and the proton conducting properties of the resulting materials. H. Kitagawa and co-workers performed impedance studies on M(OH)(bdc-R) [M = Al, Fe; R = H, NH_2 , OH, $COOH_2$]; among them, Fe(OH)(bdc- $(COOH)_2$) showed a proton conductivity of $2 \times 10^{-6} \text{ S cm}^{-1}$ at $25 \text{ }^\circ\text{C}$ and 98 % RH with E_a of 0,21 eV.

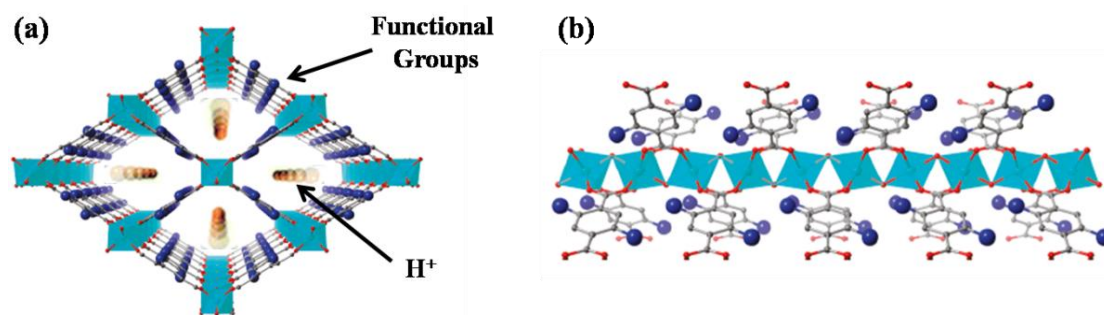


Figure 1.9. Views of the structure of MIL-53(M). (a) View down the channel lined by chains of corner-sharing $MO_4(OH)_2$. (b) The structure along the channel axis; the blue atoms show the position of functional groups ($-NH_2$, $-OH$, or $-COOH_2$).⁹³

Table 1.1. Proton conductivity of CPs and MOFs under hydrated conditions.

Compound	σ (S cm ⁻¹)	Temp. % RH	E _a (eV)	Author	Year ^{ref}
{[(Me ₂ NH ₂) ₃ (SO ₄) ₂ [Zn ₂ (ox) ₃]} ^[a]	4.2 x 10 ⁻²	25 °C 98 %	0.13	Ghosh	2014 ⁹⁴
(NH ₄) ₂ (adp)[Zn ₂ (ox) ₃ ·3H ₂ O] ^[a,b]	8 x 10 ⁻³	25 °C 98 %	0.63	H. Kitagawa	2009 ⁸⁰
La(H ₅ DTMP)·7H ₂ O ^[c]	8 x 10 ⁻³	24 °C 98 %	0.25	Cabeza	2012 ⁹⁵
Ca-PiPhA-NH ₃ ^[d]	6.6 x 10 ⁻³	24 °C 98 %	0.4	Cabeza	2014 ⁹⁶
Cd-5TIA ^[e]	3.6 x 10 ⁻³	28 °C 98 %	0.16	Banerjee	2012 ⁷³
In-IA-2D-1 ^[f]	3.4 x 10 ⁻³	27 °C 98 %	0.61	Banerjee	2013 ⁹⁷
MgH ₆ ODTMP·6H ₂ O ^[g]	1.6 x 10 ⁻³	19 °C 100 %	0.31	Cabeza	2012 ⁹⁸
PCMOF-5 ^[h]	1.3 x 10 ⁻³	21 °C 98 %	0.16	Shimizu	2013 ⁷⁹
Fe(ox)·2H ₂ O ^[a]	1.3 x 10 ⁻³	25 °C 98 %	0.37	H. Kitagawa	2009 ⁹⁹
(NH ₄) ₄ [MnCr ₂ (ox) ₆]·4H ₂ O ^[a]	1.1 x 10 ⁻³	22 °C 96 %	0.23	Verdaguer	2011 ¹⁰⁰
[Zn(5-sipH)(bpy)]·DMF·2H ₂ O ^[i]	3.9 x 10 ⁻⁴	25 °C 60 %	n.a	H. Kitagawa	2014 ⁹²
GdHPA-II ^[j]	3.2 x 10 ⁻⁴	21 °C 98 %	0.23	Cabeza	2012 ¹⁰¹
Zn-(<i>m</i> -H ₆ L) ^[k]	1.4 x 10 ⁻⁴	41 °C 98 %	0.25	Cabeza	2013 ¹⁰²
Ca-BTC-H ₂ O ^[l]	1.2 x 10 ⁻⁴	25 °C 98 %	0.18	Banerjee	2012 ¹⁰³
{NH(prol) ₃ }[MCr(ox) ₃]·2H ₂ O ^[a,m] [M = Mn ^{II} , Fe ^{II} , Co ^{II}]	~1 x 10 ⁻⁴	25 °C 75 %	n/a	H. Kitagawa	2009 ¹⁰⁴
M(dhbq) <i>n</i> ·H ₂ O ^[n] (M = Mg, Mn, Ni, Zn)	1 x 10 ⁻⁴	25 °C 98 %	n.a	H. Kitagawa	2010 ¹⁰⁵
Mg-(<i>p</i> -H ₆ L) ^[o]	9.7 x 10 ⁻⁵	41 °C 98 %	0.50	Cabeza	2013 ¹⁰²
Me-FeCr ^[p]	8 x 10 ⁻⁵	RT 65 %	n/a	H. Kitagawa	2012 ¹⁰⁶
In-5TIA ^[e]	5.3 x 10 ⁻⁵	28 °C 98 %	0.14	Banerjee	2012 ⁷³
[Zn(<i>l</i> -L _{Cl} (Cl))]·2H ₂ O ^[q]	4.4 x 10 ⁻⁵	30 °C 98 %	0.34	Banerjee	2011 ⁷⁷
Sr-SBBA ^[r]	4.4 x 10 ⁻⁵	25 °C 98 %	0.56	Banerjee	2012 ⁷⁴

PCMOF-3 ^[s]	3.5 x 10 ⁻⁵	25 °C 98 %	0.17	Shimizu	2010 ⁷⁸
[Co ₂ Na(bptc) ₂][EmIm] ₃ ^[t]	2.6 x 10 ⁻⁵	RT RH n/a single crystal	0.49	Zheng	2011 ¹⁰⁷
Cu ₃ Mo ₅ P ₂ ^[u]	2.2 x 10 ⁻⁵	28 °C 98 %	0.23	Banerjee	2012 ¹⁰⁸
HKUST-1-H ₂ O ^[v]	1.5 x 10 ⁻⁵	RT MeOH vapour	n/a	Hupp	2012 ¹⁰⁹
[Cd ₂ (L) ₃ (DMF)(NO ₃) ₃](DMF) ₃ · (H ₂ O) ₈ ^[w]	1.3 x 10 ⁻⁵	25 °C 98 %	n.a	Bharadway H. Kitagawa	2014 ¹¹⁰
Ca-SBBA ^[r]	8.6 x 10 ⁻⁶	25 °C 98 %	0.23	Banerjee	2012 ⁷⁴
(NH ₄) ₂ (adp)[Zn ₂ (ox) ₃ ·3H ₂ O] ^[a,b]	6 x 10 ⁻⁶	25 °C 70 %	n/a	H. Kitagawa	2009 ⁸⁰
MIL-53(Fe)(COOH) ₂ ^[z]	2.0 x 10 ⁶	25 °C 95 %	0.21	H. Kitagawa	2011 ⁹³
Et-M _a M _b ^[z']	1 x 10 ⁻⁷	25 °C 65 %	n.a	H. Kitagawa	2013 ¹¹¹

[a] ox²⁻ = oxalate. [b] adp = adipic acid. [c] = H₈ODTMP = octamethylenediamine-*N,N,N',N'*-tetrakis(methylenephosphonic acid). [d] = PiPhtA = 5-(dihydroxyphosphophoryl) isophthalic acid. [e] 5TIA = 5-triazole isophthalic acid. [f] = IA = isophthalic acid. [g] = H₈DTMP = hexamethylene diamine-*N,N,N',N'*-tetrakis(methylenephosphonic acid). [h] PCMOF-5 = [La(H₅L)(H₂O)₄] (L = 1,2,4,5-tetrakisphosphonomethylbenzene). [i] 5-sipH₃ = 5-sulfoisophthalic acid; bpy = 4,4'-bipyridine. [j] H₃HPA = 2-hydroxyphosphonoacetic acid. [k] Zn-*[m-H₆L]* = Zn[(HO₃PCH₂)₂N(H)-CH₂C₆H₄CH₂N(H)(CH₂PO₃H)₂]. [l] = BTC = 1,3,5-benzenetricarboxylic acid. [m] NH(prol) = tri(3-hydroxypropyl) ammonium. [n] H₂(dhbq) = 2,5-dihydroxy-1,4-benzoquinone; *n* = 2, 2.5 or 3. [o] Mg-*[p-H₆L]* = Mg[(HO₃PCH₂)₂N(H)-CH₂C₆H₄CH₂N(H)(CH₂PO₃H)₂(H₂O)₂]. [p] Me-FeCr = NMe₃(CH₂CO₂H) [FeCr(ox)₃]. [q] L = 3-methyl-2-(pyridin-4-ylmethylamino)-butanoic acid. [r] = SBBA = 4,4'-sulfobisbenzoic acid. [s] PCMOF-3 = Zn₃(btp(H₂O)₂·2H₂O; btp = 1,3,5-benzene-triphosphonate. [t] = Na₄bptc = 2,2',4,4'-biphenyl tetracarboxylic sodium; EmIm⁺ = 1-ethyl-3-methyl imidazolium. [u] = Cu₃Mo₅P₂ = [Mo₅P₂O₂₃][Cu(phen)(H₂O)]₃; phen = phenanthroline. [v] Cu-(1,3,5-benzenetricarboxylate). [w] = H₂L⁺Cl⁻ = 1,3-bis-(4-carboxyphenyl)-imidazolium chloride. [z] MIL-53(Fe) = Fe(OH)(bdc)-(COOH)₂; H₂bdc = 1,4-benzenedicarboxylic acid. [z'] = Et-M_aM_b = [NEt₃(CH₂COOH)][M_a^{II}M_b^{III}(ox)₃]; M_aM_b = MnCr, FeCr, FeFe; ox = oxalate.

Anhydrous proton conducting MOFs:

Compared with the studies of hydrated MOFs as proton conductors, fewer examples of high conductivity under anhydrous conditions have been observed and investigated (Table 1.2). In 2009 S. Kitagawa and co-workers reported the proton conductivity of $2.2 \times 10^{-5} \text{ S cm}^{-1}$ at $120 \text{ }^\circ\text{C}$ for $[\text{Al}(\text{OH})(1,4\text{-ndc})](\text{ImH})$ (ndc = 1,4-naphthalenedicarboxylate) (Figure 1.10).¹¹² In the same year H. Shimizu investigated the proton conductivity of $\text{Tz}@ \beta\text{-PCMOF-2}$ [$\text{Na}_3(2,4,6\text{-trihydroxy-1,3,5-benzenetrisulfonate})$], which resulted in $2.5 \times 10^{-4} \text{ S cm}^{-1}$ at $150 \text{ }^\circ\text{C}$.⁷² These two examples were the first to show the possibility of using MOFs as proton conductors at high temperatures by doping with proton-carriers (imidazole and triazole); more work in this area rapidly followed.^{113–116}

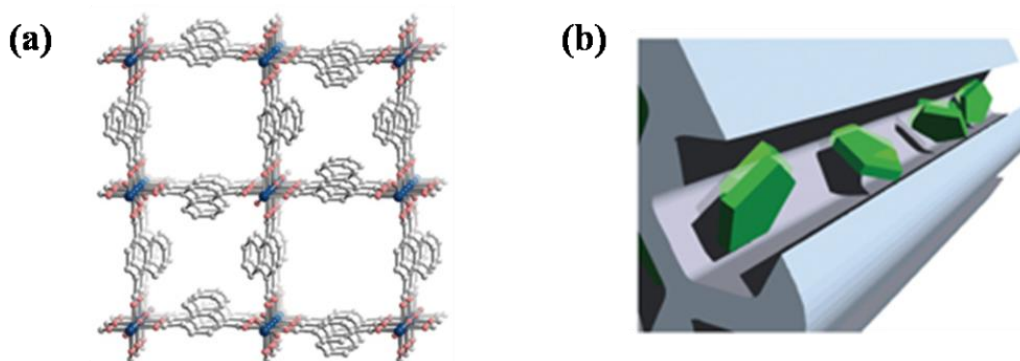


Figure 1.10. (a) Structural representation of $[\text{Al}(\mu_2\text{-OH})(1,4\text{-ndc})](\text{ImH})$ and (b) schematic representation of imidazole molecules accommodated in a nanochannel.¹¹²

Another approach to successfully obtain high proton conducting MOFs at high temperatures and under anhydrous conditions consider the substitution of water with higher boiling point solvents. For the first time, in 2012 Fedin *at al.* studied the proton conductivity of a MOF, MIL-101, soaked in different strong acids such as

H₂SO₄ and H₃PO₄.¹¹⁷ The proton conductivity of H₂SO₄@MIL-101 was found to be 1 x 10⁻² S cm⁻¹ at 150 °C.

These are very encouraging results however, these researches were unable to crystallographically locate the guest molecules loaded into the pores in order to rationalise the proton-hopping pathway.

Table 1.2. Proton conductivity of CPs and MOFs under anhydrous conditions.

Compound	σ (S cm ⁻¹)	Temp.	E _a (mV)	Author	Year ^{ref}
H ₂ SO ₄ @MIL-101 ^[a]	1 x 10 ⁻²	150 °C	0.42	Fedin	2012 ¹¹⁷
[Al(OH)(ndc)](His) ^[b,c]	1.7 x 10 ⁻³	150 °C	0.25	S. Kitagawa	2011 ¹¹⁸
[Zn ₃ (H ₂ PO ₄) ₆ (Hbim)] ^[d]	1.3 x 10 ⁻³	120 °C	0.5	S. Kitagawa	2013 ¹¹⁶
β -PCMOF-2(Tz) _{0.45} ^[e]	5 x 10 ⁻⁴	150 °C	0.34	Shimizu	2009 ⁷²
[Al(μ_2 -OH)(1,4-ndc)](ImH) ^[b]	2.2 x 10 ⁻⁵	120 °C	0.6	S. Kitagawa	2009 ¹¹²
[Zn(HPO ₄)(H ₂ PO ₄) ₂](ImH ₂) ₂ ^[b]	2.6 x 10 ⁻⁴	130 °C	0.47	S. Kitagawa	2012 ¹¹³
Zn(H ₂ PO ₄) ₂ (TzH) ₂ ^[e]	1.2 x 10 ⁻⁴	150 °C	0.6	S. Kitagawa	2012 ¹¹⁴
In-IA-2D-2 ^[f]	1.6 x 10 ⁻⁵	120 °C	n. a.	Banerjee	2013 ⁹⁷
[Co ₂ Na(bptc) ₂][EmIm] ₃ ^[g]	6.6 x 10 ⁻⁷	170 °C/	0.49	Zheng	2011 ¹¹⁹
MOF-74(Zn)-(His) ^[c,h]	4.3 x 10 ⁻⁹	146 °C	n. a.	S. Kitagawa	2012 ¹¹⁵

[a] MIL-101 = [Cr₃F(H₂O)₂O(1,4-bdc)₃]. [b] = 1,4-ndc = 1,4-naphthalene dicarboxylate; Im = imidazole. [c] = His = histamine. [d] = Hbim = benzimidazole. [e] = β -PCMOF-2 = Na₃(2,4,6-trihydroxy-1,3,5-benzenetrisulfonate); Tz = triazole. [f] = IA = isophthalic acid. [g] = Na₄bptc = 2,2',4,4'-biphenyltetracarboxylic sodium; EmIm⁺ = 1-ethyl-3-methyl imidazolium. [h] MOF-74(Zn) = [Zn₂(2,5-DOTP)]; DOTP = 2,5-dioxidoterephthalate.

Proton conductivity at high temperatures and high relative humidity:

Between 2011 and 2015, only a few proton conductivity studies on MOFs and CPs have been performed at high temperatures ($> 80\text{ }^{\circ}\text{C}$) and relatively high humidity ($\% \text{RH} > 90\%$) (Table 1.3). The outcomes of these experiments often indicate low conductivity and the experimental set up to recreate high humidity at elevated temperatures are challenging owing to condensation of water in the system. In 2011 H. Kitagawa *et al.* reported the study of MIL-53(M) analogues with selected functionalised ligands. The proton conductivity of these MOFs is reduced upon an increase of temperature from $2 \times 10^{-5}\text{ S cm}^{-1}$ at $25\text{ }^{\circ}\text{C}$ and $95\% \text{RH}$ to values comprised between 10^{-6} to 10^{-8} S cm^{-1} at $80\text{ }^{\circ}\text{C}$ and $95\% \text{RH}$.⁹³

In 2013 Shimizu *et al.* reported more encouraging results using a phosphonate-based ligand.⁷¹ The resultant MOF, PCMOF-2½ showed a proton conductivity of $2.1 \times 10^{-2}\text{ S cm}^{-1}$ at $85\text{ }^{\circ}\text{C}$ and $90\% \text{RH}$.⁷¹ Another example of good proton conductivity at high temperatures and high $\% \text{RH}$ was reported in 2013 by W. Mak and co-workers: they reported a new tetranuclear $\text{Cu}_4(\mu_3\text{-OH})_2$ based MOF with sulphonate-carboxylate ligands (Cu-DSOA) and exhibiting a proton conductivity of 10^{-3} S cm^{-1} at $85\text{-}100\text{ }^{\circ}\text{C}$ and $98\% \text{RH}$ (Figure 1.11).¹²⁰

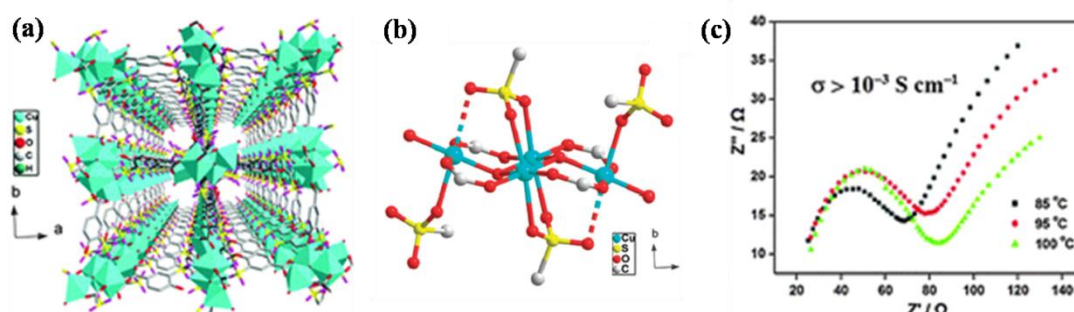


Figure 1.11. (a) Central projection of Cu-DSOA viewed down the c -axis. (b) View of tetrameric copper cluster. (c) Nyquist plot of Cu-DSOA.¹²⁰

Table 1.3. Proton conductivity of CPs and MOFs under hydrated conditions and high temperatures.

Compound	σ (S cm ⁻¹)	Temp. % RH	E _a (mV)	Author	Year ^{ref}
UiO-66(SO ₃ H) ₂ ^[a]	8.4 x 10 ⁻²	80 °C 90 %	0.32	Hong	2015 ¹²¹
PCMOF-10 ^[b]	3.5 x 10 ⁻²	70 °C 95 %	0.40	Shimizu	2015 ¹²²
PCMOF-2½ ^[c]	2.1 x 10 ⁻²	85 °C 90 %	0.21	Shimizu	2013 ⁷¹
PCMOF-5 ^[d]	4.0 x 10 ⁻³	62 °C 98 %	0.16	Shimizu	2013 ⁷⁹
Cu-DSOA ^[e]	1.9 x 10 ⁻³	85 °C 98 %	1.04	Mak	2013 ¹²⁰
[ZrF(H ₃ (O ₃ PCH ₂ NHCH ₂ COO) ₂)]	1 x 10 ⁻³	140 °C 95 %	-	Casciola	2013 ¹²³
[Cu(bpdc)(H ₂ O)] ^[f]	1.5 x 10 ⁻⁴	100 °C 98 %	n. a.	Duan	2013 ¹²⁴
Zr-L _{lp} @H ^[g]	5.4 x 10 ⁻⁵	80 °C 95 %	n. a.	Costantino	2012 ⁸⁸
[EuL(H ₂ O) ₃]·2H ₂ O ^[h]	1.6 x 10 ⁻⁵	75 °C 97 %	0.91	Zhang	2014 ¹²⁵
[DyL(H ₂ O) ₃]·2H ₂ O ^[h]	1.3 x 10 ⁻⁵	75 °C 97 %	0.87	Zhang	2014 ¹²⁵
Zr-L _{np} @H ^[g]	6.6 x 10 ⁻⁶	80 °C 95 %	n. a.	Costantino	2012 ⁸⁸
[(CH ₃) ₂ NH ₂][Zn ₃ Na ₂ (cpida) ₃]·2.5 DMF ^[i]	2.1 x 10 ⁻⁶	95 °C 97 %	0.81	Zhang	2013 ¹²⁶
MIL-53(Al)-OH ^[l]	1.9 x 10 ⁻⁶	80 °C 95 %	0.27	H. Kitagawa	2011 ⁹³
MIL-53(Al)-H ^[l]	3.6 x 10 ⁻⁷	80 °C 95 %	0.47	H. Kitagawa	2011 ⁹³
MIL-53(Al)-NH ₂ ^[l]	4.1 x 10 ⁻⁸	80 °C 95 %	0.45	H. Kitagawa	2011 ⁹³

[a] UiO-66(Zr) = Zr₆O₄(OH)₄(CO)₁₂. [b] PCMOF-10 = Mg₂(H₂O)₄(H₂L)·H₂O (H₆L = 2,5-dicarboxy-1,4-benzene-diphosphonic acid). [c] PCMOF-2½ = [Na₃L₁]_(0.66)[Na₃H₃L₂]_(0.34)(H₂O)_{1.2}; (Na₃L₁ = trisodium 2,4,6-trihydroxy-1,3,5-trisulfonate benzene; H₆L₂ = 1,3,5-benzenetriphosphonic acid). [d] PCMOF-5 = [La(H₅L)(H₂O)₄] (L = 1,2,4,5-tetrakisphosphonemethylbenzene). [e] Na₂H₃DSOA = disodium-2,2'-disulfonate-4,4'-oxydibenzoic acid. [f] H₂bpdc = 2,2'-bipyridyl-3,3'-dicarboxylic acid. [g] = H₈L = cyclohexyl,*N,N,N',N'*-diaminotetraphosphonate; *lp* = large pore; *np* = narrow pore. [h] L = N-phenyl-N'-phenyl bicyclo [2,2,2]-oct-7-ene-2,3,5,6-tetracarboxydiimide tetracarboxylic acid. [i] = H₃cpida = N-(4-carboxyphenyl) iminodiacetic acid. [l] = MIL-53(M) = M(OH)(bdc-(COOH)₂); H₂bdc = 1,4-benzenedicarboxylic acid.

Films and composite MOFs for proton conductivity:

The bulk proton conductivity of MOFs is most frequently measured in samples pressed into pellets, or more rarely on single crystals. For practical applications of MOFs as electrolytes in PEM-FCs the ultimate challenge is to fabricate membranes from these crystalline materials. Attempts to make thin-films of MOFs were conducted by H. Kitagawa *et al.* who reported the layer-by-layer growth of highly crystalline surface coordination polymers (SCPs).¹²⁷ Many studies on deposition of MOFs as thin films or composite membranes for different applications have been performed.^{128,129}

In 2013 H. Kitagawa and co-workers reported the first study of the electrical properties of a highly oriented and crystalline MOF nano-film revealing high proton conductivity ($3.9 \times 10^{-3} \text{ S cm}^{-1}$ at 25 °C and 98 % RH) and low activation energy (0.28 eV).¹³⁰ A nano-sheet of Cu-TCPP, [H₂TCPP = 5,10,15,20-tetrakis(4-carboxyphenyl)porphyrin], containing dangling carboxyl groups was deposited layer-by-layer onto a pre-fabricated Cr/Au electrode supported on a SiO₂/Si wafer to form thin film channel electrodes (Figure 1.12).

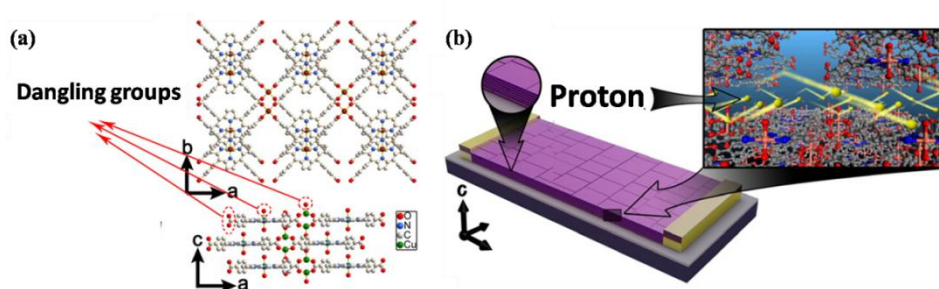


Figure 1.12. (a) Modelled crystal structure of the MOF nanofilm and (b) schematic of the nanosheet-constructed MOF nanofilm for electrical measurement.¹³⁰

In the same year T. Xu *et al.* reported proton conductivity studies of mixed matrix membranes (MMM) fabricated from the combination of Fe-MIL-101-NH₂, ([Fe₃(O)(bdc-NH₂)₃(OH)(H₂O)₂]*n*H₂O (where bdc-NH₂ = 2-aminoterephthalate), with a sulfonated polymer.¹³¹ The proton conductivity of the MMM reached a maximum of 1 x 10⁻¹ S cm⁻¹ at 25 °C and 98 % RH with 6 % MOF loading. By increasing the temperature to 90 °C and 98 % RH the conductivity was found of 2.5 x 10⁻¹ S cm⁻¹.

1.4.4 Conclusions and future perspectives

Metal-organic frameworks have been recently identified as promising candidates for use as electrolytes in PEM-FCs. They provide good models to give insight into better understanding the chemistry and mechanism behind the proton conduction process and how to improve a conductor material. This has been achieved by the design of targeted MOFs through the careful choice of organic ligands with protic chemical functionalities, and inclusion of guest proton-carriers inside the pores. During the last five years intensive studies on MOFs as efficient proton conductors have been pursued proving that these materials have good potential at different working conditions. Examples of MOFs as proton conductors under humid and anhydrous conditions and even more recently, attempts of incorporation into composite membranes have been reported. Despite the recent progress, many challenges must be overcome before it is possible to exploit MOFs for commercial applications and compete with the current PEMs used in industry. Nafion has been developed and optimised for industrial applications for over 30 years and the barrier for acceptance of new materials in commercial applications is high. The field of MOFs as proton conductors is still at preliminary stages. However, the results found so far will

encourage researchers to achieve higher levels of performances. In the next few years proton conducting modular porous solids are likely to become an important class of materials in electrochemical devices as proton conductors.

1.5 The scope of this Thesis

This Thesis focuses on the development of a method to study the proton conductivity in solid materials, and on the synthesis and characterisation of new proton conducting MOFs together with strategies to enhance their proton conducting properties.

The study of MOFs as proton conducting materials is a new research area and this is the first time such application has been studied through the Schröder group. Chapter 2 gives some insights about the basic concepts behind the impedance measurement and the analysis of the data. In order to perform impedance measurements on MOFs, the experimental set up and two home-made conductivity cells have been designed, assembled and tested becoming a fundamental part of this work. Chapter 3 describes the design and synthesis of two novel proton conducting MOFs, NOTT-500(Ni, Co). These MOFs are synthesised from phosphonate-based ligands which were chosen to increase the amount of protons within the framework. Structural analysis of NOTT-500(Ni, Co) revealed free hydroxyl groups from the ligand (P-OH) and coordinated water molecules (M-OH₂) organised in an efficient proton-hopping pathway for charge transfer. A detailed characterisation of their properties together with impedance studies combined with QENS analysis is presented. Chapter 4 and 5 focus on strategies to increase the proton conducting properties of MOFs. Chapter 4 describes the synthesis and characterisation of a new family of lanthanide MOFs. The design of two novel approaches to enhance the proton conductivity of these

complexes are herein presented for the first time. In Chapter 5 the proton conductivity of post-synthetically modified NOTT-300(Al), obtained by insertion of proton-carrier guest molecules loaded inside the pores of the framework are presented. Impedance measurements performed before and after the loading of the guest showed increased proton conducting properties.

1.6 References

- (1) Devanathan, R. *Energy Environ. Sci.* **2008**, *1*, 101–109.
- (2) Busquin, P. “*World energy, technology and climate policy outlook (WETO) 2030*”, **2003**, 1-107.
- (3) Abas, N.; Kalair, A.; Khan, N. *Futures* **2015**, *69*, 31–49.
- (4) Larcher, D.; Tarascon, J. *Nature Chem.* **2014**, *7*, 19–29.
- (5) Mahmud, K. *Int. J. Sci. Adv. Technol.* **2013**, *54*, 97–104.
- (6) Jakob, M.; Hilaire, J. *Nature* **2015**, *517*, 150–151.
- (7) Mouratiadou, I.; Luderer, G.; Bauer, N.; Kriegler, E. *Climatic Change* **2015**, 1-15.
- (8) McJeon, H.; Edmonds, J.; Bauer, N.; Krey, V.; Hilaire, J. *Nature* **2014**, *514*, 482–200.
- (9) Bauer, N.; Bosetti, V.; Hamdi-Cherif, M.; Kitous, A.; McCollum, D.; Méjean, A.; Rao, S.; Turton, H.; Paroussos, L.; Ashina, S.; Calvin, K.; Wada, K.; Van Vuuren, D. *Technol. Forecast. Soc. Change* **2013**, *90*, 243–256.
- (10) Ross, D. K. *Vacuum* **2006**, *80*, 1084–1089.
- (11) Mcglade, C.; Ekins, P. *Nature* **2014**, *517*, 187–190.
- (12) Hoffmann P. “*Tomorrow’s Energy: Hydrogen, Fuel Cells, and the Prospects for a Cleaner Planet*” **2012**.
- (13) Pollet, B. G.; Staffell, I.; Shang, J. L. *Electrochimica Acta* **2012**, *84*, 235–249.
- (14) Carrette, L.; Friedrich, A.; Stimming, U. *Fuel Cells* **2001**, *1*, 5-39.
- (15) Dupuis, A.-C. *Progress in Materials Science* **2011**, *56*, 289–327.
- (16) Ellis, M. W.; Spakovsky, M. R. Von; Nelson, D. J. *Proceedings of the IEEE* **2001**, *89*, 1808–1818.
- (17) Debe, M. K. *Nature* **2012**, *486*, 43–51.

- (18) Diat, O.; Gebel, G. *Nature Mater.* **2008**, *7*, 13–14.
- (19) Ortiz-Rivera, E. I.; Reyes-Hernandez, A. L.; Febo, R. A. *Electric Power IEEE* **2007**, 117–122.
- (20) Acres, G. *J. Power Sources* **2001**, *100*, 60–66.
- (21) Burke, K. A. “*Fuel Cells For Space Science Applications*” **2003**, 1-10.
- (22) Singh, T.; Kumar, A. *Int. J. Engineering Research* **2013**, *155*, 152–155.
- (23) Thomas, S.; Zalbowitz, M. *Fuel Cells Green Power* **1999**, 1–36.
- (24) Barbir, F.; Gómez, T. *Int. J. Hydrogen Energy* **1997**, *22*, 1027–1037.
- (25) Perry, M. L.; Fuller, T. F. *J. Electrochemical Soc.* **2002**, *149*, S59–S67.
- (26) Kordesch, K.; Hacker, V.; Gsellmann, J.; Cifrain, M.; Faleschini, G.; Enzinger, P.; Fankhauser, R.; Ortner, M.; Muhr, M.; Aronson, R. R. *J. Power Sources* **2000**, *86*, 162–165.
- (27) Steele, B. C.; Heinzl, A. *Nature* **2001**, *414*, 345–352.
- (28) Neergat, M.; Shukla, A. *J. Power Sources* **2001**, *102*, 317–321.
- (29) Sammes, N.; Bove, R.; Stahl, K. *Current Opinion in Solid State and Materials Science* **2004**, *8*, 372–378.
- (30) Ralph, T. R. *Platinum Metals Rev.* **1997**, *41*, 102–148.
- (31) Vishnyakov, V. M. *Vacuum* **2006**, *80*, 1053–1065.
- (32) McLean, G. *Int. J. Hydrogen Energy* **2002**, *27*, 507–526.
- (33) Carlson, E.; Zogg, R.; Sriramulu, S.; Roth, K.; Brodrick, J. *ASHRAE J.* **2007**, *49*, 50–51.
- (34) Bischoff, M. *J. Power Sources* **2006**, *160*, 842–845.
- (35) Lukas, M. D.; Lee K. Y.; Ghezal-Ayagh, H. *IEEE Transaction Energy Conversion* **1999**, *14*, 1651–1657.

- (36) Dicks A. L. *Current Opinion in Solid State and Materials Science* **2004**, *8*, 379-383.
- (37) Ormerod, R. M. *Chem. Soc. Rev.* **2003**, *32*, 17–28.
- (38) Yokokawa, H.; Tu, H.; Iwanschitz, B.; Mai, A. *J. Power Sources* **2008**, *182*, 400–412.
- (39) Minh, N. Q. *Solid State Ionics* **2004**, *174*, 271–277.
- (40) Buratto, S. K. *Nature Nanotechnol.* **2010**, *5*, 176.
- (41) Kreuer, K. D. *J. Membrane Science* **2001**, *185*, 29–39.
- (42) Park, K.; Lee, J.; Kim, H.-M.; Choi, K.-S.; Hwang, G. *Scientific Reports* **2014**, *4*, 4592–4597.
- (43) Casciola, M.; Alberti, G.; Sganappa, M.; Narducci, R. *J. Power Sources* **2006**, *162*, 141–145.
- (44) Peckham, T. J.; Holdcroft, S. *Adv. Mater.* **2010**, *22*, 4667-4690.
- (45) Samulski, E. T. *Nature Mater.* **2011**, *10*, 486–487.
- (46) Yang, C.; Costamagna, P.; Srinivasan, S.; Benzinger, J.; Bocarsly, A. B.; Benziger, J. *J. Power Sources* **2001**, *103*, 1–9.
- (47) Li, Q.; He, R.; Jensen, O. J.; Bjerrum, N. J. *Chem. Mater.* **2003**, *15*, 4896–4915.
- (48) Kim, D. J.; Jo, M. J.; Nam, S. Y. *Journal of Industrial and Engineering Chemistry* **2014**, *21*, 36–52.
- (49) Costamagna, P.; Yang, C.; Bocarsly, A. B.; Srinivasan, S. *Electrochimica Acta* **2002**, *47*, 1023–1033.
- (50) Yoon, M.; Suh, K.; Natarajan, S.; Kim, K. *Angew. Chem.* **2013**, *52*, 2688–2700.

- (51) Ramaswamy, P.; Wong, N. E.; Shimizu, G. K. H. *Chem. Soc. Rev.* **2014**, *43*, 5913–5932.
- (52) Kitagawa, S.; Kitaura, R.; Noro, S. *Angew. Chem.* **2004**, *43*, 2334–2375.
- (53) Hoskins, B. F.; Robson, R. *J. Am. Chem. Soc.* **1989**, *111*, 5962–5964.
- (54) Hoskin, B. F.; Robson, R. *J. Am. Chem. Soc.* **1990**, *112*, 1546–1554.
- (55) Robson, R. *Dalton Trans.* **2008**, 5113–5131.
- (56) Yaghi, O. M.; Li G.; Li, H. *Nature* **1995**, *378*, 703–706.
- (57) Furukawa, H.; Ko, N.; Go, Y. B.; Aratani, N.; Choi, S. B.; Choi, E.; Yazaydin, A. O.; Snurr, R. Q.; O’Keeffe, M.; Kim, J.; Yaghi, O. M. *Science* **2010**, *329*, 424–428.
- (58) MacGillivray, L. J. “*Metal-Organic Frameworks: Design and Application*” John Wiley and Sons, **2010**.
- (59) Yang, W.; Lin, X.; Jia, J.; Blake, A. J.; Wilson, C.; Hubberstey, P.; Champness, N. R.; Schröder, M. *Chem. Commun.* **2008**, *3*, 359–361.
- (60) Jia, J.; Lin, X.; Wilson, C.; Blake, A. J.; Champness, N. R.; Hubberstey, P.; Walker, G.; Cussen, E. J.; Schröder, M. *Chem. Commun.* **2007**, *3*, 840–842.
- (61) Farha, O. K.; Yazaydin, A. Ö.; Eryazici, I.; Malliakas, C. D.; Hauser, B. G.; Kanatzidis, M. G.; Nguyen, S. T.; Snurr, R. Q.; Hupp, J. T. *Nature Chem.* **2010**, *2*, 944–948.
- (62) Suh, M. P.; Park, H. J.; Prasad, T. K.; Lim, D. *Chem. Rev.* **2012**, *112*, 782–835.
- (63) Dailly, A.; Poirier, E. *Energy Environ. Sci.* **2011**, *4*, 3527–3534.
- (64) Yan, Y.; Lin, X.; Yang, S.; Blake, A. J.; Dailly, A.; Champness, N. R.; Hubberstey, P.; Schröder, M. *Chem. Commun.* **2009**, *9*, 1025–1027.

- (65) Yan, Y.; Telepeni, I.; Yang, S.; Lin, X.; Kockelmann, W.; Dailly, A.; Blake, A. J.; Lewis, W.; Walker, G. S.; Allan, D. R.; Barnett, S. A.; Champness, N. R.; Schröder, M. *J. Am. Chem. Soc.* **2010**, *132*, 4092–4094.
- (66) Li, J.; Sculley, J.; Zhou, H. *Chem. Rev.* **2012**, *112*, 869–932.
- (67) Dhakshinamoorthy, A.; Alvaro, M.; Hwang, Y. K.; Seo, Y. K.; Corma, A.; Garcia H. *Dalton Trans.* **2011**, 10719–10724.
- (68) Gagnon, K. J.; Perry, H. P.; Clearfield, A. *Chem. Rev.* **2012**, *112*, 1034–1054.
- (69) Whitesides, G. M.; Boncheva, M. *Proceedings of the National Academy of Science* **2002**, *99*, 4769–4774.
- (70) Stock, N.; Biswas, S. *Chem. Rev.* **2012**, *112*, 933–969.
- (71) Kim, S.; Dawson, K. W.; Gelfand, B. S.; Taylor, J. M.; Shimizu, G. K. H.; Gelfand, B. S. *J. Am. Chem. Soc.* **2013**, *135*, 963–966.
- (72) Hurd, J.; Vaidhyanathan, R.; Thangadurai, V.; Ratcliffe, C. I.; Moudrakovski, I. L.; Shimizu, G. K. H. *Nature Chem.* **2009**, *1*, 705–710.
- (73) Panda, T.; Kundu, T.; Banerjee, R. *Chem. Commun.* **2012**, *48*, 5464–5466.
- (74) Kundu, T.; Sahoo, S. C.; Banerjee, R. *Chem. Commun.* **2012**, *48*, 4998–5000.
- (75) Wu, B.; Lin, X.; Ge, L.; Wu, L.; Xu, T. *Chem. Commun.* **2012**, *3*, 1–13.
- (76) Phang, W. J.; Lee, W. R.; Yoo, K.; Kim, B.; Hong, C. S. *Dalton Trans.* **2013**, 7850–7853.
- (77) Sahoo, S. C.; Kundu, T.; Banerjee, R. *J. Am. Chem. Soc.* **2011**, *133*, 17950–17958.
- (78) Taylor, J. M.; Mah, R. K.; Moudrakovski, I. L.; Ratcliffe, C. I.; Vaidhyanathan, R.; Shimizu, G. K. H. *J. Am. Chem. Soc.* **2010**, *132*, 14055–14057.

- (79) Taylor, J. M.; Dawson, K. W.; Shimizu, G. K. H. *J. Am. Chem. Soc.* **2013**, *135*, 1193–1196.
- (80) Sadakiyo, M.; Yamada, T.; Kitagawa, H. *J. Am. Chem. Soc.* **2009**, *131*, 9906–9907.
- (81) Kanda S., Yamashita K., Ohkawa K. *Bull. Chem. Soc. Jpn.* **1979**, *52*, 3296–3301.
- (82) Furukawa, H.; Cordova, K. E.; O’Keeffe, M.; Yaghi, O. M. *Science* **2013**, *341*, 974–988.
- (83) Jiménez-García, L.; Kaltbeitzel, A.; Enkelmann, V.; Gutmann, J. S.; Klapper, M.; Müllen, K. *Adv. Funct. Mater.* **2011**, *21*, 2216–2224.
- (84) Kreuer, K. D.; Paddison, S. J.; Spohr, E.; Schuster, M. *Chem. Rev.* **2004**, *104*, 4637–4678.
- (85) Kreuer, K.; Rabenau, A.; Weppner, W. *Angew. Chem.* **1982**, *21*, 208–209.
- (86) Kreuer, K.-D. *Chem. Mater.* **1996**, *8*, 610–641.
- (87) Agmon, N. *Chem. Phys. Lett.* **1995**, *244*, 456–462.
- (88) Costantino, F.; Donnadio, A.; Casciola, M. *Inorg. Chem.* **2012**, *51*, 6992–7000.
- (89) Liang, X.; Zhang, F.; Feng, W.; Zou, X.; Zhao, C.; Na, H.; Liu, C.; Sun, F.; Zhu, G. *Chem. Sci.* **2013**, *4*, 983–992.
- (90) Sadakiyo, M.; Yamada, T.; Honda, K.; Matsui, H.; Kitagawa, H. *J. Am. Chem. Soc.* **2014**, *136*, 7701–7707.
- (91) Dong, X.; Hu, X.; Yao, H.; Zang, S.; Hou, H. *Inorg. Chem.* **2014**, *53*, 12050–12057.
- (92) Ramaswamy, P.; Matsuda, R.; Kosaka, W.; Akiyama, G.; Jeon, H. J.; Kitagawa, S. *Chem. Commun.* **2014**, *50*, 1144–1146.

- (93) Shigematsu, A.; Yamada, T.; Kitagawa, H. *J. Am. Chem. Soc.* **2011**, *133*, 2034–2036.
- (94) Nagarkar, S. S.; Unni, S. M.; Sharma, A.; Kurungot, S.; Ghosh, S. K. *Angew. Chem.* **2014**, *53*, 2638–2642.
- (95) Colodrero, R. M. P.; Olivera-Pastor, P.; Losilla, E. R.; Aranda, M. A. G.; Leon-Reina, L.; Papadaki, M.; McKinlay, A. C.; Morris, R. E.; Demadis, K. D.; Cabeza, A. *Dalton Trans.* **2012**, 4045-4051.
- (96) Bazaga-Garcia, M.; Colodrero, R. M. P.; Papadaki, M.; Garczarek, P.; Zon, J.; Olivera-Pastor, P.; Losilla, E. R.; León-Reina, L.; Aranda, M. A. G.; Choquesillo-Lazarte, D.; Demadis, D. K.; Cabeza, A. *J. Am. Chem. Soc.* **2014**, *136*, 5731–5739.
- (97) Panda, T.; Kundu, T.; Banerjee, R. *Chem. Commun.* **2013**, *49*, 6197–6199.
- (98) Colodrero, R. M. P.; Olivera-Pastor, P.; Losilla, E. R.; Hernández-Alonso, D.; Aranda, M. A. G.; Leon-Reina, L.; Rius, J.; Demadis, K. D.; Moreau, B.; Villemin, D.; Palomino, M.; Rey, F.; Cabeza, A. *Inorg. Chem.* **2012**, *51*, 7689–7698.
- (99) Yamada, T.; Sadakiyo, M.; Kitagawa, H. *J. Am. Chem. Soc.* **2009**, *131*, 3144–3145.
- (100) Pardo, E.; Train, C.; Gontard, G.; Boubekour, K.; Fabelo, O.; Liu, H.; Dkhil, B.; Lloret, F.; Nakagawa, K.; Tokoro, H.; Ohkoshi, S. I.; Verdaguer, M. *J. Am. Chem. Soc.* **2011**, *133*, 15328–15331.
- (101) Colodrero, R. M. P.; Papathanasiou, K. E.; Stavgianoudaki, N.; Olivera-Pastor, P.; Losilla, E. R.; Aranda, M. A. G.; León-Reina, L.; Sanz, J.; Sobrados, I.; Choquesillo-Lazarte, D.; García-Ruiz, J. M.; Atienzar, P.; Rey, F.; Demadis, K. D.; Cabeza, A. *Chem. Mater.* **2012**, *24*, 3780–3792.

- (102) Colodrero, R. M. P.; Angeli, G. K.; Bazaga-Garcia, M.; Olivera-Pastor, P.; Villemain, D.; Losilla, E. R.; Martos, E. Q.; Hix, G. B.; Aranda, M. A. G.; Demadis, K. D.; Cabeza, A. *Inorg. Chem.* **2013**, *52*, 8770–8783.
- (103) Mallick, A.; Kundu, T.; Banerjee, R. *Chem. Commun.* **2012**, *48*, 8829.
- (104) Shigematsu, A.; Sadakiyo, M.; Miyagawa, T. *J. Am. Chem. Soc.* **2009**, *131*, 13516–13522.
- (105) Morikawa S., Yamada T., K. H. *Bull. Chem. Soc. Jpn.* **2010**, *83*, 42–48.
- (106) Sadakiyo, M.; Okawa, H.; Shigematsu, A.; Ohba, M.; Yamada, T.; Kitagawa, H. *J. Am. Chem. Soc.* **2012**, *134*, 5472–5475.
- (107) Chen W. X., Xu H. R., Zhuang G. L., Long L. S., Huang R. B., Z. L. S. *Chem. Commun.* **2011**, *47*, 11933–11935.
- (108) Dey, C.; Kundu, T.; Banerjee, R. *Chem. Commun.* **2012**, *48*, 266–268.
- (109) Jeong, N. C.; Samanta, B.; Lee, C. Y.; Farha, O. K.; Hupp, J. T. *J. Am. Chem. Soc.* **2012**, *134*, 51–54.
- (110) Sen, S.; Yamada, T.; Kitagawa, H.; Bharadwaj, P. K. *Cryst. Growth Des.* **2014**, *14*, 1240–1244.
- (111) Okawa, H.; Sadakiyo, M.; Yamada, T.; Maesato, M.; Ohba, M.; Kitagawa, H. *J. Am. Chem. Soc.* **2013**, *135*, 2256–2262.
- (112) Bureekaew, S.; Horike, S.; Higuchi, M.; Mizuno, M.; Kawamura, T.; Tanaka, D.; Yanai, N.; Kitagawa, S. *Nature Mater.* **2009**, *8*, 831–836.
- (113) Horike, S.; Umeyama, D.; Inukai, M.; Itakura, T.; Kitagawa, S. *J. Am. Chem. Soc.* **2012**, *134*, 7612–7615.
- (114) Umeyama, D.; Horike, S.; Inukai, M.; Itakura, T.; Kitagawa, S. *J. Am. Chem. Soc.* **2012**, *134*, 12780–12785.

- (115) Inukai, M.; Horike, S.; Umeyama, D.; Hijikata, Y.; Kitagawa, S. *Dalton Trans.* **2012**, 13261.
- (116) Umeyama, D.; Horike, S.; Inukai, M.; Kitagawa, S. *J. Am. Chem. Soc.* **2013**, *135*, 11345–11350.
- (117) Ponomareva, V. G.; Kovalenko, K. A.; Chupakhin, A. P.; Dybtsev, D. N.; Shutova, E. S.; Fedin, V. P. *J. Am. Chem. Soc.* **2012**, *134*, 15640–15643.
- (118) Umeyama, D.; Horike, S.; Inukai, M.; Hijikata, Y.; Kitagawa, S. *Angew. Chem.* **2011**, *50*, 11706–11709.
- (119) Chen, W.-X.; Xu, H.-R.; Zhuang, G.-L.; Long, L.-S.; Huang, R.-B.; Zheng, L.-S. *Chem. Commun.* **2011**, *47*, 11933–11935.
- (120) Dong, X.-Y.; Wang, R.; Li, J.-B.; Zang, S.-Q.; Hou, H.-W.; Mak, T. C. W. *Chem. Commun.* **2013**, *49*, 10590–10592.
- (121) Phang, W. J.; Jo, H.; Lee, W. R.; Song, J. H.; Yoo, K.; Kim, B.; Hong, C. S. *Angew. Chem.* **2015**, *54*, 5142–5146.
- (122) Ramaswamy, P.; Wong, N. E.; Gelfand, B. S.; Shimizu, G. K. H. *J. Am. Chem. Soc.* **2015**, *137*, 7640–7643.
- (123) Taddei, M.; Donnadio, A.; Costantino, F.; Vivani, R.; Casciola, M. *Inorg. Chem.* **2013**, *52*, 12131–12139.
- (124) Wei, M.; Wang, X.; Duan, X. *Chem. Eur. J.* **2013**, *19*, 1607–1616.
- (125) Zhu, M.; Hao, Z.-M.; Song, X.-Z.; Meng, X.; Zhao, S.-N.; Song, S.-Y.; Zhang, H.-J. *Chem. Commun.* **2014**, *50*, 1912–1914.
- (126) Meng, X.; Song, X. Z.; Song, S. Y.; Yang, G. C.; Zhu, M.; Hao, Z. M.; Zhao, S. N.; Zhang, H. J. *Chem. Commun.* **2013**, *49*, 8483–8485.
- (127) Kanaizuka, K.; Haruki, R.; Sakata, O.; Yoshimoto, M.; Akita, Y.; Kitagawa, H. *J. Am. Chem. Soc.* **2008**, *130*, 15778–15779.

- (128) Bradshaw D.; Garai A.; Huo J. *Chem. Soc. Rev.* **2012**, *41*, 2344–2381.
- (129) Shah, M. N.; Gonzalez, M. A; McCarthy, M. C.; Jeong, H.-K. *Langmuir* **2013**, *29*, 7896–7902.
- (130) Xu, G.; Otsubo, K.; Yamada, T.; Sakaida, S.; Kitagawa, H. *J. Am. Chem. Soc.* **2013**, *135*, 7438–7441.
- (131) Wu, B.; Lin, X.; Ge, L.; Wu, L.; Xu, T. *Chem. Commun.* **2013**, *49*, 143–145.

Chapter 2

Electrochemical Impedance Spectroscopy:

Experimental design

List of Contents

2.1 Introduction to Electrochemical Impedance Spectroscopy	45
2.1.1 Direct (DC) and alternating (AC) current.....	46
2.1.2 Electrochemical cells	49
2.1.3 Nyquist plot.....	51
2.1.4 Bode plot.....	53
2.1.5 Equivalent circuit components.....	54
2.1.6 Proton conductivity.....	56
2.1.7 How to calculate the resistance from the Nyquist plot	57
2.1.8 Aims of Chapter 2.....	60
2.2 Results and discussion.....	60
2.2.1 Set up of the experiment	60
2.2.2 Sample preparation: tests with imidazole	63
2.2.3 Design of the conductivity cells.....	66
2.2.3.1 Design of cell A	66
2.2.3.2 Design of cell B	70
2.2.4 Control of the relative humidity	71
2.3 Conclusions	74
2.4 References	75

2.1 Introduction to Electrochemical Impedance Spectroscopy

In recent years, Electrochemical Impedance Spectroscopy (EIS) has played an important role in electrochemistry and materials science. EIS is routinely used in the characterisation of ongoing processes such as coatings, discharge and charge of batteries, electrochemical reactions in fuel cells, corrosion of metals and in many other electrochemical phenomena.¹⁻³ Impedance spectroscopy is a non-destructive technique and so can provide time dependent information about the properties of a system. Therefore, EIS has also been extensively used to investigate the dynamics of bound or mobile charge in the bulk or interfacial regions of any kind of solid or liquid material; semiconductors and insulators.¹

The general approach of EIS studies is to apply an electrical stimulus (voltage), in a defined frequency range, to the electrodes and observe the resulting response (current). The input (voltage) and output (current) signals, both in time-domains, are hardware and software processed into complex quantities which are frequency dependent and plotted in the Nyquist and Bode plot (Sections 2.1.3 and 2.1.4). The analysis of the data allow to calculate the conductivity of the sample as described in details in the following Sections.

When an electrochemical cell is electrically stimulated, a consequent electrical response dependent on a multitude of microscopic processes in the electrolyte is recorded. The processes promoted by an applied electrical potential include the transfer of charged particles at the electrode–electrolyte interfaces. The flow rate of charged particles (current) depends on the ohmic resistance of the electrodes and the electrolyte. The flow may be further impeded by structural anomalies such as grain boundaries and point defects in the bulk of the material. This is true especially in the case of microcrystalline powders, in which the single particles are disordered and the

whole sample presents structural defects that could influence the local electric field. In the majority of cases, however, it is quite common and well accepted to simplify the system by assuming smooth electrode–electrolyte interfaces with one crystallographic orientation.

An attractive aspect of EIS as a tool to investigate electrical properties of materials is the direct parallel that often exists between the charge transport processes in a real system and that of equivalent circuits of ideal resistors, capacitors and inductors. Therefore, it is possible to model the impedance data with an equivalent circuit which is representative of the physical processes taking place in the system under investigation.

Nowadays, commercially available instruments allow the measurement of high-quality impedance data as a function of frequencies in a range from millihertz to megahertz. The impedance analyser is normally interfaced to computers equipped with software for the analysis of the data. Thanks to the great improvement of these technologies, impedance studies are becoming increasingly popular as more electrochemists, materials scientists and engineers understand the theoretical basis for impedance spectroscopy and gain expertise in the interpretation of impedance data.

2.1.1 Direct (DC) and alternating (AC) current

Direct current (DC) is defined as a flow of electric charge in one constant direction and is produced by sources such as batteries, thermocouples and solar cells.

The DC potential E , measured in *volt* (V), applied to a circuit is defined by Ohm's Law as the product of the resultant current I , measured in *ampere* (A), and the

resistance R , measured in *ohm* (Ω), of the circuit (Equation 1). In DC theory, the potential and the current are always in phase.

$$E = I * R \quad (1)$$

Real circuits exhibit more complex behaviour and Ohm's Law, expressed in Equation (1), can only be used to simulate ideal resistors. An ideal resistor follows Ohm's Law at all current and voltage levels which are in phase with each other, and its resistance is independent to the frequency. Therefore, the resistance for non-ideal resistors needs to be replaced with the impedance (Z), a more general circuit parameter. Similarly to resistance, impedance is also frequency dependent and measures the ability of a circuit to resist the flow of electrical current.⁴

Alternating current (AC) impedance spectroscopy is the most common technique used to measure the conductivity of a material. This technique describes the response of a circuit to an alternating voltage as a function of frequency. In AC theory the direction of the electrical current rapidly reverses direction and a phase shift occurs between voltage and current. When an alternating current (AC) passes through a circuit the analogous Ohm's Law equation is expressed by Equation (2).^{1,4}

$$E = I * Z \quad (2)$$

The impedance (Z) is defined as the AC equivalent of resistance and is measured in *ohm* (Ω). In an AC circuit, capacitors (C) and inductors (L) are additional elements which impede the flow of current. The opposition to the current of capacitors and inductors is symbolised by X (X_C and X_L) and is measured in *ohm*.³ The impedance of a capacitor decreases as the frequency is raised while the impedance of an inductor increases as the frequency increases (Section 2.1.5).

AC methods are finding increasing applications in electrochemical research thanks to the fact that only small voltages, which do not influence the electrical properties of

the sample, need to be applied. This allows the investigation of low conductivity media. The use of small excitation amplitudes in EIS also guarantees the pseudo-linear response of the cell. In a linear or pseudo-linear system, a sinusoidal potential results in a sinusoidal current response shifted in phase.¹

One of the most commonly used test functions for a circuit is the sine wave. The reason sine waves are used is because they allow a convenient representation of complex functions and any signal going into a circuit can be represented by a sum of sine waves of varying frequency and amplitude.

If the potential excitation applied to a system is a sinusoidal at a particular frequency, ($\Delta E \sin \omega t$), then the response to this potential is also a sinusoidal containing the excitation frequency and its harmonics, with a value of $\Delta I \sin(\omega t + \phi)$. In these equations I is the current, ω is the frequency in radians per second ($\omega = 2\pi f$) and ϕ is the phase shift in radians.

Figure 2.1 represents a sine wave of the potential (E) applied across a circuit and the resulting AC current (I) measured. The potential and the current waveforms have different amplitude and are shifted in time.

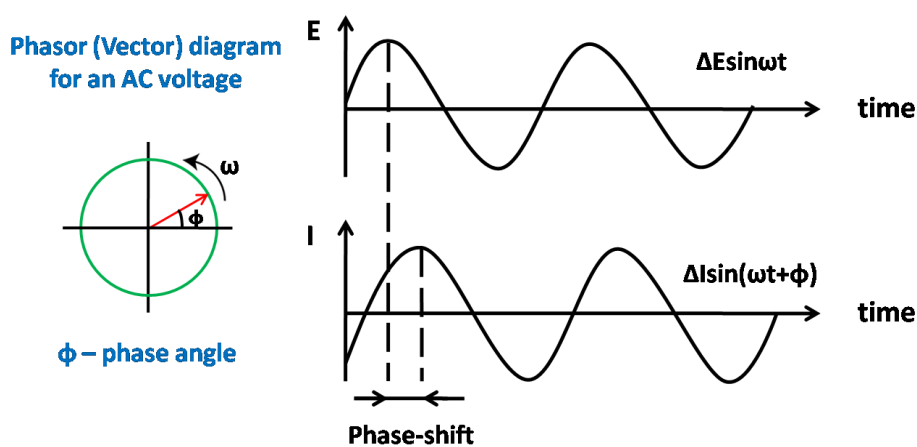


Figure 2.1. AC waveforms for an applied potential (E) and resulting current (I) and representation of the phase angle in the phasor diagram.

2.1.2 Electrochemical cells

Electrochemical cells consist of two identical electrodes positioned between the electrolyte, which can be a liquid or a solid. Solid electrolytes, such as those studied in this work, are normally circular cylinders or rectangular parallelepipeds of known dimensions. A potential (E) is applied across the first electrode (or working electrode) positioned at the interface of the electrolyte investigated. The difference of the potential between the two electrodes causes the flow of a current through the electrolyte and the current is passed to the secondary (or counter) electrode. This type of arrangement is used to study the conducting properties of a material when its resistance is the main parameter.

The impedance spectra are conveniently plotted in real (I') and imaginary (I'') axes by using a mathematical convention in order to represent the AC current as a vector defined as the sum of its real and imaginary components (Equation 3).

$$I_{\text{Total}} = I' + I'' * j \quad (3)$$

Where j is the imaginary number defined as $\sqrt{-1}$.

The real and imaginary components of an AC current or voltage are defined with respect to some reference waveform which allows them to be expressed as a vector. Vector analysis provides a convenient method of characterising an AC waveform, since it allows for a description of the wave in terms of its amplitude and phase characteristics.

As a result of this mathematical manipulation, it is possible to use Equation 2 to calculate the impedance vector (Equation 4).

$$Z_{\text{Total}} = (E' + E''j) / (I' + I''j) \quad (4)$$

Where both the AC potential vector, E , and the current vector, I , are expressed as complex numbers.

The resulting vector expression for the AC impedance is shown in Equation 5.

$$Z_{\text{Total}} = Z' + Z''j \quad (5)$$

Where Z_{Total} is identified in terms of the same coordinate axes as the current and voltage vectors.

The absolute magnitude of the impedance is represented by the length of the vector and can be expressed with Equation 6.

$$|Z| = \sqrt{(Z')^2 + (Z'')^2} \quad (6)$$

And the phase angle can be identified by Equation 7.

$$\phi = \tan^{-1}(Z'' / Z') \quad (7)$$

The real component is in phase with the reference waveform, and the imaginary component is exactly 90° out of phase (Figure 2.2).

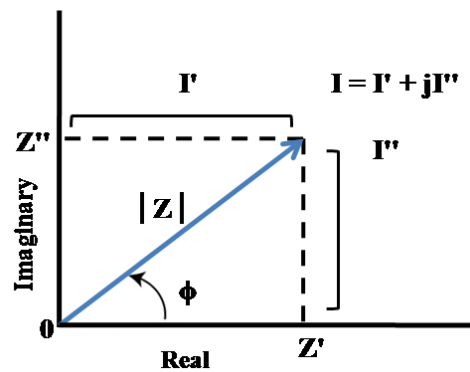


Figure 2.2. Representation of the impedance vector in AC current in terms of Real (I') and Imaginary (I'') coordinates.

When the electrolyte is a pure resistor of magnitude R , then the impedance is equal to the resistance ($Z = R$) with phase $\phi = 0$ for all frequencies (Figure 2.3a). In the opposite situation, in which the electrolyte is a pure capacitor (C), the impedance becomes dependent on the frequency ($Z = 1/\omega C$), in particular when ω increases Z decreases, and is phase shifted 90° with respect to the voltage (Figure 2.3b).⁵

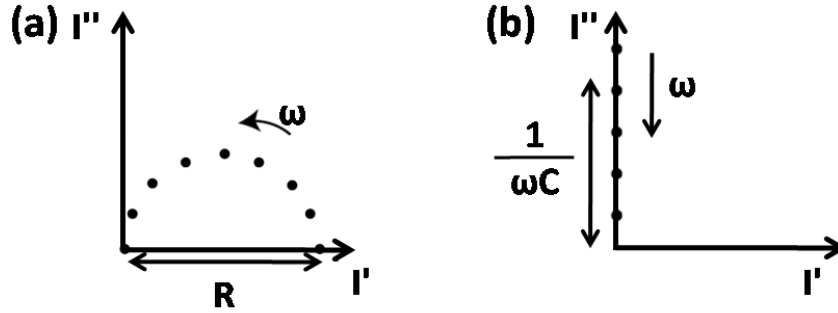


Figure 2.3. Complex plane impedance spectrum plotted against real (I') and imaginary (I'') components of (a) pure resistor and (b) pure capacitor.

2.1.3 Nyquist plot

A popular way to represent electrochemical impedance data as a function of the real (Z') and imaginary (Z'') impedance is the EIS Nyquist plot. On the y-axis the negative imaginary impedance (Z'') is indicative of the capacitive (C) and inductive (L) character of the cell. The x-axis represents the real impedance of the cell (Z') at each excitation frequency value, ω (Figure 2.4).

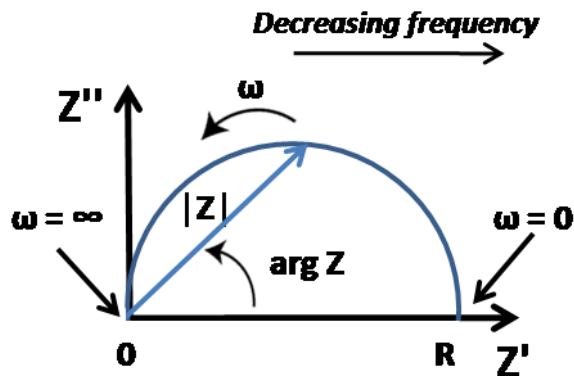


Figure 2.4. Representation of Nyquist plot for a simple electrochemical system with impedance vector as a function of Real (Z') and Imaginary (Z'') coordinates.

The main advantage of using a Nyquist plot to represent impedance data is its shape; the semi-circle in Figure 2.4 is representative of the resistance of a material. The shape of one semi-circle does not change when the ohmic resistance changes and each semi-circle is characteristic of a single time constant, τ , (defined as $R \cdot C$). However, electrochemical impedance plots often contain several time constants which result in different semi-circles. Moreover, the shape of the Nyquist curve provides insight into possible conduction mechanisms or governing phenomena.

Unfortunately, the Nyquist plot format of representing impedance data has the disadvantage of the frequency dependence being implicit. In fact, from the data points on the plot it is not possible to define at which frequency they were recorded and therefore, the AC frequency of selected data points should be indicated.

In the case of EIS data, in which impedance falls as frequency rises, it is common practice that high frequency data are on the left side of the Nyquist plot while the low frequency data are displayed on the right. In general, for ionic conductors, the Nyquist plot consists of a semi-circle at high frequencies and a tail at low frequencies (Figure 2.5). The semi-circle gives information about the resistance of the material while the tail normally provides information concerning charge transfer and diffusion phenomena.

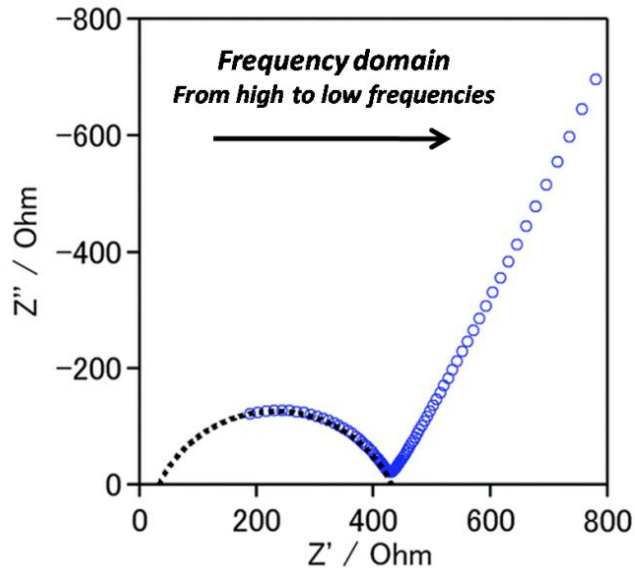


Figure 2.5. Example of a Nyquist plot for a proton conducting material; semi-circle at high frequencies and tail at lower frequencies.

2.1.4 Bode plot

The difficulties in representing EIS data come from the need to plot a complex number, (Z''_j), as a function of frequency (ω). Unlike the Nyquist plot, the Bode plot has the advantage of explicitly displaying the frequency dependence of the impedance of the material under study.⁶

Bode plots are a standard format to represent the impedance magnitude and phase angle of a system as a function of frequency (Figure 2.6). The Bode plot consists of frequency along the x -axis and the y -axis representing both the logarithmic of the absolute value of the impedance ($|Z|$) as calculated by Equation 6, and the phase-shift (ϕ) of the impedance. The magnitude of the impedance ($|Z|$) is expressed on a logarithmic scale so that a wide impedance range can be easily plotted.

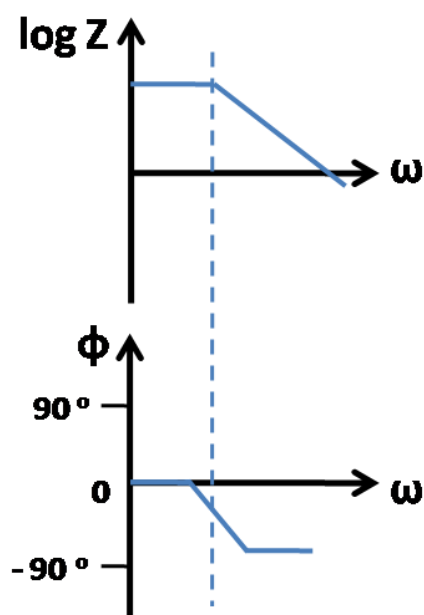


Figure 2.6. Example of Bode plots as a function of the magnitude of the impedance in the logarithmic scale (*top*) and the phase-shift (ϕ) (*bottom*).

In conclusion, Bode plots correlate the impedance with the frequency at which it has been recorded, while a Nyquist plot offers convenient visualisation of the ohmic resistance. Therefore, the most clear way to represent impedance spectroscopy data is to show both the Nyquist and Bode plots.

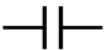
2.1.5 Equivalent circuit components

One of the main advantages of EIS is the possibility of representing an electrochemical cell with a purely electronic circuit to verify a mechanistic model for the system under study.^{1,6} The equivalent circuit consists of a combination of resistors (R), capacitors (C) and inductors (L), and the circuit can be deduced from the impedance spectrum. Once a particular model is chosen, it is possible to correlate physical or chemical properties of the investigated material with circuit elements and

extract numerical values (such as resistance, capacitance) by fitting the data to the equivalent circuit model.

In Table 2.1 are listed the most common circuit components, the equations representing the relationship between current and potential and the impedance. Very few electrochemical cells can be modelled using a single equivalent circuit element. Instead, EIS models usually consist of a network of elements combined in series and/or in parallel.

Table 2.1. Common electrical components of a circuit.

Component	Symbol	Current vs Potential	Impedance
Resistor		$E = IR$	$Z = R$
Inductor		$E = L \, di/dt$	$Z = j\omega L$
Capacitor		$I = C \, dE/dt$	$Z = 1/j\omega C$

The impedance of a resistor is independent of the frequency and has only a real component. The absence of imaginary impedance implies that the current through a resistor is always in phase with the potential. In the case of inductors, the impedance has an imaginary component and Z increases together with the frequency. As a result, the current of an inductor is phase shifted 90° with respect to the voltage. In the opposite way, the impedance of capacitors decreases as the frequency is raised. Capacitors also have an imaginary impedance component and the current passing through them is phase shifted 90° with respect to the voltage.

In EIS experiments capacitors do not always behave ideally; instead, they act like a constant phase element (CPE).^{5,7} CPE is expressed by Equation 8 and it is often used to simulate equivalent circuits for real systems.

$$Z_{\text{CPE}} = 1 / [(j\omega)^\alpha Y_o] \quad (8)$$

In Equation 8, Y_o is equal to the capacitance C and α is the exponent equal to values generally less than 1 ($\alpha = 1$ for an ideal capacitor). It is generally accepted that α accounts for the non-ideal behaviour of a capacitor ($\alpha < 1$) and is commonly treated as an empirical constant with no real physical basis.

The use of CPE components to describe a real system becomes very helpful as it takes into account the microscopic properties of a material, which are often not homogeneously distributed. This is common in polycrystalline materials where the solid electrode-solid electrolyte interface on the microscopic level is not always smooth and the surface is not uniform. In fact, more often the sample contains a large number of defects and local charge inhomogeneities. In these cases the bulk materials do not exhibit ideal behaviour; the grains are misorientated to each other leading to reductions in conductivity with respect to the single crystal.

When equivalent elements are used to take into account the nature of the material under study, the simulation of impedance data with equivalent circuits is widely accepted and many examples have been reported.⁷⁻¹³

2.1.6 Proton conductivity

An ionic conductor is an electrolyte, typically a solid material, in which the electrical charge is transported and carried by charged particles. Proton conductivity can be considered a special case of ionic transport where H^+ cations are transported through a material when an external potential is applied. Typical solid materials for practical

applications are polymers or ceramics which can play a role in the proton conduction of fuel cells (Chapter 1, Section 1.3).

Two main mechanisms have been proposed to describe the proton transport: the Vehicle mechanism and the diffusion (or Grotthuss) mechanism.¹³⁻¹⁸ The Vehicle mechanism considers the diffusion of protons assisted by a vehicle such as H_3O^+ .¹³⁻¹⁶ Whereas, in the Grotthuss mechanism protons are transferred within hydrogen bonds from one site to another.^{13-15,17,18}

The resistance of a proton conductor depends on the ionic concentration and the geometry of the sample in which the current is carried (Equation 9).

$$R = \rho * (l / A) \quad (\text{Equation 9})$$

To measure the resistance of solids the material is normally pressed into a pellet where l (expressed cm) and A (expressed in cm^2) are respectively the thickness and the surface area of the pellet. ρ is the solution resistivity (expressed in ohms). The reciprocal of ρ is the conductivity of the solution, σ , and is expressed in Equation 10.¹⁹

$$\sigma = l / (R * A) \quad (\text{Equation 10})$$

The conductivity, σ , is expressed in Siemens per centimetre (S cm^{-1}), where Siemens is the reciprocal of ohm ($1 \text{ S} = 1 \text{ ohm}^{-1}$).

2.1.7 How to calculate the resistance from the Nyquist plot

The proton conductivity (σ) of a solid material is calculated from the pellet physical parameters (thickness, l , and surface area, A) and the bulk resistance (R_b) by following Equation 10. The thickness (l) and surface area (A) of the pellet are measured with a micrometer before the performance of the experiment. The value of the bulk resistance (R_b) is obtained from the analysis of the Nyquist plot. Three

different approaches are known to extrapolate R_b according to the shape of the Nyquist plot and the properties of the material under study.

In the case of Nyquist plots showing well defined semi-circles at high frequencies, the value of R_b is determined by its diameter which can be obtained by fitting the semi-circle using ZView 2 software.⁷ This value of R_b is used to calculate the conductivity according to Equation 10 (Figure 2.7).

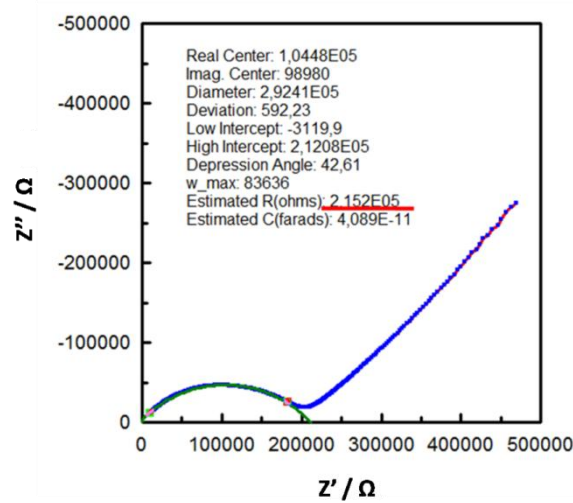


Figure 2.7. Determination of R_b by fitting the diameter of the semi-circle at high frequencies.

Many studies describe the evaluation of the bulk resistance by simply taking a linear extrapolation of the impedance spike in the Nyquist plot to the Z' -axis and by accepting the intercept as the R_b value. This approach is well accepted when the semi-circle is not complete and there are not enough points for the fitting (Figure 2.17b).^{7,9,20–22} Examples of not complete semi-circles where R_b was determined by the intercept with the x-axis in the Nyquist plot are reported in Figure 2.8.

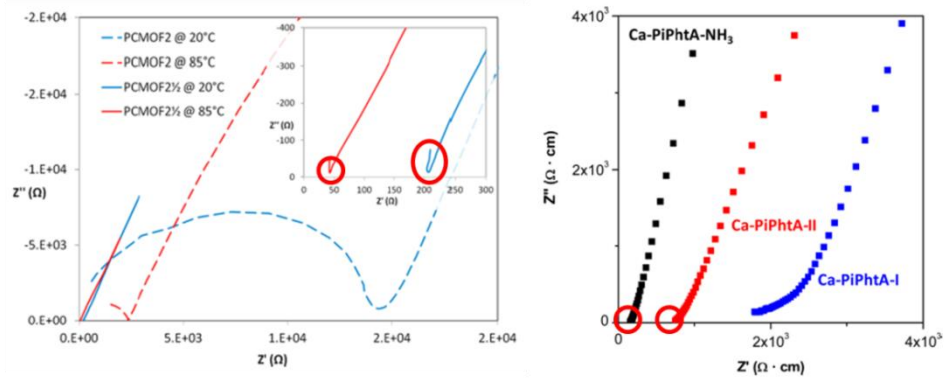


Figure 2.8. Determination of R_b using the lower intercept of the Nyquist plot with the x -axis.^{20,22}

Finally, when it is possible, the mechanism of the conduction can be modelled with an equivalent circuit which is normally a combination of resistors and capacitors combined in series and/or in parallel (Section 2.1.5).⁹ By modelling the data it is possible to assign values to each circuit component and R_b is used to calculate the conductivity (Figure 2.9).^{9,10,13,23–25}

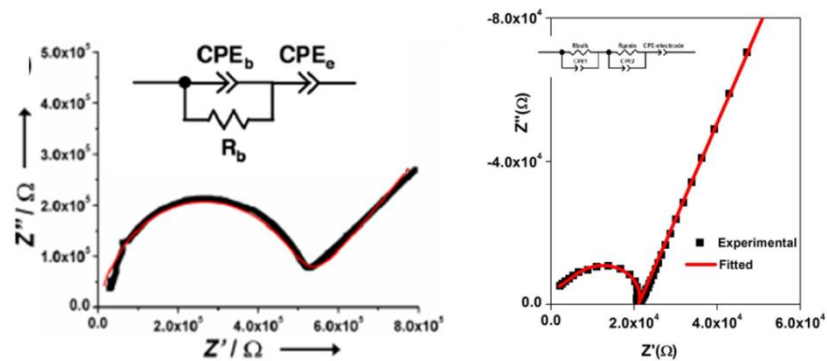


Figure 2.9. Determination of R_b by modelling the fitting of the Nyquist plot with an equivalent circuit.^{10,23}

It is important to consider each of the three methods before calculating σ and using the R_b value which better explains the properties of the material under study and better fits the experimental data.

2.1.8 Aims of Chapter 2

The main objective of the work presented in this Thesis is to design and synthesise MOFs for proton conduction applications. The investigation of proton conductivity is a new research area in the MOF field and this represents the first time such work has been carried out in the Schröder group. The system for the impedance analysis was newly designed, constructed and tested, becoming a key part of this work. A detailed description of the experimental set up for impedance measurements and tests for its calibration (performed on imidazole samples) are described in this Chapter.

2.2 Results and discussion

2.2.1 Set up of the experiment

On the basis of previous literature studies, a method for measuring the impedance of solid inorganic conductors was developed. The general approach followed to perform the measurements is illustrated in Figure 2.10. Pellet samples are sandwich-held between two electrodes connected to the impedance analyser, the Solartron SI 1260 Impedance/Gain phase Analyser. The analyser applies a sinusoidal excitation signal (alternating potential, 100 mV), to the working electrode in a frequency range between megahertz and millihertz. The electric field causes the ions to move back and forth producing a current. The sinusoidal output signal, a current, is recorded at the second electrode and sent to the analyser. The analyser measures the current which is correlated to the resistance of the sample by the modified Ohm's law (Equation 2).

Nyquist and Bode plots are produced and displayed in the computer using the SMaRT v. 3.2.1 software. From the Bode plot it is possible to follow the impedance as a function of the frequency (Section 2.1.4) and the Nyquist plot is used to

determine the resistance (Section 2.1.3) required to calculate the conductivity of the sample (Equation 10).

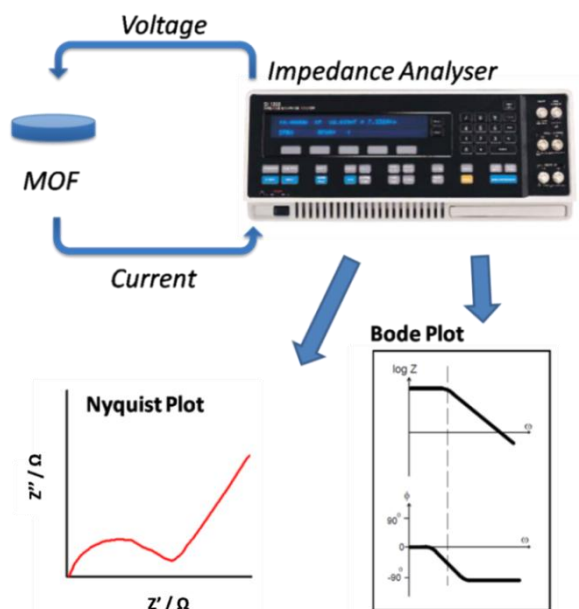


Figure 2.10. General scheme for the proton conductivity experiment; impedance analyser connected to the sample and representation of the measured data in a Nyquist and Bode plots.

In most cases, the proton conductivity of MOFs is extremely sensitive to relative humidity (% RH) and temperature, and the control of these parameters during the measurements becomes crucial in order to investigate the properties of a material in depth. The schematic of the newly constructed conductivity measurement system is showed in Figure 2.11. It consists of four main parts: the impedance analyser, the conductivity cell with sample holder, the humidification system and the temperature controller. The impedance analyser is connected by 50 Ω coaxial cables with BNC connectors to a homemade cell containing the sample. Relative humidity (% RH) control is performed by saturating the conductivity cell with humidified moistures carried by nitrogen (Section 2.2.4). To ensure the % RH remains constant throughout

an experiment, a commercial probe is inserted into the cell and the % RH is measured (Rotronic HC2-C04, humidity measuring range: 0 % to 100 %; temperature limits: -40 °C to 85 °C). The temperature of the sample is regulated by inserting the cell inside a heating block interfaced with a temperature controller. The presence of a thermocouple in proximity to the sample allows to accurately measure the temperature.

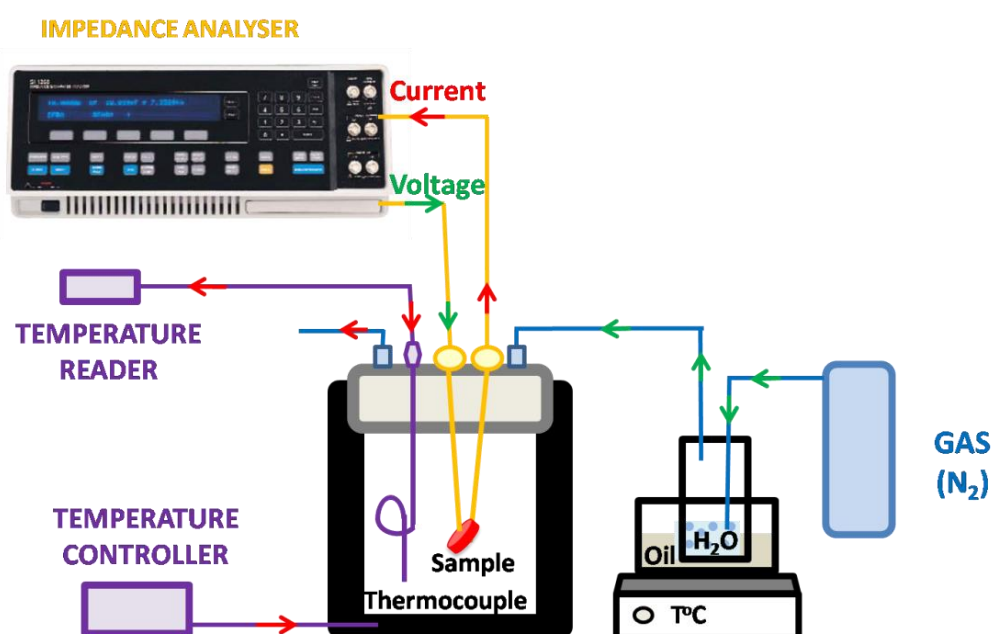


Figure 2.11. Schematic of the experimental system for proton conductivity measurements; impedance analyser, conductivity cell, humidification system and the temperature controller.

The preparation of the sample and the contact sample-electrodes are also essential to achieve accurate and repeatable measurements.

2.2.2 Sample preparation: tests with imidazole

The first step to perform proton conductivity measurements involves the preparation of the sample. A standard procedure inspired by previous proton conductivity studies on solid materials was tested and optimised by using imidazole as a reference material. Imidazole was chosen to test and calibrate the newly developed conductivity cells as a cheap and readily available material with known conductivity of $10^{-8} \text{ S cm}^{-1}$.^{19,26,27} Consequently, all the experimental examples illustrated in this Chapter were with imidazole.

AC impedance spectroscopy measurements of solid materials were performed on a dense pellet of the sample under investigation. A known mass of sample was ground into a fine powder using mortar and pestle and pressed under 5 tons for 5 minutes into a pellet of fixed diameter (0.8 cm). The physical parameters of the final pellet (thickness, l , and surface area, A) were measured before the start of the experiment using a micrometer (RS electronic digital caliper). This is a key step as the measured proton conductivity directly depends on these parameters (Equation 10).

The Nyquist plot of imidazole was collected under N_2 atmosphere at 25°C and 0 % RH, (Figure 2.12). As shown in the Bode plots, the data was collected in the frequency range from 8.7 MHz to 36 Hz as a function of the absolute resistivity and phase shift. The semi-circle at high frequency in the Nyquist plot represents the bulk resistance of the specimen. The measurements were repeated on two different batches of sample and for each batch three measurements were collected. The mean value of the proton conductivity was found to be $8.03(05) \times 10^{-8} \text{ S cm}^{-1}$, where the number in brackets indicates the calculated standard deviation.

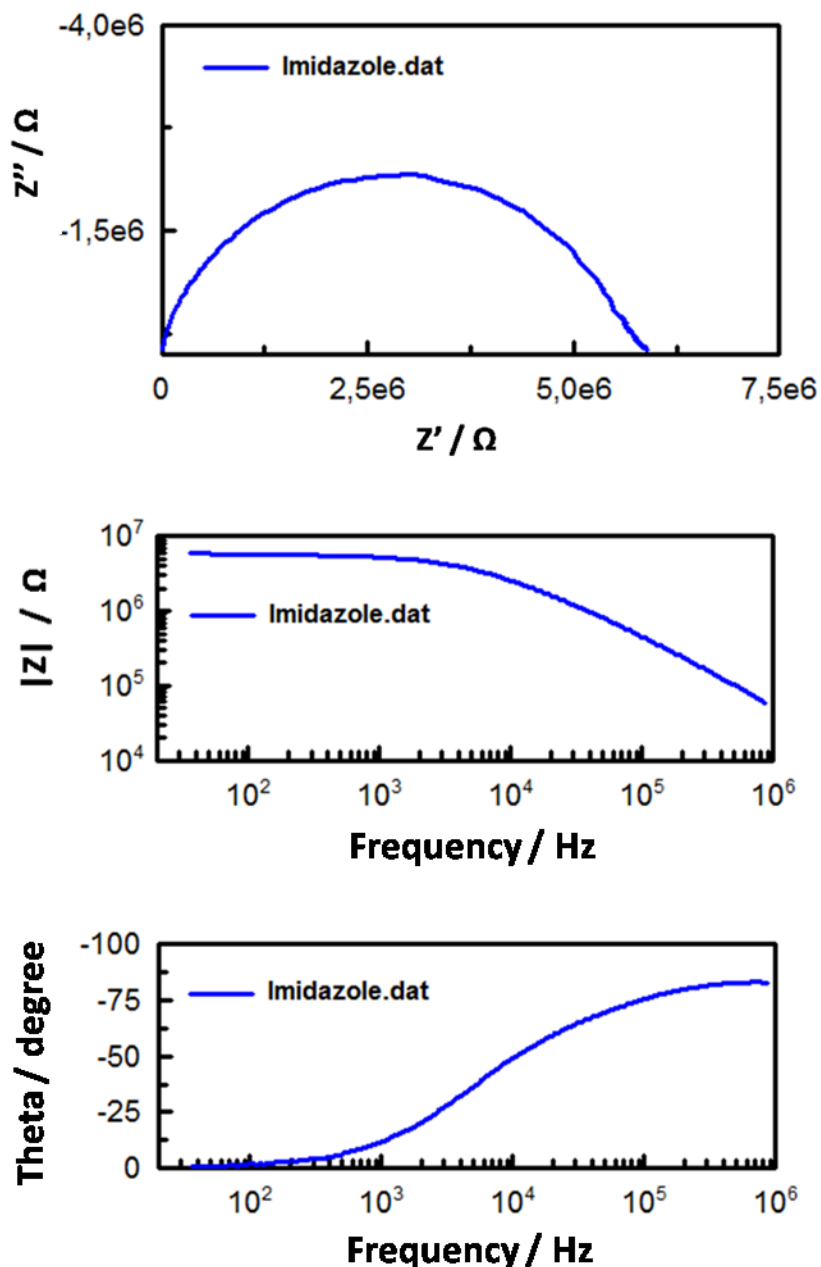


Figure 2.12. Nyquist and Bode plot of imidazole collected in the frequency range between 36 Hz and 8.7 MHz.

Whilst preparing the sample it is important to properly grind the material under study and to pack the fine powder obtained into a dense pellet. It was experimentally proved that the intrinsic conductivity of the pellet can be directly affected by the pressure applied to compress the sample. Figure 2.13 shows the Nyquist plot for

imidazole pressed under 1 ton and 5 tons collected under N_2 atmosphere at $25\text{ }^\circ\text{C}$ and 0 % RH. The conductivity of imidazole pressed at 1 ton was measured as $4.18(06) \times 10^{-8} \text{ S cm}^{-1}$ compared to $8.03(05) \times 10^{-8} \text{ S cm}^{-1}$ for the sample compressed at 5 tons.

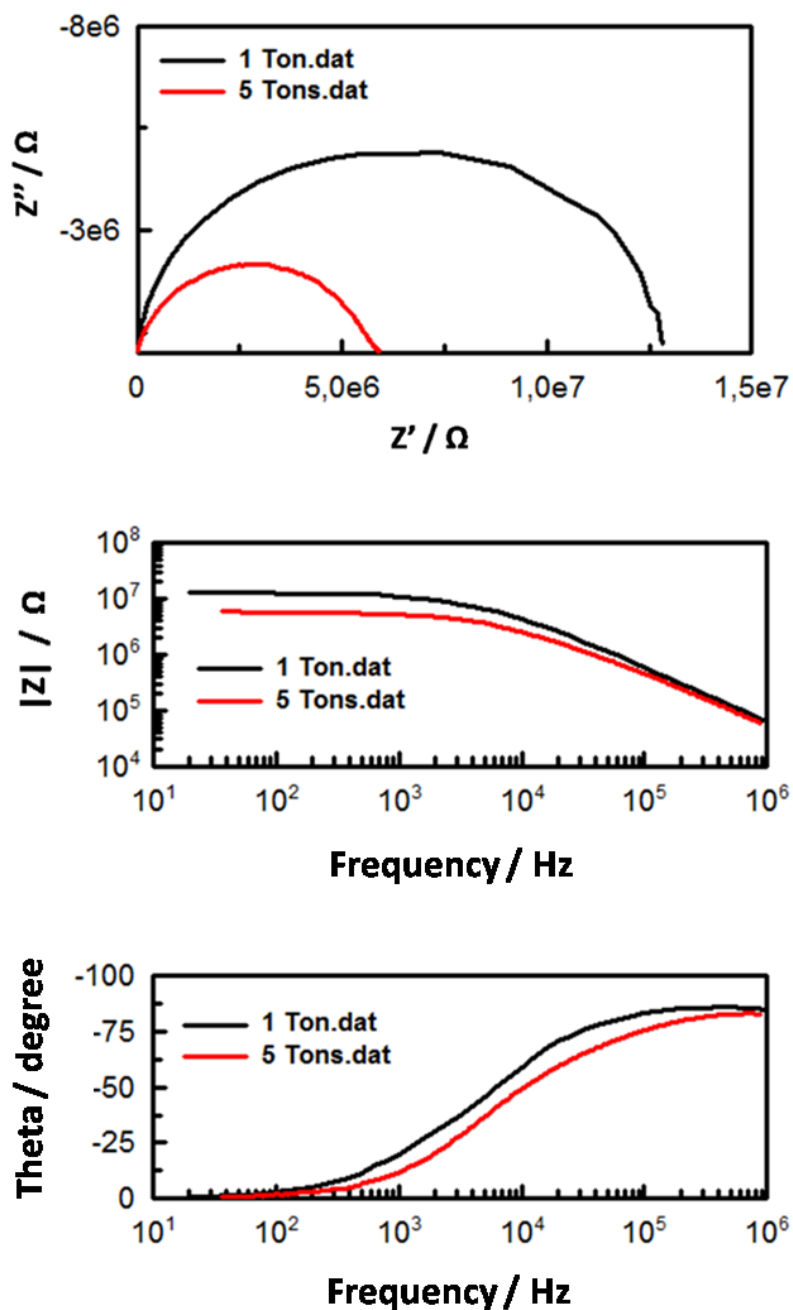


Figure 2.13. Nyquist and Bode plot of imidazole pressed at different pressures; 1 ton (*black*), 5 tons (*red*).

2.2.3 Design of the conductivity cells

One of the main components of the system designed to measure impedance data is the conductivity cell. Unfortunately, no commercial cells to load the sample and connect it to the impedance analyser were available. Therefore, a newly designed sample holder was needed in order to measure the impedance of the MOFs. For this reason, two homemade conductivity cells were designed and tested.

2.2.3.1 Design of cell A

In the early stages of this research, the first proton conductivity cell (A) was designed, built and tested (Figure 2.14). The sample holder of cell A consists of a PTFE body located inside the cell (Figure 2.14a). The sample is pressed into a pellet and both sides of its sections are in contact with two stainless steel electrodes (Figure 2.14b). A spring located inside the PTFE sample holder helps to ensure a good contact between the sample and the two electrodes (Figure 2.14c). To facilitate the interaction between the sample and the atmosphere inside the cell, holes of 1mm in diameter were drilled in the PTFE holder in correspondence where the pellet sits. A thermocouple was placed between the walls of the PTFE body in proximity to the sample in order to monitor the temperature. PTFE was chosen as an inert and thermally stable material up to 120 °C. The conductivity cell is tightened inside a can to preserve the sample environment and inserted into a heating block connected with an external digital thermal controller (Figure 2.14d).

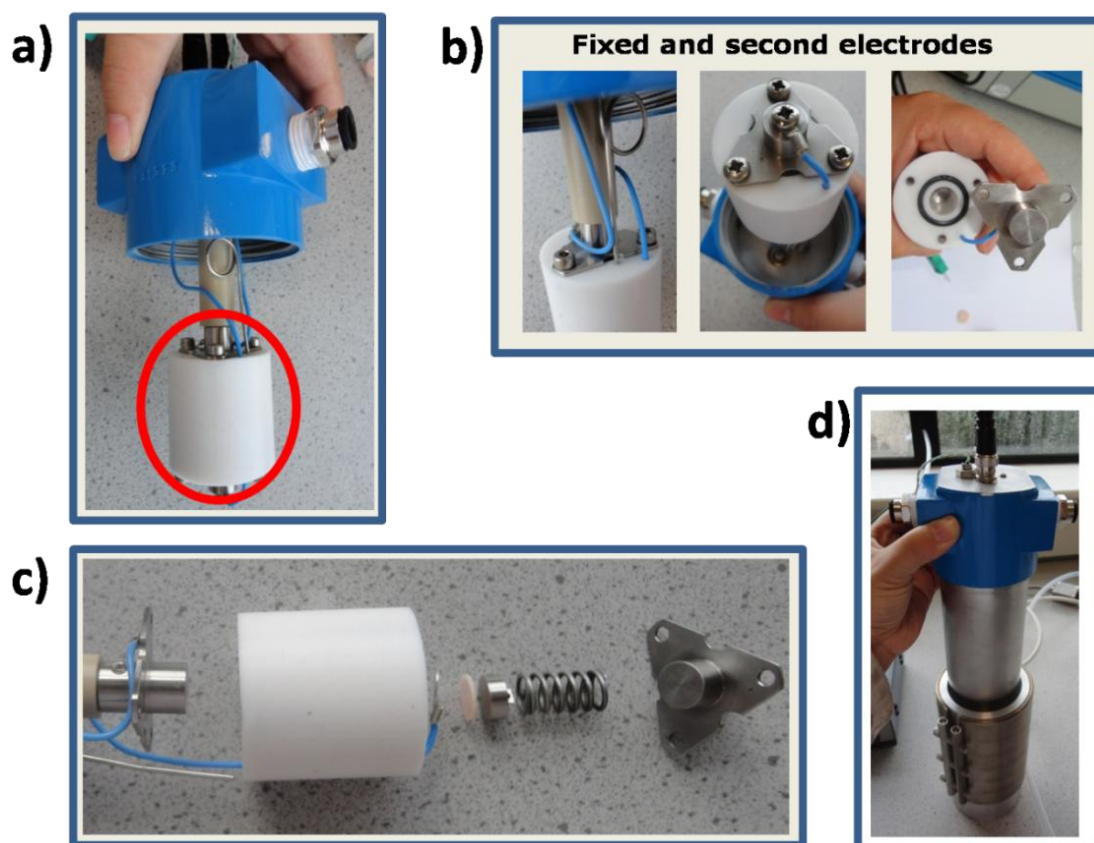


Figure 2.14. Representation of cell A; (a) conductivity cell and PTFE sample holder, (b) fixed and second electrodes, (c) electrodes, sample and spring, (d) conductivity cell tightened inside a can and inserted into a heating block.

The intrinsic conduction of a material is often affected by the quality of the contact between sample and electrodes. Therefore, one key aspect to obtain reproducible impedance data is to constantly maintain this contact. To ensure this is achieved, the same amount of each particular sample was pressed into a pellet (under 5 tons of pressure) of fixed diameter. Following this protocol several pellets of the same sample with very similar thickness to each other were studied and comparable impedance data were obtained. When samples with different thickness needed to be studied, “second electrodes” with different lengths were used (Figure 2.15). By choosing the approximate thickness of the pellet and the length of the second

electrode it was possible to reproduce similar experimental conditions each time and ensure a good sample-electrode contact.

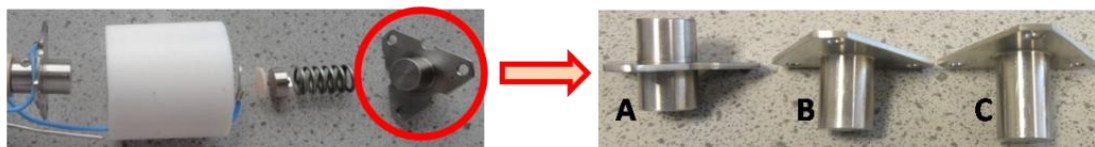


Figure 2.15. Available second electrodes compatible with cell A; the different length allows to control the contact between the sample and the electrodes.

In Figure 2.16 the dependence of the impedance to the contact sample-electrodes is shown. The proton conductivity of each imidazole pellet was measured using two electrodes of different lengths while the other experimental conditions (temperature and % RH) were kept constant. The experimental evidence proved that in cases where the electrode was too short, a poor contact resulted in the intrinsic proton conductivity of the material decreasing from $8.03(06) \times 10^{-8} \text{ S cm}^{-1}$ to $2.40(04) \times 10^{-8} \text{ S cm}^{-1}$.^{19,27,28}

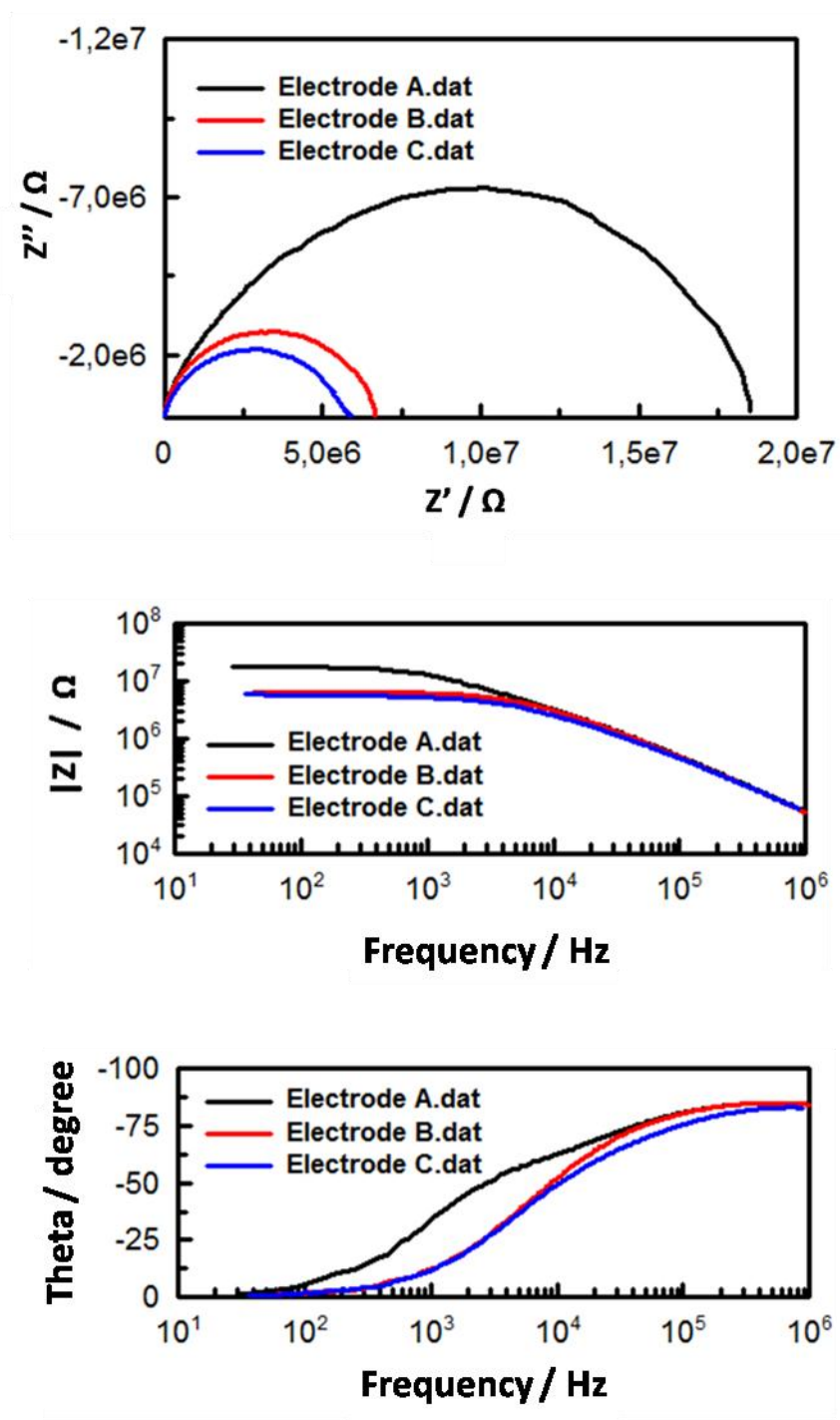


Figure 2.16. Nyquist and Bode plots of imidazole recorded using electrodes of different lengths; electrode A (*black*), electrode B (*red*), electrode C (*blue*).

A crucial aspect necessary to fully study the impedance of MOFs is the control of the exposure of the sample to the environment created inside the cell. This is important

as proton conductivity is often strongly affected by the temperature and relative humidity. Using cell A the pellet sits inside the PTFE sample holder and despite the presence of small holes across the section of the PTFE body, the sample is not fully exposed to the atmosphere created inside the cell.

Several problems with the pellet-electrodes contact and with the efficiency of the exposure of the sample to the humidity conditions were faced, making the reproducibility of the measurements very challenging. These aspects become of crucial importance when the impedance of a new MOF is studied for the first time as there are no literature reports on the specific material under study.

2.2.3.2 Design of cell B

The study of proton conduction in MOFs often requires exposure of the sample to different humidity conditions. The main limitation of cell A is the difficulty of directly exposing the pellet to the environment created inside the cell. For these reasons, a new cell (B) was designed for measurements at high relative humidity (0 to 99 % RH) and temperatures up to 80 °C (Figure 2.17).

In cell B the sample is suspended inside the cell and can directly interact with the atmosphere in the cell. This allows for precise determination of the % RH experienced by the sample. Moreover, the pellet is directly connected to two platinum wires which hold the pellet in place. Platinum has a very low resistivity (about $1.0 \times 10^{-7} \Omega \text{ m}$) and better inert chemical capacity compared with stainless steel.²⁹

In addition, to ensure good contact between the pellet and the platinum wires, a layer of carbon film (Sigracet GDL 10 BB) or silver paste (Sigma Aldrich) was applied on each side of the sample to serve as electrodes. In the first case, the powder was

sandwiched between two films of carbon film of desired dimensions before pressing for 5 minutes under 5 tons so the film can be attached to the sample. In the case of silver paste, a thin film of this material was applied to both sides of the already made pellet.

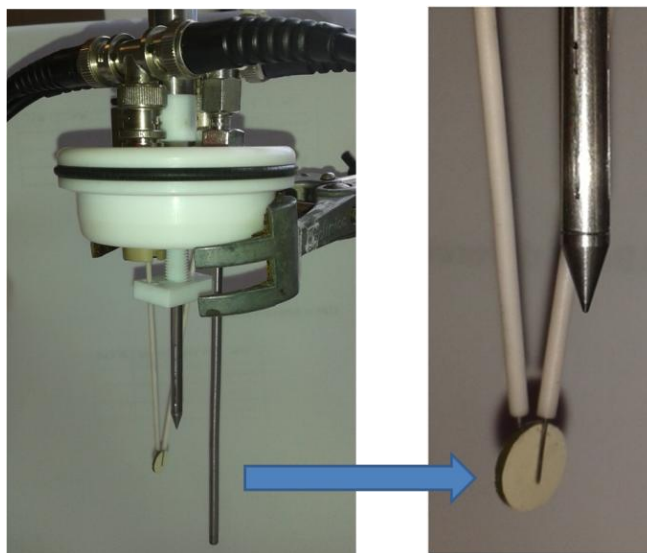


Figure 2.17. Picture of cell B highlighting the direct contact between the pellet and the platinum electrodes.

2.2.4 Control of the relative humidity

Humidity often plays a crucial role in determining the performance of polymer electrolyte membranes (PEMs) in fuel cells. It is commonly observed that low humidity causes an increase in the resistance of a fuel cell, which is dominated by the membrane resistance, indicating that the conductivity of the membrane decreases at low humidities. The dependency of the resistance on the humidity was observed in the majority of MOFs reported to date (Section 1.4.3, Table 1.1). The design, optimisation and testing of the humidity system connected to the conductivity cell was therefore necessary and is described herein.

The % RH inside the conductivity cell can be regulated in two ways. One method consists on mixing dry and wet gas to obtain the desired % RH. An alternative option is flowing gas through water solution saturated with selected salts. To control the % RH inside the cell the set up of the measurement system was designed accordingly.

The conductivity cell is connected to a N₂ cylinder through two gas lines. The first gas line (or dry line) directly connects the gas to the cell and measurements in presence of inert and dry atmosphere can be performed. One of the features of the designed cell is the relatively small cell chamber which allows for better control of the sample's % RH. Using a probe sensitive to the humidity located next to the sample, the % RH is measured. It was experimentally established that about 20 minutes after connecting the cell to the dry line 0 % RH humidity was reached inside the cell, stable over 10 h. The second gas line (or wet line) goes from the N₂ cylinder to the cell after passing through a water container. The N₂ bubbles through the water and the gas with a certain degree of humidity is directed into the cell. By flowing N₂ into deionised water for about 1 h, 99 % RH can be reached. To ensure high humidities inside the cell and in the attempt to limit drops in humidity mainly due to condensation of water inside the pipes which connect the cell to the gas cylinder, the flow of N₂ bubbles through two water containers; the first one located outside the cell and a small one inside the cell.

Measurements at intermediate % RH values can also be performed. A "T" shape connection allow to join the dry and wet gas lines before meeting the conductivity cell. Each line passes through a flow meter and by choosing the pressure of the gas passing through each line, it is possible to control the values of the % RH inside the cell.

Alternatively, the % RH can be fixed at values between 40 % and 98 % by bubbling the gas through water solutions saturated with different inorganic salts at set temperatures. Several indicative values were taken from the Omega website and experimentally reproduced in order to calibrate the cell (Figure 2.18). In particular it was observed that with a water solution saturated with potassium carbonate, 45 % RH is obtained after about 3 h. A similar experiment was performed with a saturated solution of sodium chloride in water; 75 % RH was obtained after about 3 h.

Equilibrium Relative Humidity Saturated Salt Solutions

Omega.com

Temperature °C	Relative Humidity (%RH)					
	Potassium Carbonate	Magnesium Nitrate	Sodium Chloride	Potassium Chloride	Potassium Nitrate	Potassium Sulfate
0	43.13 ± 0.66	60.35 ± 0.55	75.51 ± 0.34	88.61 ± 0.53	96.33 ± 2.9	98.77 ± 1.1
5	43.13 ± 0.50	58.86 ± 0.43	75.65 ± 0.27	87.67 ± 0.45	96.27 ± 2.1	98.48 ± 0.91
10	43.14 ± 0.39	57.36 ± 0.33	75.67 ± 0.22	86.77 ± 0.39	95.96 ± 1.4	98.18 ± 0.76
15	43.15 ± 0.32	55.87 ± 0.27	75.61 ± 0.18	85.92 ± 0.33	95.41 ± 0.96	97.89 ± 0.63
20	43.16 ± 0.33	54.38 ± 0.23	75.47 ± 0.14	85.11 ± 0.29	94.62 ± 0.66	97.59 ± 0.53
25	43.16 ± 0.39	52.89 ± 0.22	75.29 ± 0.12	84.34 ± 0.26	93.58 ± 0.55	97.30 ± 0.45
30	43.17 ± 0.50	51.40 ± 0.24	75.09 ± 0.11	83.62 ± 0.25	92.31 ± 0.60	97.00 ± 0.40
35		49.91 ± 0.29	74.87 ± 0.12	82.95 ± 0.25	90.79 ± 0.83	96.71 ± 0.38
40		48.42 ± 0.37	74.68 ± 0.13	82.32 ± 0.25	89.03 ± 1.2	96.41 ± 0.38
45		46.93 ± 0.47	74.52 ± 0.16	81.74 ± 0.28	87.03 ± 1.8	96.12 ± 0.40
50		45.44 ± 0.60	74.43 ± 0.19	81.20 ± 0.31	84.78 ± 2.5	95.82 ± 0.45
55			74.41 ± 0.24	80.70 ± 0.35		
60			74.50 ± 0.30	80.25 ± 0.41		
65			74.71 ± 0.37	79.85 ± 0.48		
70			75.06 ± 0.45	79.49 ± 0.57		
75			75.58 ± 0.55	79.17 ± 0.66		
80			76.29 ± 0.65	78.90 ± 0.77		
85				78.68 ± 0.89		
90				78.50 ± 1.0		
95						
100						

Figure 2.18. Equilibrium relative humidity obtained on bubbling N₂ through different saturated salt solutions.

2.3 Conclusions

An overview of EIS together with the key concepts necessary to understand the basics of impedance spectroscopy were presented (Section 2.1).

The impedance measurement system was designed and tested (Section 2.2). Two homemade conductivity cells and sample holders were constructed and assembled with a relative humidity and temperature control system. The designed method allows conductivity measurements over a wide range of % RH (0-99 % RH) and temperatures (15-120 °C) according to which cell is used.

A protocol for sample preparation, using imidazole as reference material, was developed and each of the experimental variables were tested in order to obtain reliable data.

Comparing the experimentally recorded proton conductivity of imidazole with literature values, it can be concluded that the developed method and the experimental system are applicable for reliable proton conductivity measurements of novel materials.

2.4 References

- (1) Evgenij, B.; Ross, M. “*Impedance Spectroscopy Theory, Experiment, and Applications*” Wiley Ed. **2005**.
- (2) MacDonald, D. D. *Electrochimica Acta* **2006**, *51*, 1376–1388.
- (3) Hladky, K.; Callow, L. M.; Dawson, J. L. *Br. Corros. J.* **1980**, *15*, 20–25.
- (4) Bard, A. J.; Faulkner, L. R. “*Electrochemical methods: fundamentals and applications*” Second Edition, **2001**.
- (5) Cogger, N.; Evans, N. *Solartron Analytical* **1999**.
- (6) Brockman, S. *Application note, Gamry Instruments* **2012**, 1–13.
- (7) Soboleva, T.; Xie, Z.; Shi, Z.; Tsang, E.; Navessin, T.; Holdcroft, S. *J. Electroanalytical Chem.* **2008**, *622*, 145–152.
- (8) Donnadio, A.; Casciola, M.; Di Vona, M. L.; Tamilvanan, M. *J. Power Sources* **2012**, *205*, 145–150.
- (9) Umeyama, D.; Horike, S.; Inukai, M.; Hijikata, Y.; Kitagawa, S. *Angew. Chem.* **2011**, *50*, 11706–11709.
- (10) Yoon, M.; Suh, K.; Kim, H.; Kim, Y.; Selvapalam, N.; Kim, K. *Angew. Chem.* **2011**, *50*, 7870–7873.
- (11) Hurd, J. A.; Vaidhyathan, R.; Thangadurai, V.; Ratcliffe, C. I.; Moudrakovski, I. L.; Shimizu, G. K. H. *Nature Chem.* **2009**, *1*, 705–710.
- (12) Chien, H. C.; Tsai, L. D.; Lai, C. M.; Lin, J. N.; Zhu, C. Y.; Chang, F. C. *J. Power Sources* **2013**, *226*, 87–93.
- (13) Ramaswamy, P.; Wong, N. E.; Shimizu, G. K. H. *Chem. Soc. Rev.* **2014**, *43*, 5913–5932.
- (14) Peighambardoust, S. J.; Rowshanzamir, S.; Amjadi, M. “*Review of the proton exchange membranes for fuel cell applications*” Elsevier Ltd, **2010**, 35.

- (15) Nasef, M. M.; Aly, A. A. *Desalination* **2012**, *287*, 238–246.
- (16) Kreuer, K.; Rabenau, A.; Weppner, W. *Angew. Chem.* **1982**, *21*, 208–209.
- (17) Agmon, N. *Chem. Phys. Letters* **1995**, *244*, 456–462.
- (18) Phang, W. J.; Lee, W. R.; Yoo, K.; Ryu, D. W.; Kim, B.; Hong, C. S. *Angew. Chem.* **2014**, *53*, 8383–8387.
- (19) Bureekaew, S.; Horike, S.; Higuchi, M.; Mizuno, M.; Kawamura, T.; Tanaka, D.; Yanai, N.; Kitagawa, S. *Nature Mater.* **2009**, *8*, 831–836.
- (20) Kim, S.; Dawson, K. W.; Gelfand, B. S.; Taylor, J. M.; Shimizu, G. K. H.; Gelfand, B. S. *J. Am. Chem. Soc.* **2013**, *135*, 963–966.
- (21) Nagarkar, S. S.; Unni, S. M.; Sharma, A.; Kurungot, S.; Ghosh, S. K. *Angew. Chem.* **2014**, *53*, 2638–2642.
- (22) Bazaga-Garcia, M.; Colodrero, R. M. P.; Papadaki, M.; Garczarek, P.; Zon, J.; Olivera-pastor, P.; Losilla, E. R.; Leo, L.; Aranda, M. A. G. *J. Am. Chem. Soc.* **2014**, *136*, 5731–5739.
- (23) Ramaswamy, P.; Wong, N. E.; Gelfand, B. S.; Shimizu, G. K. H. *J. Am. Chem. Soc.* **2015**, *137*, 7640–7643.
- (24) Umeyama, D.; Horike, S.; Inukai, M.; Itakura, T.; Kitagawa, S. *J. Am. Chem. Soc.* **2012**, *134*, 12780–12785.
- (25) Hurd, J.; Vaidhyanathan, R.; Thangadurai, V.; Ratcliffe, C. I.; Moudrakovski, I. L.; Shimizu, G. K. H. *Nature Chem.* **2009**, *1*, 705–710.
- (26) Kreuer, K. D.; Paddison, S. J.; Spohr, E.; Schuster, M. *Chem. Rev.* **2004**, *104*, 4637–4678.
- (27) Kawada, A., McGhie, L. M. *J. Chem. Phys.* **1970**, *52*, 3121–3125.
- (28) Daycock, J. T.; Jones, G. P.; Evans, J. R.; Thomas, J. M. *Nature* **1968**, *218*, 672–673.

(29) Eddy Current Technology Incorporated, “*Conductivity of Metals Sorted by Resistivity*” **2013**.

Chapter 3

**Proton conduction in two phosphonate-based
metal-organic frameworks mediated by intrinsic
“spherical free diffusion”**

List of Contents

3.1 Introduction	83
3.1.1 Phosphonate-based metal organic frameworks.....	84
3.1.2 Phosphonate-based MOFs as proton conductors	85
3.1.3 Aims of Chapter 3.....	91
3.2 Results and discussion.....	92
3.2.1 Synthesis of benzene-1,3,5- <i>p</i> -phenylphosphonic acid, H ₆ L ¹	92
3.2.2 Synthesis and structural characterisation of NOTT-500(Ni, Co).....	92
3.2.3 IR absorption spectroscopy of NOTT-500(Ni, Co)	99
3.2.4 Thermal stability of NOTT-500(Ni, Co).....	100
3.2.5 Reversible structural phase change	102
3.2.5.1 <i>In situ</i> VT-PXRD study of NOTT-500(Ni, Co).....	103
3.2.5.2 Solid-state UV-visible study of NOTT-500(Ni, Co).....	111
3.2.6 Proton conductivity study of NOTT-500(Ni, Co).....	119
3.2.7 Quasi-elastic neutron scattering study of NOTT-500(Ni).....	132
3.3 Conclusions	141
3.4 Experimental Section	143
3.4.1 Synthesis of benzene-1,3,5- <i>p</i> -phenylphosphonic acid, H ₆ L ¹	143
3.4.2 Synthesis of [Ni ₃ (H ₃ L ¹) ₂ (H ₂ O) _{10.5} , NOTT-500(Ni)	144
3.4.3 Synthesis of [Co ₃ (H ₃ L ¹) ₂ (H ₂ O) _{10.4} , NOTT-500(Co)	144
3.5 References	146

3.1 Introduction

MOFs have been proposed as alternative materials for proton conduction applications in PEM fuel cells. The key requirement for a material to be proton conductive is the presence of acidic protons within an appropriately structured framework in order to facilitate charge transport. Several studies have proved that the use of ligands with acidic functional groups such as phosphonates or sulfonates can increase the quantity of mobile protons in the structure and enhance the proton conductivity properties of the resulting material. An example of high proton conductivity derived from such functional groups is PCMOF-2½, $[\text{Na}_3\text{L}_1]_{(0.66)}[\text{Na}_3\text{H}_3\text{L}_2]_{(0.34)}(\text{H}_2\text{O})_{1.2}$ (Na_3L_1 = trisodium 2,4,6-trihydroxy-1,3,5-trisulfonate benzene, H_6L_2 = 1,3,5-benzenetriphosphonic acid), (Figure 3.1).¹ At 85 °C and 90 % RH, PCMOF-2½, a mixed sulfonate-phosphonate-ligand MOF, exhibited a proton conductivity of $2.1 \times 10^{-2} \text{ S cm}^{-1}$ with E_a of 0.21 eV. PCMOF-2½ showed one of the highest proton conductivity values reported to date in any class of proton conducting coordination materials.^{1,2}

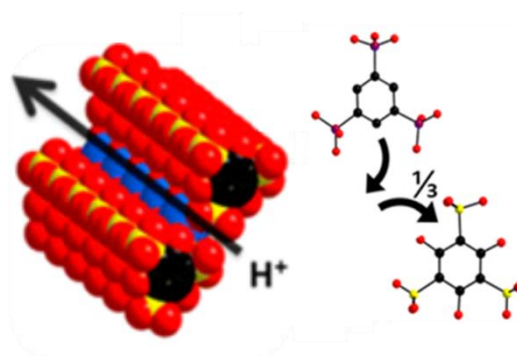


Figure 3.1 Ligands used to synthesise PCMOF-2½ and representation of space filling cross section of a pore. Carbon (*black*), oxygen (*red*), sulphur (*yellow*), phosphorus (*purple*).¹

3.1.1 Phosphonate-based metal organic frameworks

The majority of MOF materials are based on carboxylate or aromatic nitrogen containing heterocycle ligands that typically coordinate d-block metal ions giving crystalline porous frameworks.^{3,4} These MOFs often exhibit high surface areas and uniform pore size distributions and are traditionally investigated as candidates for applications in gas sorption, gas separation and catalysis.⁵ MOFs with phosphonate ligands are far less studied in comparison to those based upon carboxylate and N-heterocycle ligands, however they show interesting potential to form new functional materials.⁶ As a result of the high chemical and thermal stability of M–O(P) bonds, phosphonate groups offer an alternative set of chemical and structural possibilities to those of carboxylates.⁷ Phosphonate groups have three oxygen atoms capable of coordinating to metals and they can act as mono- or bidentate-ligands for individual or multiple metal centres. Metal phosphonate bonds are much stronger than metal carboxylate bonds, so the formation of much more thermal and chemically stable materials is possible.⁸

The main reasons that fewer phosphonate-based MOFs with open frameworks have been reported and investigated are three.^{9,10} Firstly, growing single crystals of phosphonate-based MOFs is difficult due to the rapid formation and precipitation of metal phosphonate salts. Secondly, these materials tend to pack in dense, layered or pillared solids with less potential for material applications as applied to traditional porous MOFs.¹¹ The final reason is that compared to ubiquitous carboxylate and pyridal groups, the coordination chemistry of phosphonates is more complex and less predictable owing the plethora of ligating modes and three possible states of protonation.¹²

3.1.2 Phosphonate-based MOFs as proton conductors

Phosphonate-based MOFs are appealing candidates for accessing highly proton conducting materials. Coordination of phosphonate ligands to metal ions to give multidimensional frameworks for proton conduction applications have previously been described.^{1,6,13–16} In most of these systems free phosphonate hydroxyl groups serve to anchor carrier molecules or directly transfer protons along a hopping pathway.

Of direct relevance to the work reported herein, in 2010 Shimizu *et al.* reported examples of phosphonate MOFs as proton conducting materials. PCMOF-3, $Zn_3(L)(H_2O)_2 \cdot 2H_2O$ ($L = [1,3,5\text{-benzenetriphosphonate}]^{6-}$), crystallises with a layered structure and has a proton conductivity of $3.5 \times 10^{-5} \text{ S cm}^{-1}$ at 25 °C and 98 % RH with E_a of 0.17 eV.¹⁷ More recently the same authors investigated another highly conducting phosphonate MOF, PCMOF-5 [$La(H_5L)(H_2O)_4$], $L = 1,2,4,5\text{-tetrakisphosphonomethylbenzene}$), which was the first 3D metal phosphonate MOF containing free diprotic acid groups close enough to each other to facilitate direct transport of charge (Figure 3.2). Analysis of PCMOF-5 showed a proton conductivity of $4 \times 10^{-3} \text{ S cm}^{-1}$ at 60 °C and 98 % RH with E_a of 0.16 eV.¹⁵

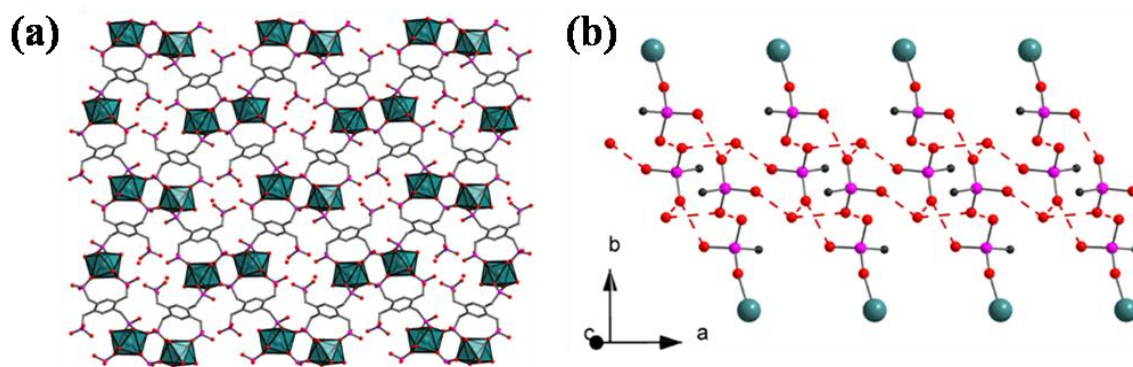


Figure 3.2. (a) Structure of PCMOF-5 as viewed down the *a*-axis. Free phosphonic acid groups and uncoordinated water molecules are located in each pore. (b) View showing the one-dimensional hydrogen-bonding array formed between phosphonic acid groups and free water molecules in the direction of the *a*-axis. Carbon (*black*), oxygen (*red*), phosphorus (*purple*), metal (*green*).¹⁵

In 2012 Cabeza and co-workers reported another MOF material with a phosphonate ligand, $\text{Mg}(\text{H}_6\text{ODTMP}) \cdot 2\text{H}_2\text{O}(\text{DMF})_{0.5}$ (H_8ODTMP = octamethylenediamine-*N,N,N',N'*-tetrakis(methylenephosphonic acid), a 3D pillared open framework containing cross-linked 1D channels filled with free water and DMF (Figure 3.3).⁶ This material could be hydrated to give $\text{MgH}_6\text{ODTMP} \cdot 6\text{H}_2\text{O}$ which was obtained upon H_2O and DMF removal and consequent rehydration. Ionic conductivity studies on the hydrated material $\text{MgH}_6\text{ODTMP} \cdot 6\text{H}_2\text{O}$ were performed. Owing to the contribution of 1D channel filled with water and the POH groups pointing toward the channel, this material showed a maximum conductivity of $1.6 \times 10^{-3} \text{ S cm}^{-1}$ at 19°C and $\sim 100\%$ RH with an activation energy of 0.31 eV. The proton conductivity of this material is strongly dependent on the % RH; with the reduction of humidity the proton conductivity drops quickly (Figure 3.3c).

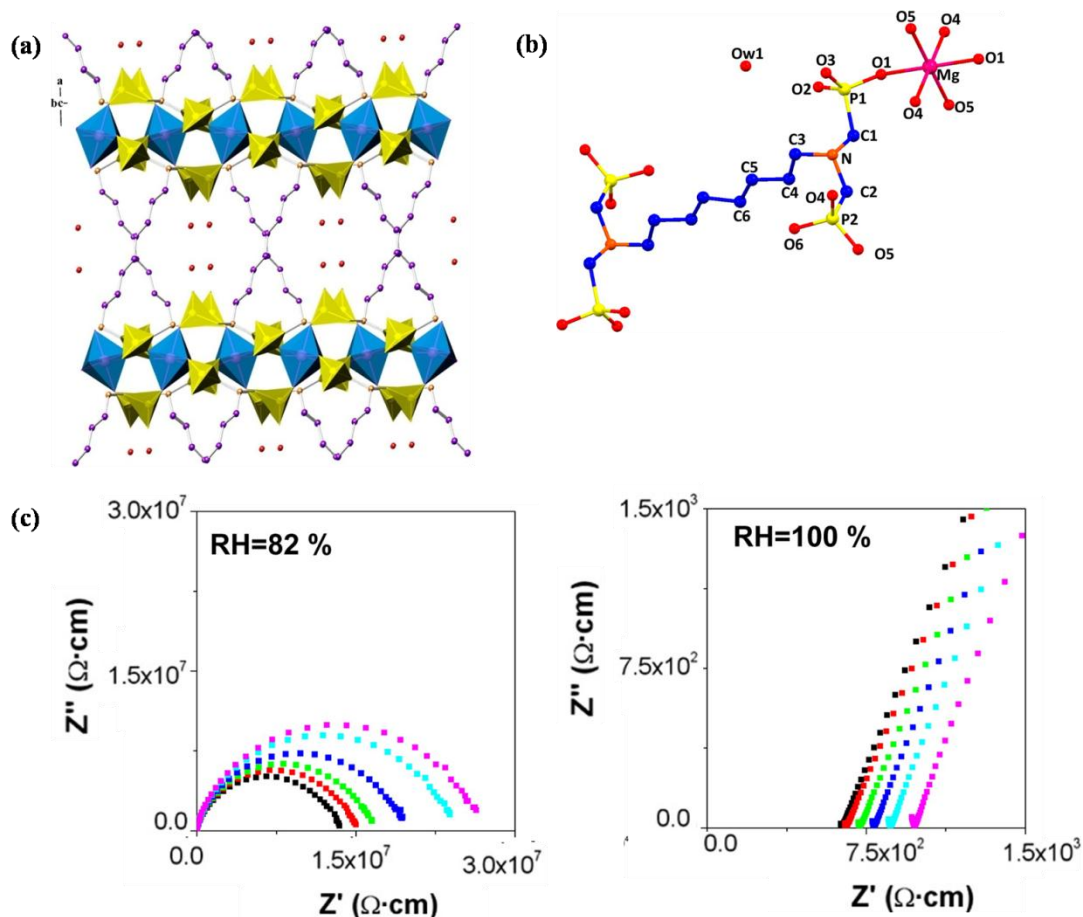


Figure 3.3. (a) Crystal structure of $\text{MgH}_6\text{ODTMP}\cdot 2\text{H}_2\text{O}(\text{DMF})_{0.5}$ as viewed along the c -axis; water molecules shown as red spheres. (b) Octahedral coordination environment of Mg in $\text{MgH}_6\text{ODTMP}\cdot 2\text{H}_2\text{O}(\text{DMF})_{0.5}$. (c) Nyquist plots for $\text{MgH}_6\text{ODTMP}\cdot 6\text{H}_2\text{O}$ at different % RH with each at six temperatures; 9 °C (*magenta*), 11 °C (*cyan*), 13 °C (*blue*), 15 °C (*green*), 17 °C (*red*), 19 °C (*black*).⁶

S. Kitagawa *et al.* contributed in this field with a coordination polymer $[\text{Zn}(\text{H}_2\text{PO}_4)_2(\text{TzH})_2]$ (Tz = triazole), consisting of a 2D layered structure with hydrogen bonds between the layers (Figure 3.4).¹⁸ In $[\text{Zn}(\text{H}_2\text{PO}_4)_2(\text{TzH})_2]$ the protons on nitrogen and oxygen (in the phosphate) atoms are organised in a continuous hydrogen bonding network in the ab plane with hydrogen bond distances of 1.76 Å and 1.78 Å for $\text{PO}(\text{H})\cdots\text{OP}$ and 2.26 Å and 2.63 Å for $\text{N}(\text{H})\cdots\text{OP}$,

respectively. The proton conductivity of this compound was $1.2 \times 10^{-4} \text{ S cm}^{-1}$ at 150°C under anhydrous conditions with an activation energy of 0.6 eV .

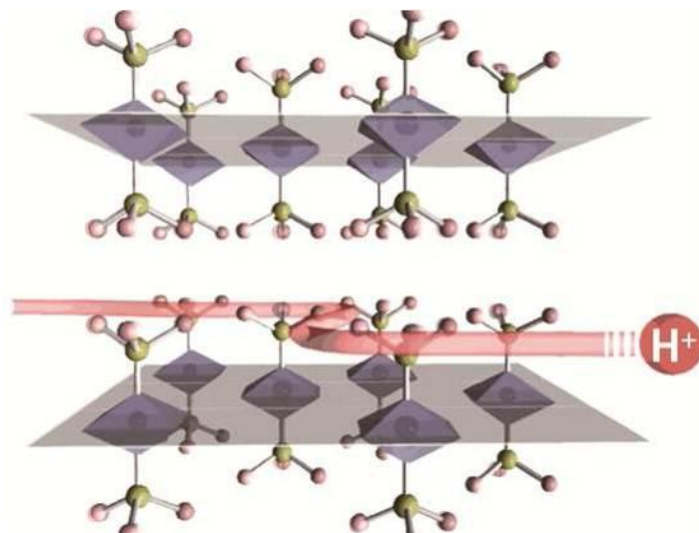


Figure 3.4. Representation of $[\text{Zn}(\text{H}_2\text{PO}_4)_2(\text{TzH})_2]$ with proton-hopping pathway.¹⁸

In 2013 Cabeza and co-workers presented two new families of divalent metal hybrid derivatives using aromatic tetraphosphonic acids 1,4- and 1,3-*bis*(aminomethyl)benzene-*N,N'*-*bis*(methylenephosphonic acid), *p*- H_8L and *m*- H_8L , with Ca, Mg, Co and Zn metal cations, (Figure 3.5).¹⁹ $\text{M}-(p\text{-H}_6\text{L})$ is composed of organic-inorganic monodimensional chains where the phosphonate moiety acts as a bidentate chelating ligand bridging two metals. The $\text{M}-(m\text{-H}_6\text{L})$ compounds exhibit 3D pillared open-frameworks with small 1D channels filled with water molecules. Proton conductivity studies revealed that both families display similar proton conductivities of $9.4 \times 10^{-5} \text{ S cm}^{-1}$ at 24°C and 98 % RH.

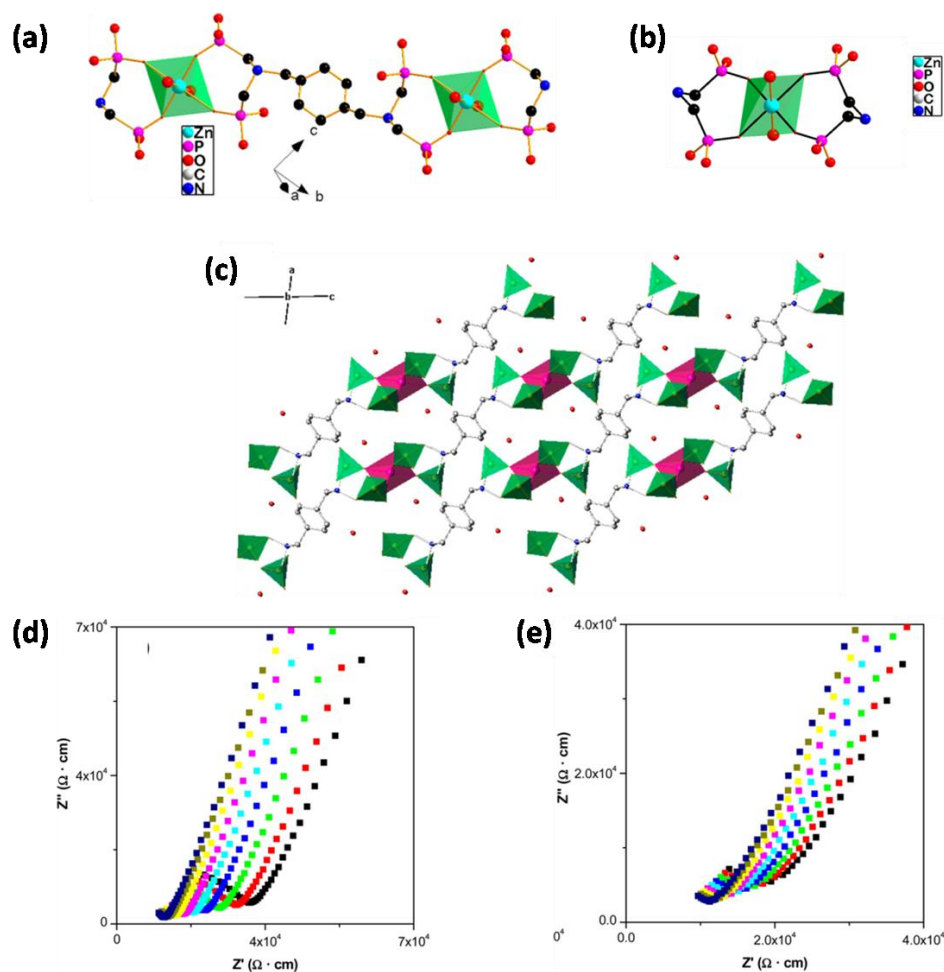


Figure 3.5. (a) Basic structural “dimeric” unit of Zn-(*p*-H₆L). (b) Zn coordination environment. (c) Packing of the hybrid chains in M-(*p*-H₆L) [O₃PC tetrahedra in green, MO₆ octahedra in purple]. (d) Nyquist plot for Mg-(*p*-H₆L) and (e) Zn-(*m*-H₆L) at 98 % RH each at six different temperatures; 10 °C (*black*), 12 °C (*red*), 13 °C (*green*), 15 °C (*blue*), 17 °C (*cyan*), 19 °C (*magenta*), 20 °C (*yellow*), 22 °C (*dark yellow*), 24 °C (*navy*).¹⁹

In 2014 Cabeza *et al.* reported the synthesis, structural characterisation and proton conductivity of an open framework containing Ca²⁺ cations and a rigid polyfunctional ligand, 5-(dihydroxyphosphoryl)isophthalic acid (PiPhtA).²⁰ The high water content resulting from water-filled 1D channels contributed to the high proton conductivity of this material. The phosphonate group coordinates to the metal via

only two oxygen atoms leaving a free POH directed into the interlamellar space which also contains an unbound carboxylic acid group. The proton conductivity for as-synthesised Ca-PiPhtA-I was $5.7 \times 10^{-4} \text{ S cm}^{-1}$ at $24 \text{ }^\circ\text{C}$ and 98 % RH, whereas the proton conductivity of the pre-heated Ca-PiPhtA-I at $75 \text{ }^\circ\text{C}$, Ca-PiPhtA-II, was 3.6×10^{-4} at $24 \text{ }^\circ\text{C}$ and 98 % RH. Upon exposure to ammonia vapour, Ca-PiPhtA-NH₃ exhibited increased proton conductivity of $6.6 \times 10^{-3} \text{ S cm}^{-1}$ at $24 \text{ }^\circ\text{C}$ and 98 % RH. Activation energies for proton transfer in the above-mentioned frameworks range between 0.23 and 0.4 eV (Figure 3.6).

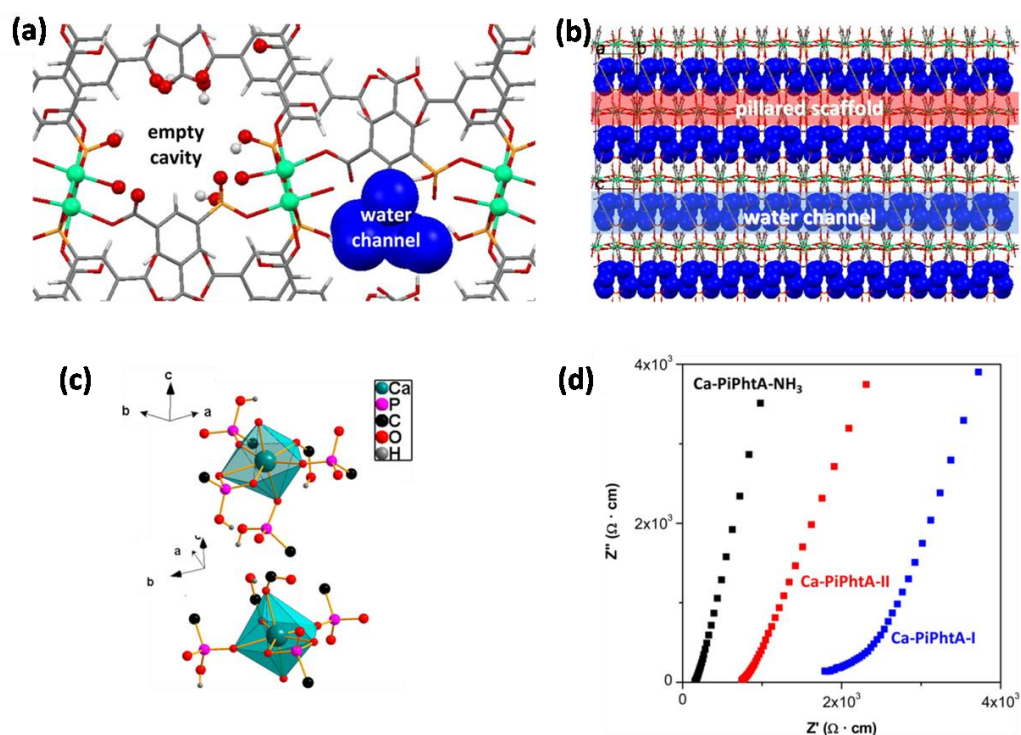


Figure 3.6. (a) 3D structure of Ca-PiPhtA-I looking down the *b*-axis, showing the arrangement of the water-filled 1D channels and the moieties protruding into the interior. Carbon (*grey*), oxygen (*red*), hydrogen (*white*), calcium (*green*). (b) Longitudinal view perpendicular to *b*-axis of the 1D column of water within the pillared scaffold. (c) Coordination environment of the two Ca²⁺ centres in Ca-PiPhtA-I. (d) Nyquist plot for Ca-PiPhtA at $24 \text{ }^\circ\text{C}$ and 98 % RH.²⁰

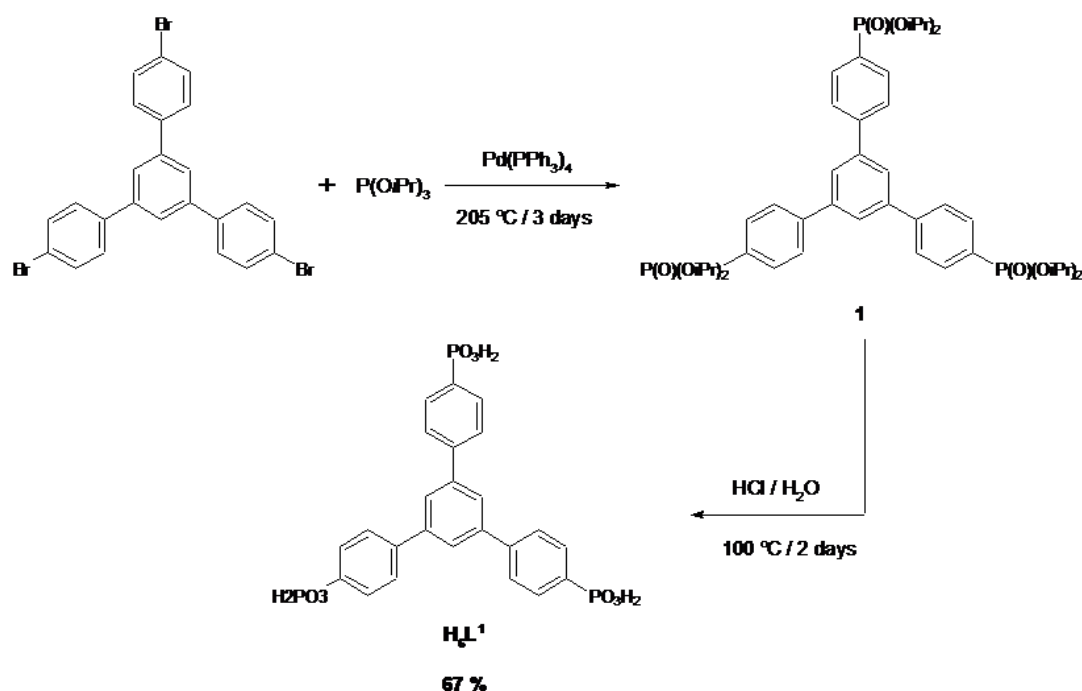
3.1.3 Aims of Chapter 3

Recent findings show the potential of phosphonate-based MOFs as proton conducting materials and inspired the research in this Chapter. The aims of the work herein described are the development of new MOFs based on phosphonate organic ligands, their characterisation by impedance spectroscopy and investigation of the proton conductivity mechanism. In Chapter 3, two new isostructural phosphonate MOFs, NOTT-500(Ni, Co) based on benzene-1,3,5-*p*-phenylphosphonic acid, H_6L^1 , were synthesised and fully characterised. The crystal structure of NOTT-500(Ni, Co), determined by single crystal X-ray diffraction, showed the presence of free hydroxyl groups from the ligand (P-OH) and coordinated water molecules (M-OH₂) organised in an efficient proton-hopping pathway for charge transfer. NOTT-500(Ni, Co) were fully characterised by several spectroscopic techniques. Both materials exhibited a reversible phase change associated with change in colour as confirmed by TGA, VT-PXRD and solid-state UV-visible. More relevant for the aims of this work are the impedance analyses on these materials combined with quasi-elastic neutron scattering studies on NOTT-500(Ni) giving insight into the mechanism of proton conductivity. Identifying the proton-hopping pathway and understanding the mechanism of proton conduction is crucial for the design of efficient and alternative candidate materials to replace in future the currently used polymers (such as Nafion) as PEMs in fuel cells.

3.2 Results and discussion

3.2.1 Synthesis of benzene-1,3,5-*p*-phenylphosphonic acid, H₆L¹

H₆L¹ was obtained *via* a modified literature procedure following the synthetic route outlined in Scheme 3.1.²¹ The [Pd(PPh₃)₄]-catalysed Hirao reaction of 1,3,5-tris(*p*-bromophenyl) benzene with P(*i*-PrO)₃ was carried out under Ar with stirring for 3 days at 205 °C. Compound **1** was isolated as a white powder, washed with hexane and reacted in a 1.5:1 HCl/H₂O solution under stirring for 2 days at 100 °C. A sticky white product was formed and recrystallised with methanol to yield H₆L¹ as white powder (67 %).



Scheme 3.1. Synthetic route to H₆L¹.

3.2.2 Synthesis and structural characterisation of NOTT-500(Ni, Co)

Hexagonal column-shaped single crystals of NOTT-500(Ni) (green crystals) and NOTT-500(Co) (pink crystals) were grown upon mixing Ni(NO₃)₂ or Co(NO₃)₂ with

H₆L¹ (ratio 2:1) in a solution of H₂O, DMSO and DMF (ratio 1.5:1:1, v/v/v) at 40 °C for two days.

Single crystal X-ray diffraction data for NOTT-500(Ni, Co) were collected at Diamond Light Source, Beamline I19, by using synchrotron X-ray source. The two MOFs with empirical formulae [Ni₃(H₃L¹)₂(H₂O)_{10.5}(DMF)₃]_∞ and [Co₃(H₃L¹)₂(H₂O)_{10.4}(DMF)₃]_∞ crystallise in the hexagonal space group *P*6₃/*m*. Both data set were collected from crystals previously suspended in their mother solutions; thus the presence of three non-coordinated DMF molecules in the voids of the frameworks.

NOTT-500(Ni, Co) adopt a 2D extended network constructed from the linkage between [M₃(H₂O)_x] clusters (M = Ni, Co) and the phosphonate ligands. Sheets of ligand molecules interact with each other *via* π-π stacking interactions along the *c*-axis and are cross-linked along the *a/b*-axes by metal ions (Figure 3.7). The metal centres are organised in chains containing a repeating three-metal motif that comprises one M¹-M² dimer unit, bridged by three oxygen atoms from the ligands, and one monometallic M³ unit (Figure 3.8).

M¹ is coordinated to four oxygen atoms from coordinated water molecules and three phosphonate oxygen atoms from three different ligands in a μ₂ bridging mode. Two types of water molecules are coordinated to M¹; (H₂O)_A and (H₂O)_B. M¹ is bound to three (H₂O)_A which are fully occupied and at distance M¹-[O(H₂)]_A of 2.053(6) Å and 2.076(4) Å for NOTT-500(Ni) and NOTT-500(Co), respectively. M¹ is also coordinated to one (H₂O)_B (0.75 and 0.72 occupancy for NOTT-500(Ni) and NOTT-500(Co), respectively) with distance M¹-[O(H₂)]_B of 2.292(12) Å for NOTT-500(Ni) and 2.240(7) Å for NOTT-500(Co). M² is coordinated to three oxygen atoms from three ligands in a μ₂ bridging mode and three water molecules. In comparison, M³ is

hepta-coordinated by four water molecules and three oxygen atoms from phosphonate groups. Similarly with M^1 , the water molecules coordinated to M^3 are also of two types. Thus, M^3 is bound to three $(H_2O)_A$ (full occupancy) and one $(H_2O)_B$ (0.75 occupancy). This explains the empirical formulae of NOTT-500(Ni, Co). NOTT-500(Ni) has a total of 10.5 water molecules; the non-integer number is due to the partial occupancy (0.75) of two $(H_2O)_B$ molecules respectively coordinated to Ni^1 and Ni^3 , while each of the three metals is bound to three water molecules, $(H_2O)_A$. Similar conclusions can be drawn for NOTT-500(Co).

In NOTT-500(Ni, Co) the phosphonate groups (PO_3H) of each ligand are bound to metal centres through one oxygen atom. The PO_3-H proton is delocalised between the two uncoordinated oxygen atoms. Being impossible to certainly define the position of this proton by X-ray spectroscopy, the structure was modelled by refining the half occupancy of the proton on each uncoordinated oxygen atom of the phosphonate group.

The short distances between the water molecules coordinated to the metal ($M-OH_2$) and the hydroxyl groups from the ligand ($P-OH$), in the range 2.0 Å to 2.9 Å, identify a promising proton-hopping pathway for charge transfer within the framework (Section 3.2.6).

Details of crystal structure for NOTT-500(Ni, Co) are summarised in Table 3.1.

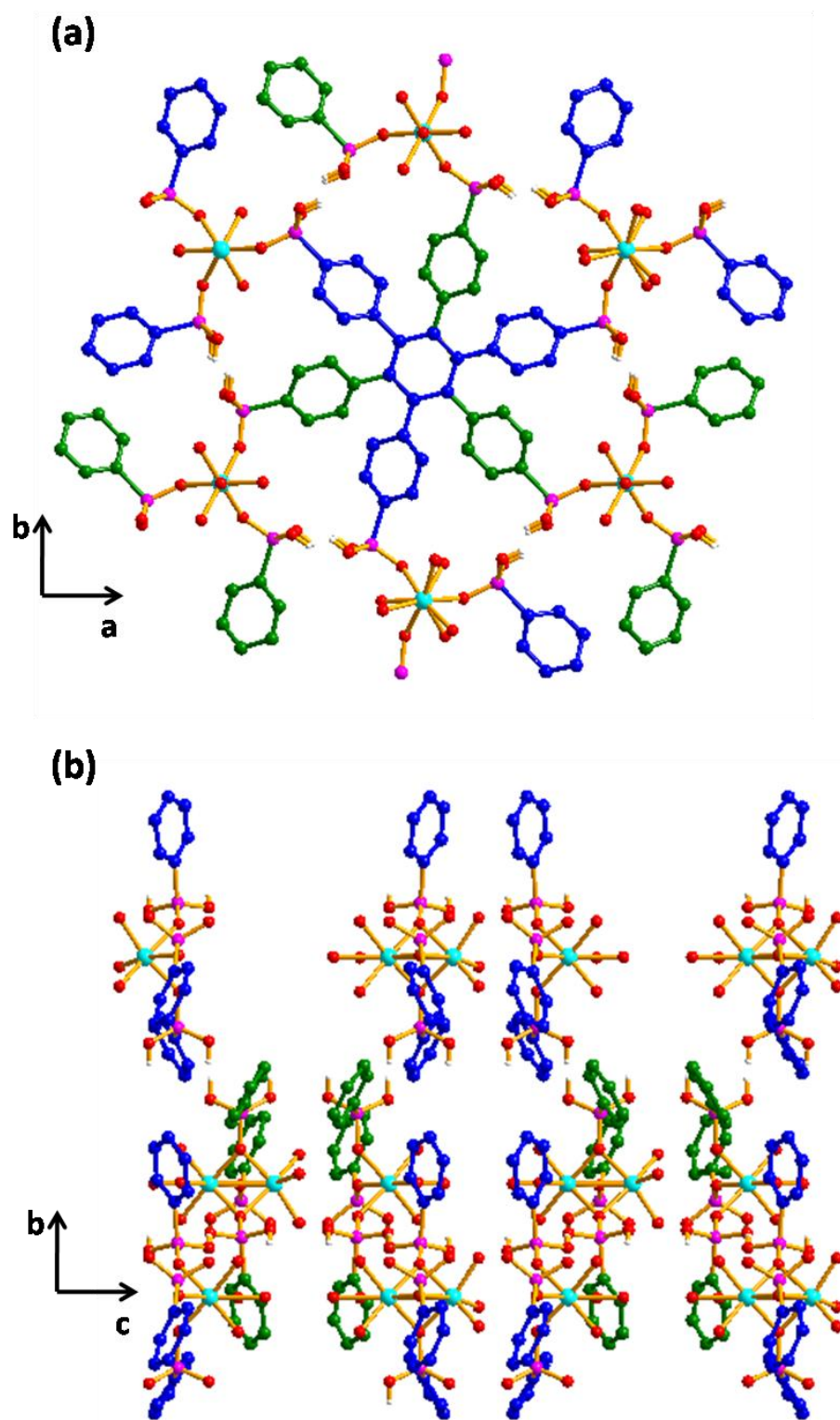


Figure 3.7. Single crystal X-ray structure of NOTT-500(M): (a) view looking down the *c*-axis; (b) view looking down the *a*-axis. Phosphorous (*purple*), oxygen (*red*), metal (*cyan*).

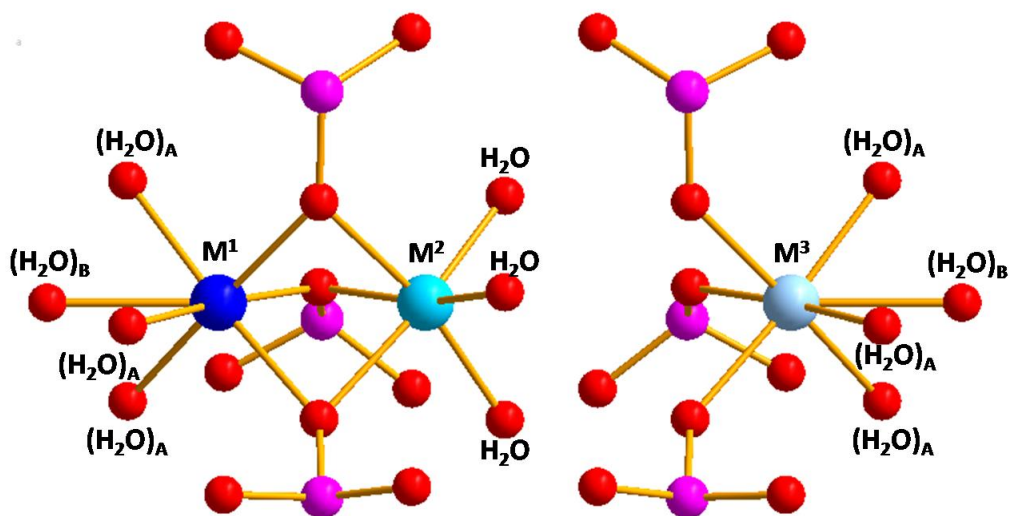


Figure 3.8. Sequence of metal dimer unit (M^1 - M^2) and metal monomer unit (M^3) in NOTT-500(Ni, Co) viewed along the *a*-axis. The protons are omitted from the picture for better clarity. Phosphor (*purple*), oxygen (*red*), metal (*blue*).

Table 3.1. Crystallographic data for NOTT-500(Ni) and NOTT-500(Co).

NOTT-500(M)	NOTT-500(Ni)		NOTT-500(Co)	
Empirical formula	[Ni ₃ (H ₃ L ¹) ₂ (H ₂ O) _{10.5} (DMF) ₃] _∞		[Co ₃ (H ₃ L ¹) ₂ (H ₂ O) _{10.4} (DMF) ₃] _∞	
Formula weight (g mol ⁻¹)	1671.22		1670.80	
Temperature, K	120		120	
Wavelength, Å	0.6889		0.6889	
Crystal system	Hexagonal		Hexagonal	
Space group	<i>P</i> 6 ₃ / <i>m</i>		<i>P</i> 6 ₃ / <i>m</i>	
	Unit cell dimensions			
<i>a</i> (Å)	16.323(6)		16.348(9)	
<i>c</i> (Å)	14.933(8)		14.922(12)	
<i>α</i> (°)	90		90	
<i>γ</i> (°)	120		120	
Cell volume (Å³)	3446(3)		3454(5)	
Z	2		2	
Total reflections/unique	21122/2737		21381/2741	
R_{int}	0.1314		0.1722	
R₁ [<i>F</i> > 4σ(<i>F</i>)] / wR₂	0.0653 / 0.1985		0.0890 / 0.2843	
GoF	0.9220		1.0360	
M¹-M²	2.698(4)		2.729(3)	
M¹-O(H₂)	2.053(6) (H ₂ O) _A	2.292(12) (H ₂ O) _B	2.076(4) (H ₂ O) _A	[2.240(7)] (H ₂ O) _B
M¹-O(P)	2.076(6)		2.127(4)	
M²-O(H₂)	1.989(6)		1.994(4)	
M²-O(P)	2.137(6)		2.169(4)	
M³-O(H₂)	2.053(6) (H ₂ O) _A	2.292(12) (H ₂ O) _B	2.076(4) (H ₂ O) _A	[2.240(7)] (H ₂ O) _B
M³-O(P)	2.076(6)		2.127(4)	

The phase purity of the bulk NOTT500(Ni, Co) was successfully confirmed by matching the high resolution powder X-ray diffraction patterns collected at Diamond Light Source, Beamline I11, to the PXRD patterns simulated from the single crystal structures (Figures 3.9).

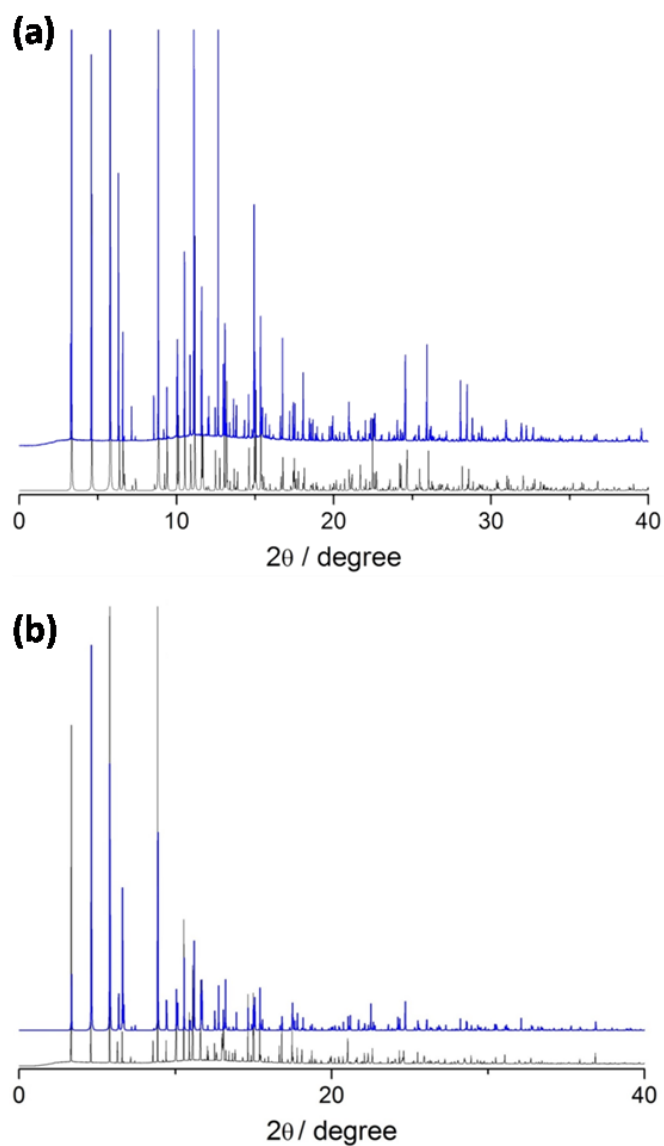


Figure 3.9. Comparison between the simulated (*blue*) and experimental (*black*) PXRD patterns for (a) NOTT-500(Ni) and (b) NOTT-500(Co).

3.2.3 IR absorption spectroscopy of NOTT-500(Ni, Co)

The presence of coordinated water molecules and P-O-H groups in NOTT-500(Ni, Co) was confirmed by infrared spectroscopy (Figure 3.10). The typical $\nu(\text{O-H})$ stretching mode of the water is the broad band centred at 3200 cm^{-1} .²² The H-O-H bending modes are found at $\sim 1600\text{ cm}^{-1}$.^{22,23} The shoulder centred at 2200 cm^{-1} is attributed to the hydroxyl groups from the phosphonate $\nu(\text{P-OH})$. The bands assigned as the $\nu(\text{P-O})$ mode are observed at $\sim 1130\text{ cm}^{-1}$ and $\sim 930\text{ cm}^{-1}$.^{22,23} In the IR spectra of the ligand, H_6L^1 , the broad bands attributed to $\nu(\text{O-H})$ are much more intense compared to NOTT-500(Ni, Co) as all the hydroxyl groups from the phosphonates are non-coordinated.

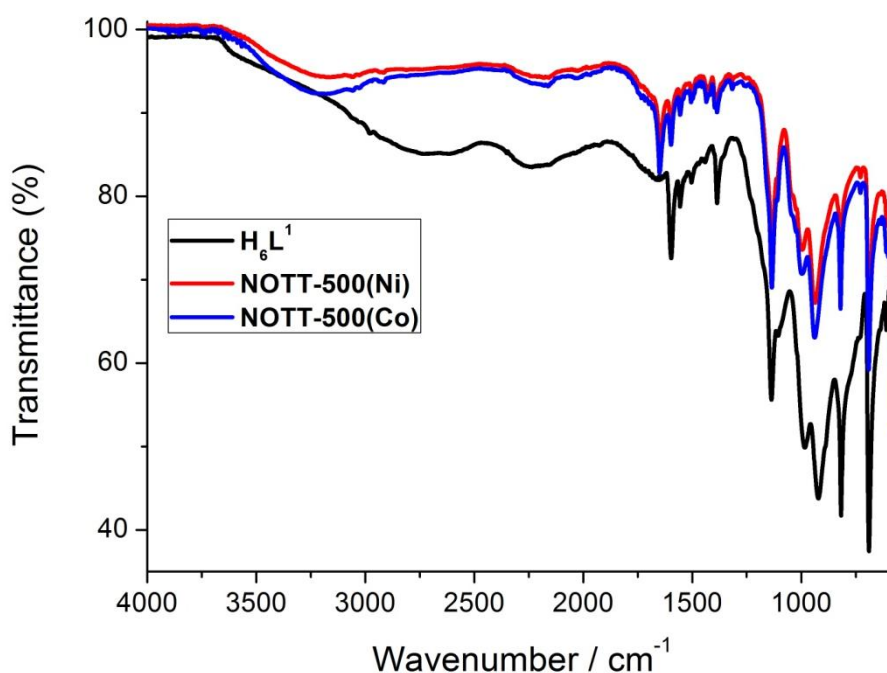


Figure 3.10. ATR infrared spectra of H_6L^1 (black), NOTT-500(Ni) (red) and NOTT-500(Co) (blue).

3.2.4 Thermal stability of NOTT-500(Ni, Co)

Thermogravimetric analyses (TGA) were performed on NOTT-500(Ni, Co) under a flow of air (Figure 3.11). To remove the non-coordinated DMF molecules in both NOTT-500(Ni, Co), $[M_3(H_3L^1)_2(H_2O)_{10.x}(DMF)_3]_{\infty}$, the samples were previously suspended in acetone over a period of three days with fresh solvent exchanges three times per day. NOTT-500(Ni, Co) were then dried under ambient temperature for a few hours.

The TGA plot of NOTT-500(Ni) shows four weight loss steps (Figure 3.11a). Around 80 °C the first loss of ~10 % in mass was observed. To investigate this drop in weight the sample was heated at 160 °C; once this temperature was reached it was held for 20 minutes and then cooled at RT under air (Figure 3.11b). By heating the sample a change in colour from green (colour at room temperature) to brown (colour after heating) was observed. After leaving the sample at room temperature and exposed to air for about 30 minutes, the original colour (green) was recovered together with the original weight; this cycle was repeated twice leading to the same observation. The experimental evidences indicate that the loss in weight is attributable to the loss of coordinated water molecules as they can be removed by heating and recovered after exposure to air. Moreover, the change in colour suggests a change in the coordination sphere of the metal ions. The water molecules in question are likely to be those uncoordinated and trapped in the voids (which replaced the DMF), and water molecules weakly bound to the metal (Section 3.2.2).

The following two weight loss steps from 220 °C to 650 °C in the TGA of NOTT-500(Ni) are assigned to the progressive decomposition of the framework to the final burning into inorganic phosphonic moieties (corresponding empirical formula $[(Ni_3P_6O_{11})]_{\infty}$).

As expected from the crystallographic data, the two isostructural MOFs showed similar thermal behaviour. Interestingly though NOTT-500(Co) shows lower thermal stability than NOTT-500(Ni) (Figure 3.11a). In the case of NOTT-500(Co) the first drop in weight (~10 %) assigned to the loss of water molecules occurs around 60 °C, compared with ~80 °C for NOTT-500(Ni).

As for NOTT-500(Ni), the first weight loss step was investigated by heating NOTT-500(Co) at 100 °C; once this temperature was reached it was held for 20 minutes and then cooled at RT under air (Figure 3.11c). By heating the sample a change in colour from pink (original colour) to blue (colour after heating) was observed. After leaving the sample at room temperature and exposed to air for about twenty minutes the original colour (pink) was recovered together with the original weight; this cycle was repeated twice leading to the same observation.

The dehydrated NOTT-500(Co) is stable up to 190 °C; two weight loss steps at higher temperatures precede the complete burning of the material (at 630 °C) into inorganic moieties, $[\text{Co}_3\text{P}_6\text{O}_{14}]$.

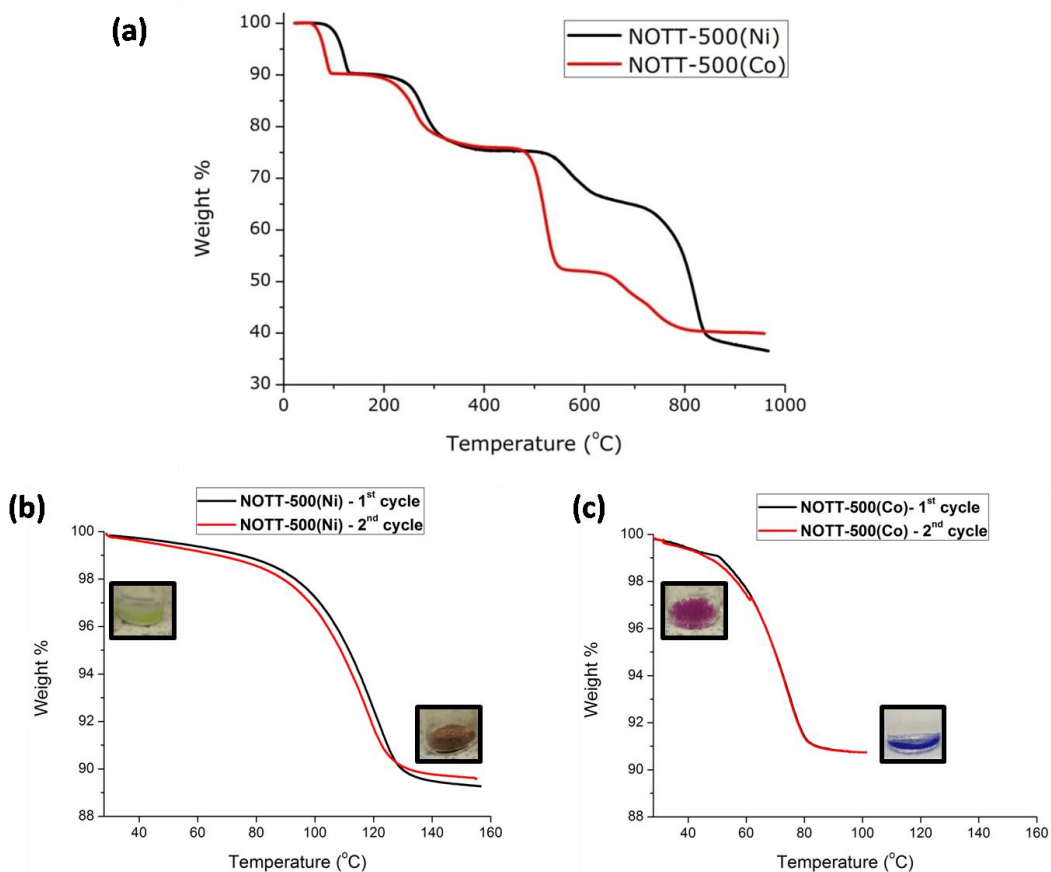


Figure 3.11. (a) Thermogravimetric profiles of NOTT-500(Ni, Co) recorded under air from 25 °C to 1000 °C at a heating rate of 5 °C min⁻¹. (b) TGA of NOTT-500(Ni) recorded under air from 25 °C to 160 °C and correlated change in colour. (c) TGA of NOTT-500(Co) recorded under air from 25 °C to 100 °C and correlated change in colour.

3.2.5 Reversible structural phase change

To further investigate the properties of the dehydrated NOTT-500(Ni, Co), *in situ* variable temperature PXRD (VT-PXRD) and solid-state UV-visible analyses were performed.

3.2.5.1 *In situ* VT-PXRD study of NOTT-500(Ni, Co)

The difference in thermal stability between NOTT-500(Ni) and NOTT-500(Co), and the properties of the dehydrated frameworks were investigated by *in situ* VT-PXRD.

A reversible structural change to a new phase corresponding with the first weight-loss step in the TGA plots was found by indexing the PXRD patterns for NOTT-500(Ni, Co). The crystallographic data is summarised in Table 3.2 and Table 3.3 and a more detailed discussion is given below.

In situ VT-PXRD analysis of NOTT-500(Ni):

In situ VT-PXRD data of NOTT-500(Ni) showed a reversible structural phase transition occurring around 100 °C associated with a colour change (previously described in Section 3.2.4) from green to brown (Figure 3.12).

The PXRD patterns collected at room temperature up to 75 °C were indexed. The results show that NOTT-500(Ni) maintained the original crystallographic phase with small changes in the unit cell due to the temperature increase (Table 3.2). A new crystallographic phase was identified at 100 °C and the new phase was stable up to 125 °C (maximum temperature investigated by VT-PXRD). The structural transition and the first weight loss step in the TGA occur at the same temperature range. By cooling the sample *in situ* and under vacuum the original phase was not recovered and the sample remained as brown powder even at room temperature. After exposing the sample to air the green colour was recovered together with the original crystallographic phase. This reversible phase transition on exposure to air confirmed that the phase change is due to removal/addition of water molecules upon dehydration/rehydration. This was further evidenced by exposing the dehydrated

sample to a flow of dry oxygen; the original crystallographic phase or the green colour of the sample was not recovered.

Unfortunately, the quality of the PXRD data recorded at high temperatures (> 100 °C) was not sufficiently good to solve the structure of the dehydrated phase and it was only possible to determine the unit cell parameters and possible space group. Attempts to repeat the same experiment on a single crystal were not successful due to the progressive decrease in the number of diffractions and physical damage of the single crystal while heating.

However, combining the findings from VT-PXRD and TGA analyses, the new crystallographic phase and the change in colour are likely to correlate to the loss of coordinated water molecules with consequent rearrangement of the framework.

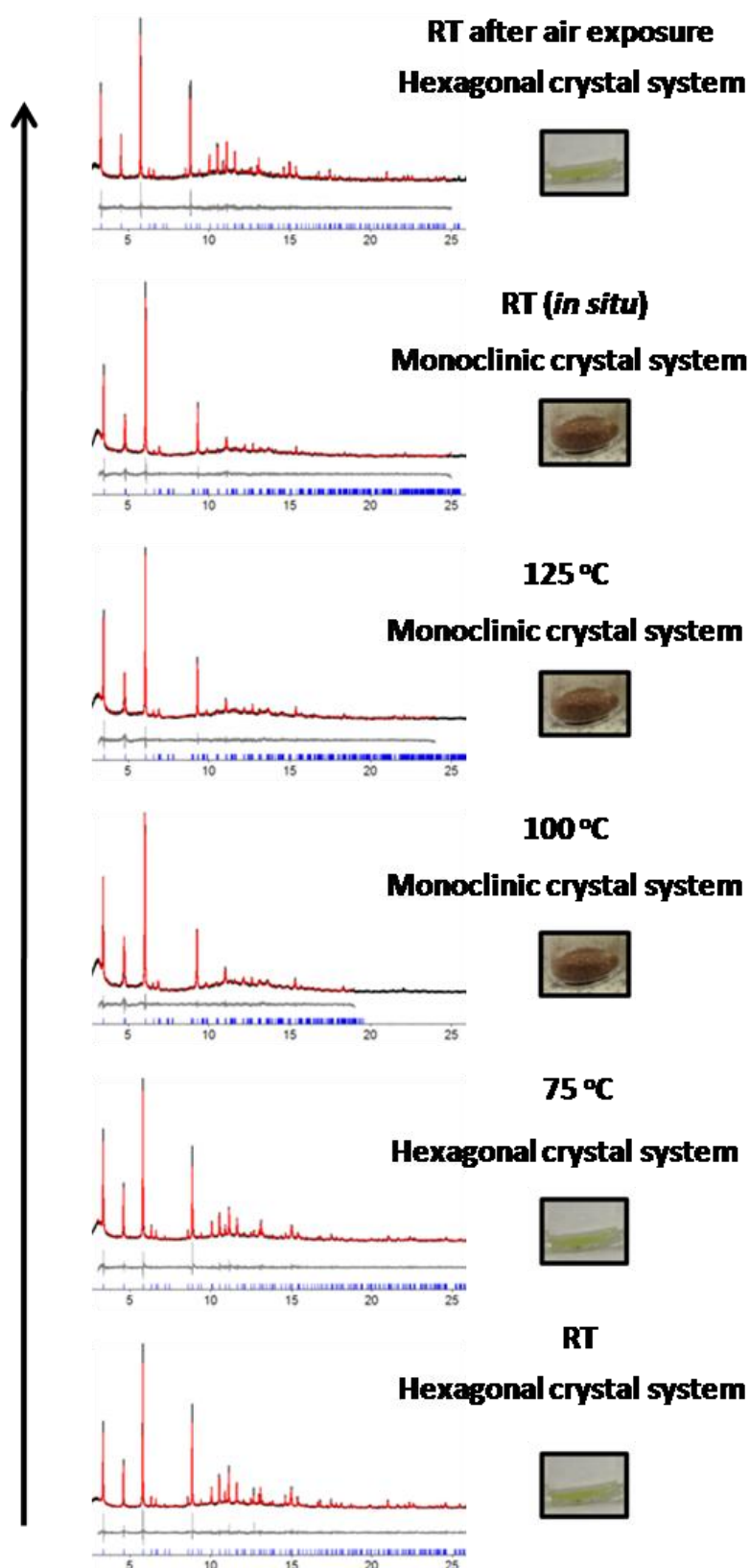


Figure 3.12. *In situ* VT-PXRD data for NOTT-500(Ni) from 25 °C (bottom) to 125 °C and back to 25 °C together with the *ex-situ* pattern of the final rehydrated compound after exposure to air for a few minutes.

Table 3.2. Unit cell parameters from VT-PXRD study for NOTT-500(Ni).

Temperature	RT	75 °C	100 °C
Crystal system	Hexagonal	Hexagonal	Monoclinic
Space group	$P6_3/m$	$P6_3/m$	I_a
a	16.3258(2)	16.3052(1)	14.3828(6)
b	16.3258(2)	16.3052(1)	15.5824(3)
c	14.9749(1)	14.9450(2)	30.3991(13)
α	90°	90°	90°
β	90°	90°	117.480(4)°
γ	120°	120°	90°
R_{wp}	8.30	7.29	6.16
GoF	1.44	1.47	1.72
Colour	Green	Green	Brown

Temperature	125 °C	RT <i>in situ</i>	RT <i>ex situ</i>
Crystal system	Monoclinic	Monoclinic	Hexagonal
Space group	I_a	I_a	$P6_3/m$
a	14.3514(7)	14.2833(8)	16.3258(2)
b	15.5308(7)	15.5040(4)	16.3258(2)
c	30.3605(13)	30.2818(20)	15.0030(2)
α	90°	90°	90°
β	117.596(4)°	117.494(4)°	90°
γ	90°	90°	120°
R_{wp}	8.42	8.96	8.46
GoF	1.56	1.64	1.32
Colour	Brown	Brown	Green

High temperature PXRD (HT-PXRD) data for NOTT-500(Ni) were recorded on a PANalytical X'Pert PRO diffractometer at ambient pressure and under air (Figure 3.13). In the HT-PXRD pattern the phase change occurring around 100 °C is confirmed. In addition, Figure 3.13 shows the subsequent gradual loss of the peak intensities to a complete collapse of the framework at higher temperatures (above 150 °C), as expected from the TGA data.

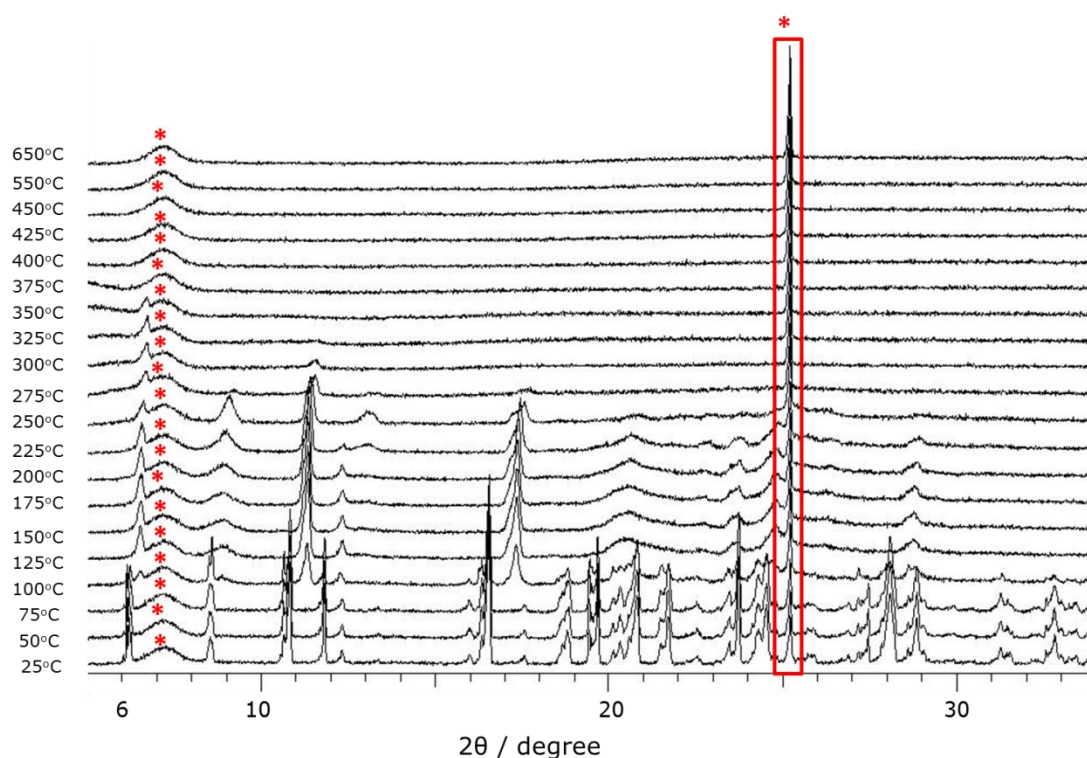


Figure 3.13. *In situ* HT-PXRD data for NOTT-500(Ni) from 25 °C to 650 °C. Stars highlight peaks coming from the sample holder.

In situ VT-PXRD analysis of NOTT-500(Co):

In situ VT-PXRD measurements for NOTT-500(Co) were performed from room temperature up to 100 °C (Figure 3.14). The PXRD patterns were indexed and detailed crystallographic data is summarised in Table 3.3. The original crystallographic phase was retained up to 50 °C; at 75 °C a different crystallographic

phase was identified together with the original one. At 100 °C only the new phase was detected. During the heating process, the colour of NOTT-500(Co) dramatically changed from pink to blue. After cooling the sample at room temperature (*in situ* and under vacuum) NOTT-500(Co) retained the blue colour and the PXRD pattern still indexes to the monoclinic I_a space group. Only after exposing the sample to air was the original phase completely recovered, together with a return to the original pink colour.

As for NOTT-500(Ni), the low quality of the PXRD data collected at high temperature for NOTT-500(Co) and the crystallographical complexity of the framework prevented to solve the structure of the new phase and only the unit cell parameters were determined.

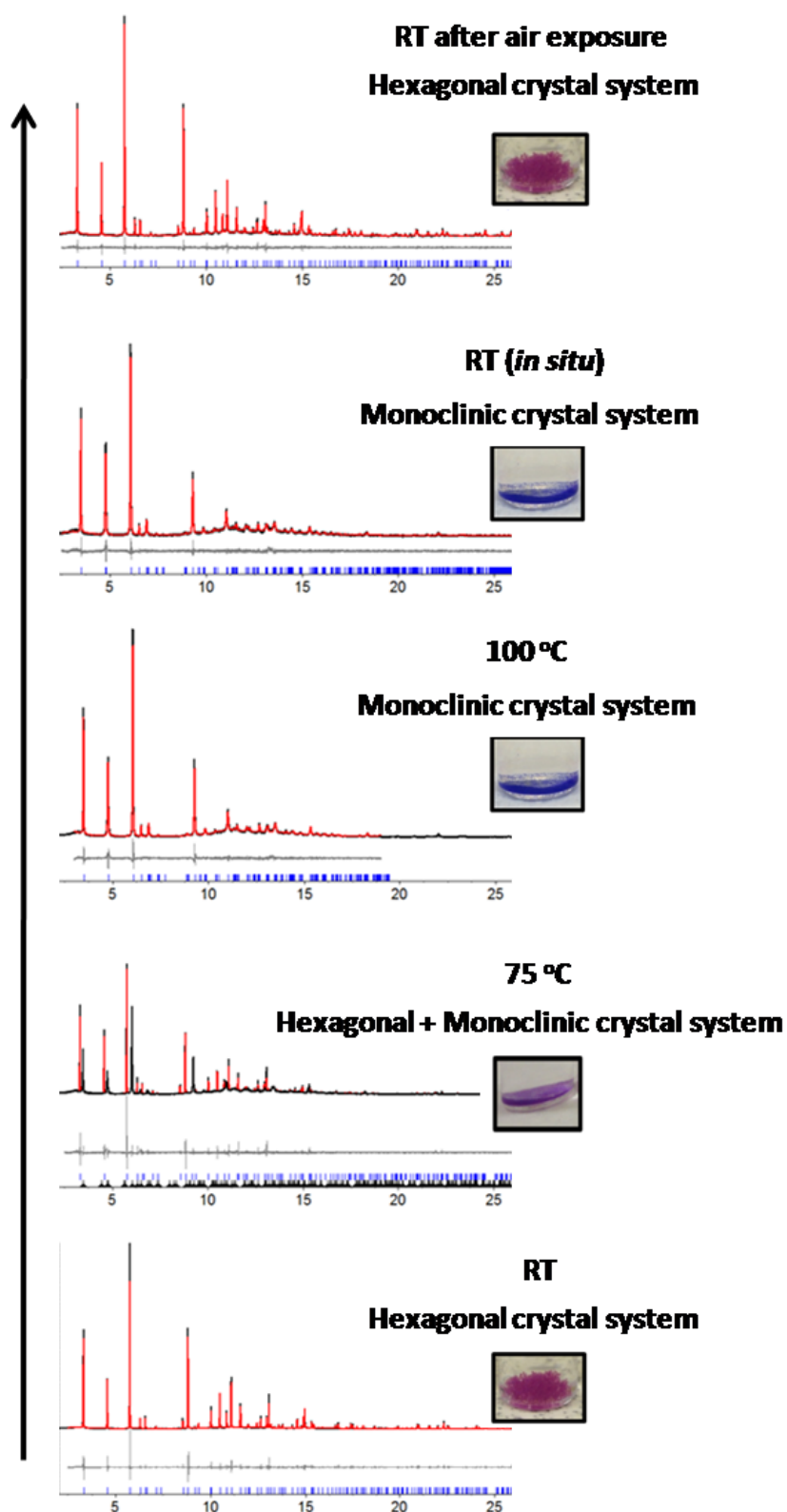


Figure 3.14. *In situ* VT-PXRD data for NOTT-500(Co) from 25 °C (bottom) to 100 °C and back to 25 °C together with the *ex-situ* pattern of the final rehydrated compound after exposure to air for a few minutes.

Table 3.3. Unit cell parameters from VT-PXRD study for NOTT-500(Co).

Temperature	RT	75 °C	
Crystal system	Hexagonal	Hexagonal	Monoclinic
Space group	$P6_3/m$	$P6_3/m$	I_a
a	16.3811(1)	16.3696(2)	14.5254(7)
b	16.3811(1)	16.3696(2)	15.6325(3)
c	14.9857(1)	14.9920(2)	30.5329(14)
α	90°	90°	90°
β	90°	90°	117.542(5)°
γ	120°	120°	90°
R_{wp}	9.79	9.57	
GoF	1.58	1.75	
Colour	Pink	indigo	

Temperature	100 °C	RT <i>in situ</i>	RT <i>ex situ</i>
Crystal system	Monoclinic	Monoclinic	Hexagonal
Space group	I_a	I_a	$P6_3/m$
a	14.5483(4)	14.4708(5)	16.3813(1)
b	15.5691(4)	15.5183(3)	16.3813(1)
c	30.5100(10)	30.4061(11)	14.9917(1)
α	90°	90°	90°
β	117.854(3)°	117.820(3)°	90°
γ	90°	90°	120°
R_{wp}	7.44	8.60	8.46
GoF	1.87	1.37	1.33
Colour	Blue	Blue	Pink

3.2.5.2 Solid-state UV-visible study of NOTT-500(Ni, Co)

To probe more insights into the possible change of the coordination environment of the metal ions in the MOFs and correlated with the change in colour, solid-state UV-visible absorption spectra were measured for NOTT-500(Ni, Co) soaked in various dry organic solvents with differing polarities and donor-acceptor properties. Single crystals of NOTT-500(Ni, Co) were suspended in dry solvents of benzene, dichloromethane, acetonitrile and methanol for one week with daily fresh solvent exchanges and solid state UV-visible absorption spectra were collected. The aim of this experiment was to investigate whether the change in colour can be promoted by polar solvents able to replace coordinated water molecules to the metal, and if this process is directly correlated to the phase change. At this end, to study the effect of dry solvents on the frameworks, high resolution PXRD (HR-PXRD) of the solvent exchanged samples were collected at Diamond Light Source, Beamline I11. In order to prevent any contact with the atmosphere, the samples soaked in dry organic solvents were gently dried under inert atmosphere and loaded and sealed into capillaries inside the glove-box.

Solid-state UV-visible absorption spectroscopy of NOTT-500(Ni):

Solid-state UV-visible absorption spectra of NOTT-500(Ni) soaked in dry benzene, dichloromethane, acetonitrile and methanol were recorded. To ensure the exchange of possible coordination solvents, the MOFs were suspended in the solvents for a few days with daily fresh solvent exchanges. UV-visible absorption spectra of NOTT-500(Ni) show an absorption band centred at *ca.* 410 nm for all the solvent-exchanged samples and no colour change was observed (Figure 3.15). For NOTT-500(Ni)

activated at 125 °C, a significant shift of the absorption band from *ca.* 410 nm to *ca.* 460 nm is observed, together with a colour change from green to brown.

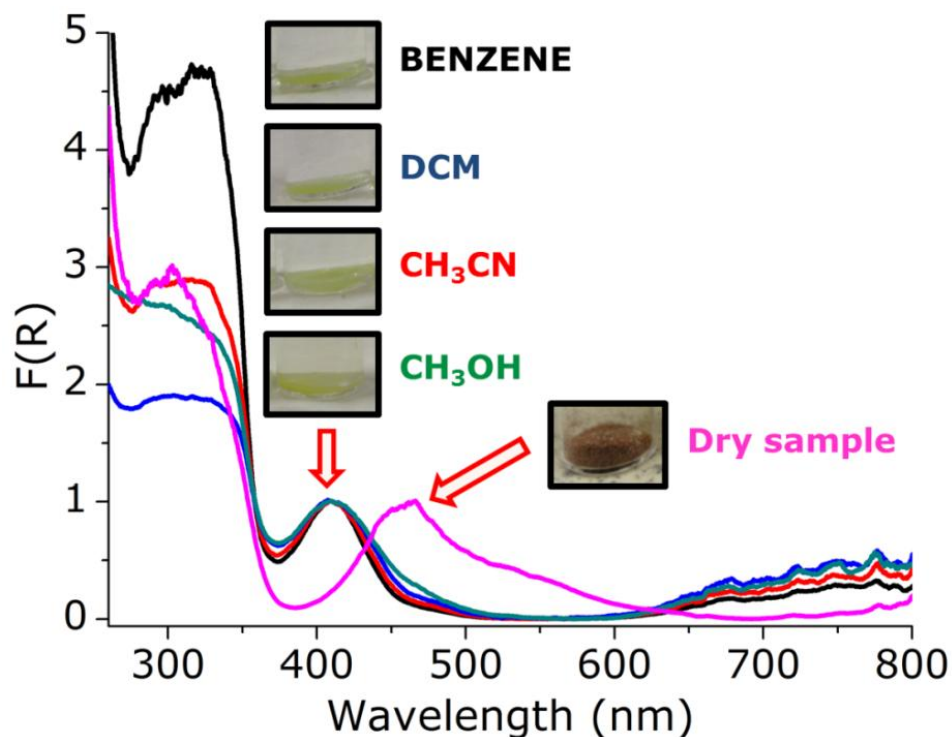


Figure 3.15. Solid-state UV-visible absorption spectra of NOTT-500(Ni) after soaking in dry organic solvents and under vacuum: benzene (*black*); dichloromethane (*blue*); acetonitrile (*red*); methanol (*green*); activated at 130 °C (*pink*).

HR-PXRD patterns of the samples soaked in organic solvents were collected and indexed to investigate any possible structural change promoted by the chosen solvents (Figure 3.16, Table 3.4). All materials were indexed in the hexagonal space group and the phase change into the monoclinic crystal system wasn't observed. In the case of benzene, DCM and CH₃CN, small changes in the unit cell parameters are attributed with the absorption of solvent molecules which are replacing water molecules in the voids of the framework preventing the phase change. The lack of

colour change is a strong indication of the non-modified coordination sphere of the metal. The sample soaked in methanol lost crystallinity, and it was not possible to extract any crystallographic information. Only in the case of the sample heated at 125 °C, both change in phase and in colour were observed.

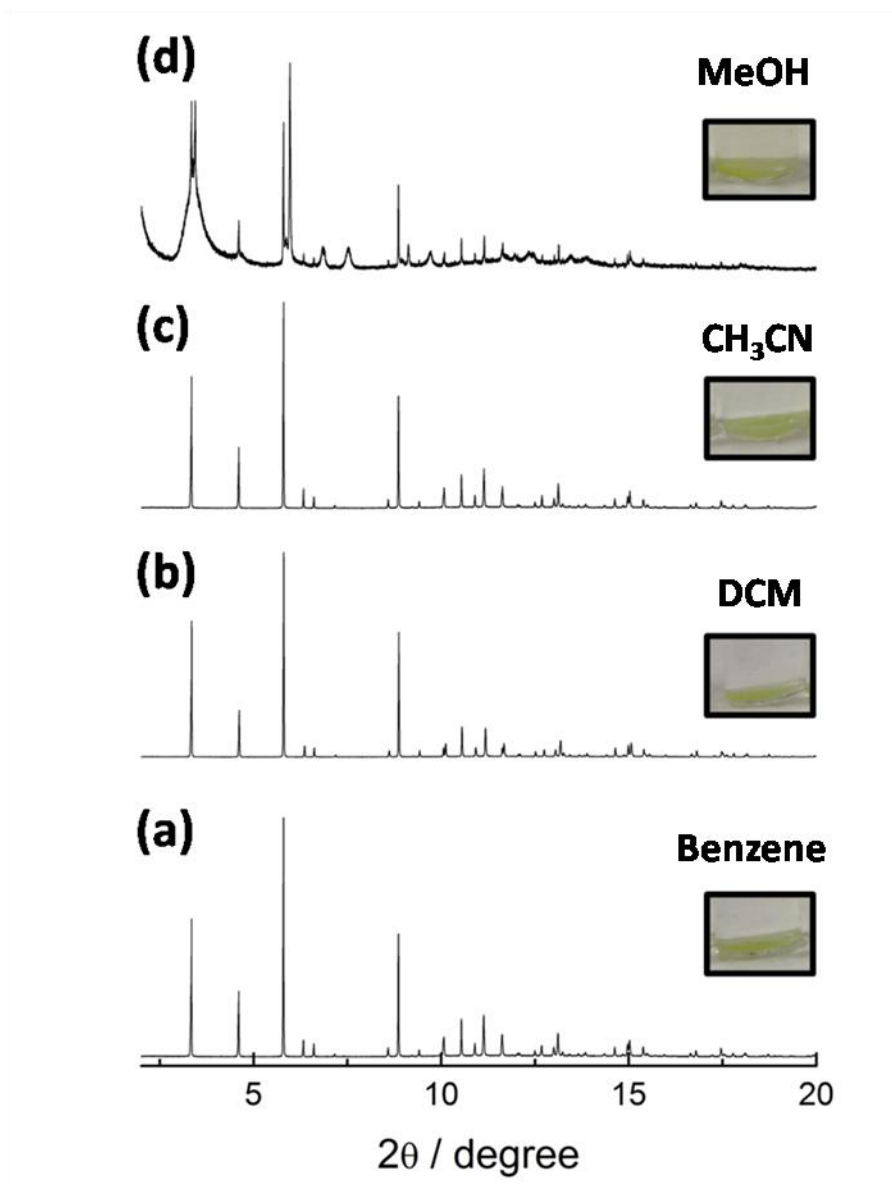


Figure 3.16. HR-PXRD for NOTT-500(Ni) in: (a) dry benzene; (b) dry dichloromethane; (c) dry acetonitrile; (d) dry methanol.

Table 3.4. Unit cell parameters from HR-PXRD study for NOTT-500(Ni) suspended in different dry organic solvents.

Sample	RT	Benzene	DCM	CH ₃ CN	Activated (125 °C)
Crystal system	Hexagonal	Hexagonal	Hexagonal	Hexagonal	Monoclinic
Space group	<i>P</i> 6 ₃ / <i>m</i>	<i>I</i> _a			
a	16.3258(2)	16.3228(1)	16.3055(1)	16.3220(1)	14.3514(7)
b	16.3258(2)	16.3228(1)	16.3055(1)	16.3220(1)	15.5308(7)
c	14.9749(1)	14.9581(1)	14.8804(1)	14.9508(1)	30.3605(13)
α	90°	90°	90°	90°	90°
β	90°	90°	90°	90°	117.596(4)°
γ	120°	120°	120°	120°	90°
R_{wp}	8.30	12.92	9.92	9.52	8.42
GoF	1.44	2.32	1.97	1.64	1.56
Colour	Green	Green	Green	Green	Brown

Solid-state UV-visible absorption spectroscopy of NOTT-500(Co):

Solid-state UV-visible absorption spectra of NOTT-500(Co) soaked in dry benzene, dichloromethane, acetonitrile and methanol were recorded (Figure 3.17). To ensure the exchange of possible coordination solvents, the samples were suspended in the dry solvents for a few days with daily fresh solvent exchanges.

After suspending the MOF in dry methanol or acetonitrile for a few minutes, an intense colour change from pink to blue was observed. Less marked colour changes from pink to lavender was observed by soaking NOTT-500(Co) in dry DCM. In the case of benzene, no colour change was observed. The initial pink colour of the as-

synthesised NOTT-500(Co) corresponds to a broad absorption band centred at 530 nm. In the solvent-soaked samples a second absorption is observed at lower energy, centred around 630 nm. This absorption is more intense for the samples suspended in dry acetonitrile and methanol, significantly less intense for the sample in dry DCM and even less in the case of benzene. This suggests that more polar solvents partially displace coordinated water molecules more efficiently than the less polar solvents.

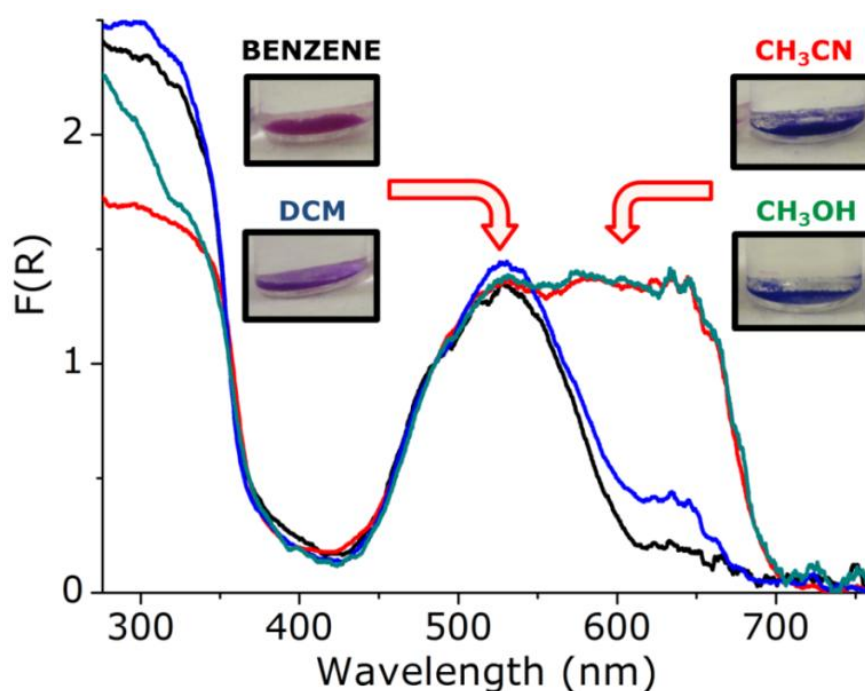


Figure 3.17. Solid-state UV-visible absorption spectra of NOTT-500(Co) after soaking in dry organic solvents: benzene (*black*); dichloromethane (*blue*); acetonitrile (*red*); methanol (*green*).

HR-PXRD data of NOTT-500(Co) suspended in dry solvents were collected and indexed to investigate the correlation between the observed change in colour and potential structural transitions of the framework (Figure 3.18). All materials were indexed in the hexagonal space group and the phase change into the monoclinic

crystal system wasn't observed; however when the colour change is observed it strongly suggests changes of the metal coordination.

In the case of the less polar solvent, benzene, no colour change was observed which strongly indicates that the coordinated water is not displaced. The change in the unit cell parameters are attributed to the absorption of solvents molecules which are replacing the water molecules in the voids of the framework without causing gross phase change. In the more polar DCM and CH₃CN, coordinated molecules are likely to be removed leading to a change in the metal coordination sphere responsible of colour change. However, the original phase is mainly retained as the solvent molecules play similar role as the water in the voids, with only small change of the unit cell parameters. Similarly with NOTT-500(Ni), the methanol causes partial collapse of the NOTT-500(Co) framework and no further crystallographic information could be extrapolated.

In conclusion, the most polar organic solvent can partially displace the water weakly coordinated to the cobalt, leading to changes in colour (Figure 3.18) while the changes in the unit cell parameters (hexagonal space group) are more likely assignable to the inclusion of the solvents in the voids of the framework (Table 3.5). The complete transition into the monoclinic unit cell (Section 3.2.5.1) was not observed as it corresponds to the fully dehydrated NOTT-500(Co) after heating above 75 °C, which leads to both the loss of solvent molecules trapped into the voids and the loss of weakly bound water.

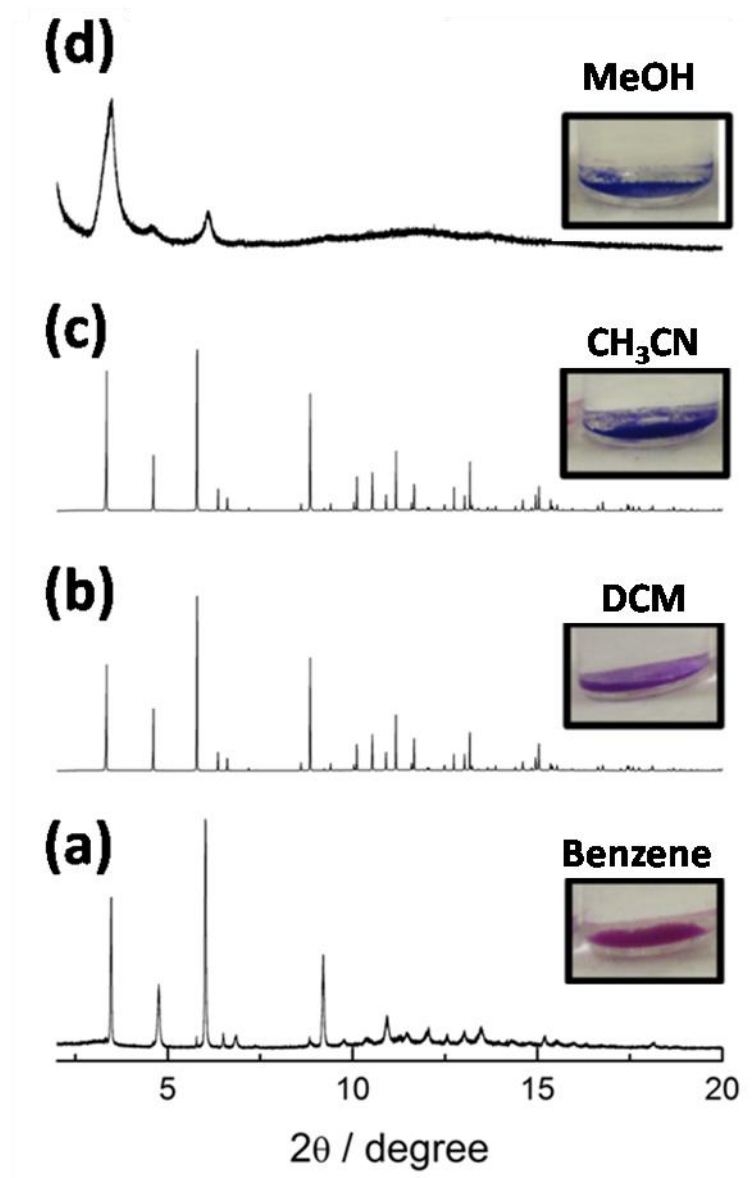


Figure 3.18. HR-PXRD for NOTT-500(Co) in: (a) dry benzene; (b) dry acetonitrile; (c) dry dichloromethane; (d) dry methanol.

Table 3.5. Unit cell parameters from HR-PXRD study for NOTT-500(Co) suspended in different dry organic solvents.

Sample	RT	Benzene	DCM	CH₃CN
Crystal system	Hexagonal	Hexagonal	Hexagonal	Hexagonal
Space group	<i>P6₃/m</i>	<i>P6₃/m</i>	<i>P6₃/m</i>	<i>P6₃/m</i>
a	16.3811(1)	15.7142(11)	16.3585(1)	16.3614(1)
b	16.3811(1)	15.7142(11)	16.3585(1)	16.3614(1)
c	14.9857(1)	14.5526(11)	14.8978(1)	14.8954(1)
α	90°	90°	90°	90°
β	90°	90°	90°	90°
γ	120°	120°	120°	120°
R_{wp}	9.79	12.87	8.76	10.92
GoF	1.58	1.94	13.36	15.93
Colour	Pink	Pink	Lavender	Blue

Comparing the data obtained for NOTT-500(Ni) and NOTT-500(Co) it can be concluded that solid-state UV-visible absorption spectroscopy indicates that water molecules coordinated to the metals are removed more easily in the case of NOTT-500(Co) than NOTT-500(Ni). The thermal stability of NOTT-500(Ni, Co) is also likely to be associated with the different binding strength of the water molecules coordinated to the metal ions.

3.2.6 Proton conductivity study of NOTT-500(Ni, Co)

Efficient proton conductors require acidic protons located sufficiently close to each other to facilitate charge transfer within the framework.¹⁵ Recent reports have demonstrated the inclusion of acidic phosphonic protons within a MOF to create promising proton conducting materials.^{1,20,24} In NOTT-500(Ni, Co), the distances (in the range of 2.0 Å to 2.9 Å) between the uncoordinated hydroxyl from the phosphonate groups (P-OH) and the water molecules coordinated to the metal (M-H₂O) define a potential proton-hopping pathway for proton conduction (Figure 3.19). Proton conductivities of NOTT-500(Ni, Co) were studied by AC impedance spectroscopy on compact pellets using cell B (Section 2.2.3.2). For each MOF about 0.120 g of sample was ground into a fine powder using mortar and pestle, sandwiched between two discs of carbon film (Sigracet GDL, 10 BB) and pressed for 5 minutes under a pressure of 5 tons using a die with 0.8 cm diameter. The resulting thickness of each pellet was measured and, together with the diameter, was used to calculate the proton conductivity of NOTT-500(Ni, Co) (Section 2.1.6, Equation 10). The impedance measurements for both NOTT-500(Ni, Co) were repeated on two different batches of sample and for each batch three measurements were collected at each value of temperature and relative humidity investigated. The data collected was used to calculate the mean value of the proton conductivity correspondent to the experimental conditions under study, together with the associated standard deviation.

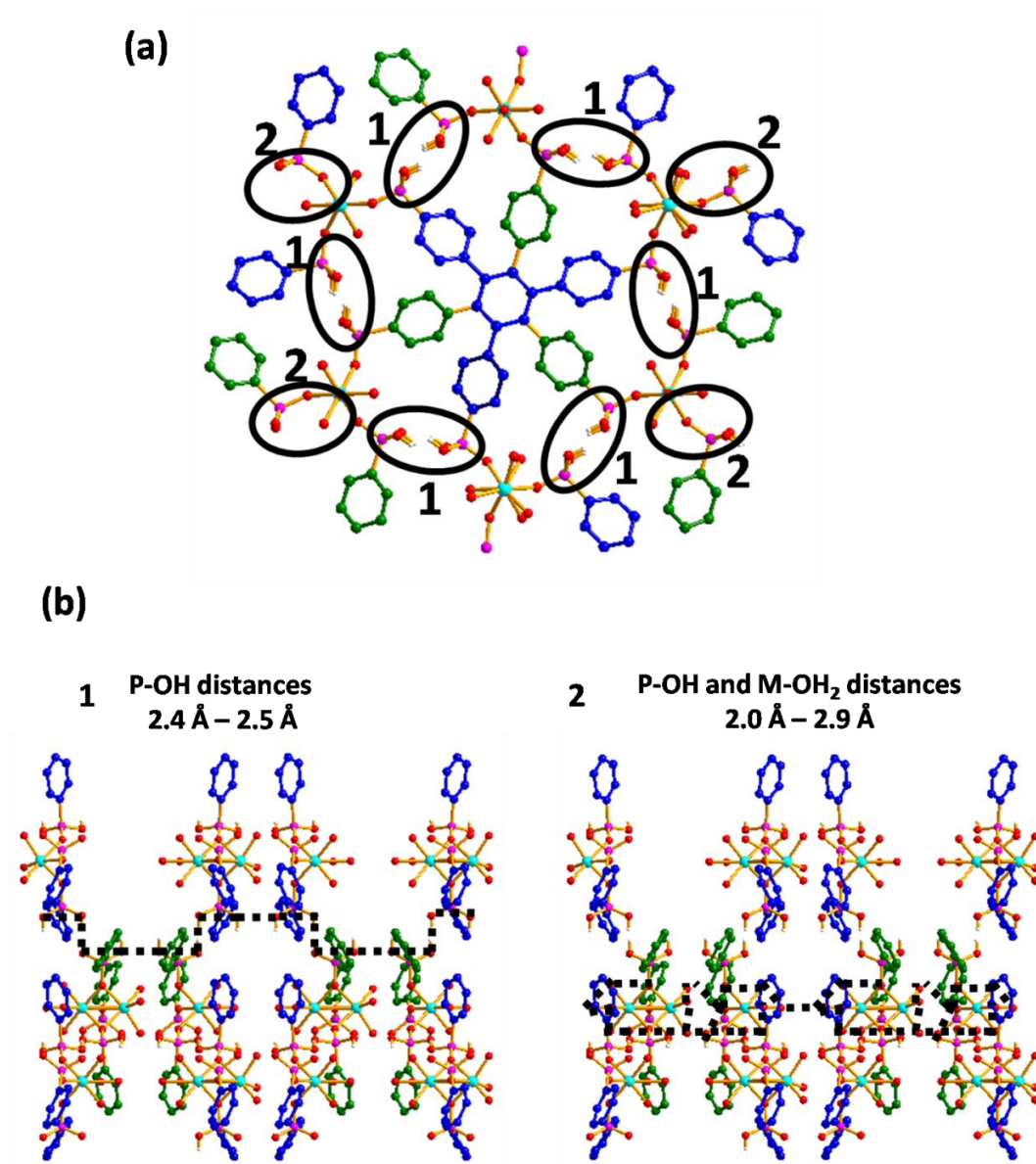


Figure 3.19. Proton-hopping pathway for NOTT-500(M): (a) view down the c -axis (b) view along the a -axis showing details of the hydrogen-bonding short distances (black dot line) between P-OH distances (1) and P-OH – M-OH₂ distances (2).

Proton conductivity at different relative humidities:

The proton conductivity properties of solid materials are often influenced by the relative humidity.^{6,15,25–27} Thus, AC impedance spectroscopy measurements on NOTT-500(Ni, Co) were performed at a range of relative humidities, from 0 % to 99 % RH and 25 °C.

The dry pellet (sandwiched between two layers of carbon film) was loaded inside the conductivity cell and exposed to 99 % RH humidity overnight to allow the sample compressed into the pellet to equilibrate under the desired conditions. The % RH was then progressively decreased to 75 % and 45 % RH. Specific relative humidities were obtained inside the conductivity cell by bubbling N₂ through water or water solutions saturated with different inorganic salts (Section 2.2.4). Measurements were collected every 45 minutes until the resistivity of the sample was stable over a period of two hours suggesting the equilibration point was reached. Nyquist and Bode plots for NOTT-500(Ni, Co) collected at 99 %, 75 % and 45 % RH at 25 °C show progressive decrease of resistance while increasing the % RH (Figure 3.20 and 3.21). Proton conductivity data for NOTT-500(Ni, Co) were measured at each % RH investigated, and both materials reached maximum conductivity at 99 % RH (Tables 3.6 and 3.7). At 99 % RH and 25 °C, the proton conductivity was $1.11(03) \times 10^{-4} \text{ S cm}^{-1}$ for NOTT-500(Ni) and $4.42(06) \times 10^{-5} \text{ S cm}^{-1}$ for NOTT-500(Co). Measurements on both materials were repeated twice and the difference of the conductivities between the isostructural NOTT-500(Ni) and NOTT-500(Co) is repeatable, unexpected, and interesting. Details about the calculation of the resistance and the proton conductivity are given below. The reduction of resistance with increasing relative humidity is a typical and well-known response observed in PEMs and MOFs when their proton conductivity is water-mediated.^{6,28-31} The water-mediated proton conductivity relies on the presence of water molecules and on hydrogen-bonding interactions of the water molecules playing an important role in the migration of protons through the hopping pathway of the material.³²

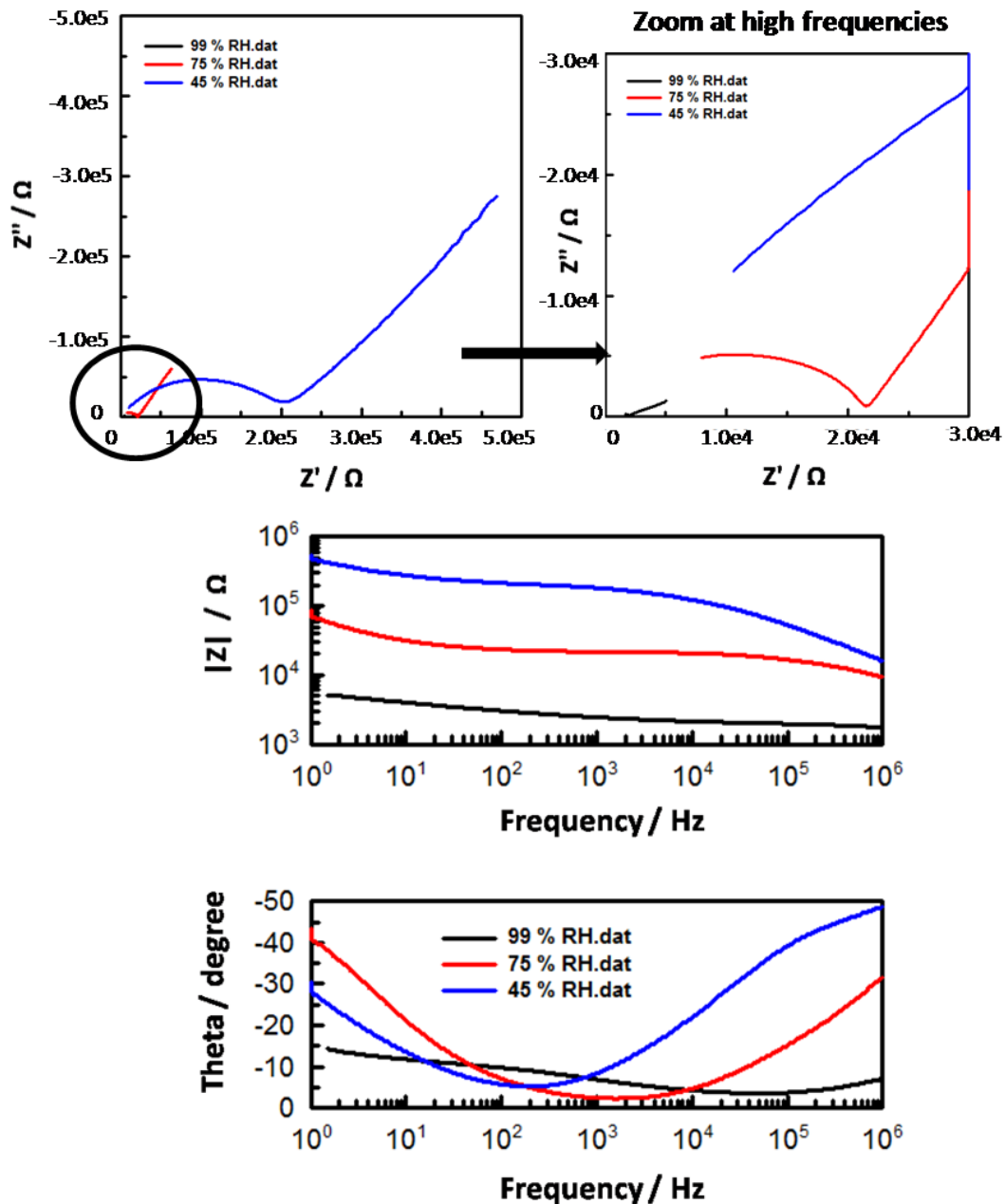


Figure 3.20. Nyquist and Bode plots for NOTT-500(Ni) measured at different % RH and 25 °C.

Table 3.6. Proton conductivities (S cm^{-1}) for NOTT-500(Ni) measured at different % RH and 25 °C.

Sample	σ at 99 % RH	σ at 75 % RH	σ at 45 % RH
NOTT-500(Ni)	$1.11(03) \times 10^{-4}$	$1.50(09) \times 10^{-5}$	$1.58(11) \times 10^{-6}$

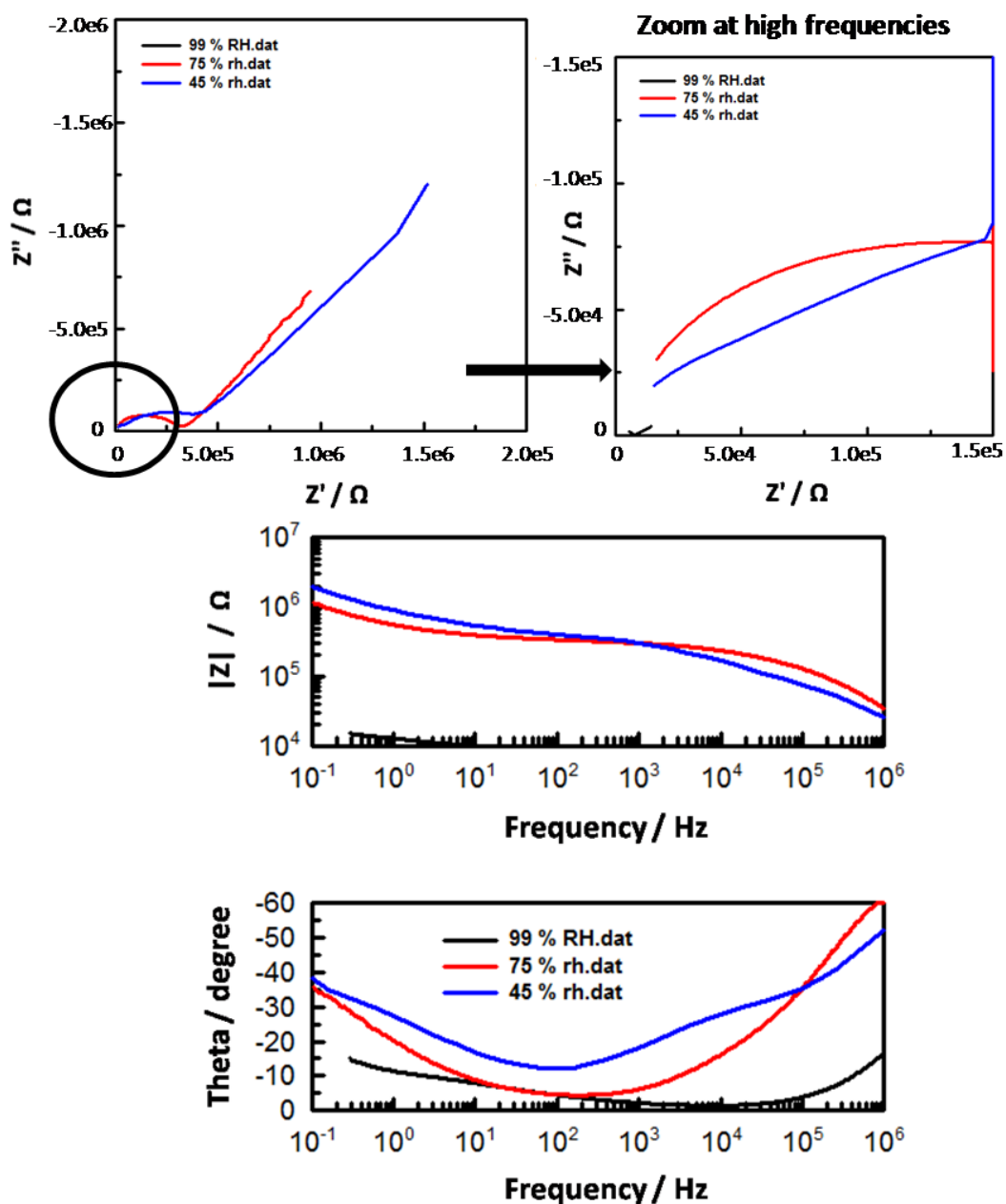


Figure 3.21. Nyquist and Bode plots for NOTT-500(Co) measured at different % RH and 25 °C.

Table 3.7. Proton conductivities (S cm^{-1}) for NOTT-500(Co) measured at different % RH and 25 °C.

Sample	σ at 99 % RH	σ at 75 % RH	σ at 45 % RH
NOTT-500(Co)	$4.42(06) \times 10^{-5}$	$1.00(08) \times 10^{-6}$	$5.10(10) \times 10^{-7}$

At 25 °C and 0 % RH, NOTT-500(Ni, Co) showed almost no conductivity. However, the proton conductivity data discussed above can be fully regained after exposing the materials at 99 % RH at room temperature.

Although NOTT-500(Ni, Co) have acidic protons within the framework, the reason for poor conductivity at low % RH probably lies in their structure, where hydrogen bonds are not continuous in all directions. The protons organised in the hopping pathway (Figure 3.19b) are mainly confined around the metal chains down the *a/b*-axes, but less along the *c*-axis where the hopping pathway is alternated by organic regions (Figure 3.19a). Moreover, the bulk proton conductivity was measured on a microcrystalline powder where single particles are randomly orientated in the pellet; examples of impedance measurements on MOFs where the proton conductivity was crucially dependent on the orientation of the crystal have been reported before.¹⁸

The proton conductivity significantly decreases with increasing temperature; this is attributable to dehydration of the samples leading to a new phase with unknown proton-hopping pathway (Section 3.2.5). In addition, the decrease of proton conductivity at high temperatures is also a characteristic behaviour of water-mediated proton conductors and arises when a drastic reduction in the number of proton-carrier occurs.²⁰

Fitting of Nyquist and Bode plots with equivalent circuit:

The Nyquist plots of NOTT-500(Ni, Co) contain a semi-circle in the high frequency region and a pronounced tail at low frequencies. The semi-circle in the high-frequency region represents the bulk and grain boundary resistance. The tail at low frequencies, which is typical of materials with predominantly ionic conductivity, may indicate blocking of H⁺ at the electrodes consistent with ion migration.

The Bode plots give information about the frequency range investigated, which doesn't appear in the Nyquist plot. In addition, they show how the absolute resistance and phase shift (Section 2.1.4) change as a function of the applied frequency.

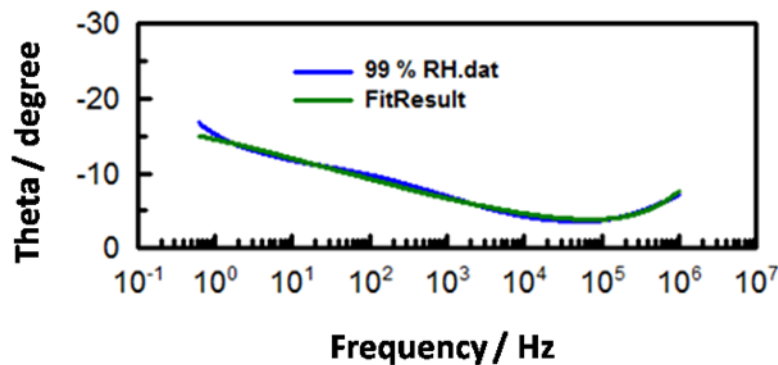
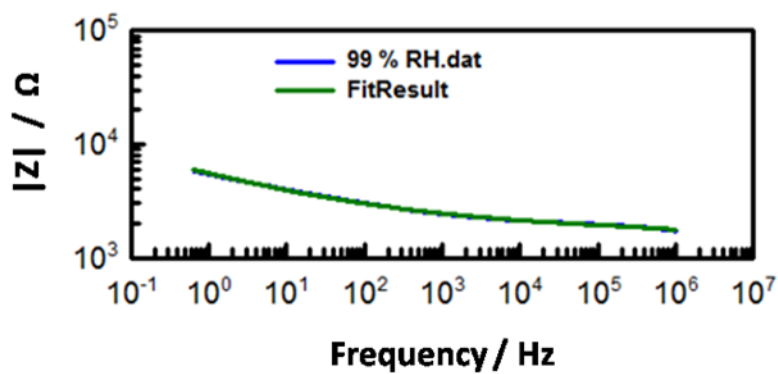
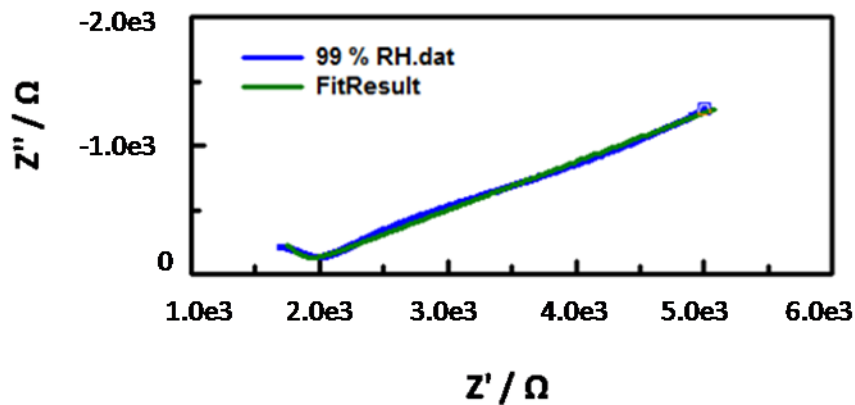
Nyquist and Bodes plots of crystalline powder samples are often resolved using equivalent circuits made of a combination of resistances (R) and constant-phase-elements (CPE) (Section 2.1.5).³³⁻³⁵ The impedance spectra of NOTT-500(Ni, Co) were fitted by the equivalent circuit (R_bQPE_b)(R_{gb}QPE_{gb}). In agreement with most of the data relating to crystalline powder samples, two distinct transport processes were considered. The first process is attributed to the bulk phase (R_bQPE_b) and is correlated to the intrinsic properties of the material. The second process is attributed to the grain boundaries (R_{gb}QPE_{gb}), which takes into account the defects and charge inhomogeneities arising from the reorganisation of the grains in the pellet.^{33,35}

QPE is defined by Equation 11 and derived from a mathematical modification of CPE (Equation 8, Section 2.1.5). QPE is the contribution to account for the depressed, *versus* perfect, semi-circle due to non-ideal capacitance.³⁶

$$Z_{\text{QPE}} = 1 / [(j\omega Y_o)^\alpha] \quad (11)$$

$$Z_{\text{CPE}} = 1 / [(j\omega)^\alpha Y_o] \quad (8)$$

The proposed equivalent circuit simulates fairly accurately the frequency response of NOTT-500(Ni, Co) (Figures 3.22 and 3.23). By fitting the experimental profiles, the values of R_b were estimated and used to calculate the bulk proton conductivity of NOTT-500(Ni, Co) (Section 2.1.7).



Equivalent circuit ($R_b QPE_b$)($R_{gb} QPE_{gb}$)

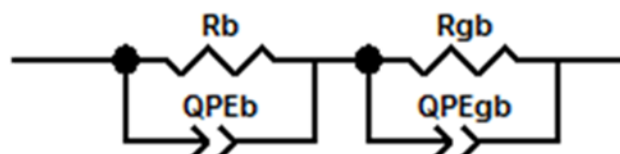


Figure 3.22. Fitting of the Nyquist and Bode plots for NOTT-500(Ni) measured at 25 °C and 99 % RH with the equivalent circuit ($R_b QPE_b$)($R_{gb} QPE_{gb}$).

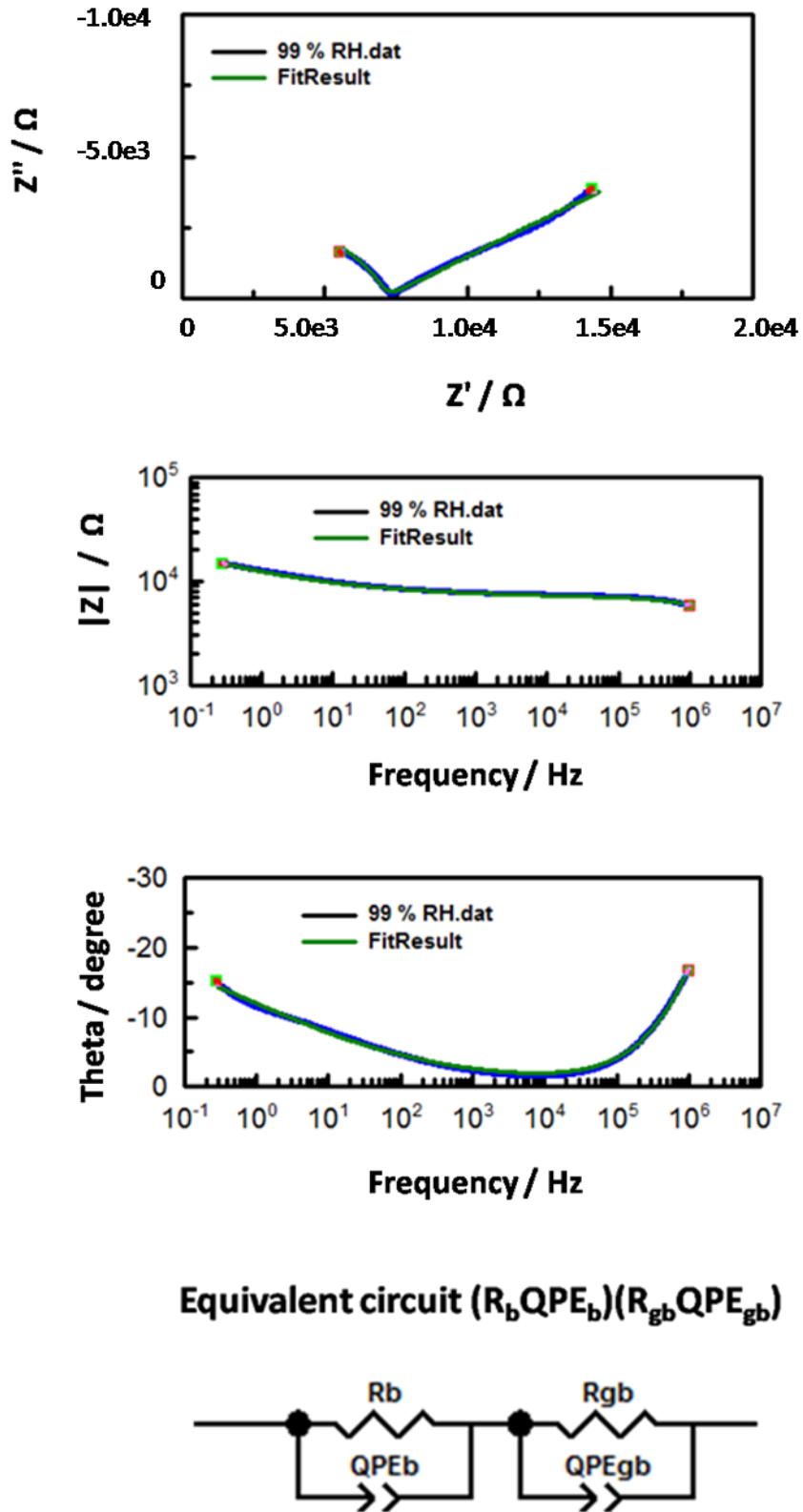


Figure 3.23. Fitting of the Nyquist and Bode plots for NOTT-500(Co) measured at 25 °C and 99 % RH with the equivalent circuit $(R_b QPE_b)(R_{gb} QPE_{gb})$.

Activation energy of the proton conduction process for NOTT-500(Ni):

Impedance analyses between 1 MHz and 0.1 Hz were performed over the temperature range of 18-31 °C at 99 % RH to calculate the activation energy of the proton conduction process for NOTT-500(Ni) (Figure 3.24 and Table 3.8). The narrow temperature range ensures constant water content; therefore the conductivity variation only depends upon temperature.^{6,17,20,37} Similar experiments to calculate the activation energy of the conduction mechanism have been widely reported in literature by Cabeza,^{19,20,38} S. Kitagawa,³⁷ and Shimizu.¹⁷ The activation energy for the proton conductivity ($\sigma = 1.6 \times 10^{-3} \text{ S cm}^{-1}$ at 19 °C at 100 % RH) of $\text{MgH}_6\text{ODTMP} \cdot 6\text{H}_2\text{O}$ [where H_8ODTMP is octamethylenediamine-*N,N,N',N'*-tetrakis(methylenephosphonic acid)] was determined in the temperature range between 9-19 °C.

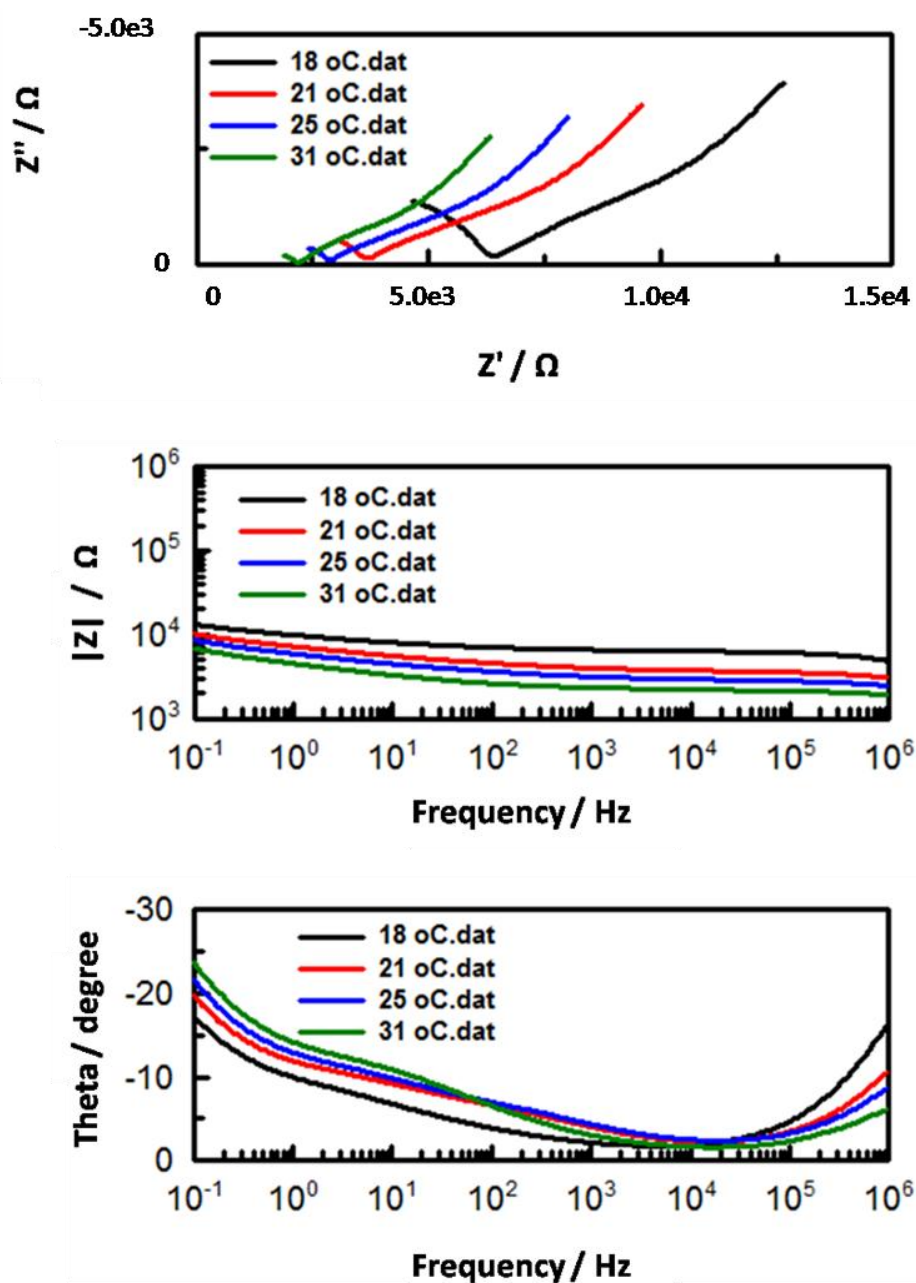


Figure 3.24. Nyquist and Bode plots for NOTT-500(Ni) measured at different temperatures and 99 % RH.

Table 3.8. Proton conductivities ($S \text{ cm}^{-1}$) of NOTT-500(Ni) measured at different temperatures and 99 % RH.

Sample	σ at 18 °C	σ at 21 °C	σ at 25 °C	σ at 31 °C
NOTT-500(Ni)	$7.00(03) \times 10^{-5}$	$9.10(05) \times 10^{-5}$	$1.11(03) \times 10^{-4}$	$1.53(04) \times 10^{-4}$

The proton conductivity for each investigated temperature was calculated and plotted in an Arrhenius plot in order to calculate the activation energy (E_a). Figure 3.25 shows the linear trend of the Arrhenius plot, which displays the logarithm of the absolute proton conductivity of bulk NOTT-500(Ni) as a function of $[1/T(K)]*1000$. The activation energy for NOTT-500(Ni) was calculated according to Equation 12 and was estimated to be 0.46 eV. Activation energy values obtained under hydrated conditions and over similar temperature ranges are reported in Table 1.1 (Chapter 1).

$$E_a = m * K_B \tag{12}$$

Where m is the slope of the line and K_B is the Boltzmann's constant equal to $8.617 * 10^{-5} \text{ eV K}^{-1}$.

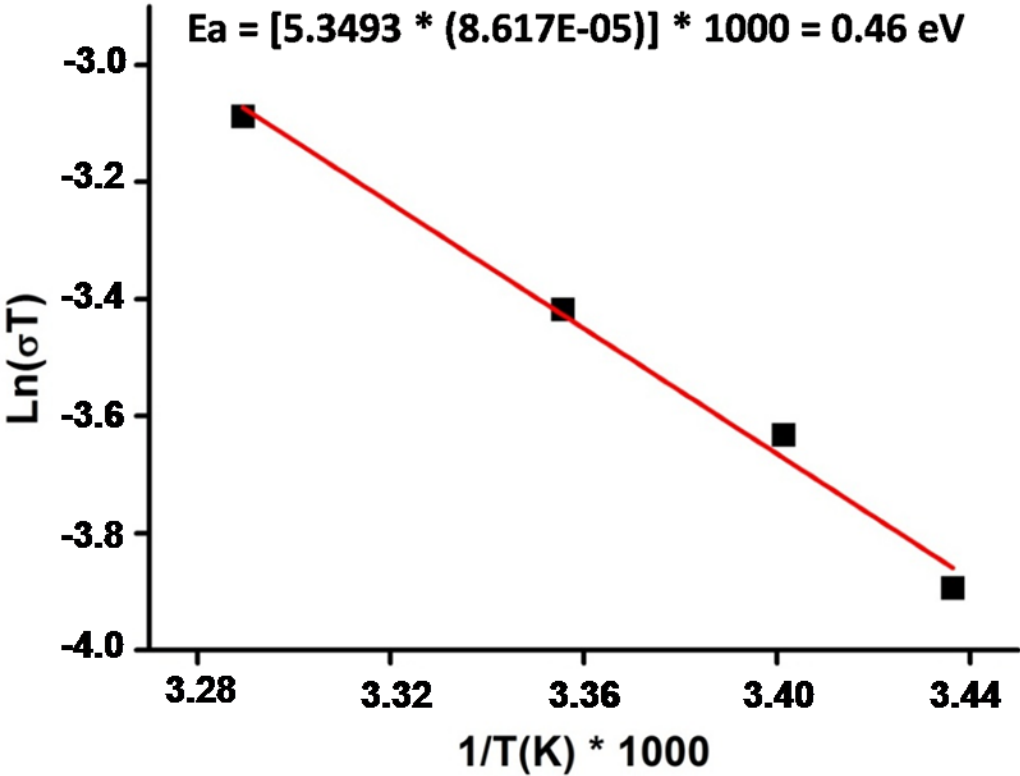


Figure 3.25. Arrhenius plot of the proton conductivity at various temperatures of NOTT-500(Ni) under 99 % RH.

The two main mechanisms for proton diffusion assisted by water molecules are the Vehicle ($E_a > 0.4$ eV) and the Grotthuss mechanism (E_a up to about 0.4 eV).³⁹ In the first case, the diffusion of protons is assisted for long distances by a vehicle (such as water molecules or H_3O^+ ions). In the Grotthuss mechanism, protons are transferred via hydrogen bonds from one site to another along the framework. The activation energy for NOTT-500(Ni) lies at the boundary of the two mechanisms and it is thus likely that proton conduction in NOTT-500(Ni) is governed by the combination of both the Grotthuss and Vehicle mechanisms. This behaviour was previously observed in a few cases.^{14,25,40,41} $(NH_4)_2(adp)[Zn_2(ox)_3] \cdot 3H_2O$ is an example of a highly proton conducting MOF ($8 \times 10^{-3} \text{ S cm}^{-1}$ at 25 °C under 98 % RH) with E_a of 0.63 eV. In this case the mechanism of proton conduction was assigned to the Grotthuss type, combined with other processes such as direct diffusion of additional protons with water molecules or ammonia molecules (Vehicle mechanism).^{25,40}

In NOTT-500(Ni) the charge is likely to diffuse by the Grotthuss mechanism through the proton-hopping pathway identified above (pathway along the bonded water molecules (M-OH₂) and hydroxyl groups (P-OH) located at distances between 2.0 Å and 2.9 Å) (Figure 3.19); water molecules assist longer-range diffusion of protons along the whole framework by the Vehicle mechanism. Since the distance between one proton-hopping pathway and the next one is longer than that between the protons from the M-OH₂ and P-OH, the presence of water is needed. This explains the increased proton conductivity under humid conditions and is consistent with the activation energy experimentally determined for the whole process.

3.2.7 Quasi-elastic neutron scattering study of NOTT-500(Ni)

Neutron scattering is a powerful experimental tool for studying the structure and dynamics of atoms in solids.⁴² This technique gives access to the correlation functions for atomic motions at distances of a few angstroms. Hydrogen nuclei dominate incoherent neutron scattering since their scattering cross section ($\sigma_{\text{inc}} = 80$ b, $1 \text{ b} = 10^{-24} \text{ cm}^2$) is more than one order of magnitude larger than that of any other atomic nuclei; in this case such as carbon ($\sigma_{\text{inc}} = 0$ b), nitrogen ($\sigma_{\text{inc}} = 0.5$ b), oxygen ($\sigma_{\text{inc}} = 0$ b), and phosphor ($\sigma_{\text{inc}} = 0.01$ b).⁴³ Therefore, self-motions of molecules/ions/functional groups with hydrogen atoms are preferentially detected through the incoherent scattering. This allows to obtain scattering spectra dominated by the scattering from hydrogen-containing species rather than from the confining matrix.

The proton conduction mechanism and the reversible phase transition associated with loss and reacquisition of water molecules in NOTT-500(Ni) were investigated through quasi-elastic neutron scattering (QENS) analyses.

QENS is measured as a function of both energy transfer and scattering vector, Q . On the energy scale, the elastic scattering appears as a peak centred on zero and its width corresponds to the spectrometer resolution, ΔE_{res} of $17.5 \mu\text{eV}$. The Lorentzian component of NOTT-500(Ni), also centred on zero, broadens with the increase of the temperature (Figure 3.26).

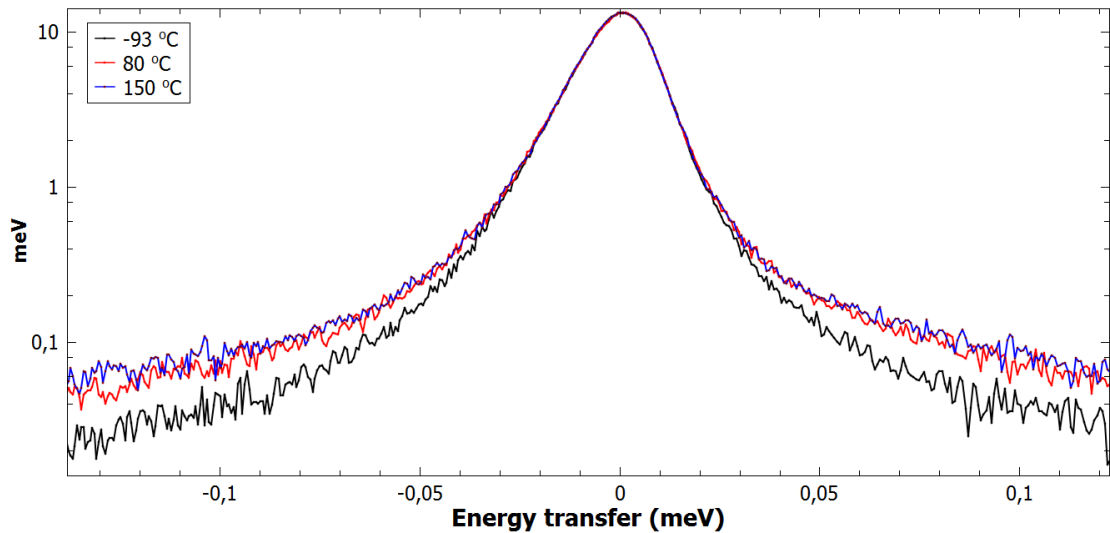


Figure 3.26. QENS normalised profiles of NOTT-500(Ni) obtained by IRIS at temperatures between -93 °C and 150 °C.

Intrinsic proton conductivity of NOTT-500(Ni) by “spherical free diffusion”:

Geometrical information of the atomic motions were analysed *via* the elastic incoherent structure factor, EISF. The EISF is defined by Equation 13.^{42,44,45}

$$\text{EISF} = I_{\text{elastic}} / (I_{\text{elastic}} + I_{\text{QENS}}) \quad (13)$$

Where I_{elastic} and I_{QENS} are the peak intensities of elastic and quasi-elastic scattering, respectively. The elastic fraction for NOTT-500(Ni) decreases with increasing temperature, indicating that the mobility of a larger fraction of protons falls into the dynamic window of the spectrometer (Figure 3.27).

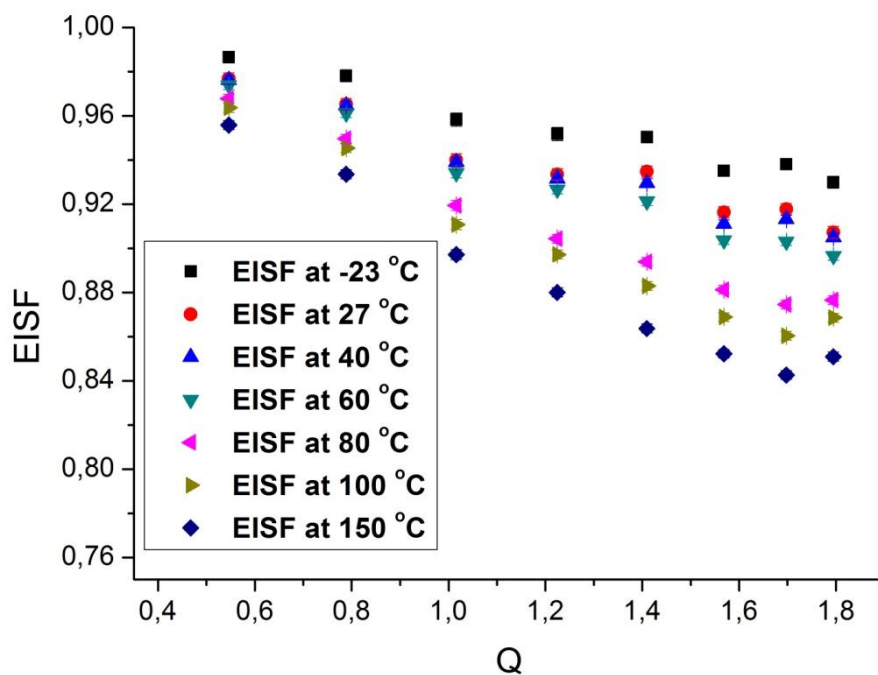


Figure 3.27. Elastic incoherent structure factor (EISF) of NOTT-500(Ni) measured by IRIS at different temperatures.

The highest proton conductivity value for NOTT-500(Ni) was measured at room temperature and 99 % RH. Under these condition the proton conductivity was described as arising from the cooperation of two mechanisms; the Grotthuss mechanism which is strictly dependent on the intrinsic properties of the material (protons in the hopping pathway) and the Vehicle mechanism whose contribution is mediated by the presence of additional water molecules (deriving from 99 % RH environment) (Section 3.2.6).

The EISF varies as a function of the scattering vector Q , depending on the dynamical model.⁴² Thus, to gain quantitative information about the motion of protons and conduction phenomena exclusively restrained in the hopping pathway, the EISF of NOTT-500(Ni) collected at 27 °C and under dry conditions (0 % RH) was analysed. This allows to focus on the protons located within the MOF (Figure 3.19) excluding

the contribution of additional water molecules (correlated to the Vehicle mechanism and whose contribution is not studied in the QENS experiment).

To explain the motion of protons within the MOF, the QENS spectra was mathematically fitted by Lorentzian functions correspondent to well-known theoretical models for diffusion processes.⁴² To establish the model that describes the diffusion of protons within the MOF, a good fitting of the experimental data needs to be combined with the structural properties of NOTT-500(Ni). The dynamics of protons in NOTT-500(Ni) at RT and 0 % RH were best fitted by the "Spherical free diffusion" model (Equation 14, Figure 3.28).^{46,47}

$$\text{EISF} = p + (1-p) * \{[3j(Qr)]/(Qr)\}^2 \quad (14)$$

Where j is the Bessel function, r is the distance at which the hydrogen atoms are free to diffuse, p represents the immobile fraction and $(1-p)$ is the mobile fraction. In Equation 14, to define the parameters r , p and $(1-p)$ it is necessary to consider the properties of the material under this study. Thus, as r represents the distance at which the protons are free to diffuse, its value (2.65 Å) was chosen as average of the distances between the protons in the hopping pathway. The immobile fraction (p) refers to the protons which move too slowly for the resolution of the backscattering spectrometer; these are the aromatic protons from the organic ligand. The mobile fraction ($1-p$), responsible for the diffusion process, consists of the protons from the water molecules bounded to the metal (M-OH₂) and the free hydroxyls from the phosphonate groups (P-OH) in the proton-hopping pathway. The values of p and $(1-p)$ were extrapolated from the EISF plot, where the low intercept of the EISF with the y-axis corresponds with the mobile fraction (~9 %). This value, correspondent to the mobile fraction, and the value of r equal to 2.65 Å were substituted in Equation 14.

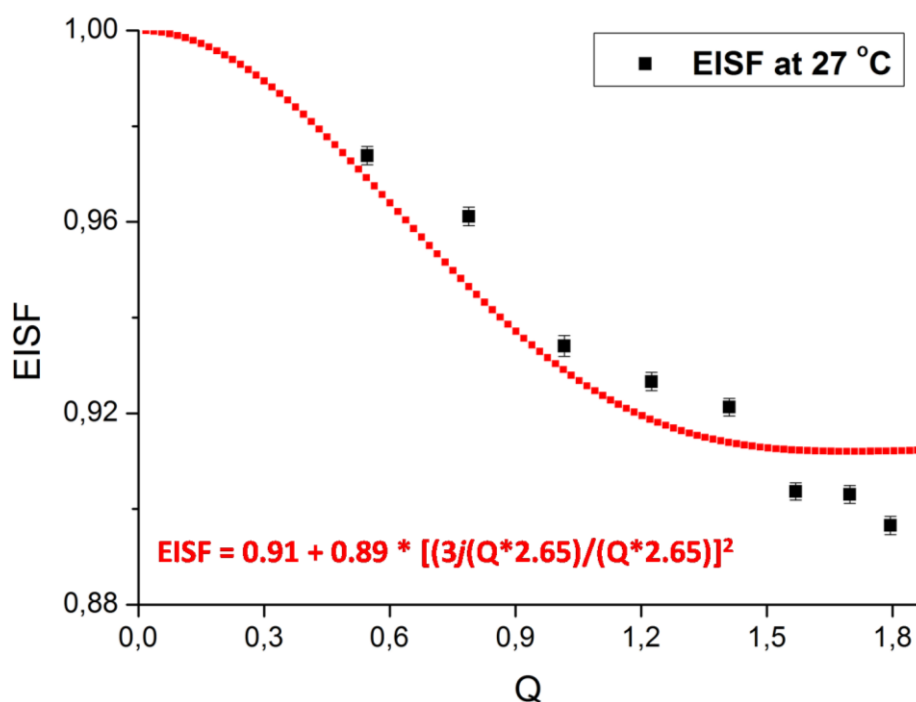


Figure 3.28. Elastic incoherent structure factor (EISF) of NOTT-500(Ni) measured by IRIS at RT under anhydrous conditions. Red curve represents the calculated EISF based on the free diffusion inside a sphere model.

According to the EISF analysis, the diffusion of protons in NOTT-500(Ni) is best described by the “spherical free diffusion” model and it occurs for protons located at average distance r equal to 2.65 Å ($Q = 1.9$) in agreement with the crystallographic data. To support the dependency of the free diffusion to the distance r , the half width of the half maximum (HWHM, Γ) of the QENS was investigated as a function of Q^2 at RT temperature (Figure 3.29). Q is correlated to the distance r by Equation 15.^{45,47}

$$Q = \pi / r \quad (15)$$

For Q^2 values larger than 1.18 \AA^{-2} (where $Q^2 = 1.18 \text{ \AA}^{-2}$ corresponds to r equal to 2.65 Å), HWHM increases with Q^2 indicating that the protons are free to diffuse (according to the “spherical free diffusion” model) within a distance of 2.65 Å. For Q^2 values below 1.18 \AA^{-2} (corresponding to r values larger than 2.65 Å), the

experimental points can be fitted with a horizontal line having no dependency on Q^2 . Therefore, the proton diffusion in NOTT-500(Ni) is a distance dependent motion where the protons can freely diffuse only at distances within 2.65 Å.

The mobile protons observed in the QENS experiment do not diffuse freely past this distance; therefore, to observe diffusion between protons located at longer distances an alternative mechanism for longer range transport is required. This is the Vehicle mechanism which occurs at 99 % RH and it was not studied with the QENS experiment as the measurements were recorded on NOTT-500(Ni) under anhydrous conditions.

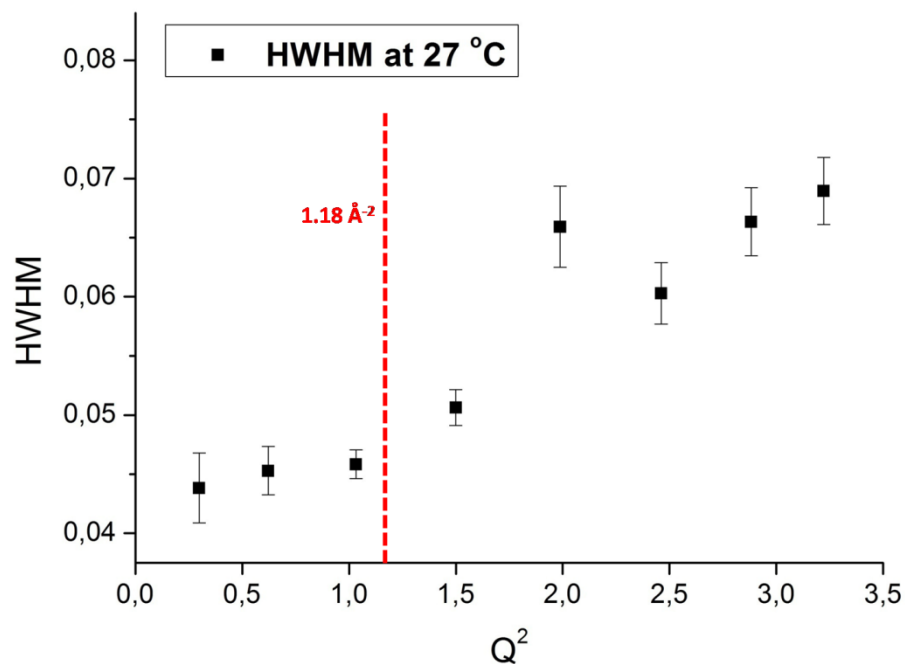


Figure 3.29. Q^2 -dependence of HWHM estimated from the fitting for the data taken on IRIS spectrometer. Red dot line at 1.18 \AA^{-2} is guide to the eye.

Activation energy of the proton diffusion in the “spherical free diffusion” model:

The activation energy of the proton diffusion described with the “spherical free diffusion” model for NOTT-500(Ni) was calculated as follows by using the QENS data. The Arrhenius plot of $\ln\tau$ (where $\tau = 1/\Gamma$) as a function of the temperature is shown in Figure 3.30. A straight-line fit (with slope $m = 0.8875$) of the Arrhenius plot gives the activation energy of proton diffusion regulated by Grotthuss mechanism through the proton-hopping pathway.

$$E_a = [0.8875 * 8.617 * 10^{-5} \text{ eV}] * 1000 = 0.076 \text{ eV}$$

This activation energy (0.076 eV) is much smaller than the activation energy calculated for the whole proton conduction process (0.46 eV) by variable temperature impedance spectroscopy (Section 3.2.6). This is an expected result as the diffusion process of protons which are free to diffuse within relatively short distances (Grotthuss mechanism through the hopping pathway) is predicted to be much lower energy than the diffusion of protons supported by water molecules which assist the charge transport through the whole framework (Vehicle mechanism). Similar behavior for a highly proton conductive MOF has been previously reported.^{25,48} The activation energy of the proton conduction process for $(\text{NH}_4)_2(\text{H}_2\text{adp})[\text{Zn}_2(\text{ox})_3] \cdot 3\text{H}_2\text{O}$, studied by variable temperature impedance spectroscopy, was equal to 0.63 eV ($\sigma = 8 \times 10^{-3} \text{ S cm}^{-1}$ at 25 °C under 98 % RH).²⁵ The proton conduction mechanism proposed for $(\text{NH}_4)_2(\text{H}_2\text{adp})[\text{Zn}_2(\text{ox})_3] \cdot 3\text{H}_2\text{O}$ was a combination between the Grotthuss and Vehicle mechanism. The activation energy for the H_2O and NH_4^+ relaxations in $(\text{NH}_4)_2(\text{H}_2\text{adp})[\text{Zn}_2(\text{ox})_3] \cdot 3\text{H}_2\text{O}$ were investigated by QENS and fell in the range between 0.024 eV and 0.133 eV.⁴⁸

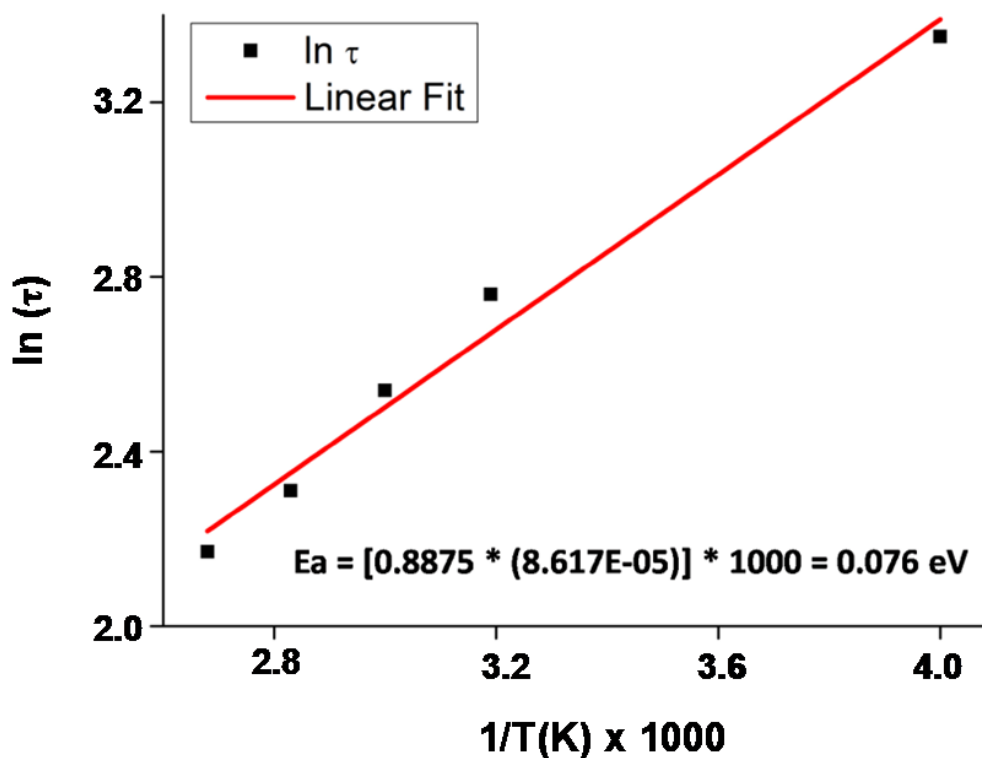


Figure 3.30. Arrhenius plot for NOTT-500(Ni) and linear fit.

Investigation of the reversible phase transition by QENS analysis:

X-ray diffraction data for the dehydrated NOTT-500(Ni) were also collected on IRIS in the temperature range from -23 °C to 150 °C showing a change in the PXRD pattern between 60 °C and 80 °C. Due to the low resolution of the diffractometer in IRIS, these data could not be indexed or quantitatively compared with the results previously investigated by VT-PXRD collected at Diamond Light Source (Section 3.2.5.1). However, information to support the phase change can be extrapolated from the EISF versus Q plot at different temperatures (Figure 3.31). The EISF gives insights about the spatial distribution of the protons, and the change in shape of the EISF between 60 °C and 80 °C is associated with the phase change.⁴⁹

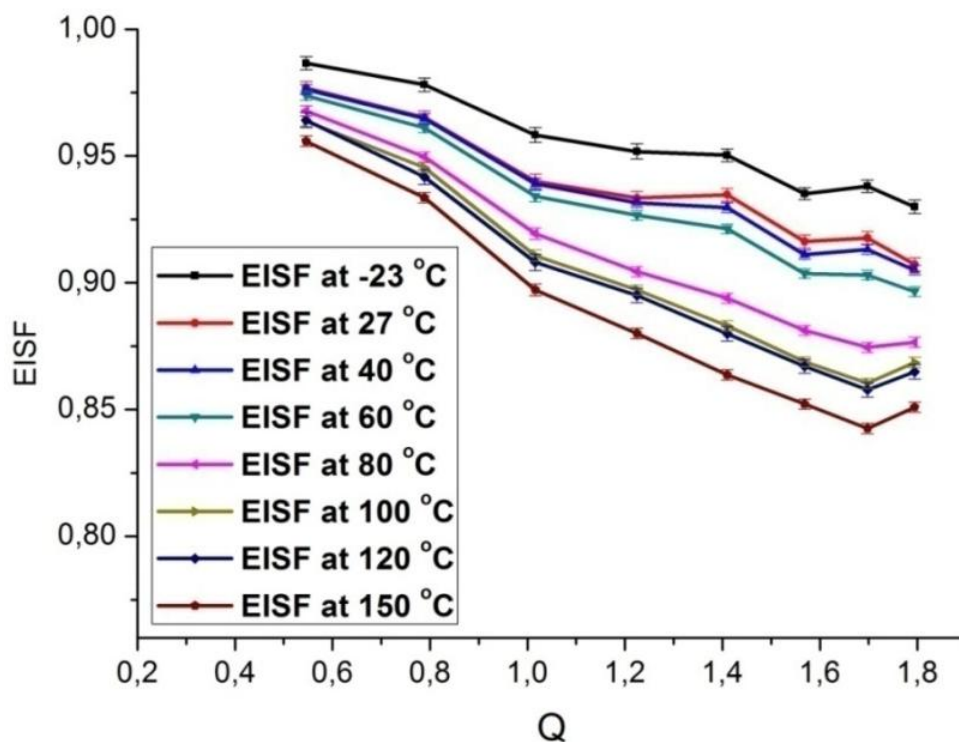


Figure 3.31. Elastic incoherent structure factor (EISF) of NOTT-500(Ni) measured from -23 °C up to 150 °C.

Furthermore, Figure 3.32 shows the dependency of the immobile fraction (p), previously defined in Equation 14, as a function of temperature (Q -range: $0.6 \text{ \AA}^{-1} < Q < 1.8 \text{ \AA}^{-1}$). This representation of the data offers a simple and model-free approach to detect transitions as changes in the elastic intensity decay.⁵⁰ The data can be divided into two groups; the first group from -23 °C to 60 °C and the second one from 80 °C to 150 °C. Each group is lying on a straight line. For NOTT-500(Ni) the phase transition is found at around 80 °C, in good agreement with the TGA (Section 3.2.4) and VT-PXRD data (Section 3.2.5.1).

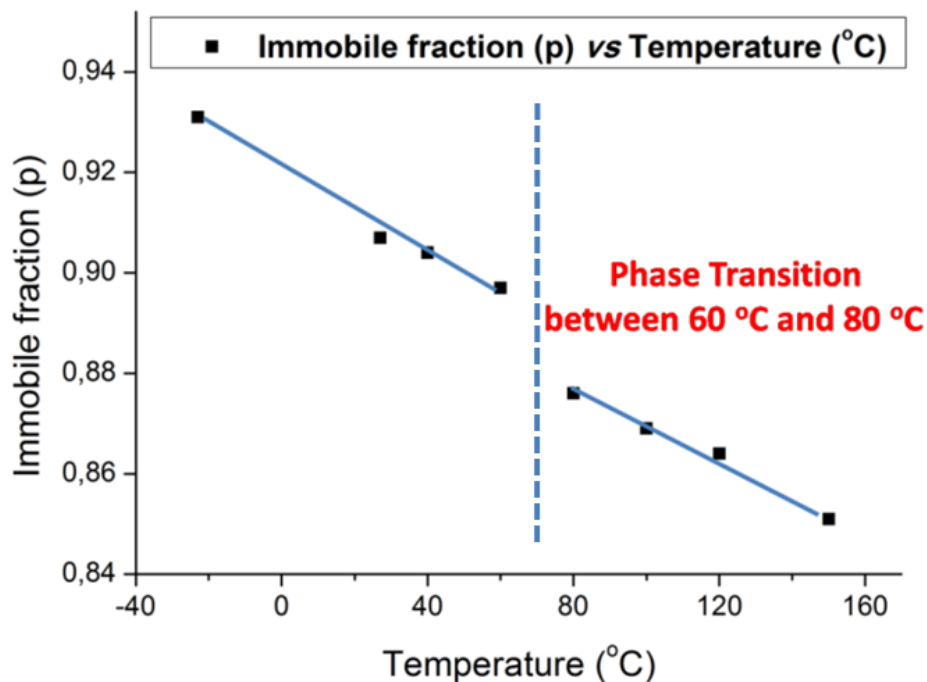


Figure 3.32. Immobile fraction (p) *versus* temperature (Q -range: $0.6 \text{ \AA}^{-1} < Q < 1.8 \text{ \AA}^{-1}$), indicating the phase transition at temperature between $60 \text{ }^\circ\text{C}$ and $80 \text{ }^\circ\text{C}$. Lines are guides to the eye.

3.3 Conclusions

Proton conduction in MOFs is a new research area for their potential applications as proton exchange membrane materials in fuel cells. The ordered structure in MOFs provides a platform for direct visualisation of the proton transfer pathway and by choosing appropriate functionalised ligands it is possible to design new efficient proton conductors.

Chapter 3 described the synthesis, crystal structure, characterisation and proton conductivity study of two new isostructural MOFs, NOTT-500(Ni, Co), based upon a phosphonate ligand. Their structures show an efficient proton-hopping pathway defined by the hydroxyl groups from the ligand (P-OH) and the water molecules bound to the metal ions (M-OH₂). The short distances ($2.0\text{-}2.9 \text{ \AA}$) between the free

hydroxyl groups and water molecules make NOTT-500(Ni) and NOTT-500(Co) promising candidate materials for proton conduction applications.

NOTT-500(Ni, Co) were fully characterised by TGA, VT-PXRD, solid-state UV-visible spectroscopy and QENS, revealing a reversible structural transition and colour change upon heating assigned to the dehydration-rehydration of the materials. Of direct relevance to the aim of this Thesis, the proton conductivity properties of NOTT-500(Ni, Co) were investigated. Impedance spectroscopy studies show a proton conductivity of $1.11(03) \times 10^{-4} \text{ S cm}^{-1}$ for NOTT-500(Ni) and $4.42(06) \times 10^{-5} \text{ S cm}^{-1}$ for NOTT-500(Co) at 99 % RH and 25 °C. The activation energy for the proton conductivity of NOTT-500(Ni) is 0.46 eV indicating the proton conduction mechanism derives from the cooperation of the Grotthuss and Vehicle mechanism.

X-ray crystallography and QENS studies were combined to investigate the atomic details for the observed proton conductivity. The intrinsic diffusion of protons in the proton-hopping pathway (regulated by the Grotthuss mechanism) is best described by the “Spherical free diffusion” model over short distances in the dehydrated sample. The activation energy for this diffusion process was estimated from the QENS analysis to be 0.076 eV. In future work, we will focus on the study of MOFs by QENS *in situ*, including measurements under different values of % RH.

3.4 Experimental Section

Single crystal X-ray diffraction, PXRD, TGA, solid-state UV-visible absorption spectra, QENS and impedance experimental details are fully discussed in the Experimental Section at the end of this Thesis.

3.4.1 Synthesis of benzene-1,3,5-*p*-phenylphosphonic acid, H_6L^1

1,3,5-tris(*p*-bromophenyl) benzene (5.4191 g, 10.0 mmol), and tetrakis(triphenylphosphine) palladium (0) (0.0836 g, 0.072 mmol) as catalyst were mixed in triisopropyl phosphite (50 mL, 202.7 mmol) with stirring and under Ar for 3 h at 120 °C. After adding tetrakis(triphenylphosphine) palladium (0) (0.0805 g, 0.070 mmol) and triisopropyl phosphite (25 ml, 101.3 mmol), the temperature was increased at 205 °C (a sand bath was used) and the reaction was carried out under Ar with stirring for 3 days. 1,3,5-[*p*-C₆H₄P(O)(OiPr)₂]₃C₆H₃, (3.900 g, 4.9 mmol), a white powder, was isolated by filtration and washed with hexane (60 mL). ¹H NMR (CDCl₃, 300 MHz): 1.29 (d, 18H), 1.43 (d, 18H), 4.77 (m, 6H, OC-H), 7.79 (m, 6H, Ar-H), 7.86 (s, 3H, Ar-H), 7.95 (m, 6H, Ar-H). Mass (ESI) *m/z* (M-H⁺): 799.32. Elemental analysis (%): anal. calc. for C₄₂H₅₇O₉P₃: C 63.15, H 7.19, N 0; found: C 62.78, H 6.97, N 0.00. FTIR: ν (cm⁻¹) = 1595 (m), 1559 (w), 1503 (w), 1467 (w), 1453 (w), 1384 (m), 1236 (s), 1178 (m), 1132 (m), 1102 (m), 975 (s), 885 (m), 835 (m), 769 (s), 686 (s), 632 (w), 612 (w). 4,4'-[P(O)(OiPr)₂]₂-*p*-tertphenyl (3.900 g, 4.9 mmol) was dissolved in a HCl/H₂O solution (ratio 2:1) and reacted under stirring for 2 days at 100 °C. At room temperature the reagent is insoluble in the HCl/H₂O solution. Increasing the temperature the solubility of 4,4'-[P(O)(OiPr)₂]₂-*p*-tertphenyl progressively increases until an homogeneous mixture was obtained at high temperature. After reacting the resultant mixture for 2 days at 100 °C, it was cooled

down at room temperature and a sticky and white product was isolated and recrystallised with methanol to yield a white powder. Yield: 1.7968 g (3.3 mmol), 67%. ^1H NMR (CDCl_3 , 300 MHz): 7.80 (m, 6H, Ar-H), 7.99 (m, 9H, Ar-H). ^{31}P NMR (DMSO, 400 MHz): 13.40. Mass (ESI) m/z (M-H^+): 547.05. Elemental analysis (%): anal. calc. for $\text{C}_{24}\text{H}_{21}\text{O}_9\text{P}_3$: C 52.76, H 3.87, N 0; found: C 51.90, H 3.94, N 0.00. FTIR: ν (cm^{-1}) = 2703 (w), 2216 (w), 1663 (w), 1596 (m), 1555 (w), 1503 (w), 1441 (w), 1386 (w), 1136 (s), 984 (s), 921 (s), 816 (s), 729 (w), 689 (s), 609 (w), 549 (s).

3.4.2 Synthesis of $[\text{Ni}_3(\text{H}_3\text{L}^1)_2(\text{H}_2\text{O})_{10.5}]$, NOTT-500(Ni)

H_6L^1 (0.0136 g, 0.025 mmol) and $\text{Ni}(\text{NO}_3)_2 \cdot 6\text{H}_2\text{O}$ (0.0145 g, 0.05 mmol) were dissolved in water, DMSO and DMF (3.5 mL, 1.5:1:1, v/v/v) at room temperature. The clear pale green solution was sealed in a vial and heated in an aluminium heating block at 40 °C for 2 days. The solvent was then filtered off, and the product washed with DMF, and dried in air to afford green hexagonal block single crystals of NOTT-500(Ni). Elemental analysis (%): anal. calc. for $\text{C}_{48}\text{H}_{57}\text{N}_0\text{O}_{28.5}\text{P}_6\text{Ni}_3$: C 39.71, H 3.96, N 0.00; found: C 39.78, H 4.36, N 0.12. FTIR: ν (cm^{-1}) = 3200 (m), 2100 (w), 1620 (m), 1500 (w), 1460 (w), 1270 (w), 1260 (w), 1250 (w), 1120 (w), 1050 (s), 890 (w), 800 (s), 760 (m), 700 (s).

3.4.3 Synthesis of $[\text{Co}_3(\text{H}_3\text{L}^1)_2(\text{H}_2\text{O})_{10.4}]$, NOTT-500(Co)

The same synthetic conditions as with NOTT-500(Ni) were used for the synthesis of NOTT-500(Co). The clear pale pink solution was sealed in a vial and heated at 40 °C for 1 day. The solvent was filtered off, the product washed with DMF, and dried in air to afford pink hexagonal block single crystals of NOTT-500(Co). Elemental

analysis (%): anal. calc. for $C_{48}H_{56.8}N_0O_{28.4}P_6Co_3$: C 39.74, H 3.95, N 0.00; found: C 39.92, H 4.18, N 0.08. FTIR: ν (cm^{-1}) = 3200 (m), 2100 (w), 1620 (m), 1500 (w), 1460 (w), 1270 (w), 1260 (w), 1250 (w), 1120 (w), 1050 (s), 890 (w), 800 (s), 760 (m), 700 (s).

3.5 References

- (1) Kim, S.; Dawson, K. W.; Gelfand, B. S.; Taylor, J. M.; Shimizu, G. K. H. *J. Am. Chem. Soc.* **2013**, *135*, 963–966.
- (2) Shimizu, G. K. H.; Taylor, J. M.; Kim, S. *Science* **2013**, *341*, 354–355.
- (3) Cheetham, A. K.; Rao, C. N. R.; Feller, R. K. *Chem. Commun.* **2006**, *46*, 4780–4795.
- (4) Rosseinsky, M. J. *Microporous Mesoporous Mater.* **2004**, *73*, 15–30.
- (5) Gagnon, K. J.; Perry, H. P.; Clearfield, A. *Chem. Rev.* **2012**, *112*, 1034–1054.
- (6) Aranda, M. A. G.; Leon-Reina, L.; Rius, J.; Demadis, K. D.; Moreau, B.; Villemin, D.; Palomino, M.; Rey, F.; Cabeza, A. *Inorg. Chem.* **2012**, *51*, 7689–7698.
- (7) Wharmby, M. T.; Miller, S. R.; Groves, J. A.; Margiolaki, I.; Ashbrook, S. E.; Wright, P. A. *Dalton Trans.* **2010**, 6389–6391.
- (8) Plabst, M.; Bein, T. *Inorg. Chem.* **2009**, *48*, 4331–4341.
- (9) Kong, D.; Zon, J.; McBee, J.; Clearfield, A. *Inorg. Chem.* **2006**, *45*, 977–986.
- (10) Liang, J.; Shimizu, G. K. H. *Inorg. Chem.* **2007**, *46*, 10449–10451.
- (11) Clearfield, A. *Dalton Trans.* **2008**, 6089–6102.
- (12) Natarajan, S.; Mahata, P. *Curr. Opin. Solid State Mater. Sci.* **2009**, *13*, 46–53.
- (13) Costantino, F.; Donnadio, A.; Casciola, M. *Inorg. Chem.* **2012**, *51*, 6992–7000.
- (14) Liang, X.; Zhang, F.; Feng, W.; Zou, X.; Zhao, C.; Na, H.; Liu, C.; Sun, F.; Zhu, G. *Chem. Sci.* **2013**, *4*, 983–992.
- (15) Taylor, J. M.; Dawson, K. W.; Shimizu, G. K. H. *J. Am. Chem. Soc.* **2013**, *135*, 1193–1196.

- (16) Colodrero, R. M. P.; Papathanasiou, K. E.; Stavgianoudaki, N.; Olivera-Pastor, P.; Losilla, E. R.; Aranda, M. a G.; León-Reina, L.; Sanz, J.; Sobrados, I.; Choquesillo-Lazarte, D.; García-Ruiz, J. M.; Atienzar, P.; Rey, F.; Demadis, K. D.; Cabeza, A. *Chem. Mater.* **2012**, *24*, 3780–3792.
- (17) Taylor, J. M.; Mah, R. K.; Moudrakovski, I. L.; Ratcliffe, C. I.; Vaidhyanathan, R.; Shimizu, G. K. H. *J. Am. Chem. Soc.* **2010**, *132*, 14055–14057.
- (18) Umeyama, D.; Horike, S.; Inukai, M.; Itakura, T.; Kitagawa, S. *J. Am. Chem. Soc.* **2012**, *134*, 12780–12785.
- (19) Colodrero, R. M. P.; Angeli, G. K.; Bazaga-Garcia, M.; Olivera-Pastor, P.; Villemin, D.; Losilla, E. R.; Martos, E. Q.; Hix, G. B.; Aranda, M. A. G.; Demadis, K. D.; Cabeza, A. *Inorg. Chem.* **2013**, *52*, 8770–8783.
- (20) Bazaga-Garcia, M.; Colodrero, R. M. P.; Papadaki, M.; Garczarek, P.; Zon, J.; Olivera-pastor, P.; Losilla, E. R.; Leo, L.; Aranda, M. A. G. *J. Am. Chem. Soc.* **2014**, *136*, 5731–5739.
- (21) Beckmann, J.; Rüttinger, R.; Schwich, T. *Cryst. Growth Des.* **2008**, *8*, 3271–3276.
- (22) Poojary, D. M.; Zhang, B.; Bellinghausen, P.; Clearfield, A. *Inorg. Chem.* **1996**, *35*, 4942–4949.
- (23) Amghouz, Z.; García-Granda, S.; García, J. R.; Clearfield, A.; Valiente, R. *Cryst. Growth Des.* **2011**, *11*, 5289–5297.
- (24) Shigematsu, A.; Yamada, T.; Kitagawa, H. *J. Am. Chem. Soc.* **2011**, *133*, 2034–2036.
- (25) Sadakiyo, M.; Yamada, T.; Kitagawa, H. *J. Am. Chem. Soc.* **2009**, *131*, 9906–9907.

- (26) Sadakiyo, M.; Yamada, T.; Honda, K.; Matsui, H.; Kitagawa, H. *J. Am. Chem. Soc.* **2014**, *136*, 7701–7707.
- (27) Sahoo, S. C.; Kundu, T.; Banerjee, R. *J. Am. Chem. Soc.* **2011**, *133*, 17950–17958.
- (28) Pardo, E.; Train, C.; Gontard, G.; Boubekeur, K.; Fabelo, O.; Liu, H.; Dkhil, B.; Lloret, F.; Nakagawa, K.; Tokoro, H.; Ohkoshi, S. I.; Verdaguer, M. *J. Am. Chem. Soc.* **2011**, *133*, 15328–15331.
- (29) Ponomareva, V. G.; Kovalenko, K. A.; Chupakhin, A. P.; Dybtsev, D. N.; Shutova, E. S.; Fedin, V. P. *J. Am. Chem. Soc.* **2012**, *134*, 15640–15643.
- (30) Dey, C.; Kundu, T.; Banerjee, R. *Chem. Commun.* **2012**, *48*, 266–268.
- (31) Okawa, H.; Sadakiyo, M.; Yamada, T.; Maesato, M.; Ohba, M.; Kitagawa, H. *J. Am. Chem. Soc.* **2013**, *135*, 2256–2262.
- (32) Yoon, M.; Suh, K.; Natarajan, S.; Kim, K. *Angew. Chem.* **2013**, *52*, 2688–2700.
- (33) Hurd, J.; Vaidhyanathan, R.; Thangadurai, V.; Ratcliffe, C. I.; Moudrakovski, I. L.; Shimizu, G. K. H. *Nature Chem.* **2009**, *1*, 705–710.
- (34) Umeyama, D.; Horike, S.; Inukai, M.; Hijikata, Y.; Kitagawa, S. *Angew. Chem.* **2011**, *50*, 11706–11709.
- (35) Bureekaew, S.; Horike, S.; Higuchi, M.; Mizuno, M.; Kawamura, T.; Tanaka, D.; Yanai, N.; Kitagawa, S. *Nature Mater.* **2009**, *8*, 831–836.
- (36) Córdoba-Torres, P.; Mesquita, T. J.; Devos, O.; Tribollet, B.; Roche, V.; Nogueira, R. P. *Electrochimica Acta*, **2012**, *72*, 172–178.
- (37) Horike, S.; Kamitsubo, Y.; Inukai, M.; Fukushima, T.; Umeyama, D.; Itakura, T.; Kitagawa, S. *J. Am. Chem. Soc.* **2013**, *135*, 4612–4615.

- (38) Colodrero, R. M. P.; Olivera-Pastor, P.; Losilla, E. R.; Aranda, M. A. G.; Leon-Reina, L.; Papadaki, M.; McKinlay, A. C.; Morris, R. E.; Demadis, K. D.; Cabeza, A. *Dalton Trans.* **2012**, 4045.
- (39) Ramaswamy, P.; Wong, N. E.; Shimizu, G. K. H. *Chem. Soc. Rev.* **2014**, *43*, 5913–5932.
- (40) Sadakiyo, M.; Yamada, T.; Kitagawa, H. *J. Am. Chem. Soc.* **2014**, *136*, 13166–13169.
- (41) Kundu, T.; Sahoo, S. C.; Banerjee, R. *Chem. Commun.* **2012**, *48*, 4998–5000.
- (42) Bee, M. “*Quasielastic Neutron Scattering*” **1988**.
- (43) Sears, V. F. *Neutron News* **1992**, *3*, 26–37.
- (44) Heitjans, P.; Kärger, J. “*Diffusion in Condensed Matter: Methods, Materials, Models*” Springer, Ed.; **2005**.
- (45) Mukhopadhyay, R.; Mitra, S. *Indian J. Pure Appl. Phys.* **2006**, *44*, 732–740.
- (46) Russo, D.; Pérez, J.; Zanotti, J.-M.; Desmadril, M.; Durand, D. *Biophys. J.* **2002**, *83*, 2792–2800.
- (47) Volino, F.; Dianoux, A. J. *Mol. Phys.* **1980**, *41*, 271–279.
- (48) Miyatsu, S.; Kofu, M.; Nagoe, A.; Yamada, T.; Sadakiyo, M.; Yamada, T.; Kitagawa, H.; Tyagi, M.; García Sakai, V.; Yamamuro, O. *Phys. Chem. Chem. Phys.* **2014**, *16*, 17295–17304.
- (49) Yildirim, T.; Gehring, P.; Neumann, D.; Eaton, P.; Emrick, T. *Phys. Rev. B* **1999**, *60*, 314–321.
- (50) Trapp, M.; Gutberlet, T.; Juranyi, F.; Unruh, T.; Demé, B.; Tehei, M.; Peters, J. *J. Chem. Phys.* **2010**, *133*, 164505.

Chapter 4

**New strategies to enhance proton conductivity in a
family of lanthanide MOFs**

List of Contents

4.1 Introduction	155
4.1.1 Aims of Chapter 4.....	159
4.2 Results and discussion.....	160
4.2.1 Synthesis of biphenyl-4,4'-diphosphonic acid, H_4L^2	160
4.2.2 Solid-state NMR spectroscopy of H_4L^2	160
4.2.3 Synthesis of $[M(HL^2)]$	162
4.2.4 Structural characterisation of $[M(HL^2)]$	164
4.2.5 Solid-state NMR spectroscopy of $[M(HL^2)]$	168
4.2.6 Thermal stability of $[M(HL^2)]$	171
4.2.7 IR and Solid-state UV-visible absorption spectroscopies of $[M(HL^2)]$	174
4.2.8 Proton conductivity study of $[M(HL^2)]$	179
4.3 Design of novel strategies to enhance proton conductivity of $[M(HL^2)]$..	196
4.3.1 Increase the concentration of protons in a fixed volume	197
4.3.1.1 Synthesis of benzene-1,4-diphosphonic acid, H_4L^3 , and preparation of $[M(HL^3)]$	197
4.3.1.2 Structural characterisation of $[M(HL^3)]$	199
4.3.1.3 Thermal stability of $[M(HL^3)]$	203
4.3.1.4 IR and Solid-state UV-visible absorption spectroscopies of $[M(HL^3)]$	204
4.3.1.5 Proton conductivity study of $[M(HL^3)]$	207
4.3.2 Substitution of 3+ metals with 2+ metals to increase the number of protons in $[M(HL^2)]$	225
4.3.2.1 Synthesis and structural characterisation of $[Ba(H_2L^2)]$	226
4.3.2.2 Solid-state NMR of $[Ba(H_2L^2)]$	230

4.3.2.3 Thermal stability of [Ba(H ₂ L ²)]	232
4.3.2.4 Infrared spectroscopy of [Ba(H ₂ L ²)].....	234
4.3.2.5 Proton conductivity study of [Ba(H ₂ L ²)]	235
4.4 Conclusions	240
4.5 Experimental Section.....	244
4.5.1 Synthesis of biphenyl-4,4'-diphosphonic acid, H ₄ L ²	244
4.5.2 Synthesis of La[C ₁₂ H ₈ P ₂ O ₆ H], [La(HL ²)].....	245
4.5.3 Synthesis of Ce[C ₁₂ H ₈ P ₂ O ₆ H], [Ce(HL ²)]	245
4.5.4 Synthesis of Nd[C ₁₂ H ₈ P ₂ O ₆ H], [Nd(HL ²)]	246
4.5.5 Synthesis of Sm[C ₁₂ H ₈ P ₂ O ₆ H], [Sm(HL ²)]	246
4.5.6 Synthesis of Gd[C ₁₂ H ₈ P ₂ O ₆ H], [Gd(HL ²)]	246
4.5.7 Synthesis of Ho[C ₁₂ H ₈ P ₂ O ₆ H], [Ho(HL ²)]	247
4.5.8 Synthesis of benzene-1,4-diphosphonic acid, H ₄ L ³	247
4.5.9 Synthesis of La[C ₆ H ₄ P ₂ O ₆ H], [La(HL ³)].....	248
4.5.10 Synthesis of Ce[C ₆ H ₄ P ₂ O ₆ H], [Ce(HL ³)]	248
4.5.11 Synthesis of Nd[C ₆ H ₄ P ₂ O ₆ H], [Nd(HL ³)].....	249
4.5.12 Synthesis of Sm[C ₆ H ₄ P ₂ O ₆ H], [Sm(HL ³)].....	249
4.5.13 Synthesis of Gd[C ₆ H ₄ P ₂ O ₆ H], [Gd(HL ³)].....	249
4.5.14 Synthesis of Ho[C ₆ H ₄ P ₂ O ₆ H], [Ho(HL ³)].....	250
4.5.15 Synthesis of Ba[C ₁₂ H ₈ P ₂ O ₆ H ₂], [Ba(H ₂ L ²)]	250
4.6 References	251

4.1 Introduction

Control and optimisation of the proton conductivity of MOFs by modulation of their structures is a challenge and requires the design of new materials with improved properties. Three main approaches to enhance proton conductivity in MOFs have been reported so far.^{1,2} Type I systems involve the introduction of proton carriers as counter ions (such as NH_4^+ , H_3O^+ and HSO^-) into the pores of a framework. In Type II systems acidic groups (e.g., $-\text{COOH}$, PO_3H_2 , SO_4H_3) are incorporated into the main framework which decorate the ligands with functional groups. Type III systems incorporate charge-neutral proton conducting species (e.g., heterocycles, acidic molecules such as H_2SO_4 and H_3PO_4) into the voids of the material.

In 2009, H. Kitagawa *et al.* reported a highly proton conductive MOF, $(\text{NH}_4)_2(\text{H}_2\text{adp})[\text{Zn}_2(\text{ox})_3]\cdot 3\text{H}_2\text{O}$ (ox^{2-} = oxalate, H_2adp = adipic acid), obtained by introducing NH_4^+ counter ions into the framework and decorating the voids with carboxylic groups (Types I and II) (Figure 4.1a,b).¹ This complex showed a proton conductivity of $8 \times 10^{-3} \text{ S cm}^{-1}$ at 25 °C and 98 % RH. In 2014, the same group reported the synthesis of $\text{K}_2(\text{H}_2\text{adp})[\text{Zn}_2(\text{ox})_3]\cdot 3\text{H}_2\text{O}$, isostructural with $(\text{NH}_4)_2(\text{H}_2\text{adp})[\text{Zn}_2(\text{ox})_3]\cdot 3\text{H}_2\text{O}$, obtained by substitution of NH_4^+ with the non-hydrogen-bonding cation K^+ (Figure 4.1c). They measured the proton conductivity of $\text{K}_2(\text{H}_2\text{adp})[\text{Zn}_2(\text{ox})_3]\cdot 3\text{H}_2\text{O}$ and investigated the effect of ion substitution on the proton conductivity (Type I).² A remarkable reduction in conductivity was observed in the case of $\text{K}_2(\text{H}_2\text{adp})[\text{Zn}_2(\text{ox})_3]\cdot 3\text{H}_2\text{O}$ ($\sigma = 1.2 \times 10^{-4} \text{ S cm}^{-1}$ at 25 °C and 98 % RH) compared with $(\text{NH}_4)_2(\text{H}_2\text{adp})[\text{Zn}_2(\text{ox})_3]\cdot 3\text{H}_2\text{O}$ ($\sigma = 8 \times 10^{-3} \text{ S cm}^{-1}$ at 25 °C and 98 % RH). This was assigned to changes in the proton-hopping pathway due to the introduction of non-hydrogen-bonding cations.

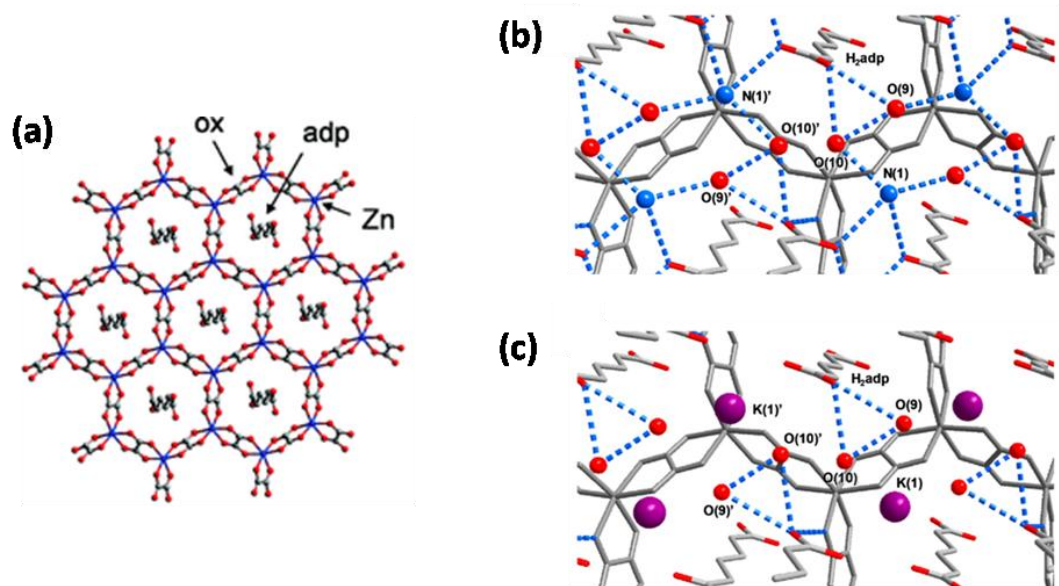


Figure 4.1. (a) Honeycomb layer structure of $(\text{NH}_4)_2(\text{H}_2\text{adp})[\text{Zn}_2(\text{ox})_3] \cdot 3\text{H}_2\text{O}$. (b) Hydrogen-bond arrangements of $-\text{COOH}$, H_2O and NH_4^+ in the interlayer of $(\text{NH}_4)_2(\text{H}_2\text{adp})[\text{Zn}_2(\text{ox})_3] \cdot 3\text{H}_2\text{O}$. (c) Hydrogen-bond arrangements of $-\text{COOH}$, H_2O and K^+ in the interlayer of $\text{K}_2(\text{H}_2\text{adp})[\text{Zn}_2(\text{ox})_3] \cdot 3\text{H}_2\text{O}$. Hydrogen bonds are shown as blue dot lines. The colours of red, blue and purple correspond to oxygen, nitrogen and potassium.^{1,2}

In 2011, H. Kitagawa *et al.* proposed the control of proton conductivity in MIL-53 by using functionalised ligands (Type II). They decorated the organic ligand with several functional groups ($-\text{H}$, $-\text{NH}_2$, $-\text{OH}$, $-\text{COOH}$) without modifying the structure of the framework and investigated their effect on the proton conductivity of the resultant material (Figure 4.2).³

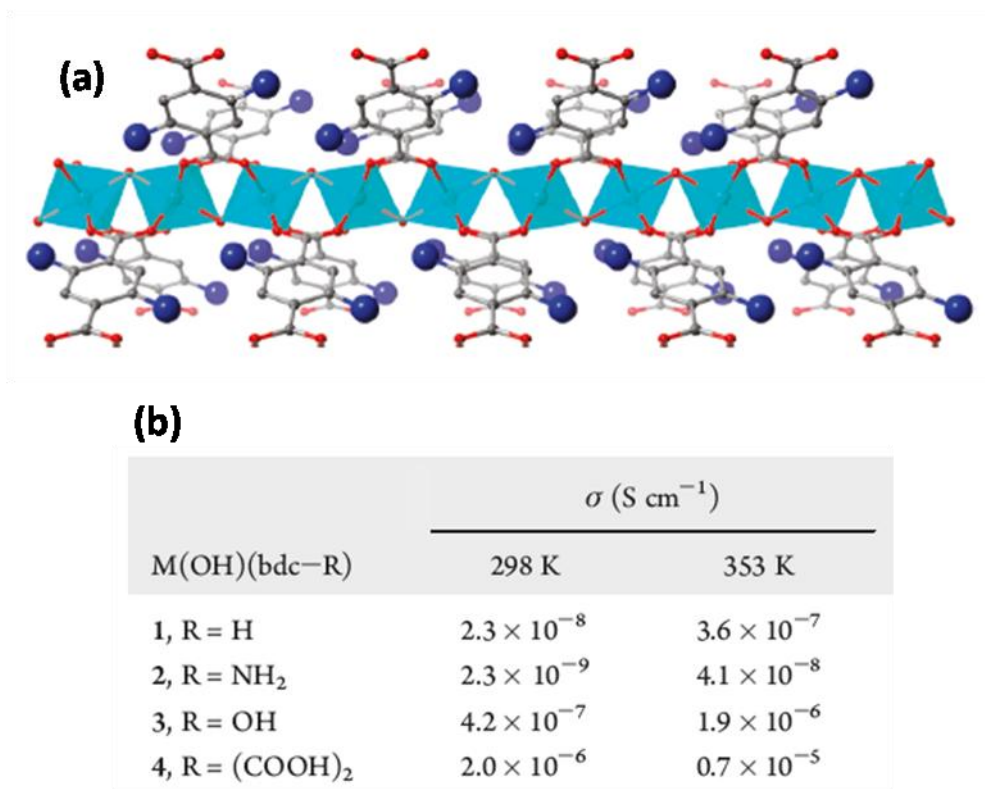


Figure 4.2. (a) Structure of MIL-53(M) along the channel. The blue atoms show functional groups (H, NH₂, OH, COOH). (b) Proton conductivities at 298 and 353 K and 95 % RH.³

Several examples of introducing proton carriers inside the pore of MOFs have been reported (Type III). Doping MOFs by inserting heterocycles in their cavity has been investigated with quite encouraging results. In 2009, S. Kitagawa *et al.* proposed the encapsulation of imidazole in an aluminium porous coordination polymer, [Al(μ_2 -OH)(1,4-ndc)] (1,4-ndc²⁻ = 1,4-naphthalenedicarboxylate) (Figure 4.3).⁴ Impedance studies revealed the proton conductivity of the guest-free framework was lower than 10^{-13} S cm⁻¹; the conductivity increased to 5.5×10^{-8} S cm⁻¹ at room temperature and reached 2.2×10^{-5} S cm⁻¹ at 120 °C. In 2011, the same group studied the proton conductivity of the same material, [Al(μ_2 -OH)(1,4-ndc)], loaded with histamine; a proton conductivity of 1.7×10^{-3} S cm⁻¹ at 150 °C was observed.⁵ Similar findings

were presented in 2009 by G. Shimizu *et al.*; they modulated the proton conductivity of β -PCMOF2 by loading 1*H*-1,2,4-triazole into the voids.⁶

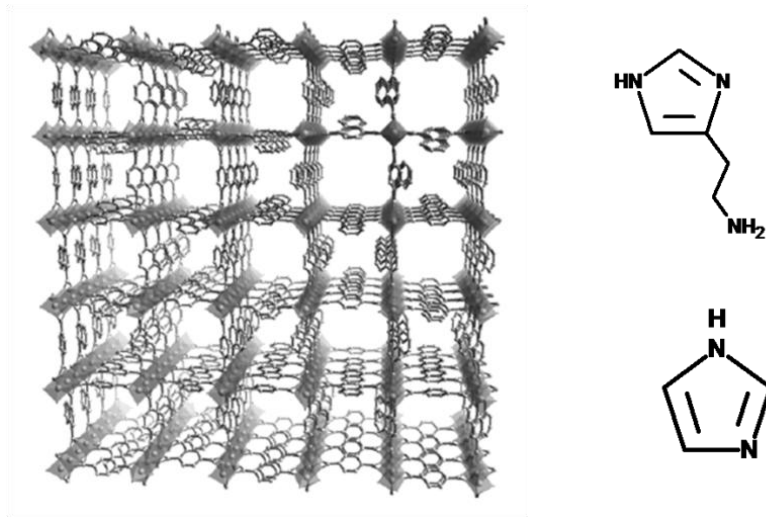


Figure 4.3. $[\text{Al}(\mu_2\text{-OH})(1,4\text{-ndc})]$ loaded with imidazole and histamine.^{4,5}

Another example to control the proton conductivity by loading proton carrier guests into a MOF (Type III) was presented in 2012 by Fedin *et al.*⁷ By impregnation of MIL-101 with non-volatile acids (H_2SO_4 and H_3PO_4) they generated materials with high proton conductivities at high temperature (H_2SO_4 @MIL-101, $\sigma = 1 \times 10^{-2} \text{ S cm}^{-1}$ at 150 °C; H_3PO_4 @MIL-101 = $3 \times 10^{-3} \text{ S cm}^{-1}$ at 150 °C). A similar approach was followed in 2014 by Hong *et al.* who reported the synthesis of $[\text{Ni}_2(\text{dobdc})(\text{H}_2\text{O})_2] \cdot 6\text{H}_2\text{O}$ (dobdc⁴⁻ = 2,5-dioxido-1,4-benzenedicarboxylate) and studied its proton conductivity after soaking the material in sulphuric acid solutions at different pHs to form H^+ @ $\text{Ni}_2(\text{dobdc})$.⁸ At pH 1.8, the acidified MOF shows a proton conductivity of $2.2 \times 10^{-2} \text{ S cm}^{-1}$ at 80 °C and 95 % RH.

4.1.1 Aims of Chapter 4

The design of novel and creative strategies to improve proton conductivity in MOFs is a major challenge. The aim of the work described in this Chapter is to introduce two new approaches to increase the concentration of protons in a given framework without significantly modifying its structure.

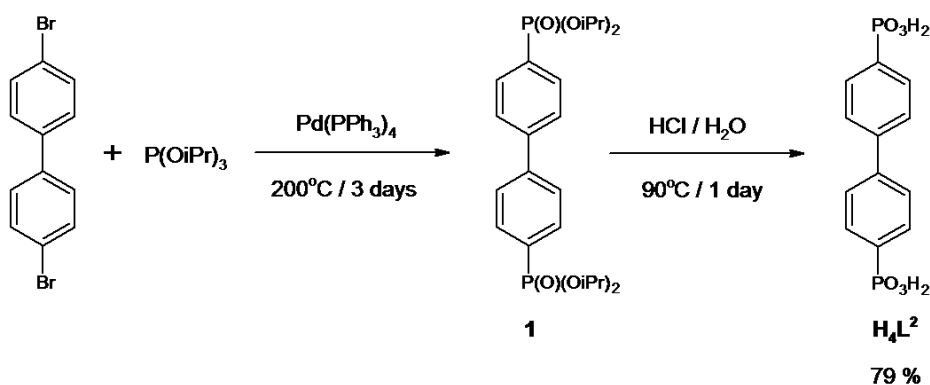
A new family of lanthanide complexes, $[M(HL^2)]$ ($H_4L^2 =$ biphenyl-4,4'-diphosphonic acid; $M =$ La, Ce, Nd, Sm, Gd, Ho), was synthesised, characterised and studied by impedance spectroscopy. Our methodology to increase the concentration of protons in $[M(HL^2)]$ was to use a shorter version of the organic ligand in order to decrease the distance between the metal chains (where the mobile protons are localised) and consequently increase the number of protons in a fixed volume. Thus $[M(HL^3)]$ ($H_4L^3 =$ benzene-1,4-diphosphonic acid; $M =$ La, Ce, Nd, Sm, Gd, Ho) were synthesised and characterised.

Another approach involves the synthesis of $[Ba(H_2L^2)]$, isostructural to $[M(HL^2)]$ with an excess of protons derived from the replacement of a 3+ metal with a 2+ metal of similar size. Impedance spectroscopy measurements of all the synthesised materials were recorded at different temperature and % RH, and compared to each other. We thus sought to establish if these strategies, presented herein for the first time, impacted on the proton conductivity properties of the materials.

4.2 Results and discussion

4.2.1 Synthesis of biphenyl-4,4'-diphosphonic acid, H_4L^2

The synthetic route to synthesise 4,4'-diphosphonic acid, H_4L^2 is shown in Scheme 4.1. The intermediate product **1** was synthesised from a $[Pd(PPh_3)_4]$ -catalysed Hirao reaction followed by stirring **1** in an acidic solution to obtain H_4L^2 . A wide range of conditions were studied for the Hirao reaction. At temperatures below 190 °C only the mono-substituted precursor of **1** was identified by 1H NMR spectrometry and mass spectrometry. Total conversion was observed in low yields when additional aliquots of catalyst were added during the progress of the reaction. Successful synthesis of **1** was achieved by heating the mixture at 200 °C under Ar with vigorous stirring for 3 days. Compound **1** was then dissolved in a mixture of HCl and H_2O (ratio 2:1) and the suspension stirred for 1 day at 90 °C to form H_4L^2 in good yields (79 %).



Scheme 4.1. Synthetic route to H_4L^2 .

4.2.2 Solid-state NMR spectroscopy of H_4L^2

Solid-state NMR spectroscopy is a well suited technique to characterise solid materials with phosphonate groups as both 1H and ^{31}P nuclei are NMR active due to their high gyromagnetic ratio, high natural abundance, and spin $1/2$.

Solid-state ^1H and $^{31}\text{P}\{^1\text{H}\}$ NMR spectra of H_4L^2 were collected in order to better understand the structure of two MOFs presented later in this Chapter. To this end, comparisons between the ^1H and ^{31}P NMR spectra of H_4L^2 and the MOFs, along with further comments, are discussed in depth in Sections 4.2.5 and 4.3.2.2.

The solid-state ^1H NMR spectrum of H_4L^2 was recorded on a Bruker Avance III spectrometer at room temperature with three broad peaks resolved (Figure 4.4). The two peaks at lower chemical shift (6.24 ppm and 8.20 ppm) are assigned to the aromatic protons (C-H) in the ortho- and meta-positions, respectively, with the third peak at 12.78 ppm corresponding to the protons of the phosphonate group (PO-H). This assignment is supported by the 2:1 integration of H(aromatic):H(phosphonate) peaks as expected from H_4L^2 structure (Scheme 4.1).

In the solid-state $^{31}\text{P}\{^1\text{H}\}$ NMR spectrum only one peak at 16.01 ppm was observed (Figure 4.5) as expected from the target molecule; since the ligand is symmetric only one type of phosphorous environment is present.

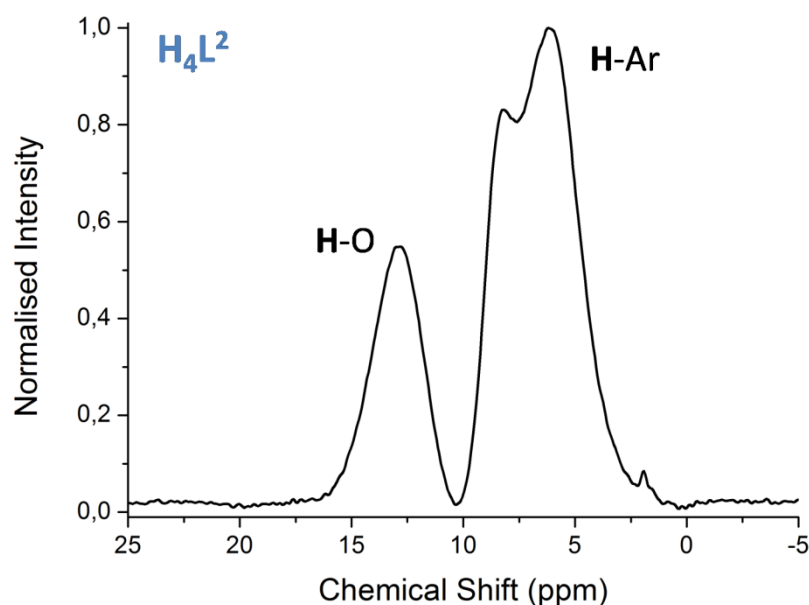


Figure 4.4. Solid-state ^1H NMR spectra of H_4L^2 .

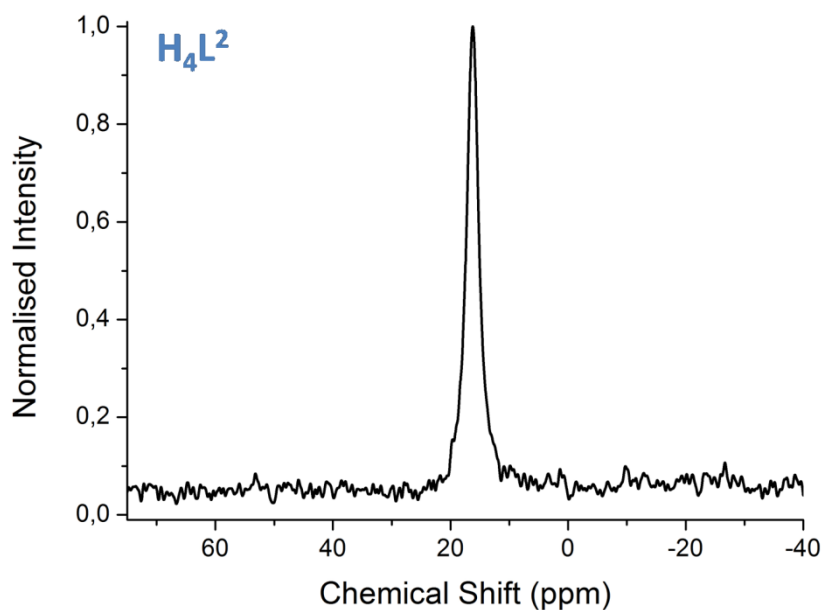


Figure 4.5. Solid-state $^{31}\text{P}\{^1\text{H}\}$ NMR spectra of H_4L^2 .

4.2.3 Synthesis of $[\text{M}(\text{HL}^2)]$

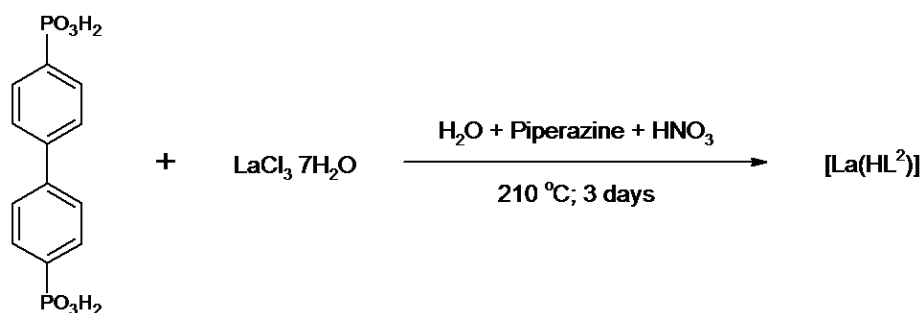
A wide set of conditions were investigated for the synthesis of new metal organic materials from H_4L^2 and 3+ metals. Lanthanide metal ions were chosen for their high coordination numbers and because their coordination geometries are well controlled by ligands with large functional groups, such as phosphonates.⁹ Lanthanide-based materials can also offer distinctive physical properties, such as luminescence. The chemistry of lanthanides is dominated by the most stable oxidation state +3 and along the series there are only small changes in the size of the ions. Thanks to these aspects, the elements of the lanthanide series show very similar chemical properties and reactivities.

A number of reactions with H_4L^2 and La(III) chlorides were carried out in both Ace pressure tubes and PARR pressure vessels. Four main factors were varied in the synthesis: ligand and metal ratio, solvent mixture, temperature, and duration of the reaction. The time of reaction was progressively increased from 1 to 4 days, the temperature was varied between 90 °C and 210 °C and the solvent mixture was

prepared from DMF, CH₃CN, CH₃OH and H₂O in different combinations and concentrations.

Reactions between H₄L² and LaCl₃ in DMF, CH₃CN and CH₃OH at relatively low temperatures and short reaction times usually produced amorphous white solids or starting materials. The best conditions resulted in the formation of highly crystalline materials were found to combine very high temperature (210 °C) and H₂O as solvent. To perform the reaction at such high temperatures and afford crystalline metal-organic frameworks, a hydrothermal synthetic methodology was used. The reaction components were mixed in water and sealed in a steel PARR pressure vessel; during the heating step an autogenous pressure is generated inside the vessel. For the formation of [La(HL²)], with empirical formula [Ln(HO₆P₂C₁₂H₈)], high temperatures (210 °C) and relatively high pressures (23 bar) were needed, probably to overcome the problem of the poor solubility of the phosphonate ligand.

In the most successful reactions, the ligand and the metal salts (1:1 ratio) were suspended in H₂O in the presence of HNO₃ (2.6 M solution) and piperazine (0.3 M). The reaction mixture was sealed in a PARR pressure vessel and heated at 210 °C; the product [La(HL²)] was formed after 3 days as highly crystalline powder (Scheme 4.2). The structure of [La(HL²)] was solved from refinement of the powder X-ray diffraction (PXRD) data (Section 4.2.4).



Scheme 4.2. Synthesis of [La(HL²)].

Reactions with five lanthanide metal salts and H_4L^2 were performed using the same conditions exploited for the successful synthesis of $[\text{La}(\text{HL}^2)]$ and a family of isostructural new MOFs, $[\text{M}(\text{HL}^2)]$ ($\text{M} = \text{La}, \text{Ce}, \text{Nd}, \text{Sm}, \text{Gd}, \text{Ho}$), were isolated.

The as-synthesised materials $[\text{M}(\text{HL}^2)]$ are insoluble in common organic solvents and were characterised by PXRD, elemental and thermogravimetric analysis, infrared, solid-state UV-visible and impedance spectroscopy. Solid-state ^1H and $^{31}\text{P}\{^1\text{H}\}$ NMR and high temperature PXRD (HT-PXRD) studies for $[\text{La}(\text{HL}^2)]$ were also performed.

4.2.4 Structural characterisation of $[\text{M}(\text{HL}^2)]$

The complexes $[\text{M}(\text{HL}^2)]$ were synthesised as microcrystalline powders and no single crystals were grown for any of them. Their crystal structures were solved from high-resolution synchrotron PXRD data using *ab initio* methods. Rietveld refinements were carried out and the compounds with empirical formula $[\text{M}(\text{HO}_6\text{P}_2\text{C}_{12}\text{H}_8)]_\infty$ exhibit a diffraction pattern that was indexed in a monoclinic cell. The model used fits quite well with the experimental data and final Rietveld refinements plots for the compounds are shown in Figure 4.6. The complexes $[\text{M}(\text{HL}^2)]$ are isostructural with small changes tuned by the presence of different Ln(III) cations in the framework. The ionic radius of the lanthanide metals progressively decrease from Ln to Gd. Consequently, small contractions in the unit cell parameters and shorter Ln-Ln distances are observed on moving from $[\text{La}(\text{HL}^2)]$ to $[\text{Gd}(\text{HL}^2)]$ (Table 4.1).

In the case of $[\text{Ho}(\text{HL}^2)]$ the PXRD shows some extra peaks attributable to some not yet identified impurities; therefore, it was not possible to index the pattern and refine its structures.

The bond lengths discussed in the text below refers to $[\text{Ce}(\text{HL}^2)]$. Adjacent parallel inorganic chains of lanthanide metals and oxygen atoms are bridged by the organic ligands to afford a three dimensional layered framework (Figure 4.7a). Each phosphonate group consists of three crystallographically different oxygen atoms O(1), O(2) and O(3) (Figure 4.7b). O(1) and O(2) are coordinated by chelating modes to one lanthanide metal (Ln') with bond distances of 2.5218(53) Å for Ce'-O(1) and 2.8511(60) Å for Ce'-O(2). O(2) also acts as a bridge to the adjacent Ln(III) cation (Ce''-O(2), 2.2602(46) Å), and O(3) is bonded to a third metal cation, (Ce'''-O(3), 2.4249(62) Å) (Table 4.1). The coordination geometry of each Ln(III) can be described as a distorted bicapped trigonal-prism with a $\{\text{MO}_8\}$ node (Figure 4.7c). Each Ln(III) centre is coordinated to eight oxygens from six phosphonate groups; two pairs of O(2) bridging two adjacent Ln, two O(1) and two O(3). The distance between adjacent Ce(III) cations is between 4.166 Å and 4.254 Å (Table 4.1).

One free proton for each ligand (PO-H) is delocalised in the framework; its presence is supported by both balanced charge in the formula and by solid-state ^1H and $^{31}\text{P}\{^1\text{H}\}$ NMR studies, (see Section 4.2.5).

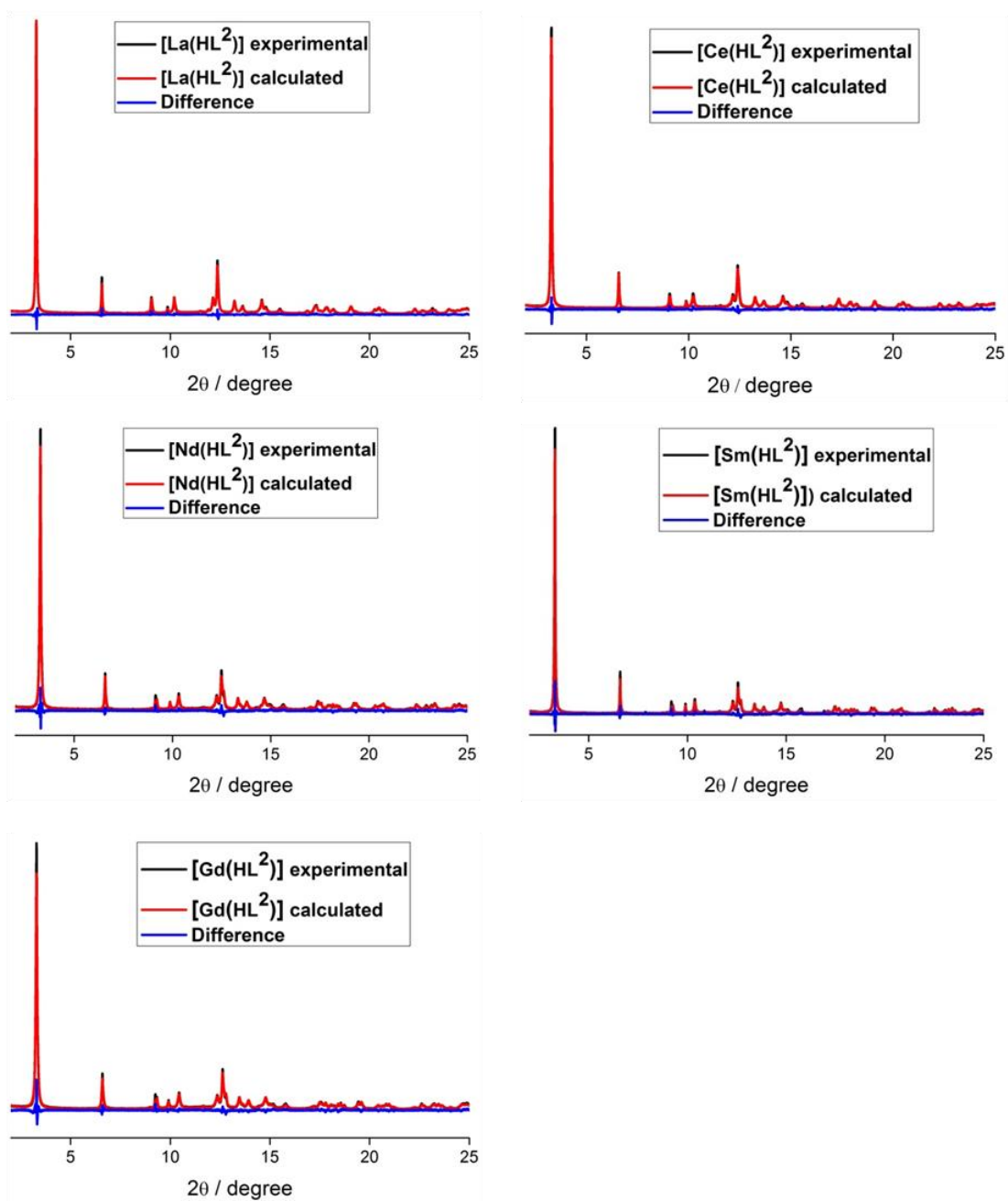


Figure 4.6. Observed (*red*) and calculated (*blue*) profiles for the Rietveld refinements of the complexes [M(HL²)] (M = La, Ce, Nd, Sm, Gd).

Table 4.1. Crystallographic data for [M(HL²)].

[M(HL ²)]	La	Ce	Nd	Sm	Gd
Empirical formula	C ₁₂ H ₉ P ₂ O ₆ La	C ₁₂ H ₉ P ₂ O ₆ Ce	C ₁₂ H ₉ P ₂ O ₆ Nd	C ₁₂ H ₉ P ₂ O ₆ Sm	C ₁₂ H ₉ P ₂ O ₆ Gd
Formula weight (g mol⁻¹)	450.05	451.26	455.39	461.55	468.40
R_{Shannon}/Å	1.160	1.143	1.109	1.079	1.053
Crystal system	Monoclinic	Monoclinic	Monoclinic	Monoclinic	Monoclinic
Space group	C2/c	C2/c	C2/c	C2/c	C2/c
a (Å)	5.63067(12)	5.62846(6)	5.56396(8)	5.53464(6)	5.49419(8)
b (Å)	28.7822(8)	28.7487(2)	28.7597(5)	28.6935(4)	28.6642(6)
c (Å)	8.4244(2)	8.38674(10)	8.28718(14)	8.22501(11)	8.17211(14)
β (°)	109.3025(17)	109.3347(8)	109.0120(10)	108.9716(8)	108.8366(8)
γ (°)	90	90	90	90	90
Cell volume (Å³)	1288.54	1280.53(2)	1253.76(4)	1235.25(3)	1218.07(4)
R_{wp}	6.16	7.61	9.41	10.00	9.14
GoF	4.00	2.83	2.16	2.21	1.94
Ln-Ln	4.2733(3)	4.2542(2)	4.2181(3)	4.1920(2)	4.1690(3)
Ln'-O(1)	2.5638(90)	2.5218(53)	2.5317(68)	2.4911(63)	2.5157(62)
Ln'-O(2)	2.7836(105)	2.8511(60)	2.7070(67)	2.6688(62)	2.6596(60)
Ln''-O(2)	2.3233(79)	2.2602(46)	2.3263(55)	2.3541(50)	2.3296(47)
Ln'''-O(3)	2.5112(107)	2.4249(62)	2.4968(72)	2.4613(64)	2.3679(63)

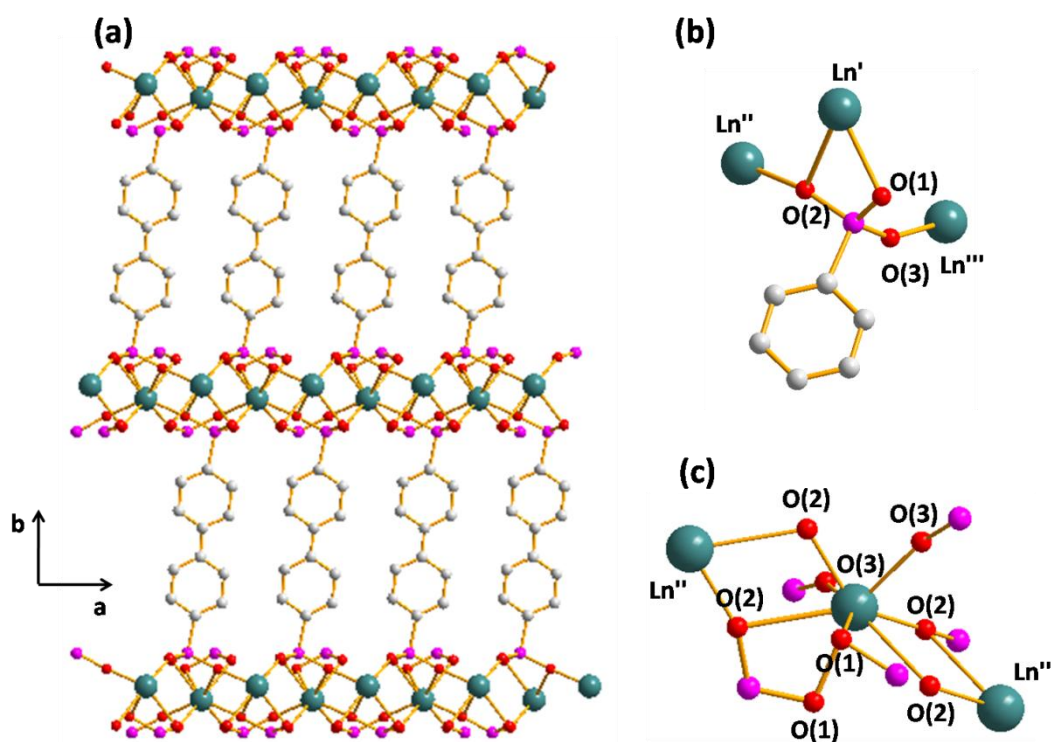


Figure 4.7. Refined structure of $[M(HL^2)]$ MOFs derived from PXRD data. (a) Projection of the structure along the c -axis. (b) Coordination nodes of the phosphonate group from the ligand. (c) Perspective view of the coordination environment at Ln(III) centres.

4.2.5 Solid-state NMR spectroscopy of $[M(HL^2)]$

The detection of protons from X-ray diffraction experiments is quite difficult and often not conclusive. In order to locate the protons in $[M(HL^2)]$ and investigate their environment, solid-state ^1H and $^{31}\text{P}\{^1\text{H}\}$ NMR analyses were performed on $[\text{La}(HL^2)]$.

The quantitative solid-state ^1H NMR spectrum of $[\text{La}(HL^2)]$ obtained at room temperature under magic-angle spinning (MAS) conditions shows two well-resolved resonances with chemical shifts of 7.40 ppm and 18.56 ppm (8:1 ratio) corresponding to two distinct proton sites in the structure (Figure 4.8a). The first peak at lower frequency is assigned to the aromatic protons from the organic ligand

(C-H) while the second peak is assigned to the protons of the free –OH from the protonated phosphonate group (P-O-H).

Comparing the ^1H NMR spectra of $[\text{La}(\text{HL}^2)]$ with that of H_4L^2 , the integration of the peaks is 8:4 for the latter and 8:1 for the former. This is consistent with what is expected. The difference in the chemical shift of the O-H protons is probably due to differences in electronic deshielding effects.

The presence of O-H groups close to the P centre is supported further by the 2D correlation spectrum (Figure 4.9) which shows two peaks corresponding to two different protons coupled to ^{31}P . The more intense signal is assigned to the protons from the OH while the other is attributable to the aromatic protons. This is not a quantitative technique, however the relative intensity correlates to the distance between the P centre and the protons. The difference in intensity is a result of the distance between the P and the proton in the phosphonate group (P-O-H) being much shorter than the distance between the phosphorous and the aromatic protons (P-C-C-H). This correlation spectrum supports the presence of free protons from the phosphonate group as opposed to other sources, such as water. The absence of free water in the dry MOF is confirmed by the solid-state ^1H NMR spectroscopy, since the peak for water protons (that would be expected around 5-6 ppm) is not observed. In the solid-state $^{31}\text{P}\{^1\text{H}\}$ NMR only one peak at 10.67 ppm is observed (Figure 4.10). However, a small, low intensity shoulder was detected at higher frequencies. In $[\text{La}(\text{HL}^2)]$ only one phosphonate group per ligand is protonated while the others are deprotonated and coordinated to the metal. The shoulder might be due to a difference in the relaxation times of the P environments. In particular, the deprotonated phosphonate group would be expected to have slower relaxation times and therefore lower intensity, as observed.

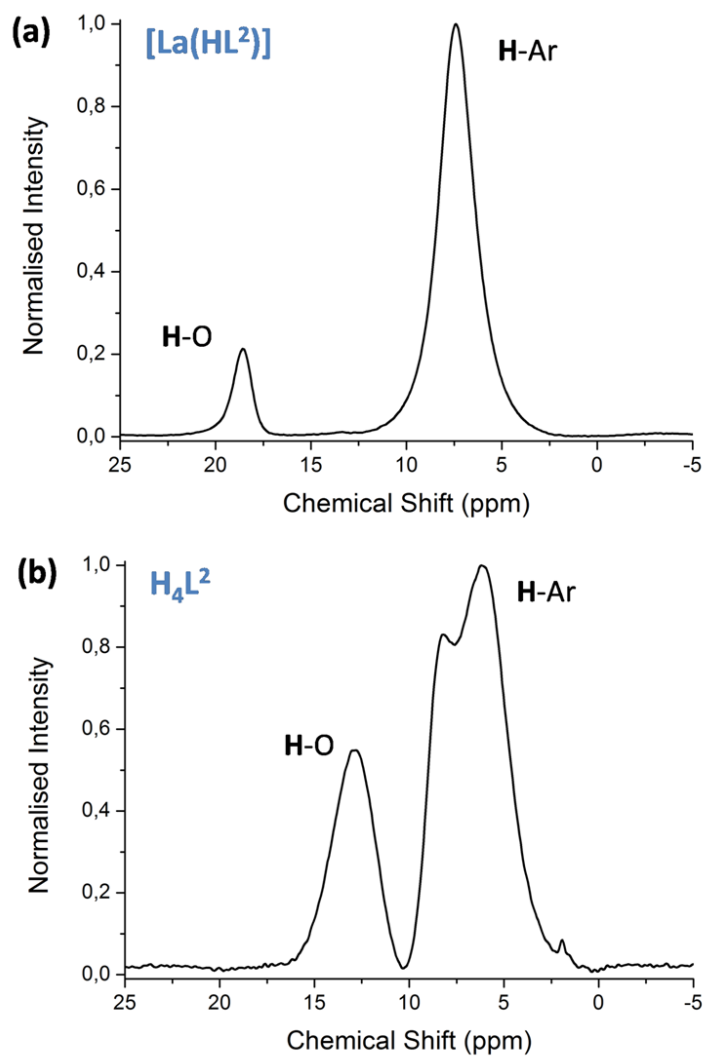


Figure 4.8. Comparison of solid-state ¹H NMR spectra of (a) [La(HL²)] and (b) H₄L².

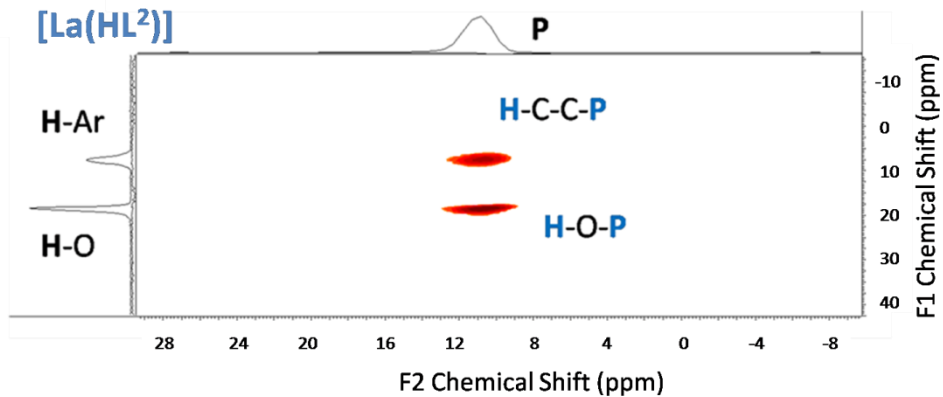


Figure 4.9. Correlation spectrum of phosphorus to proton in [La(HL²)].

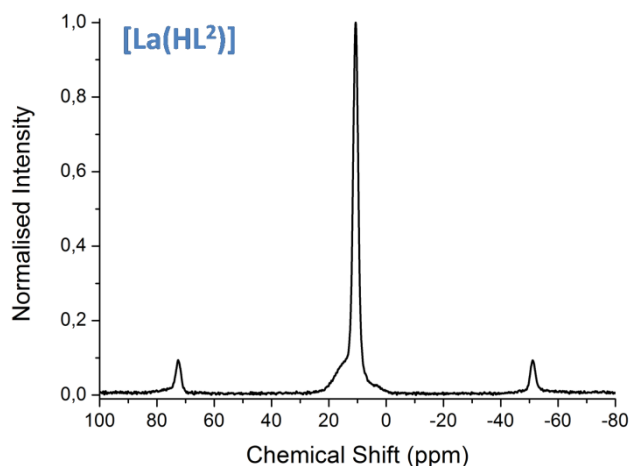


Figure 4.10. Solid-state $^{31}\text{P}\{^1\text{H}\}$ NMR spectrum of $[\text{La}(\text{HL}^2)]$.

4.2.6 Thermal stability of $[\text{M}(\text{HL}^2)]$

The thermal stability and retention of crystallinity of $[\text{M}(\text{HL}^2)]$ was analysed by combining TGA and PXRD.

Thermal gravimetric analyses were performed from 25 to 1000 °C with heating rate of 5 °C per minute at ambient pressure under a flow of air. The thermogravimetric curves of $[\text{M}(\text{HL}^2)]$ show very similar behaviour to each other consistent with these complexes being isostructural and the properties of lanthanide-based materials are expected to be similar (Figure 4.11). The MOFs show great thermal stability to above 500 °C, followed by the decomposition of the framework. The weight lost at about 500 °C matches well with the decomposition of the MOFs into organic moieties and phosphonate metal salts. In particular, the drop in weight of 30-34 % (depending on the metal) is due to the decomposition of the organic ligand; the remaining material corresponds to metal phosphonate salts. A detailed analysis of the thermogravimetric curves for each $[\text{M}(\text{HL}^2)]$ is shown in Table 4.2. The high thermostability of $[\text{M}(\text{HL}^2)]$ is attributed to the strong bond between lanthanide metals and phosphonate groups from the organic ligand.^{9,10} The absence of weight loss at low temperatures, characteristic of loss of solvent molecules trapped inside the pores, confirms

[M(HL²)] are very compact frameworks, which is in agreement with their refined structures. In most of the thermogravimetric curves the plateau is not well defined; however for technical reasons it was not possible to extend the temperature range over 1000 °C.

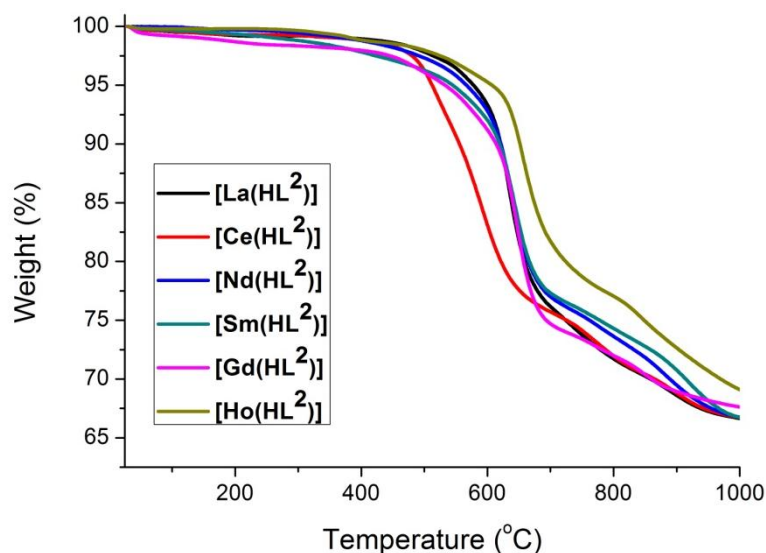


Figure 4.11. Thermogravimetric profiles of [M(HL²)] recorded under a flow of air at a heating rate of 5 °C min⁻¹. Colour scheme: [La(HL²)] (*black*), [Ce(HL²)] (*red*), [Nd(HL²)] (*blue*), [Sm(HL²)] (*green*), [Gd(HL²)] (*pink*), [Ho(HL²)] (*dark green*).

Table 4.2. Analysis of the experimental TGA data for [M(HL²)].

[M(HL ²)]	Weight % organic moieties (C ₁₂ H ₈)	Weight % metal phosphonate salts (P ₂ O ₆ LnH)
La	33.48	66.52
Ce	33.40	66.60
Nd	33.37	66.63
Sm	33.43	66.57
Gd	32.50	67.50
Ho	31.24	68.76

In situ PXRD studies on [La(HL²)] were carried out under vacuum at Diamond Light Source, Beamline I11. As shown in Figure 4.12, the crystallinity and the overall structure is perfectly retained up to 530 °C. Loss in crystallinity is observed at 610 °C when the structure starts to collapse.

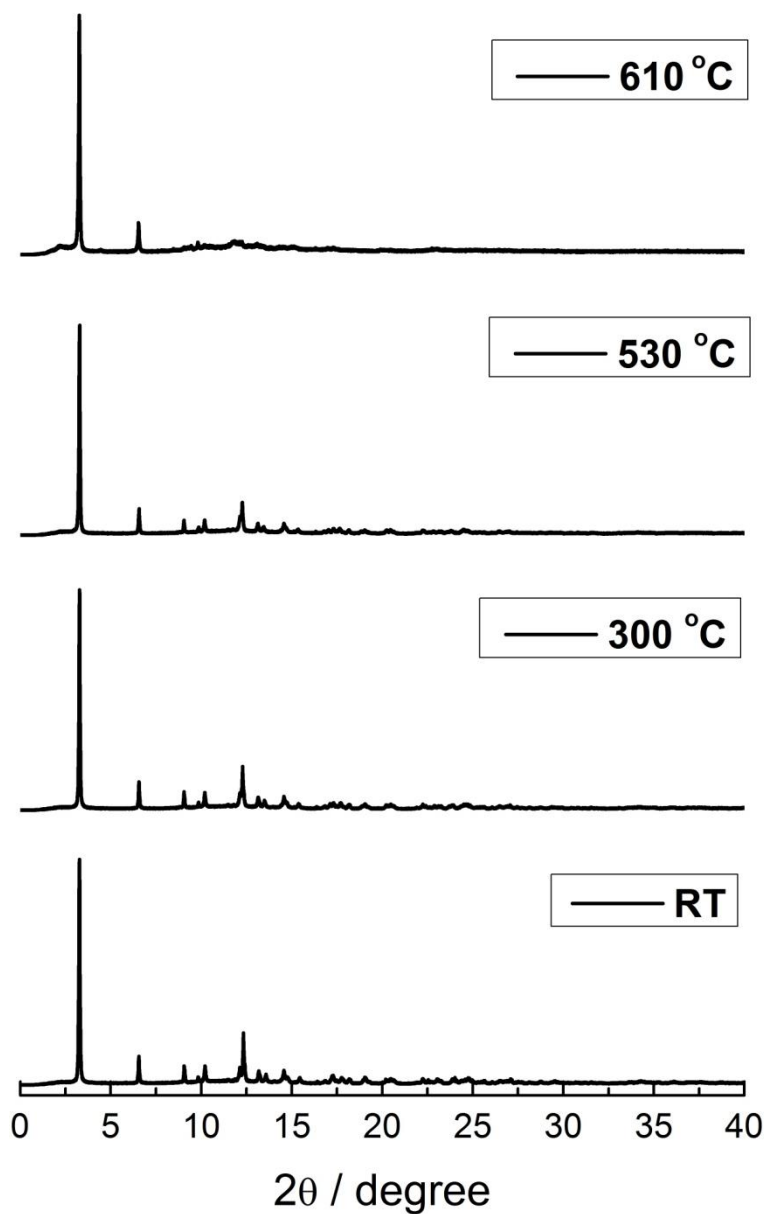


Figure 4.12. PXRD for [La(HL²)] as a function of temperature.

4.2.7 IR and Solid-state UV-visible absorption spectroscopies of [M(HL²)]

Infrared spectroscopy:

The infrared absorption spectra of [M(HL²)] were collected in the frequency range between 4000 cm⁻¹ to 550 cm⁻¹. All the compounds showed very similar IR spectra and detailed assignment of the bands for each material is reported in the Experimental Section of this Chapter, Section 4.5.

The infrared spectra of [Ho(HL²)] is shown in Figure 4.13, and the peaks were assigned according to the literature.¹¹⁻¹³ The bands at 1148 cm⁻¹ and 1077 cm⁻¹ are assigned to the stretching vibration of the phosphonate P-O group by comparison with the literature. The signals at 1737 cm⁻¹ and 916 cm⁻¹ are respectively attributed to the stretching vibrations $\nu(\text{P}=\text{O})$ and $\nu(\text{P}-\text{C})$. The bands centred at 1385 cm⁻¹ and 716 cm⁻¹ correspond to the C-C stretching vibrations of the phenylene group and in-plane deformation vibrations of para-disubstituted aromatic ring with identical groups. The band at 814 cm⁻¹ arises from the C-H out-of-plane vibrations for para-disubstituted phenylene rings. The peak centred at 2360 cm⁻¹ is attributed to the hydroxyl group from the phosphonate (P-OH), and the broad band at 3282 cm⁻¹ and 3045 cm⁻¹ are assigned to the O-H stretching vibrations of the protonated phosphonate oxygen.

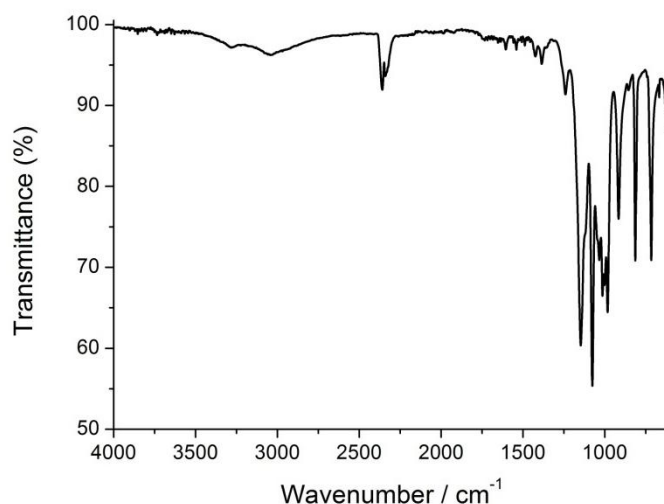


Figure 4.13. ATR infrared spectrum of $[\text{Ho}(\text{HL}^2)]$.

Solid-state UV-Visible absorption spectroscopy:

Electronic absorption spectra result from the absorption of electromagnetic radiation from an ion/atom/molecule due to the promotion of electrons from the ground state to excited states. The majority of transitions observed for trivalent lanthanide ions involve a redistribution of electrons within the 4f orbitals, which is forbidden by symmetry. Despite this selection rule, bands due to Ln(III) centres are typically detectable in the UV-visible region thanks to the effect of the crystal field in distorting the symmetry of the metal ion.

In metal organic compounds with Ln(III) ions, the energy of the electronic states of the metal can be slightly affected by the nature of the ligand. This variability is extremely low in inorganic salts of the rare earths; therefore they are often used as standards.¹⁴ Solid-state UV-visible absorption spectra of $[\text{M}(\text{HL}^2)]$ and related metal salts were collected as powders between 300 nm and 800 nm (Figure 4.14 and Figure 4.16). The compounds $[\text{M}(\text{HL}^2)]$ and correspondent metal salts show the characteristic absorbances for lanthanide metals.

In the case of $[\text{La}(\text{HL}^2)]$, $[\text{Ce}(\text{HL}^2)]$ and $[\text{Gd}(\text{HL}^2)]$ and corresponding metal salts, no absorbances attributable to the lanthanide metals are observed in the visible region (300 nm to 800 nm) (Figure 14). This can be explained with the fact that the energy gap between the ground level and the first excited state is found in the ultraviolet region above 200 nm.^{15,14} This is consistent with the partial energy level diagram reported in Figure 4.15.

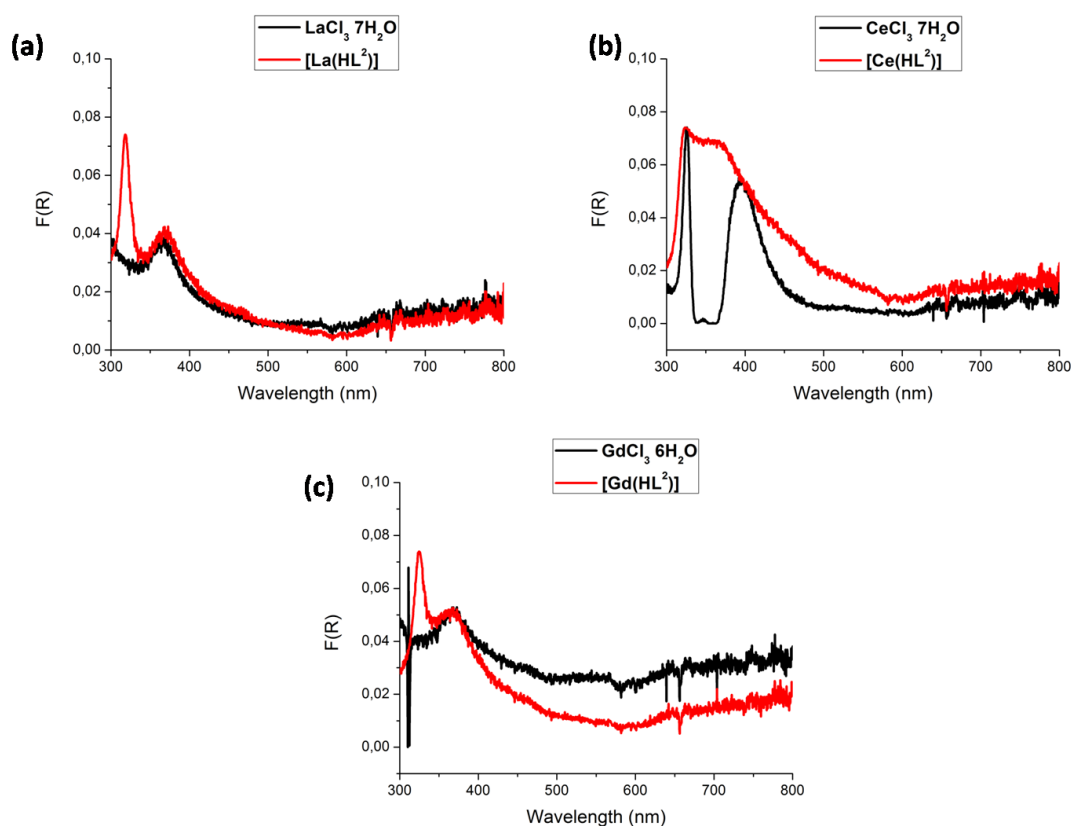


Figure 4.14. Absorbance spectra of (a) $[\text{La}(\text{HL}^2)]$ (red), $\text{LaCl}_3 \cdot 7\text{H}_2\text{O}$ (black). (b) $[\text{Ce}(\text{HL}^2)]$ (red), $\text{CeCl}_3 \cdot 7\text{H}_2\text{O}$ (black). (c) $[\text{Gd}(\text{HL}^2)]$ (red), $\text{GdCl}_3 \cdot 6\text{H}_2\text{O}$ (black).

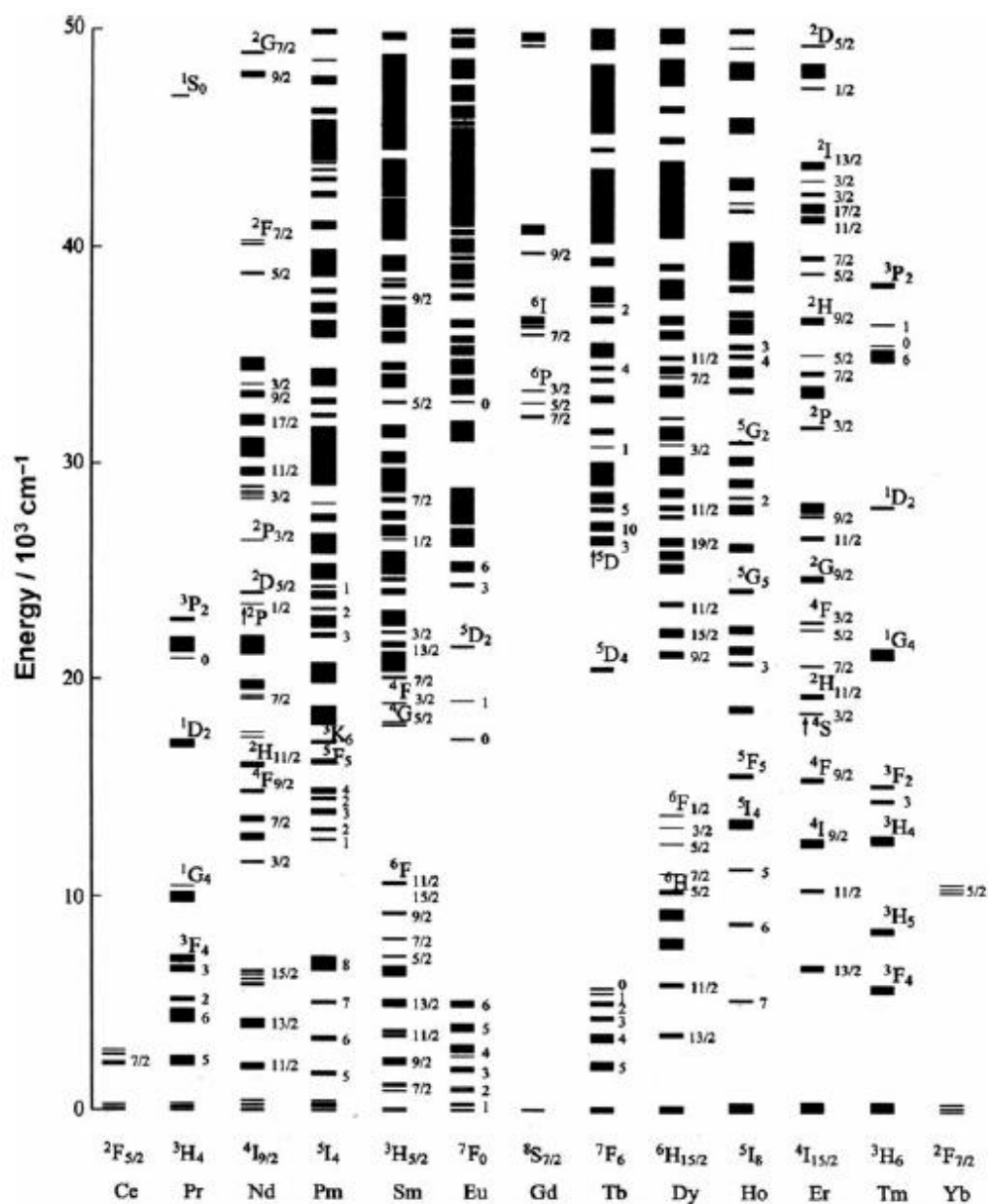


Figure 4.15. Energy level diagram for Ln(III) ions doped in a low-symmetry, LaF₃.¹⁵

The presence of several $^{2S+1}L_J$ electronic energy levels in Nd(III), Sm(III) and Ho(III) ions give rise to a large number of transitions in the visible and near-infrared regions of the spectra, sometimes of difficult assignment.¹⁵ Typical absorption bands of the lanthanide metals in both MOFs and inorganic salts were identified and supported by literature evidence (Figure 16).¹⁴⁻¹⁷

The broad band centred between 300 nm and 400 nm is observed in each of the absorbance spectra of the MOFs. This band is most likely due to the presence of

organic ligands in the complexes. This means that the f-f transitions that might be expected in the 300-400 nm region, observed for the inorganic metal salts, are obscured in the corresponding absorption spectra of the MOF materials. Changes in the intensities and slight shifts of some of the bands are generally attributable to the different environment of the metal ions in the framework. The disappearance of some transitions can be assigned to the different hydration of the metal. This is the case of the $^4G_{5/2}$ band at 560 nm in $\text{Sm}(\text{NO}_3)_3 \cdot 6\text{H}_2\text{O}$, which reflects the degree of hydration of Sm^{III} . This band is absent in $[\text{Sm}(\text{HL}^2)]$, offering further confirmation of the structure predicted by PXRD and described above, in which no water is found coordinated to the dry MOF.

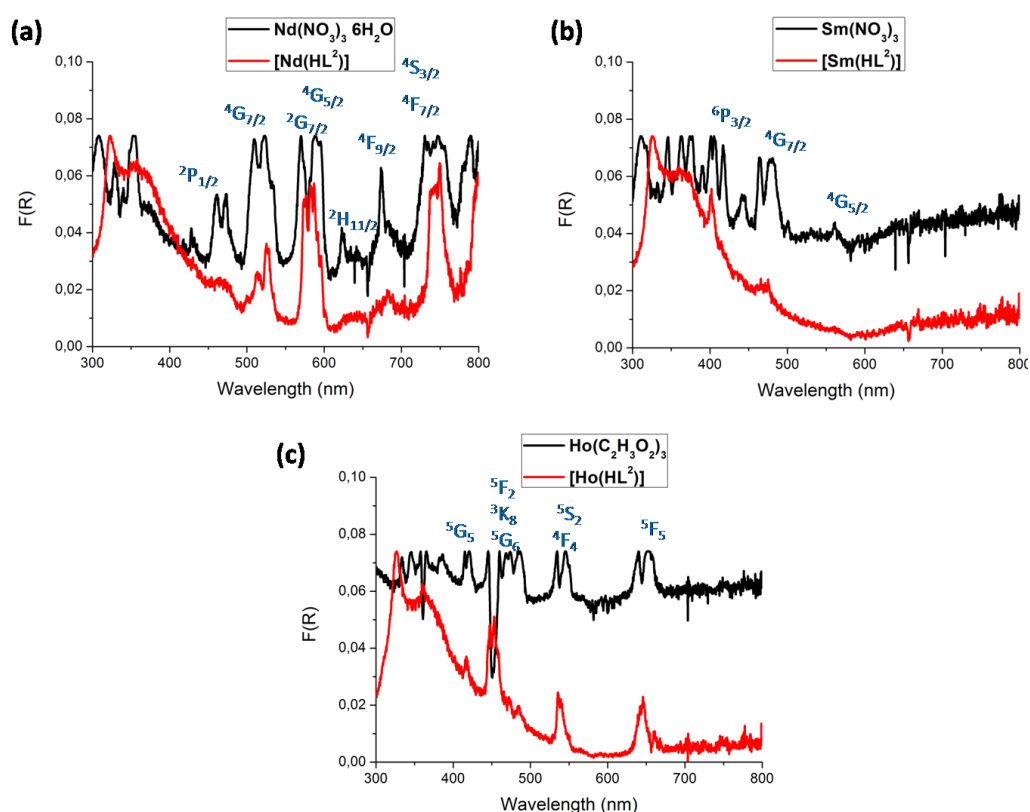


Figure 4.16. Absorbance spectra of (a) $[\text{Nd}(\text{HL}^2)]$ (red), $\text{Nd}(\text{NO}_3)_3 \cdot 6\text{H}_2\text{O}$ (black). (b) $[\text{Sm}(\text{HL}^2)]$ (red), $\text{Sm}(\text{NO}_3)_3 \cdot 6\text{H}_2\text{O}$ (black). (c) $[\text{Ho}(\text{HL}^2)]$ (red), $\text{Ho}(\text{CH}_3\text{CO}_2)_3 \cdot 6\text{H}_2\text{O}$ (black).

4.2.8 Proton conductivity study of [M(HL²)]

Proton conductivities of [M(HL²)] were studied by AC impedance spectroscopy on compact pellets using cell B (Section 2.2.3.2). For each MOF about 0.120 g of sample was ground into a fine powder using mortar and pestle and pressed for 5 minutes under a pressure of 5 tons using a die with 0.8 cm diameter. A silver paste (Sigma Aldrich) was applied to either side of the sample to serve as electrode. The thickness and the diameter of the pellet were measured and used to calculate the proton conductivities of [M(HL²)] (Section 2.1.6, Equation 10). For each sample measurements were repeated on two different batches; for each batch three measurements were collected at each temperature and relative humidity investigated. The data collected was used to calculate the mean value of the proton conductivity correspondent to the experimental conditions under study, together with the associated standard deviation.

Proton conductivity at different relative humidities:

Impedance measurements on [M(HL²)] were recorded at different values of % RH to investigate any correlation between the proton conductivity of [M(HL²)] and the relative humidity. Measurements between 99 % and 45 % RH at 20 °C were collected for each material by following the same procedure. The dry pellet (previously coated with silver paste) was loaded inside the conductivity cell and exposed to 99 % RH humidity overnight to allow the compressed sample to equilibrate. Three measurements were then collected to ensure stable resistivity of the sample (after equilibration at the desired conditions) and reproducibility of the measurements. The % RH was then decreased at 75 % by adjusting the flow of wet and dry gas inside the conductivity cell (Section 2.2.4). Measurements were collected

every 45 mins until the resistivity of the sample was stable over a period of 2 h suggesting the equilibration point had been reached. This process normally took about 4 h. The same procedure was repeated at 45 % RH.

Nyquist and Bode plots for each complex collected at 99 %, 70 % and 45 % RH at 20 °C are shown in Figures 4.17-4.22 together with the corresponding proton conductivity data measured using the resistivity obtained by fitting the data (Tables 4.3-4.8). The Bode plots give information about the frequency range investigated, which doesn't appear in the Nyquist plot. In addition, they show how the absolute resistance and phase shift (Section 2.1.4) change as a function of the applied frequency. More enlightening information about the conduction process are given by the Nyquist plots. At 99 % RH the Nyquist plots show a semi-circle in the high frequency region and a tail at low frequencies. The semi-circle plot in the high-frequency region represents the bulk resistance, while the tail at low frequencies, which is typical of materials with predominantly ionic conductivity, may indicate blocking of H^+ at the electrodes consistent with ion migration. At low values of % RH the resistivity of the sample remarkably increases (as commonly observed for water mediated proton conductors) and in the frequency range investigated the tail in the Nyquist plot is not present.

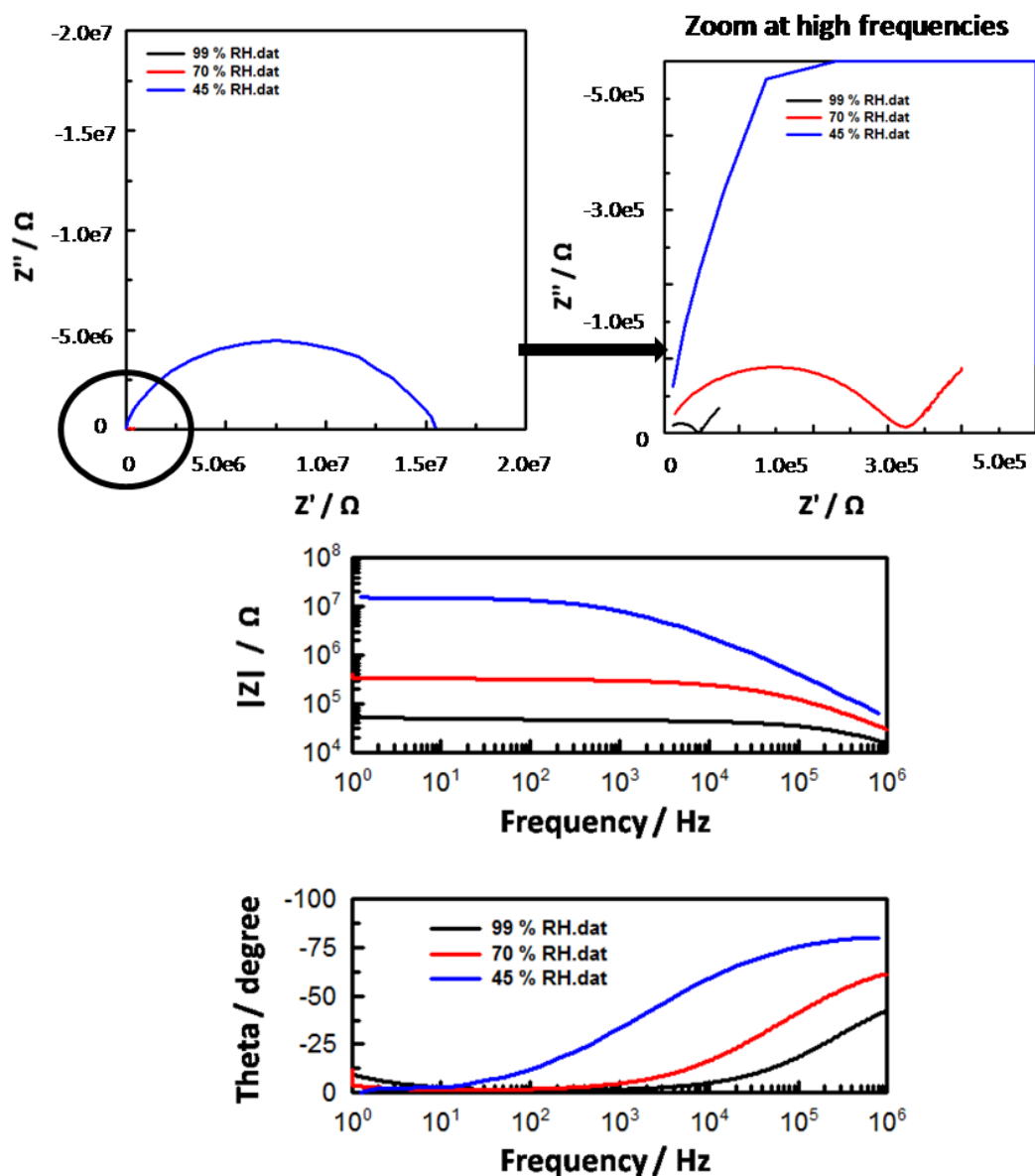


Figure 4.17. Nyquist and Bode plots for [La(HL²)] measured at different % RH and 20 °C.

Table 4.3. Proton conductivity (S cm⁻¹) for [La(HL²)] measured at different % RH and 20 °C.

[La(HL ²)]	σ at 99 % RH	σ at 70 % RH	σ at 45 % RH
σ	$4.00(15) \times 10^{-6}$	$6.09(11) \times 10^{-7}$	$1.24(10) \times 10^{-8}$

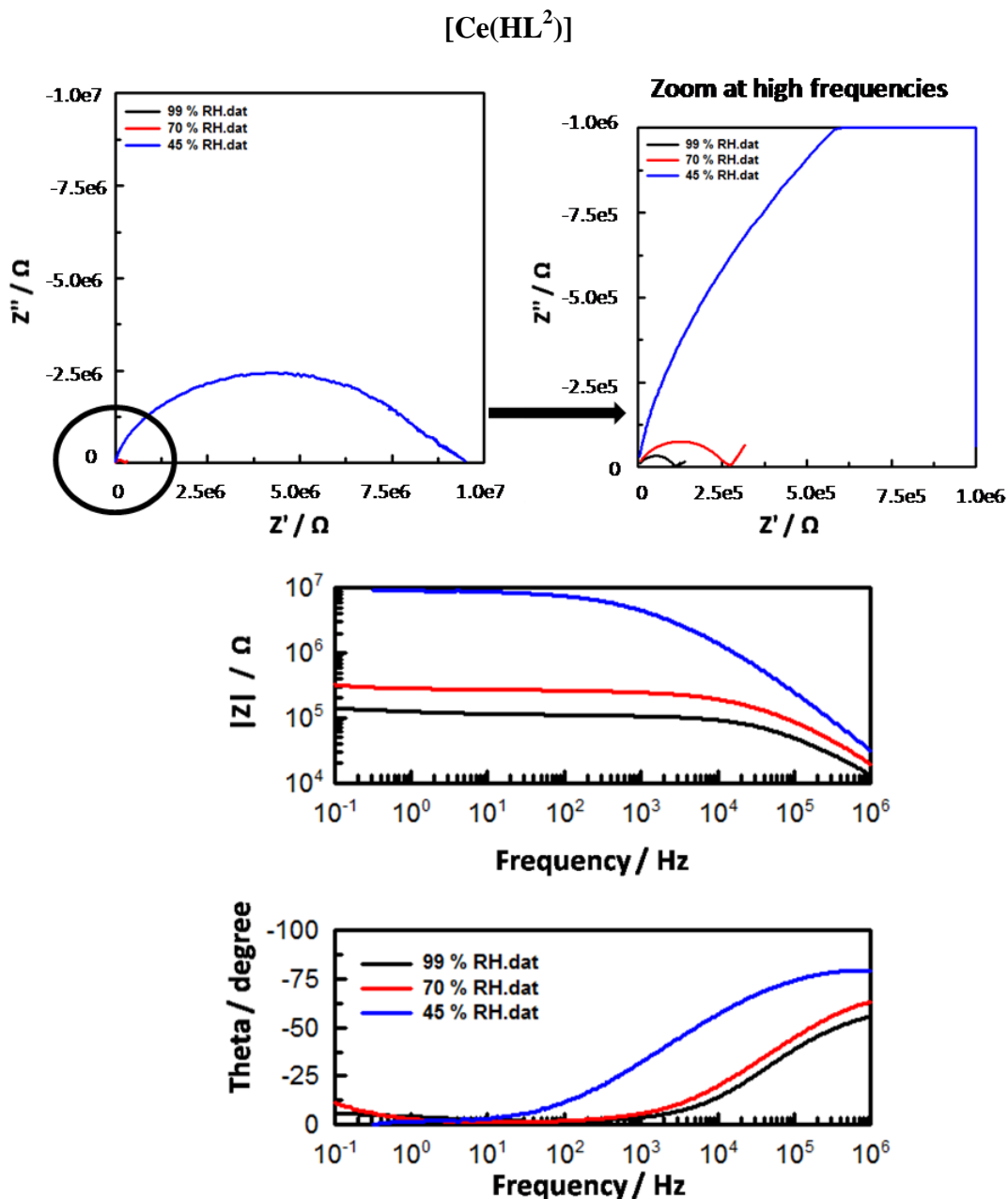


Figure 4.18. Nyquist and Bode plots for [Ce(HL²)] measured at different % RH and 20 °C.

Table 4.4. Proton conductivity (S cm⁻¹) for [Ce(HL²)] measured at different % RH and 20 °C.

[Ce(HL ²)]	σ at 99 % RH	σ at 70 % RH	σ at 45 % RH
σ	$1.46(11) \times 10^{-6}$	$5.05(12) \times 10^{-7}$	$1.82(09) \times 10^{-8}$

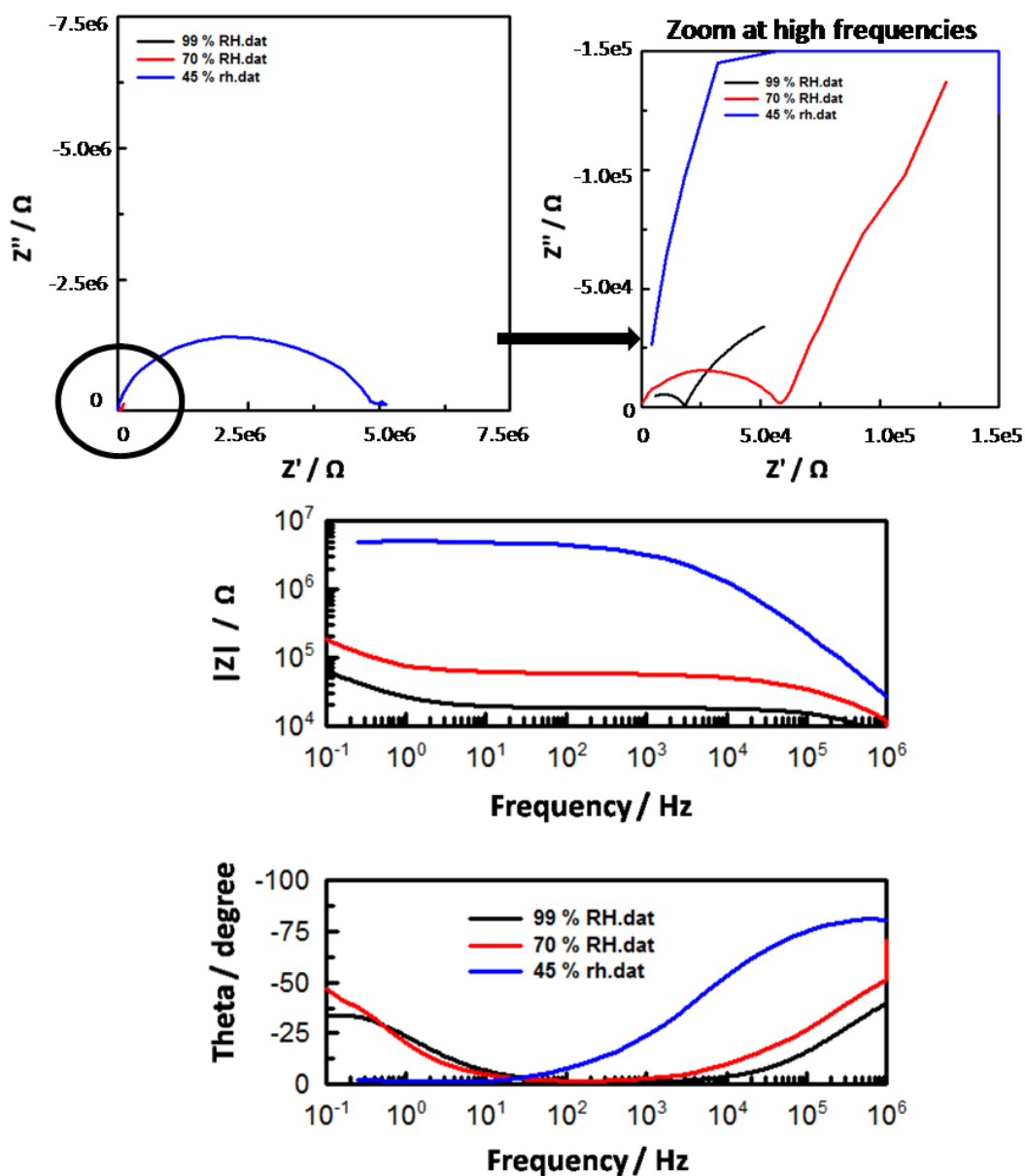


Figure 4.19. Nyquist and Bode plots for [Nd(HL²)] measured at different % RH and 20 °C.

Table 4.5. Proton conductivity (S cm⁻¹) for [Nd(HL²)] measured at different % RH and 20 °C.

[Nd(HL ²)]	σ at 99 % RH	σ at 70 % RH	σ at 45 % RH
σ	7.85(09) x 10 ⁻⁶	2.47(10) x 10 ⁻⁶	2.86(12) x 10 ⁻⁸

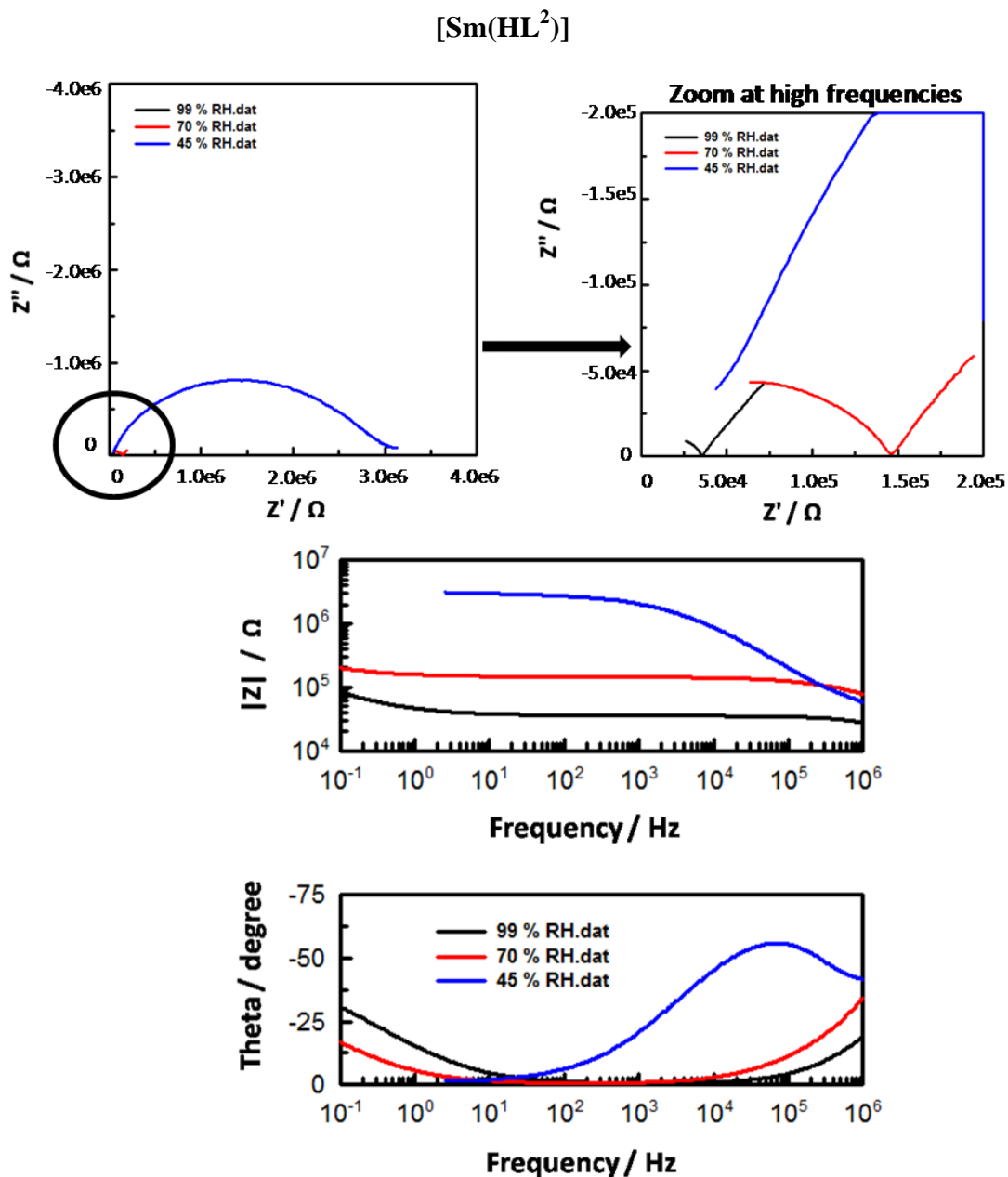


Figure 4.20. Nyquist and Bode plots for [Sm(HL²)] measured at different % RH and 20 °C.

Table 4.6. Proton conductivity (S cm⁻¹) for [Sm(HL²)] measured at different % RH and 20 °C.

[Sm(HL ²)]	σ at 99 % RH	σ at 70 % RH	σ at 45 % RH
σ	$3.83(11) \times 10^{-6}$	$9.22(08) \times 10^{-7}$	$4.47(10) \times 10^{-8}$

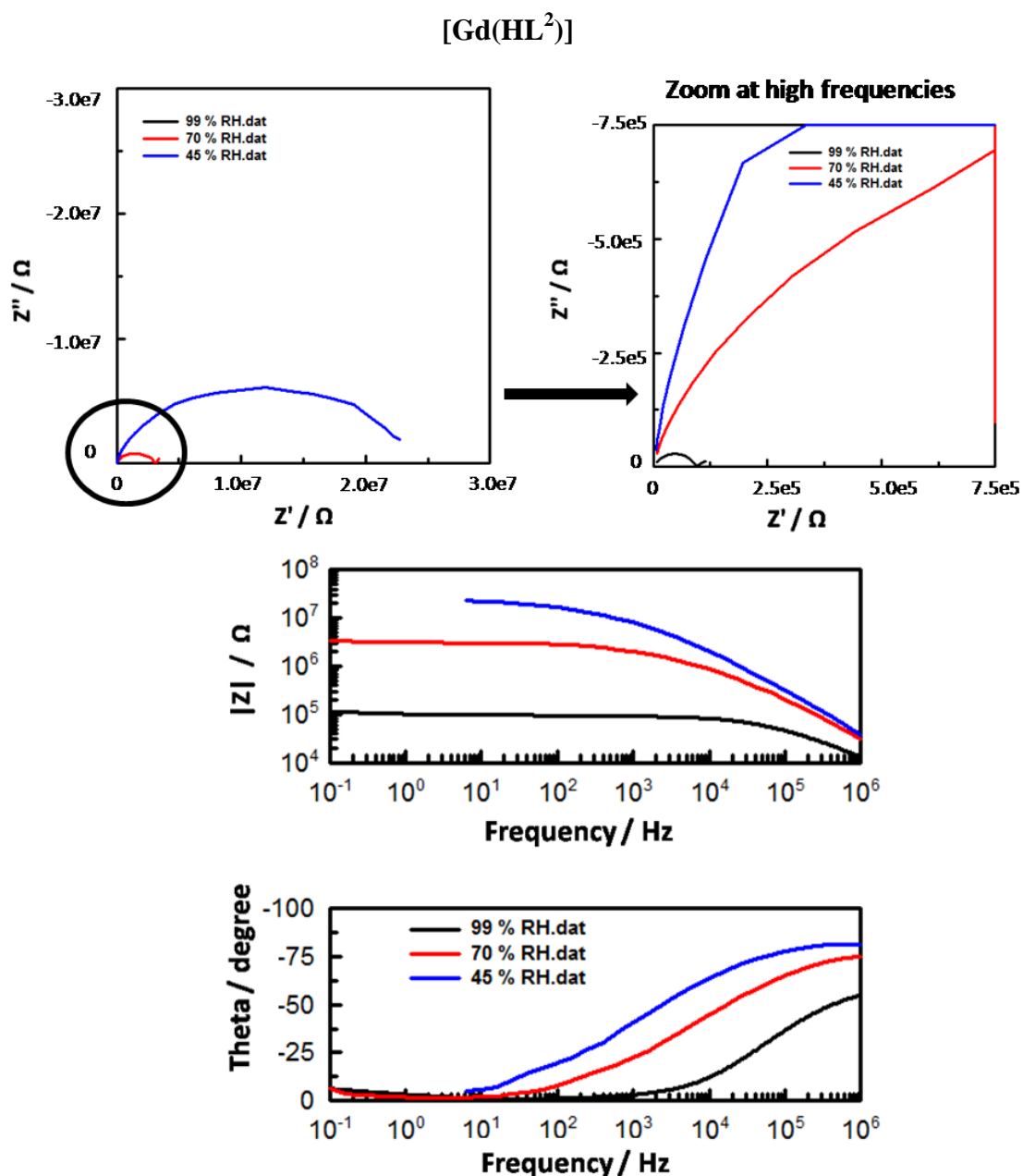


Figure 4.21 Nyquist and Bode plots for [Gd(HL²)] measured at different % RH and 20 °C.

Table 4.7. Proton conductivity (S cm⁻¹) for [Gd(HL²)] measured at different % RH and 20 °C.

[Gd(HL ²)]	σ at 99 % RH	σ at 70 % RH	σ at 45 % RH
σ	$1.87(08) \times 10^{-6}$	$5.63(11) \times 10^{-8}$	$7.38(13) \times 10^{-9}$

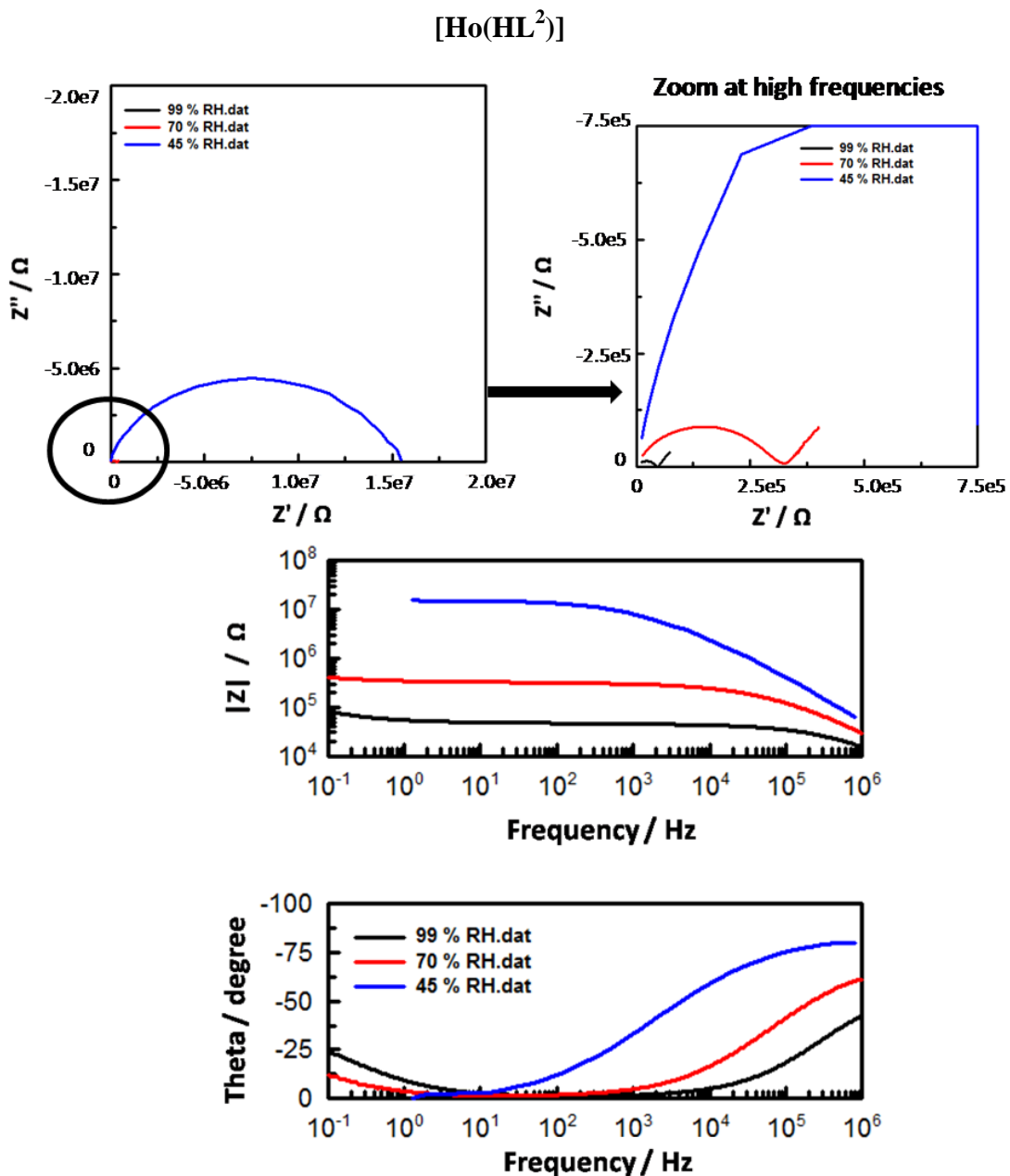


Figure 4.22. Nyquist and Bode plots for [Ho(HL²)] measured at different % RH and 20 °C.

Table 4.8. Proton conductivity (S cm⁻¹) for [Ho(HL²)] measured at different % RH and 20 °C.

[Ho(HL ²)]	σ at 99 % RH	σ at 70 % RH	σ at 45 % RH
σ	5.22(13) x 10 ⁻⁶	7.52(10) x 10 ⁻⁷	1.53(09) x 10 ⁻⁸

Proton conductivity measurements for each complex collected at 99 %, 70 % and 45 % RH at 20 °C are summarised in Table 4.9. For each sample the proton conductivity reaches its maximum value at 99 % RH and progressively decreases at lower values of % RH. The reduction of resistivity with increasing relative humidity is a well-known response observed in PEMs and MOFs when their proton conductivity is water-mediated.^{7,18–21} The proton conductivity of water-mediated materials relies on both the presence of water molecules and on hydrogen-bonding interactions between the water molecules and the protons within the framework.²²

It is noteworthy that the proton conductivities measured at 99 % RH and 20 °C for all complexes are very similar to each other. This result was expected as all the materials are isostructural and only small changes in the unit cell parameter were observed which will not have a major impact on the proton conductivity of the materials.

Table 4.9. Summary of proton conductivities (S cm^{-1}) for $[\text{M}(\text{HL}^2)]$ measured at different % RH and 20 °C.

$[\text{M}(\text{HL}^2)]$	σ at 99 % RH	σ at 70 % RH	σ at 45 % RH
La	$4.00(15) \times 10^{-6}$	$6.09(11) \times 10^{-7}$	$1.24(10) \times 10^{-8}$
Ce	$1.46(11) \times 10^{-6}$	$5.05(12) \times 10^{-7}$	$1.82(09) \times 10^{-8}$
Nd	$7.85(09) \times 10^{-6}$	$2.47(10) \times 10^{-6}$	$2.86(12) \times 10^{-8}$
Sm	$3.83(11) \times 10^{-6}$	$9.22(08) \times 10^{-7}$	$4.47(10) \times 10^{-8}$
Gd	$1.87(08) \times 10^{-6}$	$5.63(11) \times 10^{-8}$	$7.38(13) \times 10^{-9}$
Ho	$5.22(13) \times 10^{-6}$	$7.52(10) \times 10^{-7}$	$1.53(09) \times 10^{-8}$

Proton conductivity at different temperatures:

Impedance measurements for [M(HL²)] were collected in the range between 20 °C and 80 °C at 99 % RH to investigate the behaviour of the proton conductivity at different temperatures (Figures 4.23-4.28, Tables 4.10-4.15).

The dry sample (pellet coated with silver paste) was first equilibrated to 99 % RH humidity overnight as described above. The temperature was then progressively increased from 20 °C to 80 °C. At each investigated temperature the samples were equilibrated for 2 h. During this period several measurements were recorded until the proton conductivity was stable and the equilibration point had been reached. At each stabilised temperature three measurements were recorded to ensure stability and reproducibility of the measurement.

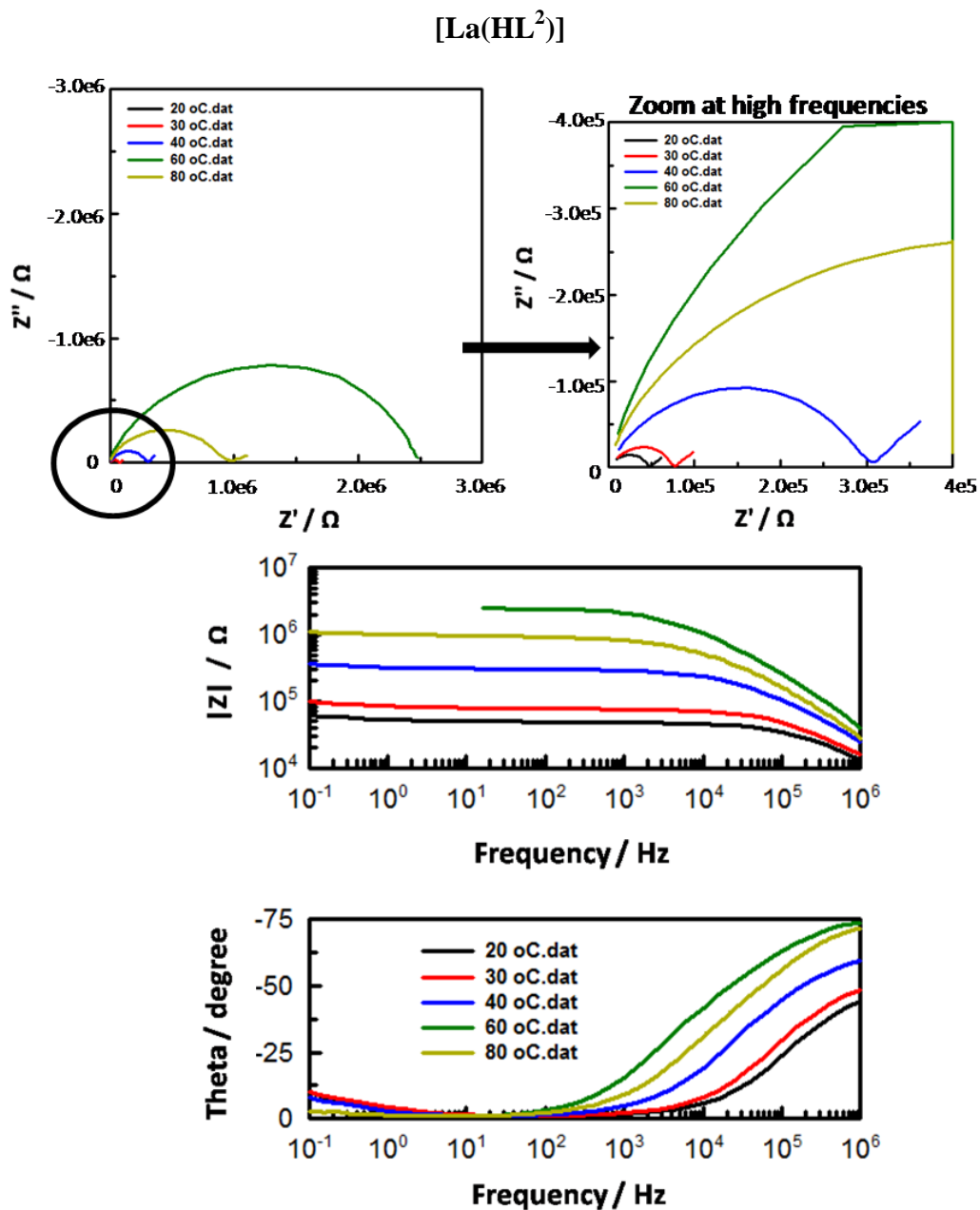


Figure 4.23. Nyquist and Bode plots for [La(HL²)] measured at different temperatures and 99 % RH.

Table 4.10. Proton conductivity (S cm⁻¹) for [La(HL²)] measured at different temperatures and 99% RH.

[La(HL ²)]	σ at 20 °C	σ at 30 °C	σ at 40 °C	σ at 60 °C	σ at 80 °C
σ	$4.00(15) \times 10^{-6}$	$2.53(13) \times 10^{-6}$	$6.36(15) \times 10^{-7}$	$7.87(12) \times 10^{-8}$	$2.00(16) \times 10^{-7}$

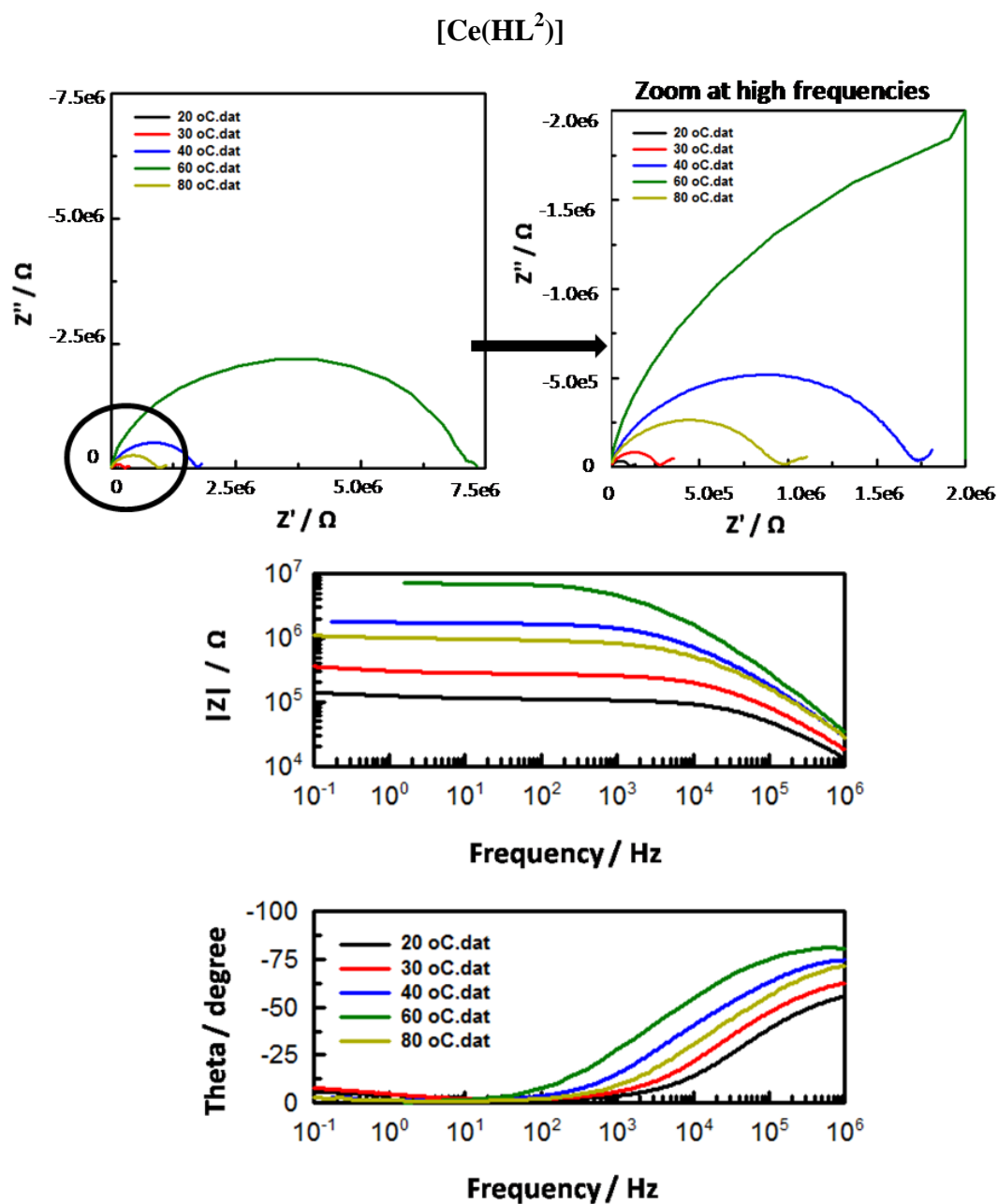


Figure 4.24. Nyquist and Bode plots for [Ce(HL²)] measured at different temperatures and 99 % RH.

Table 4.11. Proton conductivity ($S\ cm^{-1}$) for [Ce(HL²)] measured at different temperatures and 99 % RH.

[Ce(HL ²)]	σ at 20 °C	σ at 30 °C	σ at 40 °C	σ at 60 °C	σ at 80 °C
σ	$1.46(11) \times 10^{-6}$	$7.14(13) \times 10^{-7}$	$1.00(12) \times 10^{-7}$	$2.29(12) \times 10^{-8}$	$1.66(11) \times 10^{-7}$

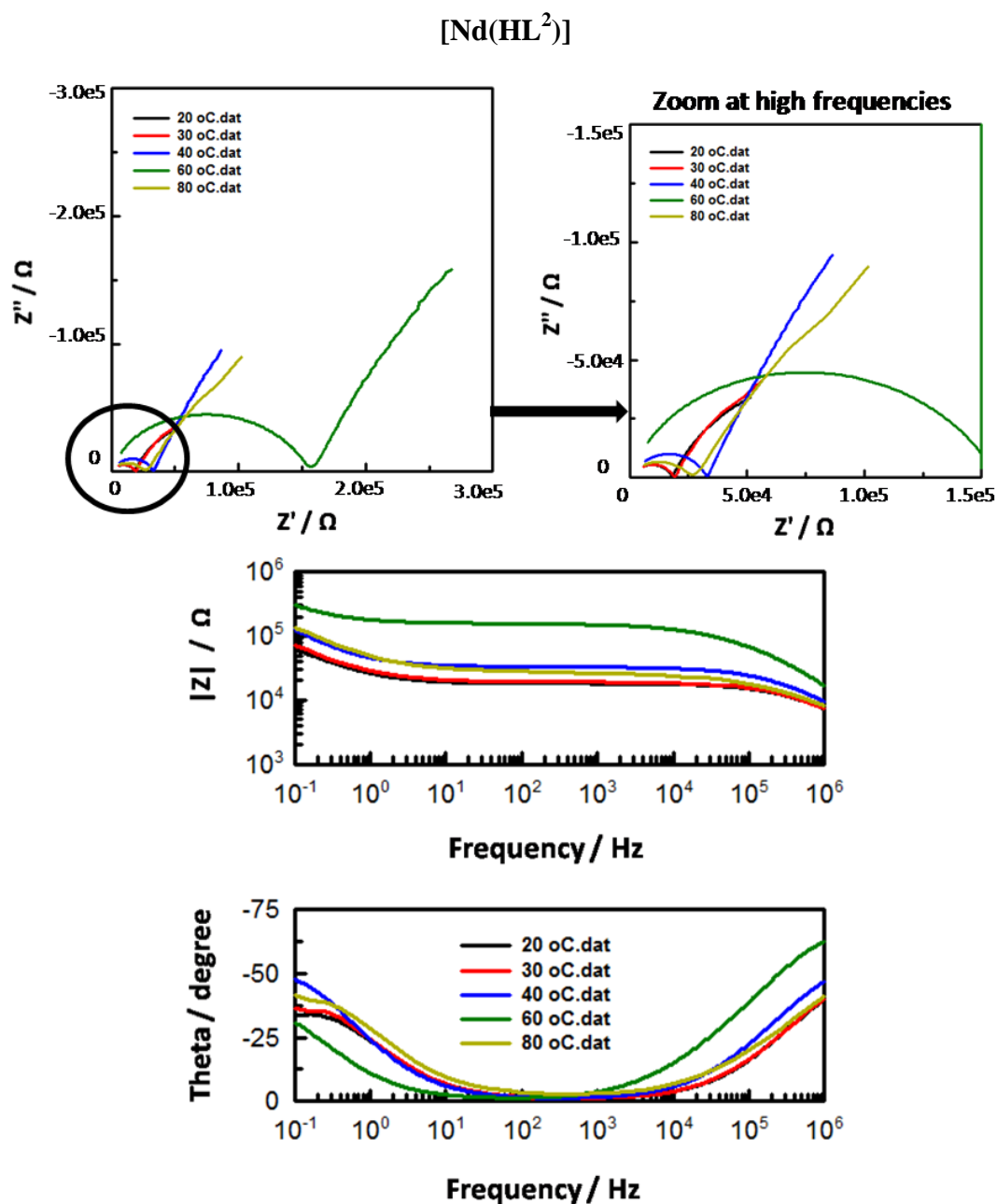


Figure 4.25. Nyquist and Bode plots for [Nd(HL²)] measured at different temperatures and 99 % RH.

Table 4.12. Proton conductivity (S cm⁻¹) for [Nd(HL²)] measured at different temperatures and 99 % RH.

[Nd(HL ²)]	σ at 20 °C	σ at 30 °C	σ at 40 °C	σ at 60 °C	σ at 80 °C
σ	$7.85(09) \times 10^{-6}$	$7.47(15) \times 10^{-6}$	$4.39(10) \times 10^{-6}$	$9.17(11) \times 10^{-7}$	$5.39(14) \times 10^{-6}$

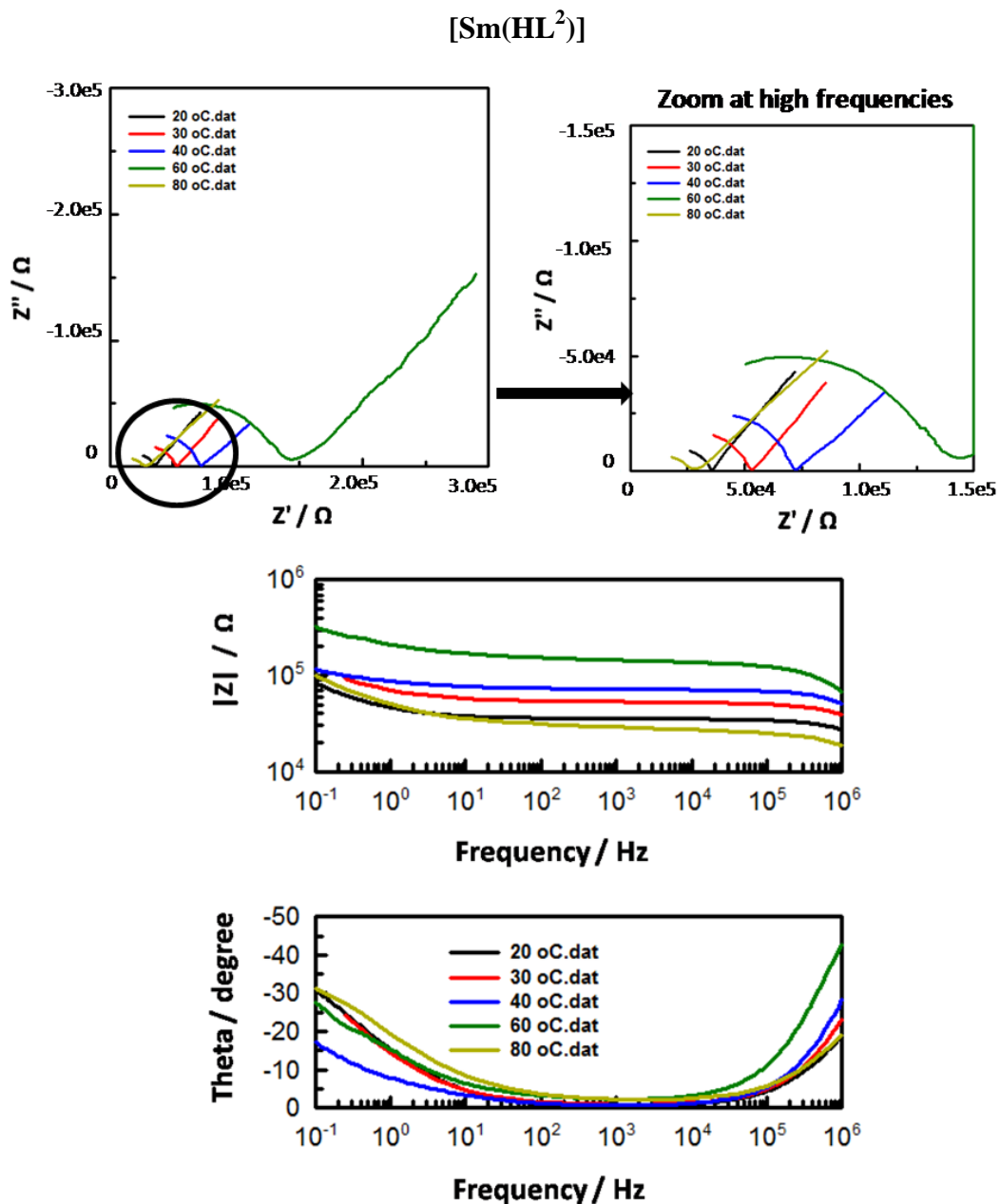


Figure 4.26. Nyquist and Bode plots for [Sm(HL²)] measured at different temperatures and 99 % RH.

Table 4.13. Proton conductivity (S cm⁻¹) for [Sm(HL²)] measured at different temperatures and 99 % RH.

[Sm(HL ²)]	σ at 20 °C	σ at 30 °C	σ at 40 °C	σ at 60 °C	σ at 80 °C
σ	$3.82(11) \times 10^{-6}$	$2.55(10) \times 10^{-6}$	$1.89(13) \times 10^{-6}$	$9.51(12) \times 10^{-6}$	$4.79(11) \times 10^{-6}$

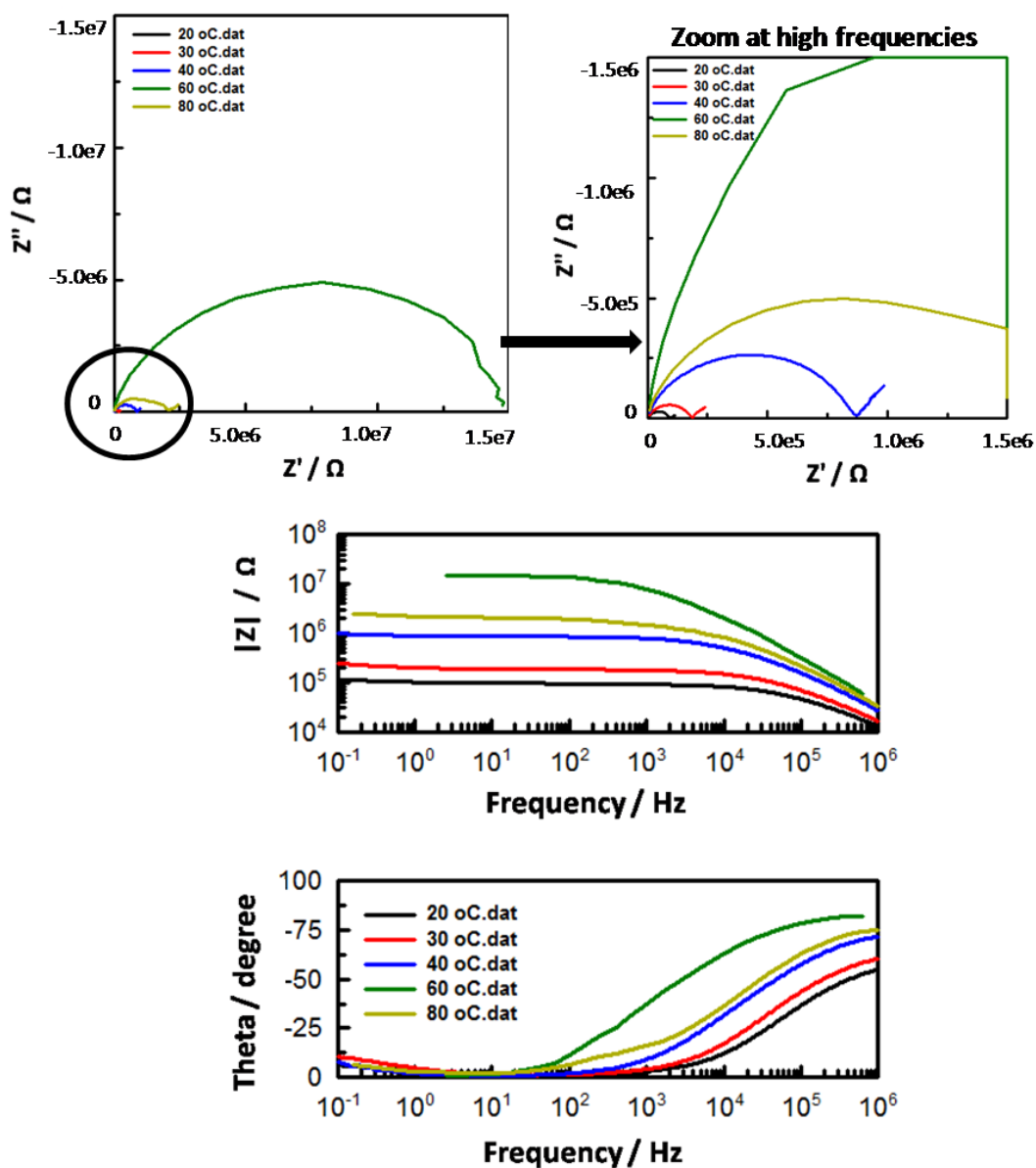


Figure 4.27. Nyquist and Bode plots for [Gd(HL²)] measured at different temperatures and 99 % RH.

Table 4.14. Proton conductivity (S cm⁻¹) for [Gd(HL²)] measured at different temperatures and 99 % RH.

[Gd(HL ²)]	σ at 20 °C	σ at 30 °C	σ at 40 °C	σ at 60 °C	σ at 80 °C
σ	1.87(08) x 10 ⁻⁶	9.66(11) x 10 ⁻⁶	2.06(07) x 10 ⁻⁷	1.21(18) x 10 ⁻⁸	1.03(14) x 10 ⁻⁷

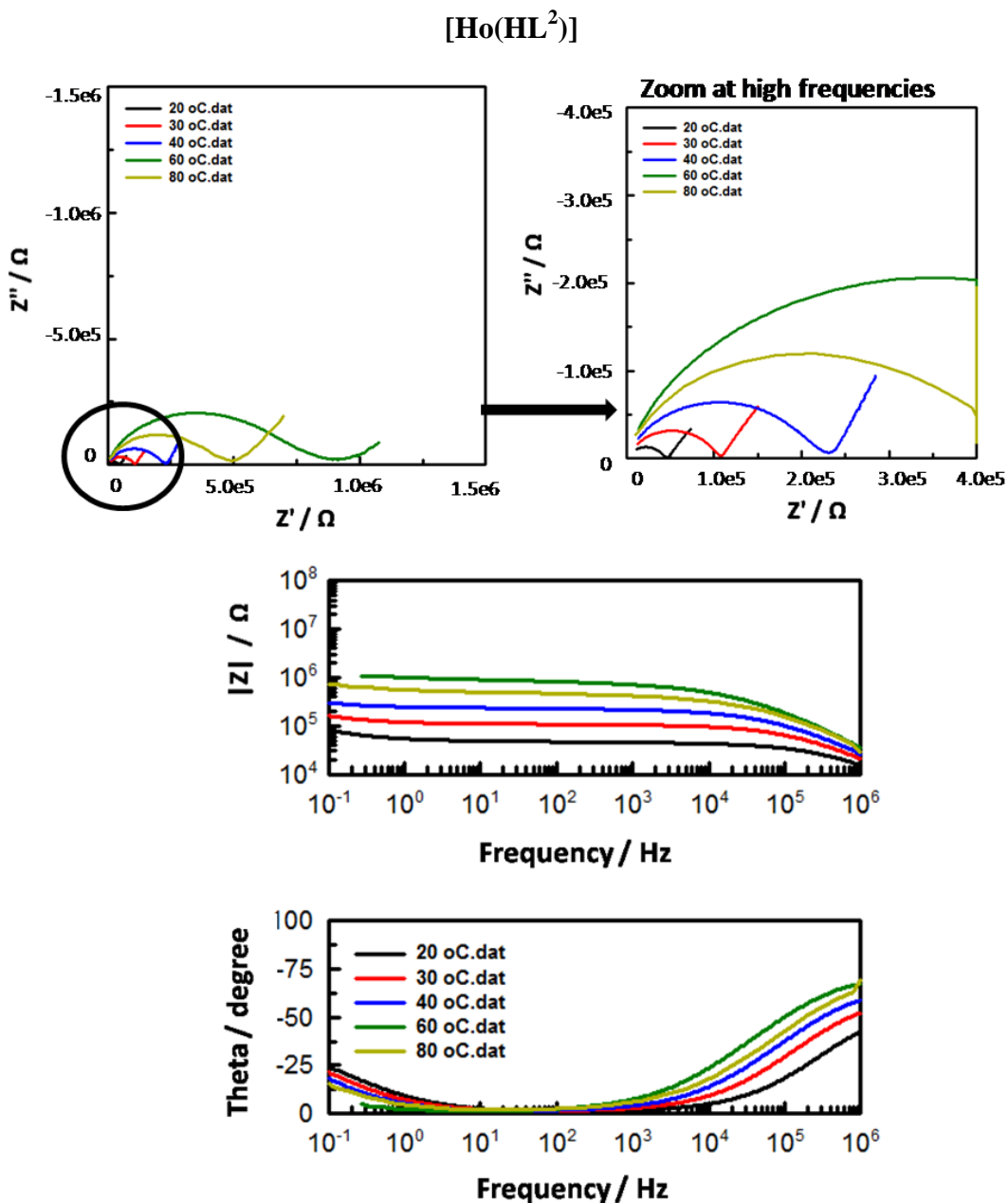


Figure 4.28. Nyquist and Bode plots for [Ho(HL²)] measured at different temperatures and 99 % RH.

Table 4.15. Proton conductivity (S cm⁻¹) for [Ho(HL²)] measured at different temperatures and 99 % RH.

[Ho(HL ²)]	σ at 20 °C	σ at 30 °C	σ at 40 °C	σ at 60 °C	σ at 80 °C
σ	$5.22(13) \times 10^{-6}$	$2.20(15) \times 10^{-6}$	$1.06(13) \times 10^{-6}$	$2.49(09) \times 10^{-7}$	$5.01(06) \times 10^{-7}$

In Table 4.16 are summarised the proton conductivity data measured for $[M(HL^2)]$ at different temperatures and 99 % RH. Between 20 °C and 60 °C the proton conductivity progressively decreases from 10^{-6} S cm⁻¹ to 10^{-7} - 10^{-8} S cm⁻¹ for all complexes. Decreasing of conductivity with increasing the temperature is a known trend for proton conduction assisted by water. However, it is interesting that a slight increase in proton conductivity was observed at 80 °C for each of the materials. Additional studies at higher temperatures are needed to investigate this trend further. However, due to technical issues based upon the design of the conductivity cell it was not possible to investigate the proton conductivity at higher temperatures.

Table 4.16. Summary of proton conductivity (S cm⁻¹) for $[M(HL^2)]$ measured at different temperatures and 99 % RH.

$[M(HL^2)]$	σ at 20 °C	σ at 30 °C	σ at 40 °C	σ at 60 °C	σ at 80 °C
La	$4.00(15) \times 10^{-6}$	$2.53(13) \times 10^{-6}$	$6.36(15) \times 10^{-7}$	$7.87(12) \times 10^{-8}$	$2.00(16) \times 10^{-7}$
Ce	$1.46(11) \times 10^{-6}$	$7.14(13) \times 10^{-7}$	$1.00(12) \times 10^{-7}$	$2.29(12) \times 10^{-8}$	$1.66(11) \times 10^{-7}$
Nd	$7.85(09) \times 10^{-6}$	$7.47(15) \times 10^{-6}$	$4.39(10) \times 10^{-6}$	$9.17(11) \times 10^{-7}$	$5.39(14) \times 10^{-6}$
Sm	$3.82(11) \times 10^{-6}$	$2.55(10) \times 10^{-6}$	$1.89(13) \times 10^{-6}$	$9.51(12) \times 10^{-6}$	$4.79(11) \times 10^{-6}$
Gd	$1.87(08) \times 10^{-6}$	$9.66(11) \times 10^{-6}$	$2.06(07) \times 10^{-7}$	$1.21(18) \times 10^{-8}$	$1.03(14) \times 10^{-7}$
Ho	$5.22(13) \times 10^{-6}$	$2.20(15) \times 10^{-6}$	$1.06(13) \times 10^{-6}$	$2.49(09) \times 10^{-7}$	$5.01(06) \times 10^{-7}$

Summary of proton conductivity for $[M(HL^2)]$:

All the complexes $[M(HL^2)]$ showed similar proton conductivity to each other. The proton conductivity of $[M(HL^2)]$ recorded at 20 °C and 99 % RH is about 10^{-6} S cm⁻¹ which is lower compared to many of the MOFs reported under hydrated conditions (Table 1.1). The low proton conductivity can be assigned to the proton channels not

being continuous in all directions. The protons are mainly confined along the metal chains and the presence of water molecules (deriving from 99 % RH environment) are needed for proton conduction along the framework. Two different approaches to improve the proton conduction property of these materials have been designed and described in Section 4.3.

4.3 Design of novel strategies to enhance proton conductivity of $[M(HL^2)]$

Two fundamental features lead to good proton conductivity in solid materials. First, the presence of free protons in the structure is essential and secondly, they need to be close to each other and arranged within a favourable proton-hopping pathway. With this in mind, the more protons that are present within a framework, the higher the proton conductivity is expected to be. Three different methods have been recently reported to design highly proton-conductive MOFs; these involve the introduction of proton carriers as counter ions (Type I), the functionalisation of the ligands with proton-rich functional groups (Type II) or the doping of MOF with neutral proton carrier guests (Type III) (Section 4.1).

In the following Sections the development of two novel strategies to improve the proton conductivity of a solid material are presented. Both approaches are based on synthesising frameworks with similar structure to that $[M(HL^2)]$ but with higher levels of protons. The first methodology aims to increase the number of protons in a fixed volume (Figure 4.29). This was accomplished with the use of benzene-1,4-diphosphonic acid, H_4L^3 , the shorter version of the H_4L^2 linker (Section 4.3.1). The second approach was to increase the concentration of protons by replacing 3+ metals with 2+ metals (Figure 4.30, Section 4.3.2). Both approaches together with the characterisation of the materials and their proton conductivity properties are described in detail below.

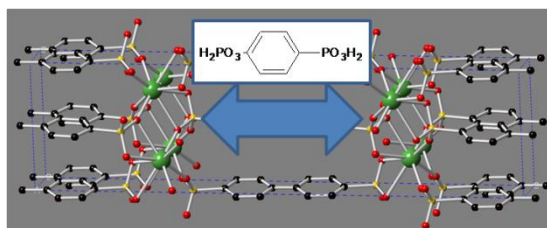


Figure 4.29. First strategy: increase the concentration of protons in a fixed volume.

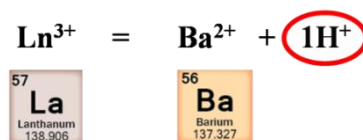


Figure 4.30. Second strategy: increase the concentration of protons by replacing 3+ metals with 2+ metals.

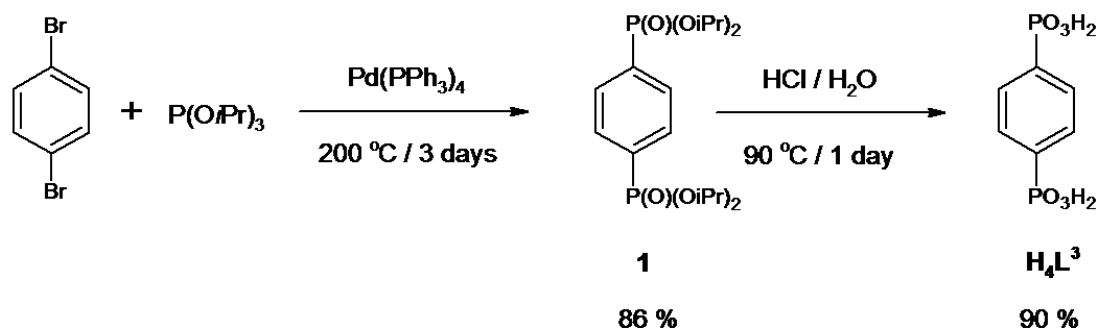
4.3.1 Increase the concentration of protons in a fixed volume

By decreasing the length of the organic linker it was argued that we might be able to increase the number of protons in a fixed volume of MOF without significant changes in the main framework. In order to investigate this effect on the proton conductivity properties, H_4L^3 was used to form a family of lanthanide materials $[\text{M}(\text{HL}^3)]$ similar to $[\text{M}(\text{HL}^2)]$. The main difference between the two MOF systems is the distance between the adjacent metal chains (where the free protons are located), responsible for the different number of protons in a given volume.

4.3.1.1 Synthesis of benzene-1,4-diphosphonic acid, H_4L^3 , and preparation of $[\text{M}(\text{HL}^3)]$

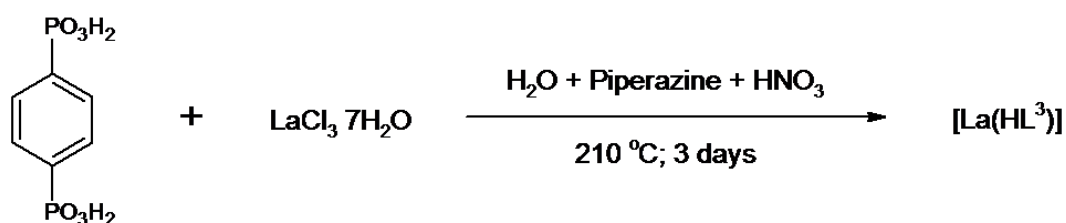
Benzene-1,4-diphosphonic acid, H_4L^3 , was synthesised using similar conditions as those described for H_4L^2 (Scheme 4.3). The $[\text{Pd}(\text{PPh}_3)_4]$ -catalysed Hirao reaction of 1,4-dibromophenyl with $\text{P}(i\text{-PrO})_3$ was carried out at 200 °C for 3 days to yield the

ligand precursor, **1**. Hydrolysis reaction of **1** in a solvent mixture of 1.5:1 HCl/H₂O for 1 day at 90°C afforded H₄L³ (yield 90 %).



Scheme 4.3. Synthetic route to H₄L³.

Solvothermal reactions of H₄L³ and lanthanide salts in a 1:1 ratio were carried out in H₂O in the presence of HNO₃ (2.6 M) and piperazine (0.3 M) at 210 °C for 3 days (Scheme 4.4). As for H₄L², a family of lanthanide MOFs [M(HL³)] (M = La, Ce, Nd, Sm, Gd, Ho) with empirical formula [M(HO₆P₂C₆H₅)]_∞ were synthesised with H₄L³. [M(HL³)] were synthesised as crystalline powders but no single crystals were grown.



Scheme 4.4. Synthesis of [La(HL³)].

The as-synthesised materials are insoluble in common organic solvents and were characterised by powder X-ray crystal diffraction, elemental analyses, thermogravimetric analyses, IR, solid-state UV-visible and impedance spectroscopy.

4.3.1.2 Structural characterisation of $[M(HL^3)]$

High resolution PXRD patterns for $[M(HL^3)]$ were collected at Diamond Light Source, Beamline I11 and their structures were solved using *ab initio* methods (Figure 4.31). The connectivity of the metal and ligand in the framework is the same as $[M(HL^2)]$ compounds (Section 4.2.4) (Figure 4.32). Structural details for each $[M(HL^3)]$ are reported in Table 4.17 and Table 4.18.

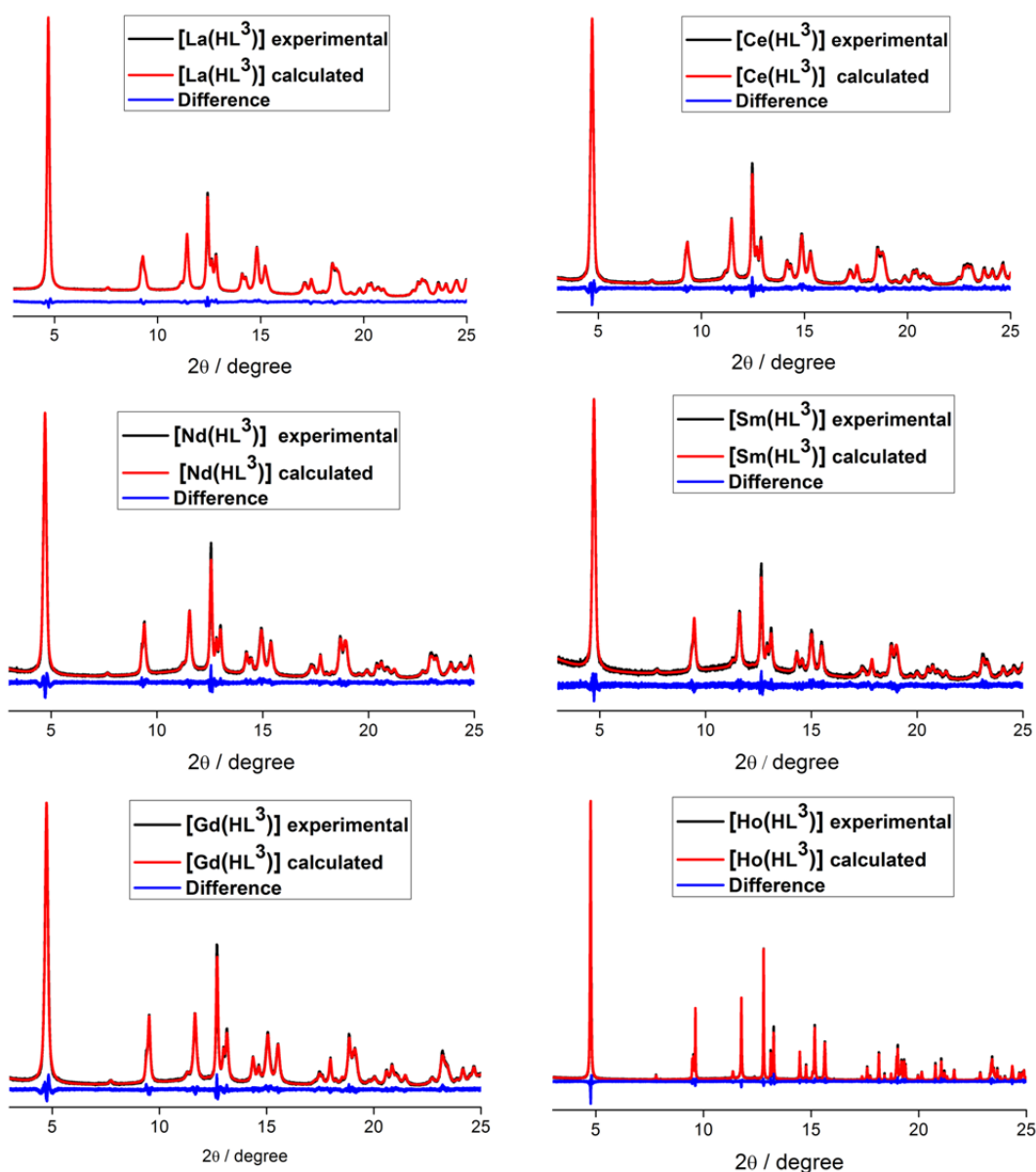


Figure 4.31. Observed (*red*) and calculated (*blue*) profiles for the Rietveld refinements of the complexes $[M(HL^3)]$ (M = La, Ce, Nd, Sm, Gd, Ho).

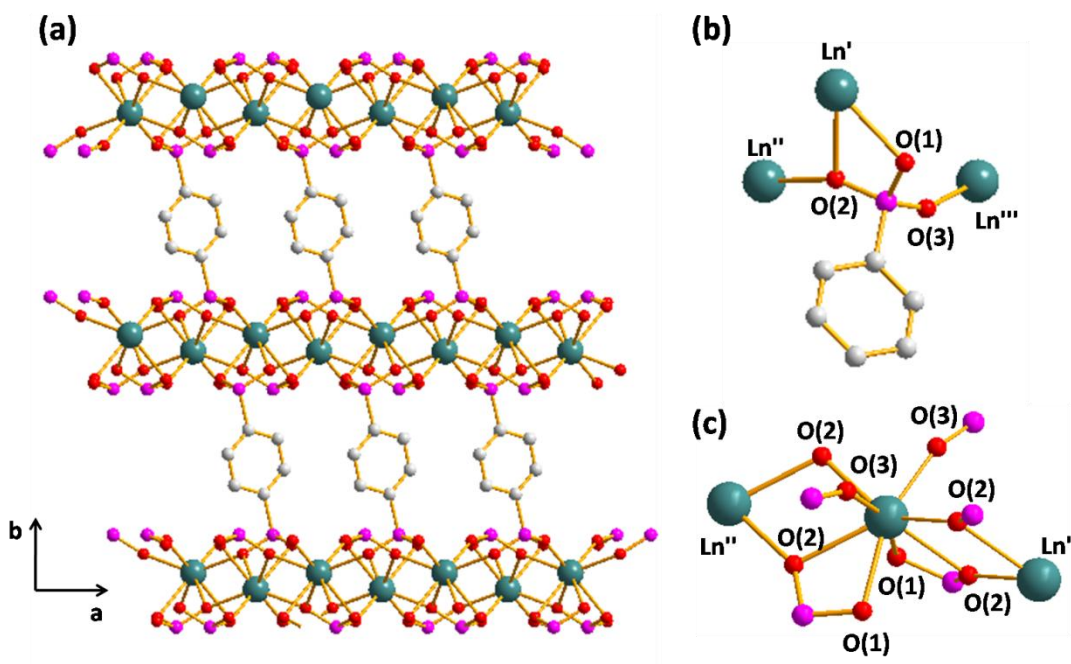


Figure 4.32. Refined structure of $[M(HL^3)]$ MOFs derived from PXRD data. (a) Projection of the structure along the c -axis. (b) Coordination nodes of the phosphonate group from the ligand. (c) Perspective view of the coordination environment at Ln(III) centres.

Table 4.17. Crystallographic data for [M(HL³)] (M = La, Ce, Nd).

[M(HL ³)]	La	Ce	Nd
Empirical formula	C ₆ H ₅ P ₂ O ₆ La	C ₆ H ₅ P ₂ O ₆ Ce	C ₆ H ₅ P ₂ O ₆ Nd
Formula weight (g mol⁻¹)	373.95	375.17	279.29
R_{Shannon}/Å	1.160	1.143	1.109
Crystal system	Monoclinic	Monoclinic	Monoclinic
Space group	C2/c	C2/c	C2/c
a (Å)	5.63224(11)	5.60974(9)	5.56742(8)
b (Å)	20.1936(4)	20.1193(3)	20.0812(4)
c (Å)	8.40071(15)	8.35146(12)	8.26948(11)
β (°)	108.6557(8)	108.6302(7)	108.4976(7)
γ (°)	90	90	90
Cell volume (Å³)	905.25(3)	893.19(2)	876.77(2)
R_{wp}	2.64	5.23	5.42
GoF	1.57	1.50	1.50
Ln-Ln	4.3005(2)	4.2779(1)	4.2407(1)
Ln'-O(1)	2.6045(63)	2.5920(62)	2.5508(69)
Ln'-O(2)	2.6923(76)	2.6854(75)	2.6635(81)
Ln-O''(2)	2.5152(62)	2.4885(46)	2.3724(90)
Ln'''-O(3)	2.3800(84)	2.3955(84)	2.4471(50)

Table 4.18. Crystallographic data for [M(HL³)] (M = Sm, Gd, Ho).

[M(HL ³)]	Sm	Gd	Ho
Empirical formula	C ₆ H ₅ P ₂ O ₆ Sm	C ₆ H ₅ P ₂ O ₆ Gd	C ₆ H ₅ P ₂ O ₆ Ho
Formula weight (g mol⁻¹)	385.45	392.30	399.98
R_{Shannon}/Å	1.079	1.053	1.015
Crystal system	Monoclinic	Monoclinic	Monoclinic
Space group	C2/c	C2/c	C2/c
a (Å)	5.53357(13)	5.49730(6)	5.442226(14)
b (Å)	20.0089(6)	19.9857(3)	19.89009(7)
c (Å)	8.20134(18)	8.15652(9)	8.08209(2)
β (°)	108.4567(11)	108.2964(6)	108.17228(16)
γ (°)	90	90	90
Cell volume (Å³)	861.35(4)	850.831(19)	831.222(4)
R_{wp}	6.95	5.26	7.84
GoF	1.35	1.55	1.70
Ln-Ln	4.2093(2)	4.1921(1)	4.1585(1)
Ln'-O(1)	2.5358(125)	2.4769(64)	2.3256(43)
Ln'-O(2)	2.6722(118)	2.6322(74)	2.6302(74)
Ln-O''(2)	2.2275(119)	2.3111(79)	2.2512(76)
Ln'''-O(3)	2.3647(71)	2.4263(45)	2.3256(43)

4.3.1.3 Thermal stability of $[M(HL^3)]$

TGA data for $[M(HL^3)]$ MOFs were collected between 25 °C and 1000 °C with heating rate of 5 °C per minute under a flow of air (Figure 4.33). All the $[M(HL^3)]$ materials have similar thermal behaviour to each other and high thermal stability up to 550 °C. The slightly higher thermal stability (by about 50 °C) of $[M(HL^3)]$ compared with $[M(HL^2)]$ is probably due to the more compact structure of $[M(HL^3)]$ due to the use of a shorter ligand. The weight loss of about 20 % corresponds to the loss of the organic ligand while the residual 80 % of the material was assigned to the formation of metal phosphonate salts in the same way as for $[M(HL^2)]$. Table 4.19 shows detailed calculations for each complex. In most of the thermogravimetric curves the plateau at high temperature is not well defined; however for technical reasons it was not possible to extend the temperature range over 1000 °C.

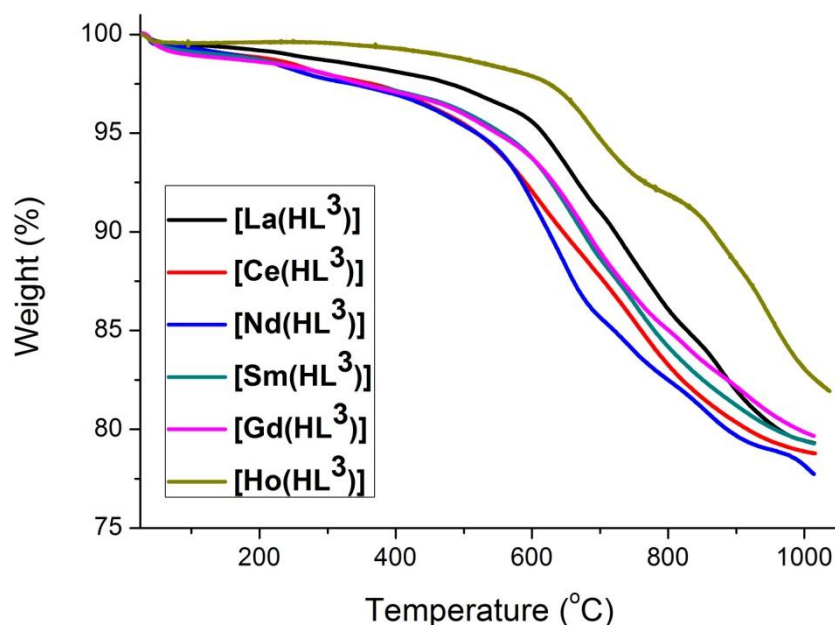


Figure 4.33. Thermogravimetric profiles of $[M(HL^3)]$ recorded under a flow of air at a heating rate of 5 °C min⁻¹.

Table 4.19. Analysis of the experimental TGA data for [M(HL³)].

[M(HL ³)]	Weight % organic moieties (C ₆ H ₄)	Weight % metal phosphonate salts (P ₂ O ₆ LnH)
La	20.65	79.35
Ce	21.2	78.80
Nd	22.26	77.74
Sm	20.72	79.28
Gd	20.33	79.67
Ho	18.09	81.91

4.3.1.4 IR and Solid-state UV-visible absorption spectroscopies of [M(HL³)]

Infrared spectroscopy:

Infrared analysis for [M(HL³)] show very similar vibration and stretching bands compared with [M(HL²)]. The IR spectra of [M(HL³)] were recorded between 4000 cm⁻¹ to 550 cm⁻¹ and the peaks were assigned according to the literature.¹¹⁻¹³ Figure 4.34 shows the infrared spectrum of [Gd(HL³)]. The bands at 1134 cm⁻¹ and 1063 cm⁻¹ are characteristic of the stretching vibration of the phosphonate P-O group. The bands centred at 1736 cm⁻¹ and 977 cm⁻¹ correspond to the stretching vibration $\nu(\text{P}=\text{O})$ and $\nu(\text{P}-\text{C})$ respectively. The signals at 1387 cm⁻¹ and 663 cm⁻¹ arise from the C-C stretching vibrations. The band at 839 cm⁻¹ is attributed to the C-H out-of-plane vibrations for para-disubstituted phenylene rings. The broad signal at 3370 cm⁻¹ is assigned to the O-H stretching vibrations of the protonated phosphonate oxygens (P-OH).

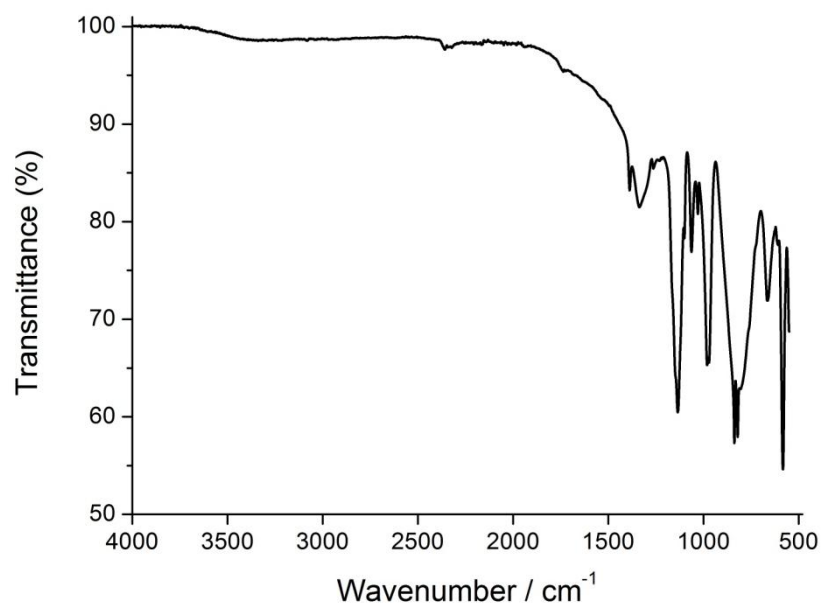


Figure 4.34. ATR infrared spectrum of $[\text{Gd}(\text{HL}^3)]$.

Solid-state UV-Visible absorption spectroscopy:

Absorption spectra in the UV-visible region (300 nm to 800 nm) were collected for $[\text{M}(\text{HL}^3)]$ as powders (Figure 4.35 and Figure 4.36). Spectra of metal salts of the analogous Ln(III) ions were recorded as standards and the absorption transitions were assigned accordingly with the literature as discussed in Section 4.2.7.¹⁴⁻¹⁷

The absence of bands in the UV-visible absorption spectra of those samples containing lanthanum, cerium and gadolinium as metal ions is due to the big energy gap between the ground level and the first excited state which therefore puts the first transition in the ultraviolet region above 200 nm (Figure 4.35).¹⁵

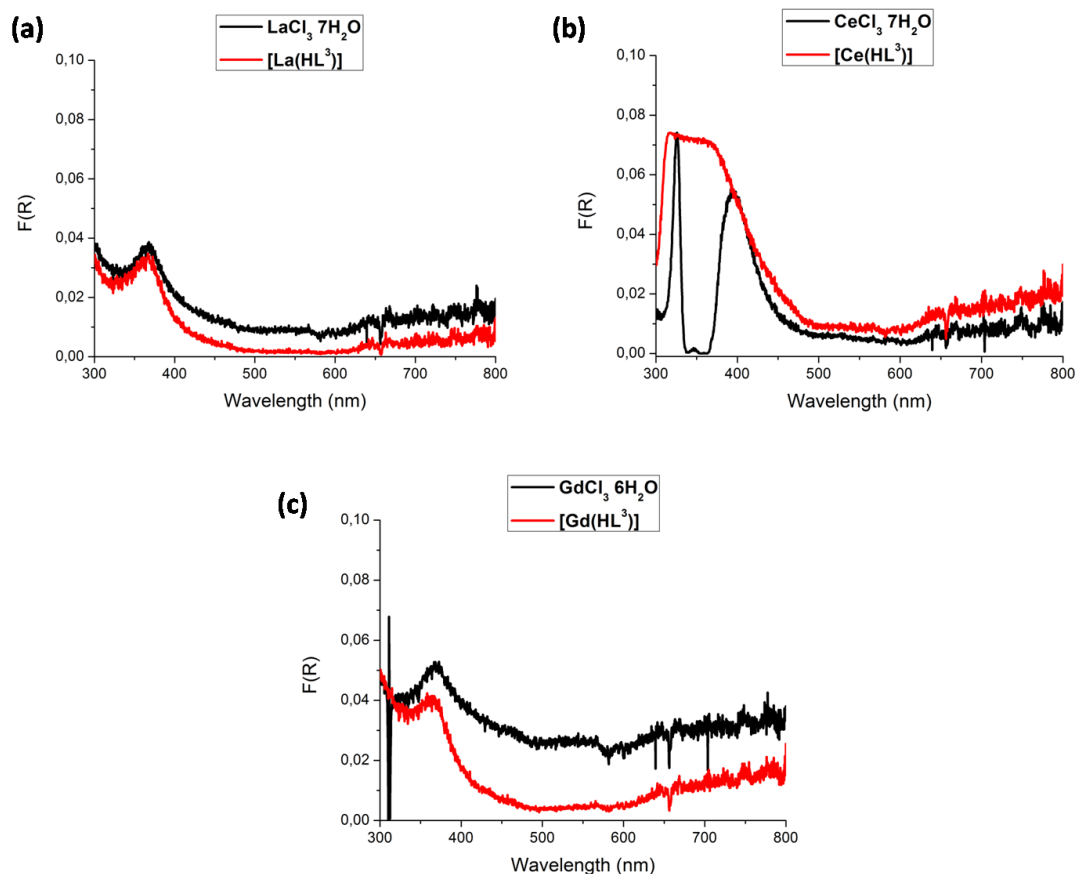


Figure 4.35. Absorbance spectra of (a) $[\text{La}(\text{HL}^3)]$ (red), $\text{LaCl}_3 \cdot 7\text{H}_2\text{O}$ (black). (b) $[\text{Ce}(\text{HL}^3)]$ (red), $\text{CeCl}_3 \cdot 7\text{H}_2\text{O}$ (black). (c) $[\text{Gd}(\text{HL}^3)]$ (red), $\text{GdCl}_3 \cdot 6\text{H}_2\text{O}$ (black).

In the absorption spectra of $[\text{Nd}(\text{HL}^3)]$, $[\text{Sm}(\text{HL}^3)]$ and $[\text{Ho}(\text{HL}^3)]$ and the corresponding inorganic salts, a significant number of bands were observed. The absorption spectra are shown in Figure 4.36 together with the attribution of the characteristic transitions of the lanthanide metals, previously discussed in Section 4.2.7.

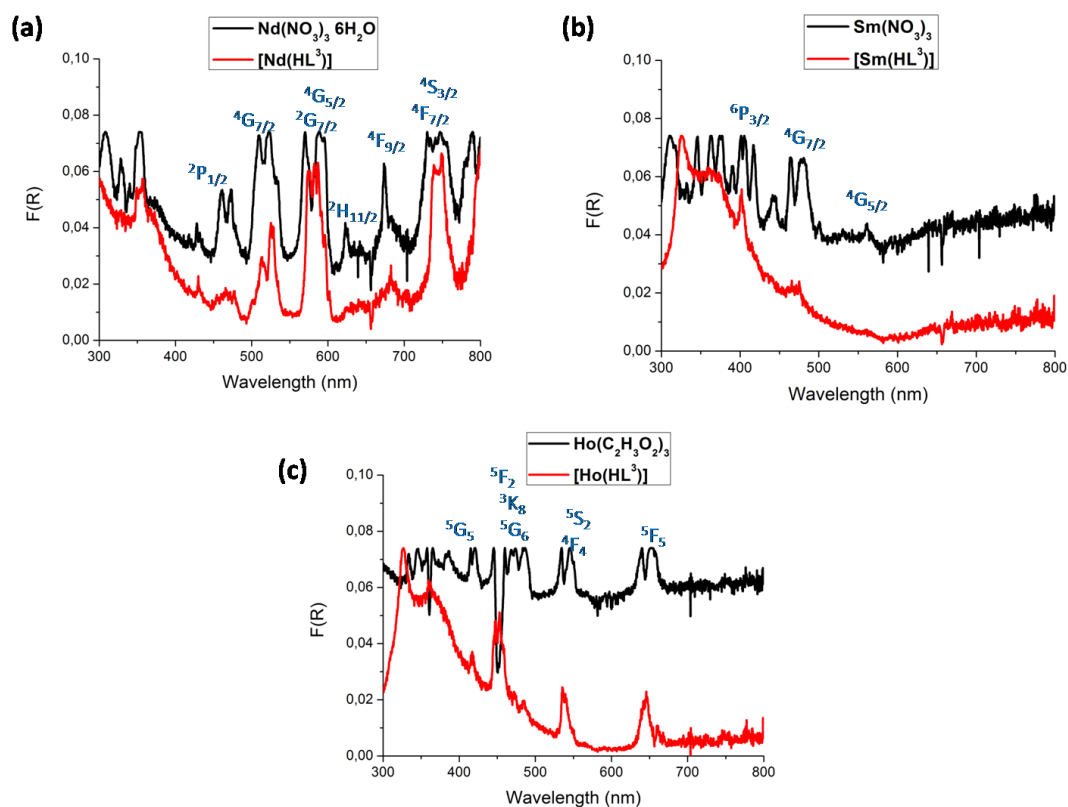


Figure 4.36. Absorbance spectra of (a) $[\text{Nd}(\text{HL}^3)]$ (red), $\text{Nd}(\text{NO}_3)_3 \cdot 6\text{H}_2\text{O}$ (black). (b) $[\text{Sm}(\text{HL}^3)]$ (red), $\text{Sm}(\text{NO}_3)_3 \cdot 6\text{H}_2\text{O}$ (black). (c) $[\text{Ho}(\text{HL}^3)]$ (red), $\text{Ho}(\text{CH}_3\text{CO}_2)_3 \cdot 6\text{H}_2\text{O}$ (black).

4.3.1.5 Proton conductivity study of $[\text{M}(\text{HL}^3)]$

The proton conductivities of $[\text{M}(\text{HL}^3)]$ were studied by AC impedance spectroscopy on compact pellets using cell B (Section 2.2.3.2). The samples were methodically prepared using the same procedure described in Section 4.2.8 and the measurements were repeated at the same experimental conditions investigated for $[\text{M}(\text{HL}^2)]$. This allows a direct comparison between the proton conductivities of the two families of materials at different % RH and temperatures. The effect on the proton conductivity of using a shorter organic ligand to increase the concentration of protons in a fix volume by decreasing the distance between the metal chains was investigated and herein discussed.

For each MOF about 0.120 g of sample was ground into a fine powder using mortar and pestle and pressed for 5 minutes under a pressure of 5 tons using a die with 0.8 cm diameter. A silver paste was applied to either side of the samples to serve as electrodes. The thickness and the diameter of the pellet were measured and used to calculate the proton conductivities of $[M(HL^3)]$ (Section 2.1.6, Equation 10). For each sample measurements were repeated on two different batches; for each batch three measurements were collected at each temperature and relative humidity investigated. The data collected was used to calculate the mean value of the proton conductivity correspondent to the experimental conditions under study, together with the associated standard deviation.

Proton conductivity at different relative humidities:

Impedance measurements on $[M(HL^3)]$ were recorded at different % RH to investigate any relationship between their proton conductivity properties and the relative humidity. Measurements were collected between 99 % and 45 % at 20 °C. The dry pellet coated with silver paste was loaded inside the cell and exposed to 99 % RH humidity overnight to allow the compressed sample to equilibrate. After equilibration, three impedance measurements were recorded to ensure stable resistivity of the sample and reproducibility of the measurements. The % RH was then progressively decreased at 70 % and 45 % by regulating the flow of wet and dry gas inside the cell. For each % RH, measurements were collected every 45 minutes until the resistivity of the sample was stable over a period of 2 h suggesting the equilibration point had been reached.

Nyquist and Bode plots for each complex collected at 99 %, 70 % and 45 % RH at 20 °C are shown in Figures 4.37-4.42 together with the corresponding proton

conductivity data (Tables 4.20-4.25). The Bode plots give information about the frequency range investigated, which doesn't appear in the Nyquist plot. In addition, they show how the absolute resistance and phase shift (Section 2.1.4) change as a function of the applied frequency. More enlightening information about the conduction process are given by the Nyquist plots. Nyquist plots of $[M(HL^3)]$ show a semi-circle in the high frequency region (which represents the bulk resistivity) and a tail at low frequencies characteristic of ionic conductivity. The Nyquist plots of $[M(HL^3)]$ at low humidity show a well defined semi-circle in the high frequency region and the proton conductivity was calculated by its fitting. At higher humidities, due to the remarkable increasing of conductivity, the semi-circle plot cannot be fitted as it is not well defined in the frequency range investigated. To obtain a complete semi-circle plot in these cases it is necessary to measure the impedance at higher frequency (> 1 MHz) which however cannot be accurately investigated with the impedance analyser used to perform the measurements. In those cases the proton conductivity was calculated using the intercept with the real axis.

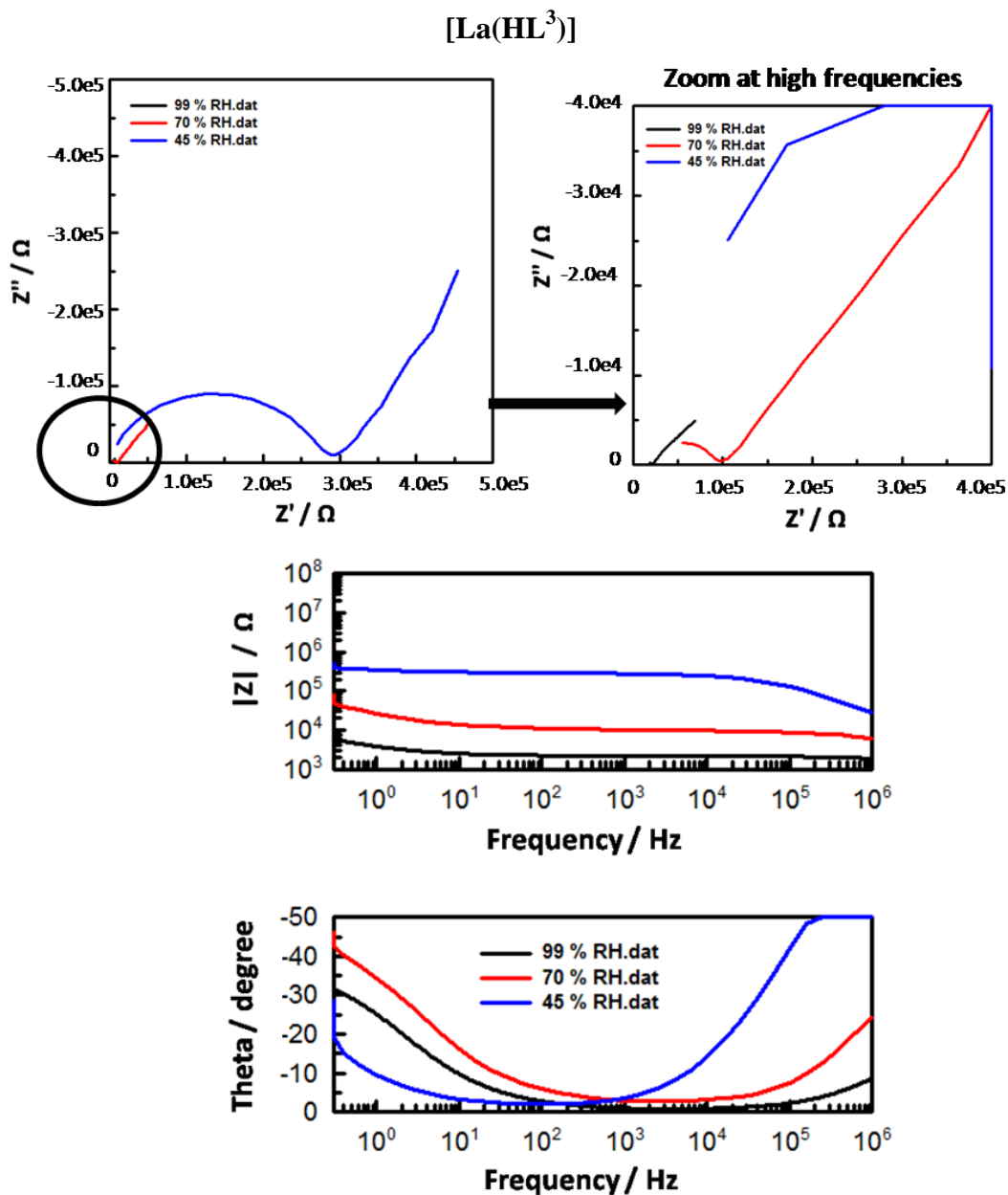


Figure 4.37. Nyquist and Bode plots for [La(HL³)] measured at different % RH and 20 °C.

Table 4.20. Proton conductivity (S cm⁻¹) for [La(HL³)] measured at different % RH and 20 °C.

[La(HL ³)]	σ at 99 % RH	σ at 70 % RH	σ at 45 % RH
σ	$1.00(12) \times 10^{-4}$	$2.14(14) \times 10^{-5}$	$7.37(10) \times 10^{-7}$

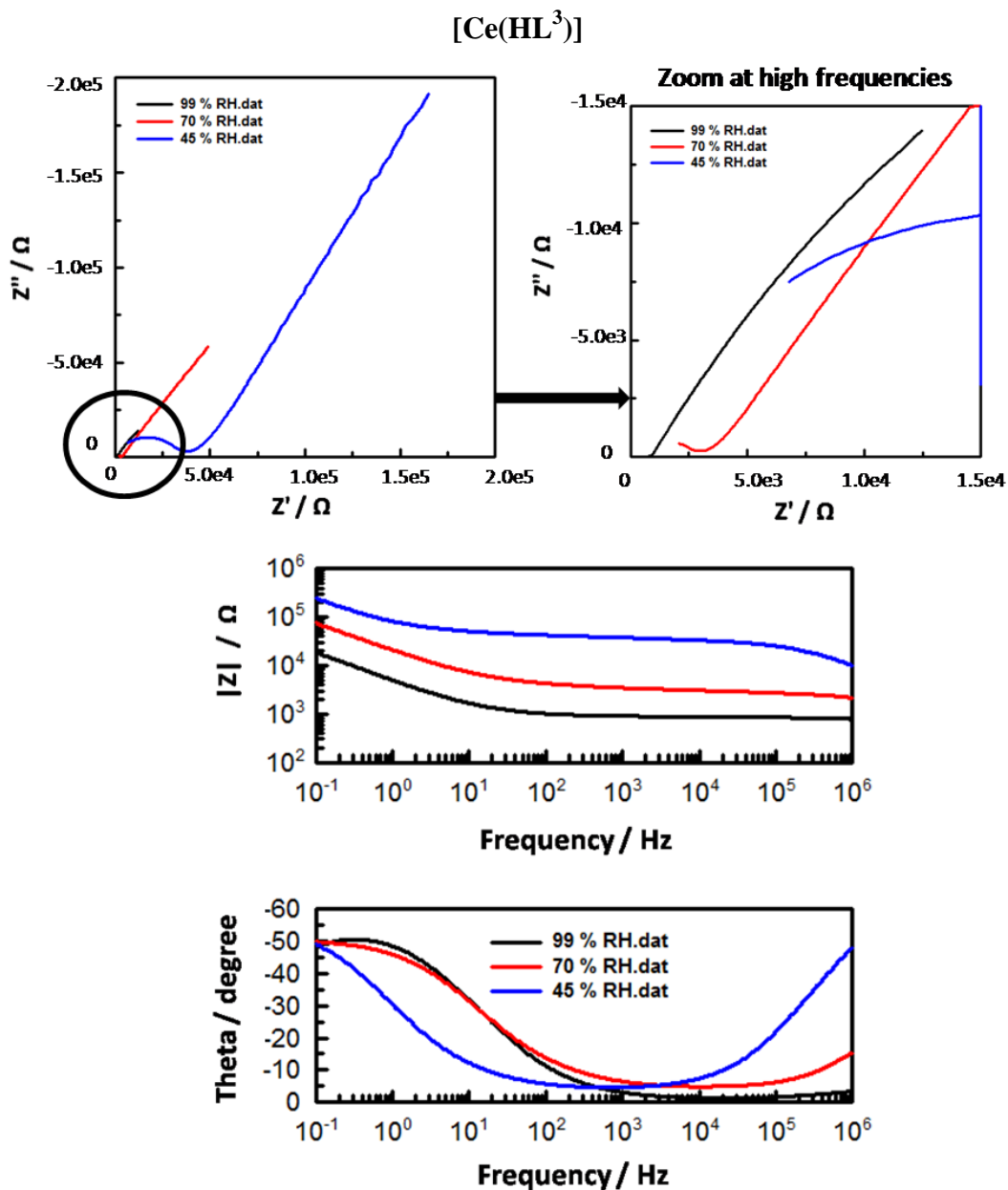


Figure 4.38. Nyquist and Bode plots for [Ce(HL³)] measured at different % RH and 20 °C.

Table 4.21. Proton conductivity (S cm⁻¹) for [Ce(HL³)] measured at different % RH and 20 °C.

[Ce(HL ³)]	σ at 99 % RH	σ at 70 % RH	σ at 45 % RH
σ	$1.62(10) \times 10^{-4}$	$4.74(11) \times 10^{-5}$	$3.84(15) \times 10^{-6}$

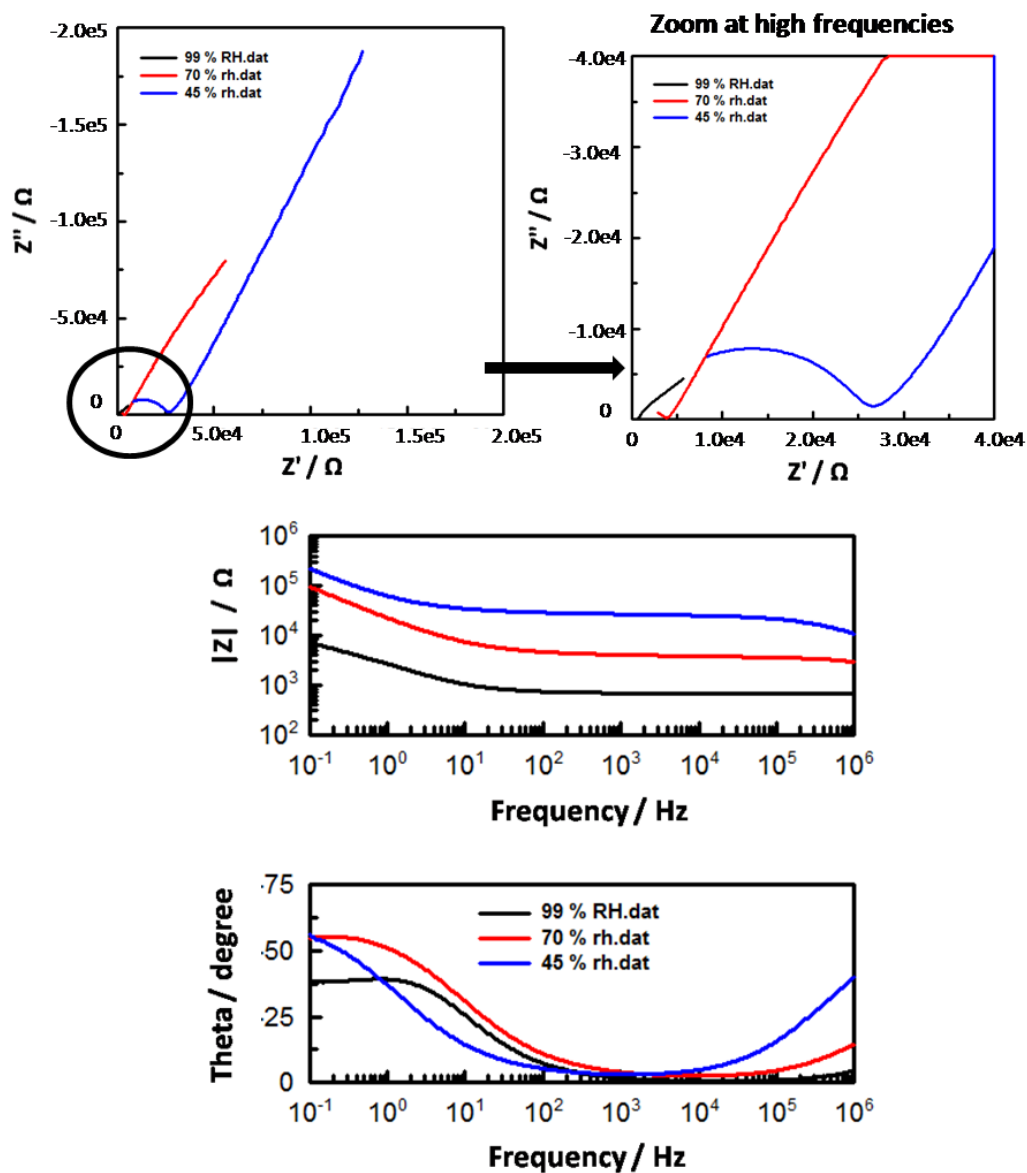


Figure 4.39. Nyquist and Bode plots for [Nd(HL³)] measured at different % RH and 20 °C.

Table 4.22. Proton conductivity (S cm⁻¹) for [Nd(HL³)] measured at different % RH and 20 °C.

[Nd(HL ³)]	σ at 99 % RH	σ at 70 % RH	σ at 45 % RH
σ	$2.91(13) \times 10^{-4}$	$5.08(08) \times 10^{-5}$	$7.15(11) \times 10^{-6}$

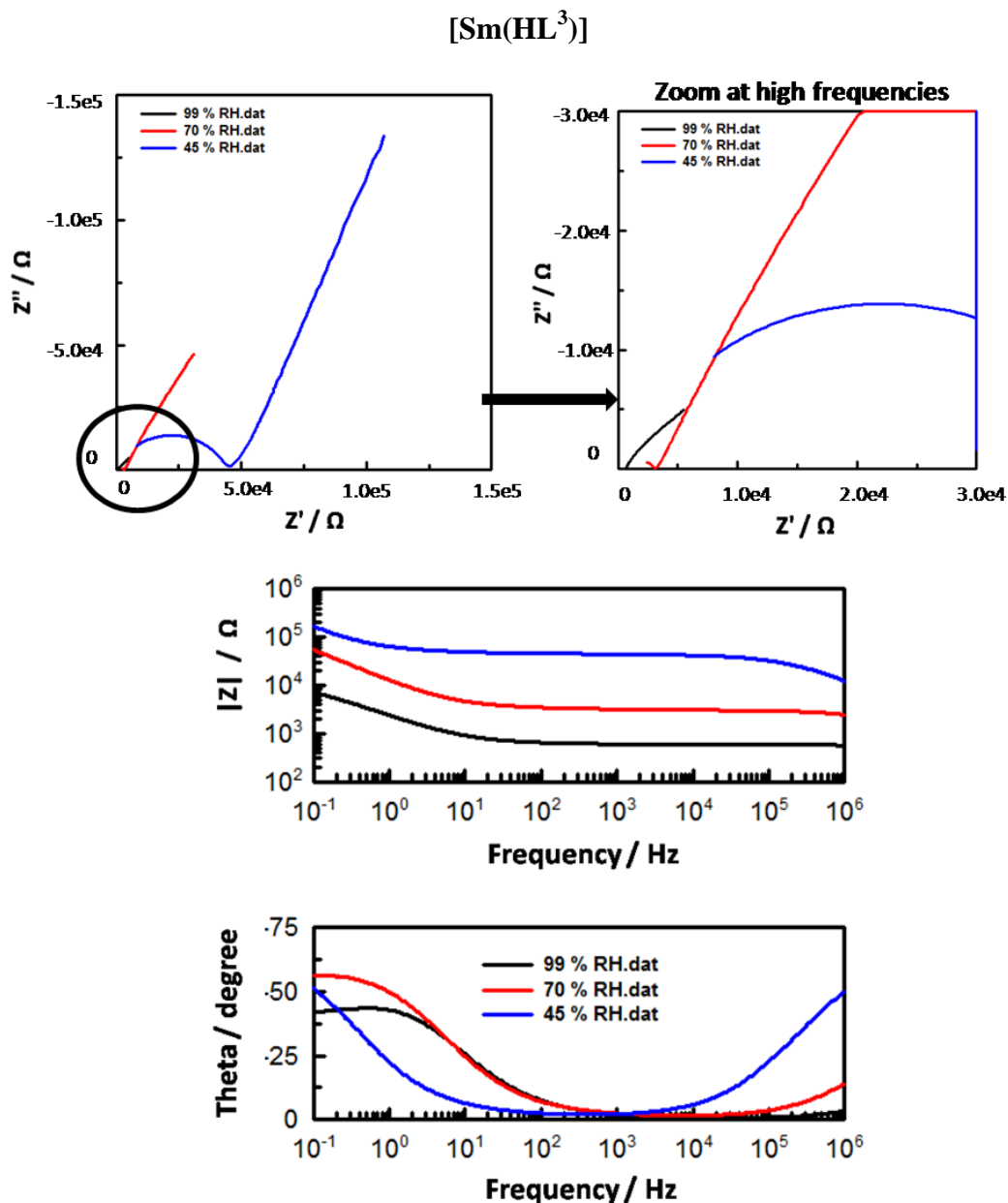


Figure 4.40. Nyquist and Bode plots for [Sm(HL³)] measured at different % RH and 20 °C.

Table 4.23. Proton conductivity (S cm⁻¹) for [Sm(HL³)] measured at different % RH and 20 °C.

[Sm(HL ³)]	σ at 99 % RH	σ at 70 % RH	σ at 45 % RH
σ	$2.89(09) \times 10^{-4}$	$5.48(14) \times 10^{-5}$	$3.79(10) \times 10^{-6}$

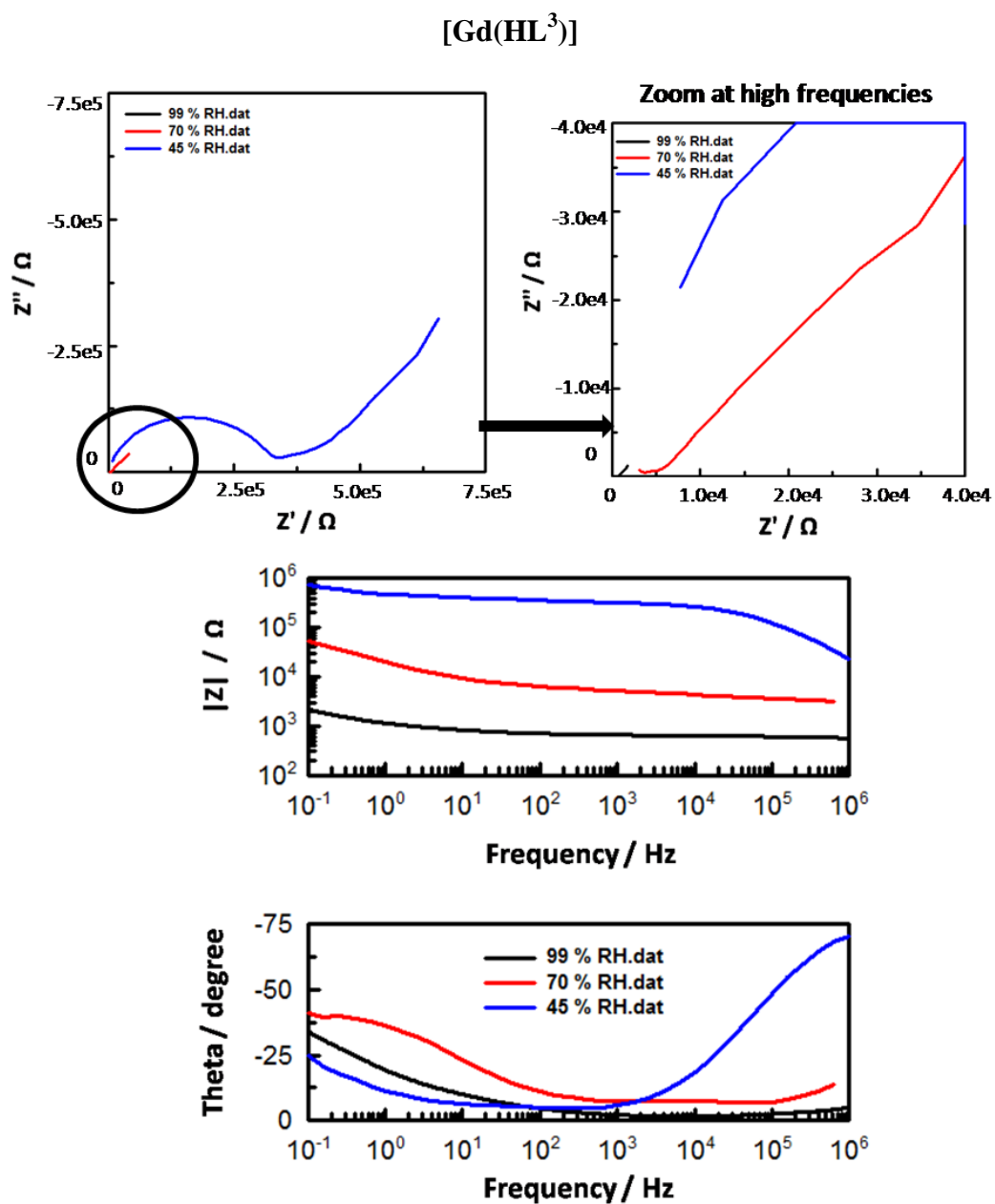


Figure 4.41. Nyquist and Bode plots for [Gd(HL³)] measured at different % RH and 20 °C.

Table 4.24. Proton conductivity (S cm⁻¹) for [Gd(HL³)] measured at different % RH and 20 °C.

[Gd(HL ³)]	σ at 99 % RH	σ at 70 % RH	σ at 45 % RH
σ	$2.97(06) \times 10^{-4}$	$4.64(09) \times 10^{-5}$	$5.56(11) \times 10^{-6}$

[Ho(HL³)]

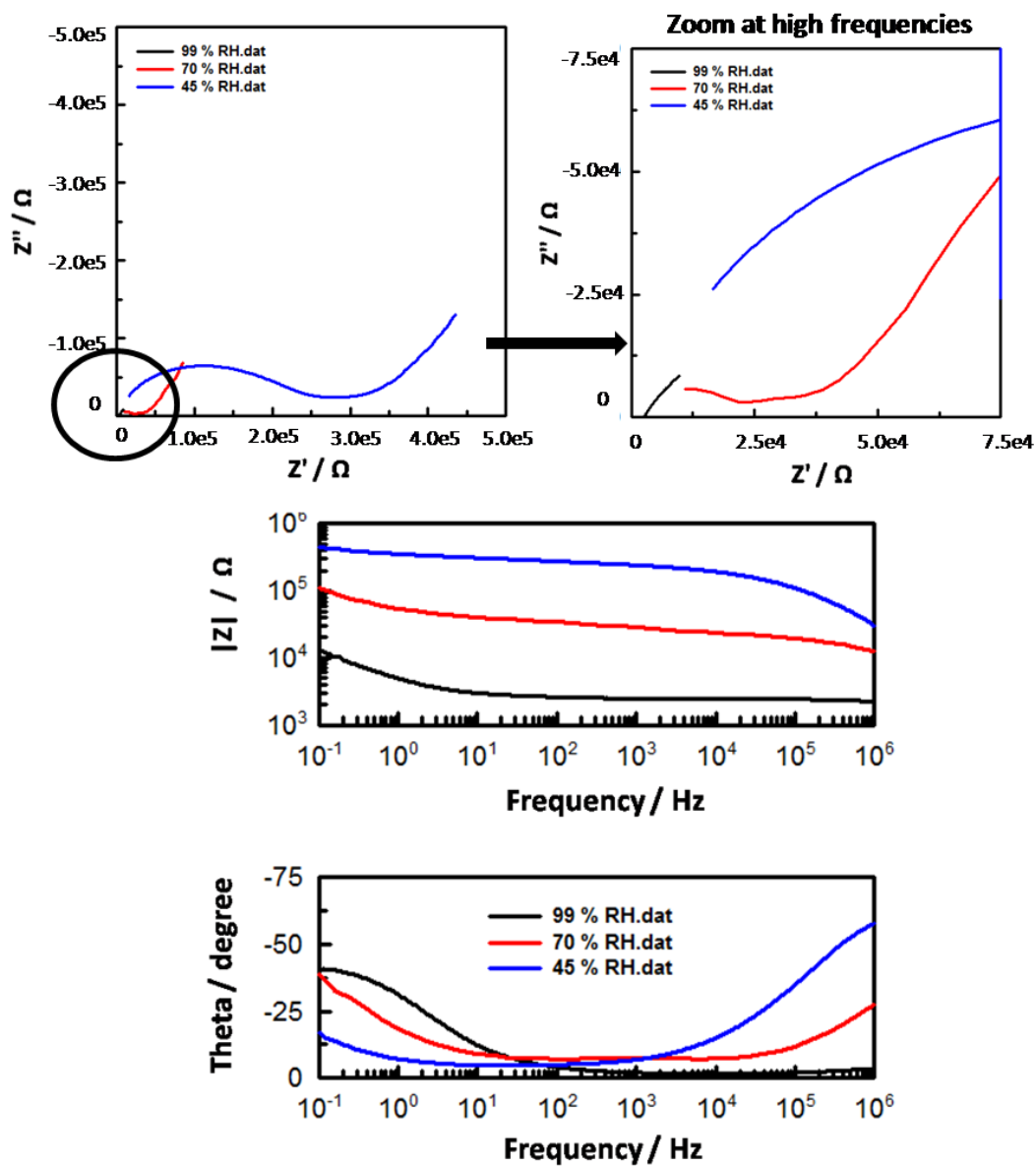


Figure 4.42. Nyquist and Bode plots for [Ho(HL³)] measured at different % RH and 20 °C.

Table 4.25. Proton conductivity (S cm⁻¹) for [Ho(HL³)] measured at different % RH and 20 °C.

[Ho(HL ³)]	σ at 99 % RH	σ at 70 % RH	σ at 45 % RH
σ	$2.51(05) \times 10^{-4}$	$7.72(11) \times 10^{-6}$	$7.11(13) \times 10^{-7}$

Proton conductivity measurements for each $[M(HL^3)]$ collected at 99 %, 70 % and 45 % RH at 20 °C are summarised in Table 4.26. As for $[M(HL^2)]$, the maximum conductivity was recorded at 99 % RH followed by a progressive decrease of conductivity with decreasing the humidity inside the conductivity cell. Comparing the results obtained for each $[M(HL^3)]$, the proton conductivity is constant as expected being all materials similar. Most relevant is the comparison between the proton conductivity of $[M(HL^2)]$ and $[M(HL^3)]$ at 99 % RH and 20 °C which goes from $10^{-6} \text{ S cm}^{-1}$ to $10^{-4} \text{ S cm}^{-1}$ with a remarkable increase of two orders of magnitude in the case of $[M(HL^3)]$ (Table 4.27). The increase in proton conductivity was observed for each member of $[M(HL^3)]$ and confirms the success of the strategy; increasing the number of the protons in a fixed volume by reducing the distance between the metal chains (where the free protons are located in the framework) positively impacts on the proton conducting property of a material. For the first time the proton conductivity of MOFs was significantly improved by decreasing the length of the ligand without inserting additional functional groups or proton carrier guests.

Table 4.26. Summary of proton conductivity ($S\text{ cm}^{-1}$) for $[M(\text{HL}^3)]$ measured at different % RH and 20 °C.

$[M(\text{HL}^3)]$	σ at 99 % RH	σ at 70 % RH	σ at 45 % RH
La	$1.00(12) \times 10^{-4}$	$2.14(14) \times 10^{-5}$	$7.37(10) \times 10^{-7}$
Ce	$1.62(10) \times 10^{-4}$	$4.74(11) \times 10^{-5}$	$3.84(15) \times 10^{-6}$
Nd	$2.91(13) \times 10^{-4}$	$5.08(08) \times 10^{-5}$	$7.15(11) \times 10^{-6}$
Sm	$2.89(09) \times 10^{-4}$	$5.48(14) \times 10^{-5}$	$3.79(10) \times 10^{-6}$
Gd	$2.97(06) \times 10^{-4}$	$4.64(09) \times 10^{-5}$	$5.56(11) \times 10^{-6}$
Ho	$2.51(05) \times 10^{-4}$	$7.72(11) \times 10^{-6}$	$7.11(13) \times 10^{-7}$

Table 4.27. Comparison of proton conductivities for $[M(\text{HL}^2)]$ and $[M(\text{HL}^3)]$.

Proton conductivity ($S\text{ cm}^{-1}$) at 99 % RH and 20 °C			
$[\text{La}(\text{HL}^2)]$	$4.00(15) \times 10^{-6}$	$[\text{La}(\text{HL}^3)]$	$1.00(12) \times 10^{-4}$
$[\text{Ce}(\text{HL}^2)]$	$1.46(11) \times 10^{-6}$	$[\text{Ce}(\text{HL}^3)]$	$1.62(10) \times 10^{-4}$
$[\text{Nd}(\text{HL}^2)]$	$7.85(09) \times 10^{-6}$	$[\text{Nd}(\text{HL}^3)]$	$2.91(13) \times 10^{-4}$
$[\text{Sm}(\text{HL}^2)]$	$3.83(11) \times 10^{-6}$	$[\text{Sm}(\text{HL}^3)]$	$2.89(09) \times 10^{-4}$
$[\text{Gd}(\text{HL}^2)]$	$1.87(08) \times 10^{-6}$	$[\text{Gd}(\text{HL}^3)]$	$2.97(06) \times 10^{-4}$
$[\text{Ho}(\text{HL}^2)]$	$5.22(13) \times 10^{-6}$	$[\text{Ho}(\text{HL}^3)]$	$2.51(05) \times 10^{-4}$

Proton conductivity at different temperatures:

The proton conductivity of $[M(\text{HL}^3)]$ at different temperatures was investigated in the range between 20 °C and 80 °C at 99 % RH (Figures 4.43-4.48, Tables 4.28-4.33). As with $[M(\text{HL}^2)]$, the samples were equilibrated for 2 h at each chosen temperature. Once the equilibration point was reached three measurements were collected to ensure the conductivity was stable and the measurement reproducible.

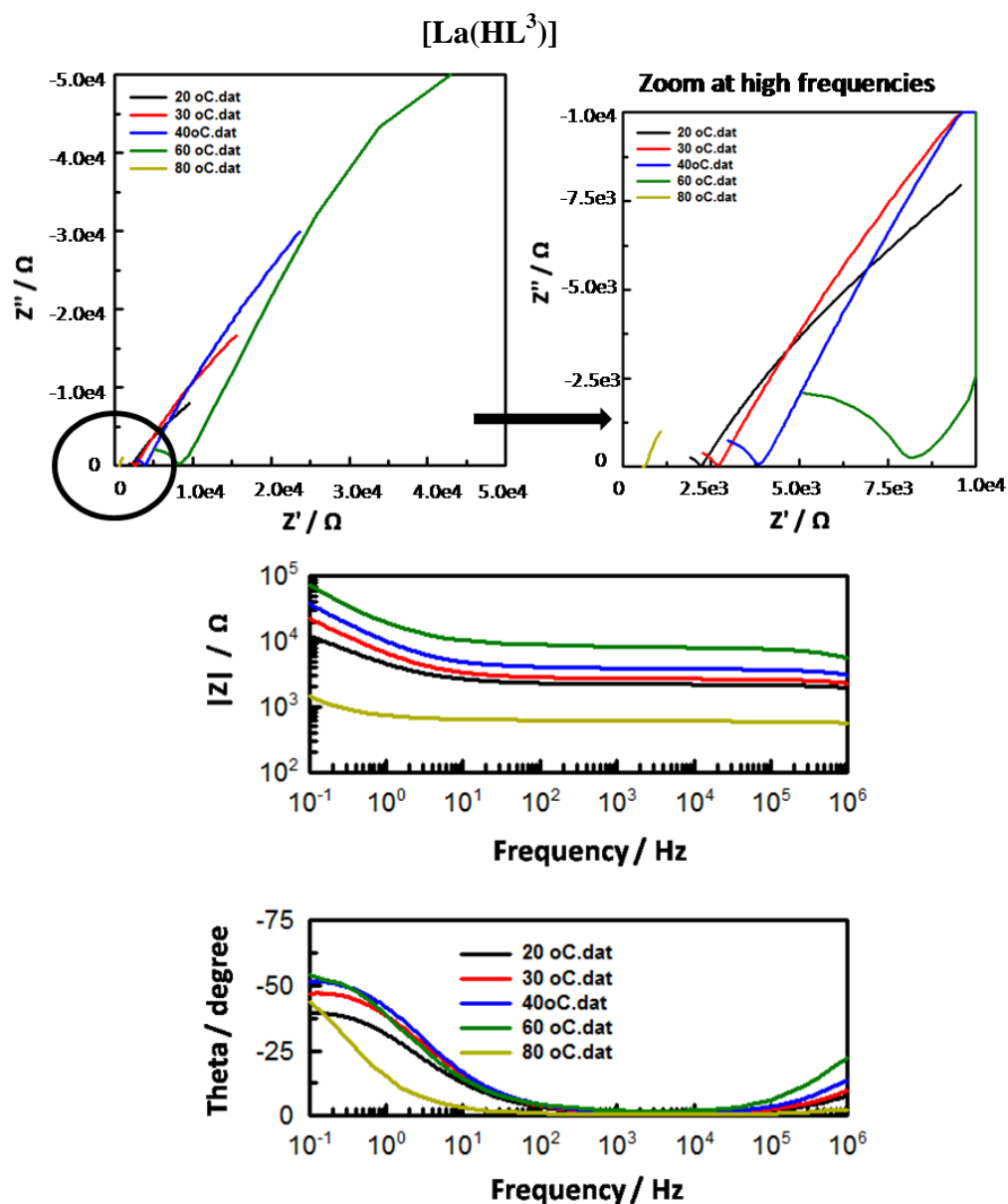


Figure 4.43. Nyquist and Bode plots for [La(HL³)] measured at different temperatures and 99 % RH.

Table 4.28. Proton conductivity (S cm⁻¹) for [La(HL³)] measured at different temperatures and 99 % RH.

[La(HL ³)]	σ at 20 °C	σ at 30 °C	σ at 40 °C	σ at 60 °C	σ at 80 °C
σ	$1.00(12) \times 10^{-4}$	$8.02(08) \times 10^{-5}$	$7.42(10) \times 10^{-5}$	$2.76(15) \times 10^{-5}$	$3.53(13) \times 10^{-4}$

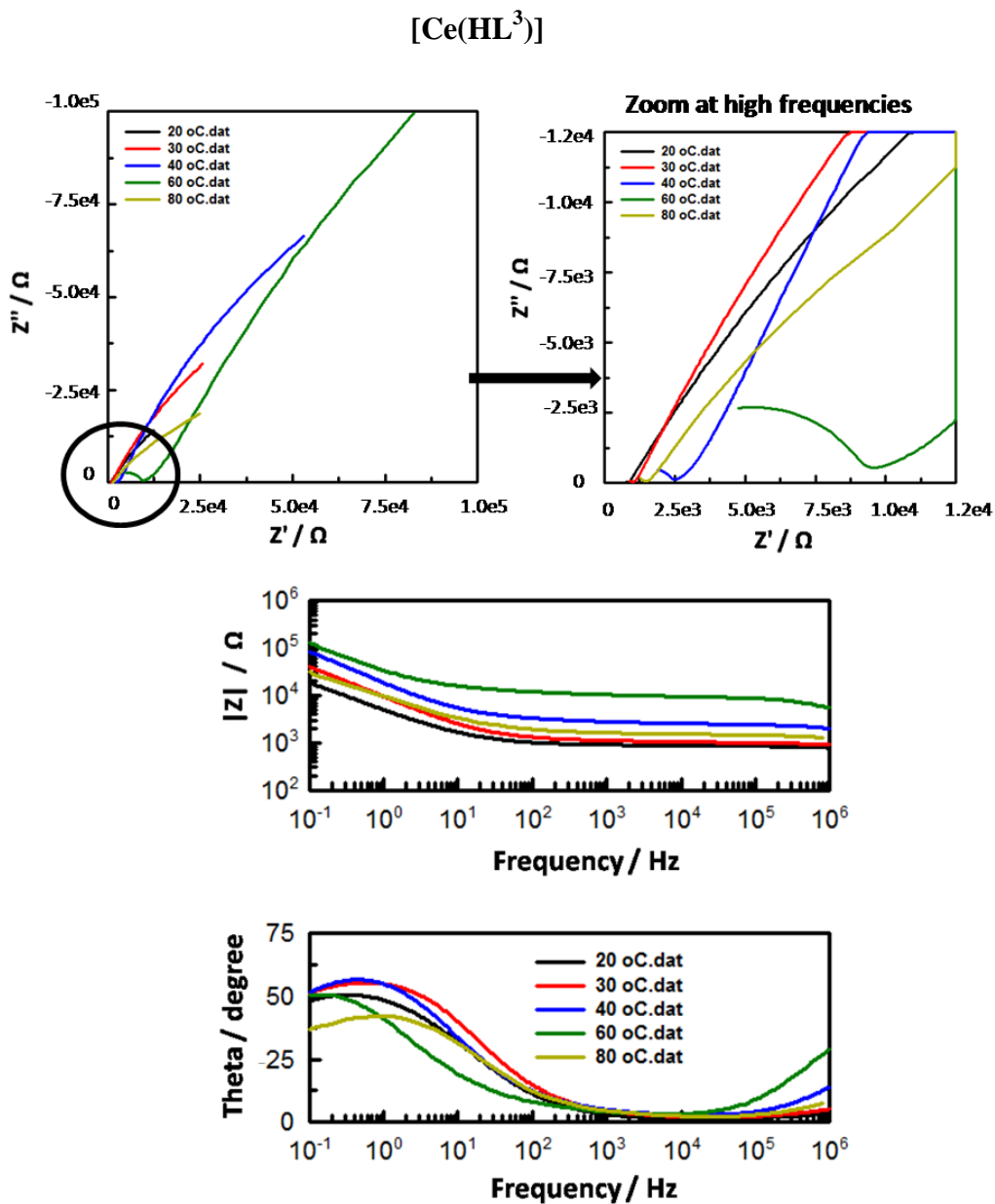


Figure 4.44. Nyquist and Bode plots for [Ce(HL³)] measured at different temperatures and 99 % RH.

Table 4.29. Proton conductivity ($S\ cm^{-1}$) for [Ce(HL³)] measured at different temperatures and 99 % RH.

[Ce(HL ³)]	σ at 20 °C	σ at 30 °C	σ at 40 °C	σ at 60 °C	σ at 80 °C
σ	$1.62(10) \times 10^{-4}$	$1.38(08) \times 10^{-4}$	$5.67(16) \times 10^{-5}$	$1.45(09) \times 10^{-5}$	$1.00(13) \times 10^{-4}$

[Nd(HL³)]

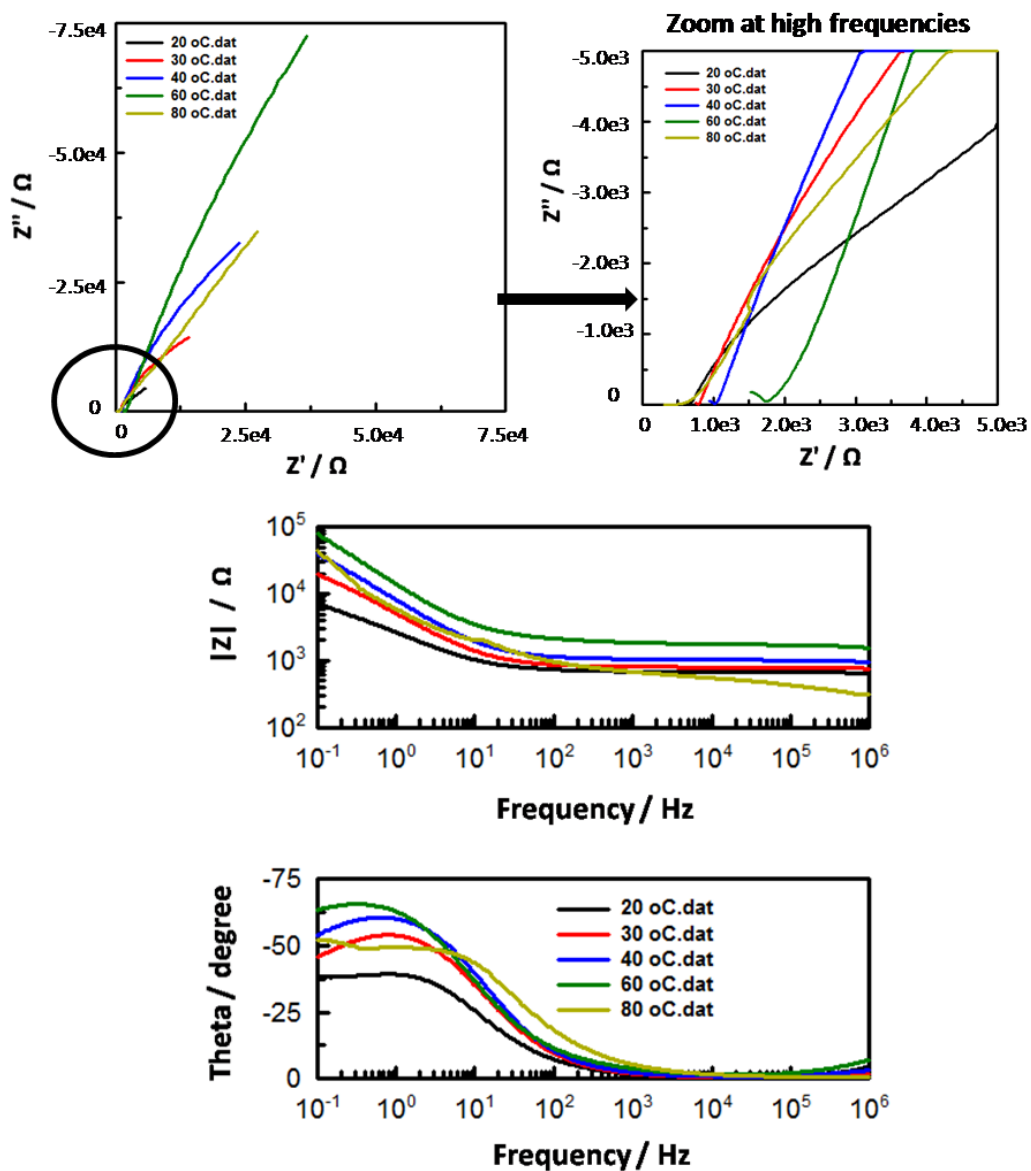


Figure 4.45. Nyquist and Bode plots for [Nd(HL³)] measured at different temperatures and 99 % RH.

Table 4.30. Proton conductivity (S cm⁻¹) for [Nd(HL³)] measured at different temperatures and 99 % RH.

[Nd(HL ³)]	σ at 20 °C	σ at 30 °C	σ at 40 °C	σ at 60 °C	σ at 80 °C
σ	$2.91(09) \times 10^{-4}$	$2.39(11) \times 10^{-4}$	$1.85(15) \times 10^{-4}$	$1.08(08) \times 10^{-4}$	$3.80(13) \times 10^{-4}$

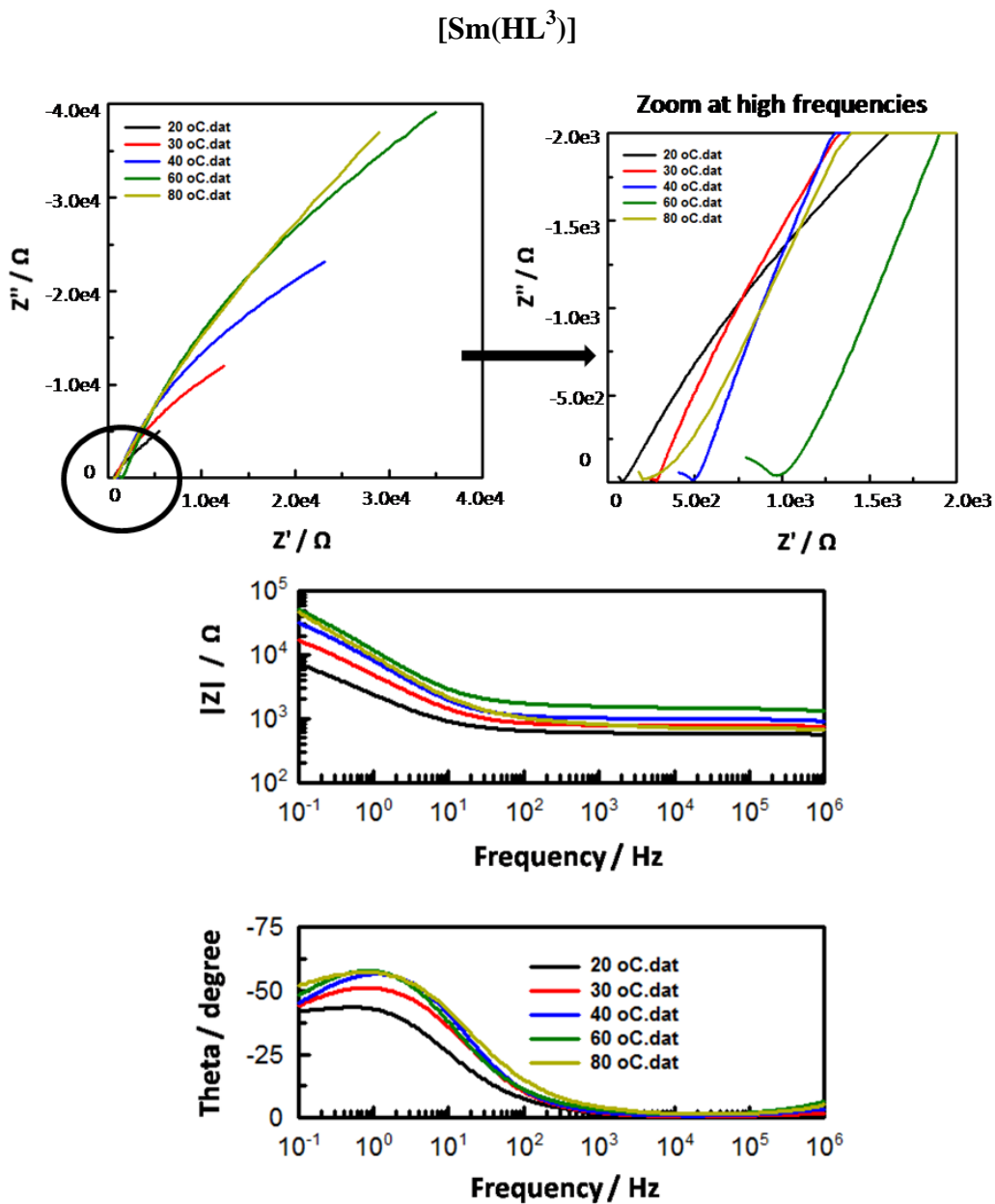


Figure 4.46. Nyquist and Bode plots for [Sm(HL³)] measured at different temperatures and 99 % RH.

Table 4.31. Proton conductivity (S cm⁻¹) for [Sm(HL³)] measured at different temperatures and 99 % RH.

[Sm(HL ³)]	σ at 20 °C	σ at 30 °C	σ at 40 °C	σ at 60 °C	σ at 80 °C
σ	$2.89(11) \times 10^{-4}$	$2.17(07) \times 10^{-4}$	$1.72(12) \times 10^{-4}$	$1.15(15) \times 10^{-4}$	$2.40(08) \times 10^{-4}$

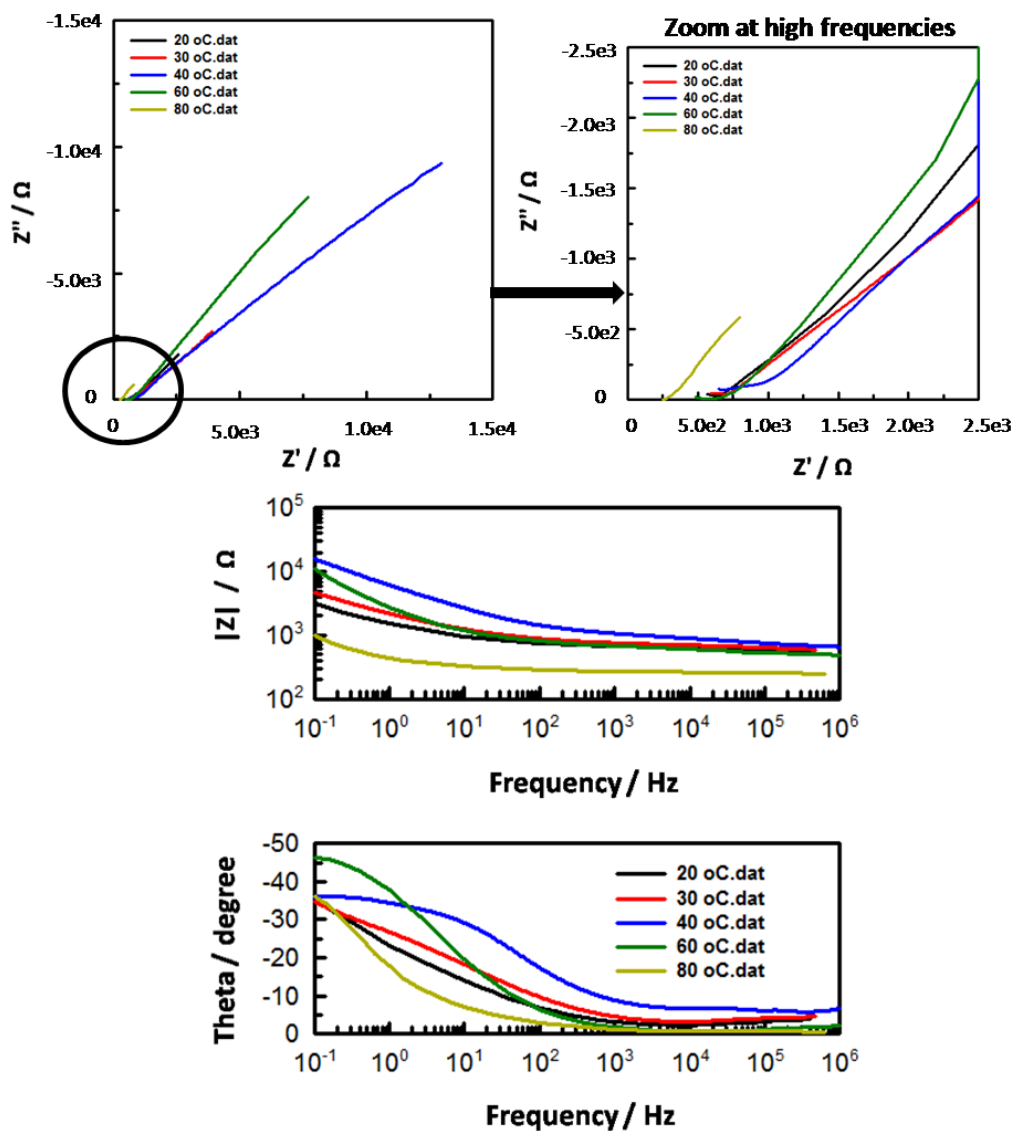


Figure 4.47. Nyquist and Bode plots for [Gd(HL³)] measured at different temperatures and 99 % RH.

Table 4.32. Proton conductivity (S cm⁻¹) for [Gd(HL³)] measured at different temperatures and 99 % RH.

[Gd(HL ³)]	σ at 20 °C	σ at 30 °C	σ at 40 °C	σ at 60 °C	σ at 80 °C
σ	$2.97(08) \times 10^{-4}$	$2.64(14) \times 10^{-4}$	$2.70(11) \times 10^{-4}$	$2.80(13) \times 10^{-4}$	$7.12(12) \times 10^{-4}$

[Ho(HL³)]

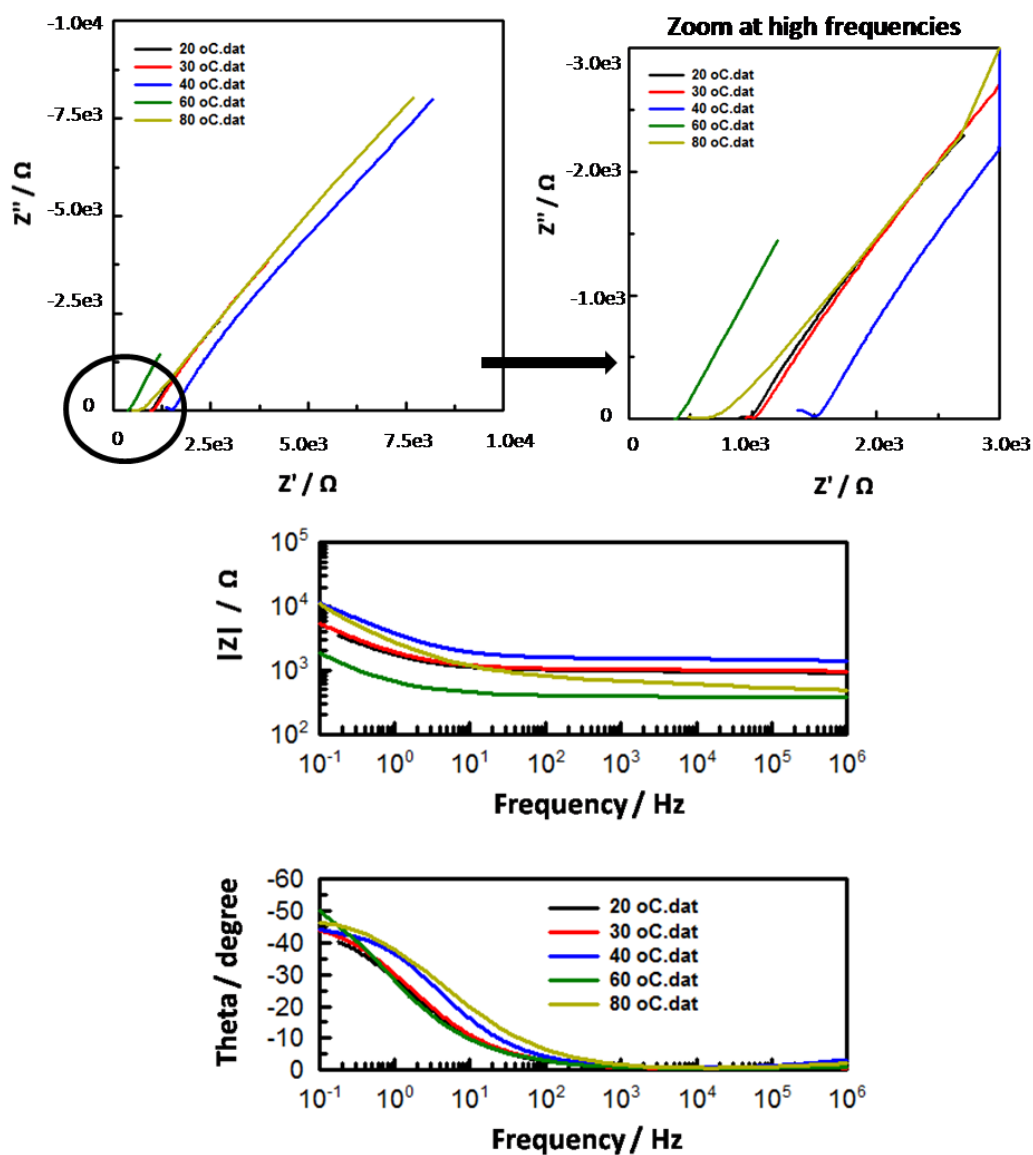


Figure 4.48. Nyquist and Bode plots for [Ho(HL³)] measured at different temperatures and 99 % RH.

Table 4.33. Proton conductivity (S cm⁻¹) for [Ho(HL³)] measured at different temperatures and 99 % RH.

[Ho(HL ³)]	σ at 20 °C	σ at 30 °C	σ at 40 °C	σ at 60 °C	σ at 80 °C
σ	$1.84(13) \times 10^{-4}$	$1.74(14) \times 10^{-4}$	$1.17(10) \times 10^{-4}$	$4.58(11) \times 10^{-3}$	$2.72(13) \times 10^{-4}$

In Table 4.34 are summarised the proton conductivity data measured for $[M(HL^3)]$ at different temperatures and 99 % RH. Consistently with what observed for $[M(HL^2)]$, all the $[M(HL^3)]$ samples showed a slight decrease of conductivity between 20 °C and 60 °C and an increase at 80 °C. The increase in conductivity at 80 °C was observed for all complexes in both $[M(HL^2)]$ and $[M(HL^3)]$. Due to technical issues based upon the design of the conductivity cell it was not possible to investigate the proton conductivity at higher temperatures.

Table 4.34. Summary of proton conductivity ($S\ cm^{-1}$) for $[M(HL^3)]$ measured at different temperatures and 99 % RH.

$[M(HL^3)]$	σ at 20 °C	σ at 30 °C	σ at 40 °C	σ at 60 °C	σ at 80 °C
La	$1.00(12) \times 10^{-4}$	$8.02(08) \times 10^{-5}$	$7.42(10) \times 10^{-5}$	$2.76(15) \times 10^{-5}$	$3.53(13) \times 10^{-4}$
Ce	$1.62(10) \times 10^{-4}$	$1.38(08) \times 10^{-4}$	$5.67(16) \times 10^{-5}$	$1.45(09) \times 10^{-5}$	$1.00(13) \times 10^{-4}$
Nd	$2.91(09) \times 10^{-4}$	$2.39(11) \times 10^{-4}$	$1.85(15) \times 10^{-4}$	$1.08(08) \times 10^{-4}$	$3.80(13) \times 10^{-4}$
Sm	$2.89(11) \times 10^{-4}$	$2.17(07) \times 10^{-4}$	$1.72(12) \times 10^{-4}$	$1.15(15) \times 10^{-4}$	$2.40(08) \times 10^{-4}$
Gd	$2.97(08) \times 10^{-4}$	$2.64(14) \times 10^{-4}$	$2.70(11) \times 10^{-4}$	$2.80(13) \times 10^{-4}$	$7.12(12) \times 10^{-4}$
Ho	$1.84(13) \times 10^{-4}$	$1.74(14) \times 10^{-4}$	$1.17(10) \times 10^{-4}$	$4.58(11) \times 10^{-3}$	$2.72(13) \times 10^{-4}$

Summary of proton conductivity for $[M(HL^3)]$:

The proton conductivities of $[M(HL^3)]$ were investigated at different values of % RH and temperatures and compared with the proton conductivity obtained for $[M(HL^2)]$ recorded at the same experimental conditions. At 20 °C and 99 % RH an increase in conductivity of two orders of magnitude for $[M(HL^3)]$ compared to $[M(HL^2)]$ was observed. This confirms the success of the strategy herein reported for the first time. Moreover, the proton conductivity measured for $[M(HL^3)]$ at 20 °C and 99 % RH is comparable with those reported in the literature (Table 1.1). This also represents one

of the few cases reported so far of high proton conductivity recorded at high temperatures (Tables 1.3 and 4.41).

4.3.2 Substitution of 3+ metals with 2+ metals to increase the number of protons in $[M(HL^2)]$

In the final part of this Chapter, is outlined an innovative method inspired by zeolite chemistry to increase the number of protonic charge carriers in $[M(HL^2)]$ and therefore to improve its proton conductivity properties.

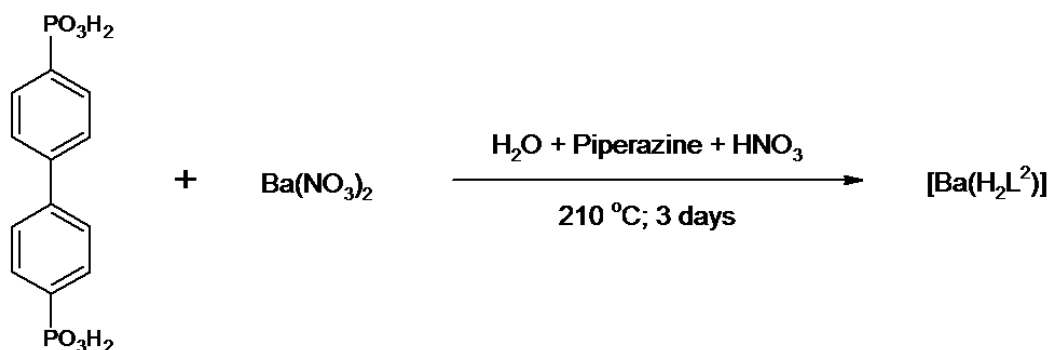
Zeolites are microporous, aluminosilicate minerals commonly used as commercial adsorbents and catalysts. It is generally acknowledged that their properties and catalytic reactivity strongly depends on the concentration and strength of the Brønsted acid sites. The control of acidity in zeolites is commonly achieved by controlling the ratio of silicon to aluminium. In fact, the Brønsted acidity of aluminosilicates relies on the cation substitution of Si^{4+} by Al^{3+} at the tetrahedral sites of the zeolite framework. This imposes a net negative charge on the framework counterbalanced by nearby cations that maintain charge neutrality. Moreover, because Si^{4+} and Al^{3+} have similar size and can be arranged in a similar geometry, the framework of the Al-doped zeolites are isostructural to the original.

We thus wish to adopt a similar approach via cation substitution which has not been exploited previously to increase the concentration of protons in a MOF for conductivity applications. This was achieved by substituting Ln(III) ions with Ba(II), with the loss of positive charge being made up by additional protons in the framework. In this Section the control of the proton conductivity of a MOF by changing the metal ion without significantly modifying the main framework is presented.

The case discussed herein goes beyond simply doping the Ln(III) framework with Ba(II), as in the zeolite examples; rather the successful synthesis of the 100 % Ba form of the framework is presented. This has the added advantage of avoiding difficulties to characterise the degrees of disorder/order of the two types of ions within the same framework, as would be expected by simple doping.

4.3.2.1 Synthesis and structural characterisation of [Ba(H₂L²)]

[Ba(H₂L²)] was obtained by solvothermal reaction under similar synthetic conditions used for [M(HL²)] (Section 4.2.3). One equivalent of H₄L² ligand was reacted with one equivalent of Ba(NO₃)₂·2H₂O in water in the presence of HNO₃ (2.6 M) and piperazine (0.3 M) (Scheme 4.5). [Ba(H₂L²)] was synthesised as a crystalline powder in PARR pressure vessels after reacting the mixture at 210 °C for 3 days.



Scheme 4.5. Synthesis of [Ba(H₂L²)].

[Ba(H₂L²)] was characterised by powder X-ray diffraction, elemental analyses, thermogravimetric analyses, IR spectroscopy, ¹H and ³¹P{¹H} solid-state NMR and impedance spectroscopy.

Synchrotron PXRD data for [Ba(H₂L²)] was collected at Diamond Light Source and the structure was solved using *ab initio* methods (Figure 4.49 and Figure 4.50).

$[\text{Ba}(\text{H}_2\text{L}^2)]$, with formula $[\text{Ba}(\text{H}_2\text{O}_6\text{P}_2\text{C}_{12}\text{H}_8)]_\infty$, crystallises in a monoclinic space group; detailed crystallography data for $[\text{Ba}(\text{H}_2\text{L}^2)]$ are listed in Table 4.35. The overall structure and coordination of the Ba(II) ions in $[\text{Ba}(\text{H}_2\text{L}^2)]$ are very similar to $[\text{M}(\text{HL}^2)]$ which were fully described in Section 4.2.4.

For charge balance, two protons per ligand (PO-H) are expected for $[\text{Ba}(\text{H}_2\text{L}^2)]$. Further studies to confirm the presence of protons, likely delocalised along the metal-phosphonate chains, were performed through ^1H and $^{31}\text{P}\{^1\text{H}\}$ solid-state NMR and are further discussed in Section 4.3.2.2.

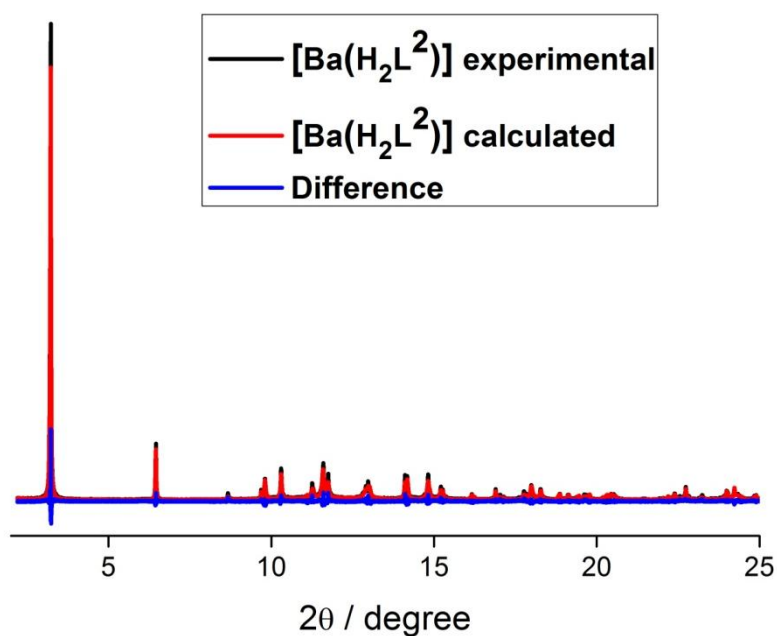


Figure 4.49. Observed (red) and calculated (blue) profiles for the Rietveld refinement of $[\text{Ba}(\text{H}_2\text{L}^2)]$.

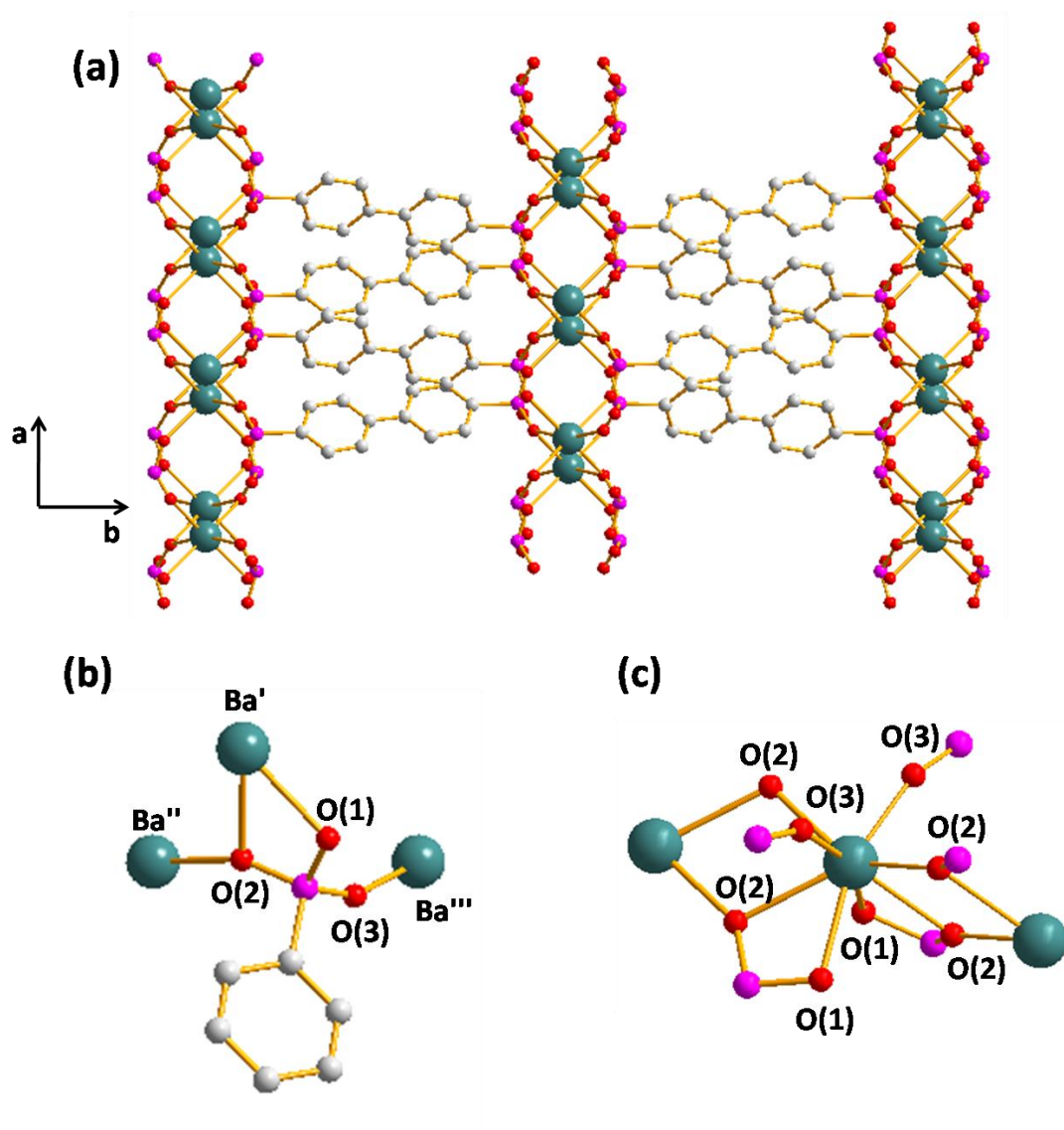


Figure 4.50. Refined structure of $[\text{Ba}(\text{H}_2\text{L}^2)]$ MOFs derived from PXRD data. (a) Projection of the structure along the c -axis. (b) Coordination nodes of the phosphonate group from the ligand. (c) Perspective view of the coordination environment at Ba(II) centre.

Table 4.35. Crystallographic data for [Ba(H₂L²)].

Crystallography data	[Ba(H ₂ L ²)]
Empirical formula	C ₁₂ H ₁₀ P ₂ O ₆ Ba
Formula weight (g mol ⁻¹)	449.49
Crystal system	Monoclinic
Space group	C2/c
<i>a</i> (Å)	5.55326(5)
<i>b</i> (Å)	29.3205(2)
<i>c</i> (Å)	8.52728(10)
<i>β</i> (°)	90.3611(14)
<i>γ</i> (°)	90
Cell volume (Å ³)	1388.42(2)
R _{wp}	11.99
GoF	1.89
Ba-Ba	4.4217(4)
Ba'-O(1)	2.9610(85)
Ba'-O(2)	2.8032(80)
Ba''-O(2)	2.7752(80)
Ba'''-O(3)	2.6690(83)

4.3.2.2 Solid-state NMR of [Ba(H₂L²)]

Quantitative solid-state ¹H NMR spectrum of [Ba(H₂L²)] shows two signals; the first peak at 7.09 ppm is attributed to the aromatic protons (Ar-H) of the organic ligand while the second peak at 13.24 ppm is the signal correspondent to free protons from the phosphonate group (O-H) (Figure 4.51). The difference in the chemical shift of the O-H peak in H₄L² (12.78 ppm), [M(HL²)] (18.56 ppm) and [Ba(H₂L²)] (13.24 ppm) is due to different shielding of the protons; in particular the protons are likely to be more shielded in H₄L², than [Ba(H₂L²)] and particularly [M(HL²)] as fewer protons share the same P centres.

The integration of the ¹H NMR spectra of [Ba(H₂L²)] corresponds to integrals predicted from the structure, with a ratio of aromatic protons to OH protons of 4:1. Comparing the ¹H NMR results for H₄L², [La(HL²)] and [Ba(H₂L²)] it is clear that the ratio of aromatic protons and free –OH varies as expected. In the case of H₄L² the integration ratio is 8:4, and for [La(HL²)] the ratio drops to 8:1 indicating that only one –OH per ligand is protonated. In [Ba(H₂L²)] the ratio is 8:2, unequivocally confirming that substituting La(III) with Ba(II) increases the number of protons in the framework in order to charge balance.

As for [La(HL²)], the correlation spectra of the P to the protons in the complex [Ba(H₂L²)] shows two signals, the more intense attributed to the P-O-H coupling and the less intense to the H-C-C-P coupling (Figure 4.52). As previously discussed in Section 4.2.5, this is not a quantitative technique but the difference in intensity is broadly assignable to the distance between the protons and the P centre.

In the solid-state ³¹P{¹H} NMR, only one peak at 9.71 ppm is observed suggesting that both phosphonate groups in the ligand are mono-protonated (Figure 4.53). The

phosphorous in H_4L^2 is more deshielded, therefore it is shifted at lower fields (16.01 ppm) compared with $[La(HL^2)]$ (10.67 ppm) and $[Ba(H_2L^2)]$ (9.74 ppm).

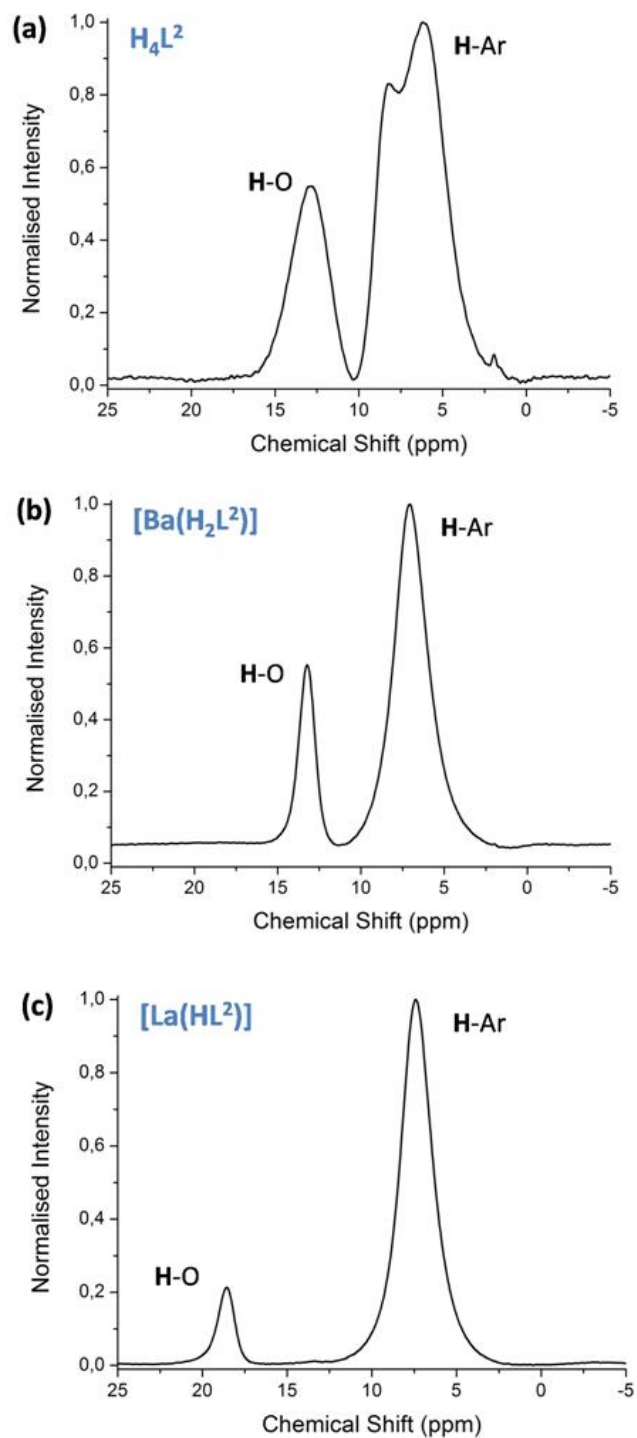


Figure 4.51. Comparison of solid-state 1H NMR spectra of (a) H_4L^2 , (b) $[Ba(H_2L^2)]$ and (c) $[La(HL^2)]$.

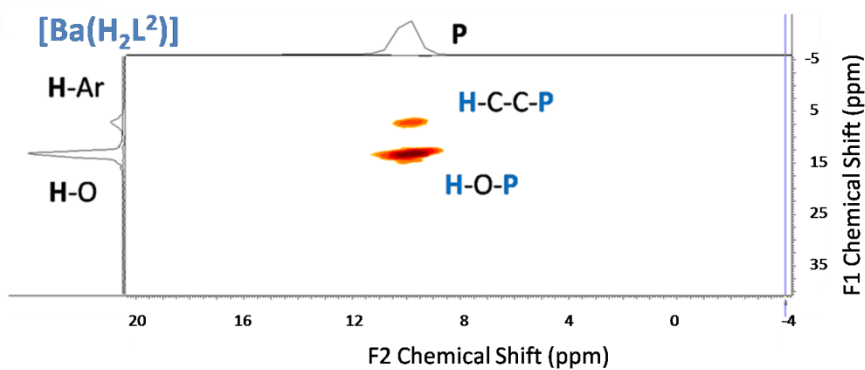


Figure 4.52. Correlation spectrum of phosphorus to proton in $[\text{Ba}(\text{H}_2\text{L}^2)]$.

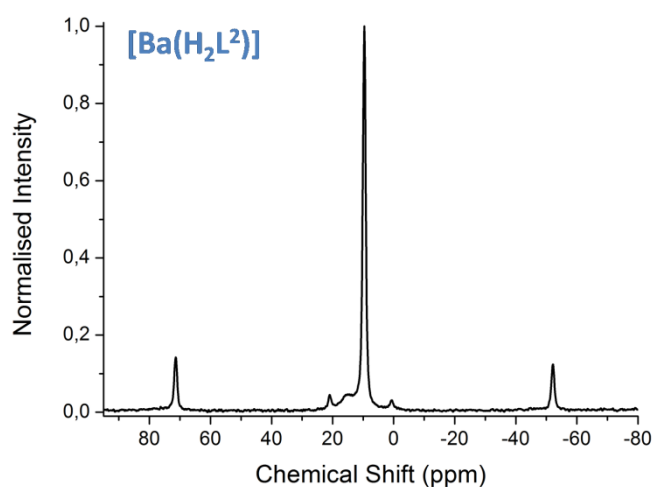


Figure 4.53. Solid-state $^{31}\text{P}\{^1\text{H}\}$ NMR spectra of $[\text{Ba}(\text{H}_2\text{L}^2)]$.

4.3.2.3 Thermal stability of $[\text{Ba}(\text{H}_2\text{L}^2)]$

To examine the thermal stability and retention of crystallinity of $[\text{Ba}(\text{H}_2\text{L}^2)]$, thermogravimetric analysis and PXRD were performed. Thermogravimetric analysis were collected between 25 °C and 1000 °C at a heating rate of 5 °C per minute under a flow of air (Figure 4.54). The TGA curve shows a plateau between 25 °C and 300 °C; from 300 °C a weight loss of 5 % of uncertain attribution occurs. Decomposition of the structure takes place at temperature above 440 °C. The weight loss of 35 % was assigned to the decomposition of the organic linker and the formation of metal phosphonate salts (Table 4.36).

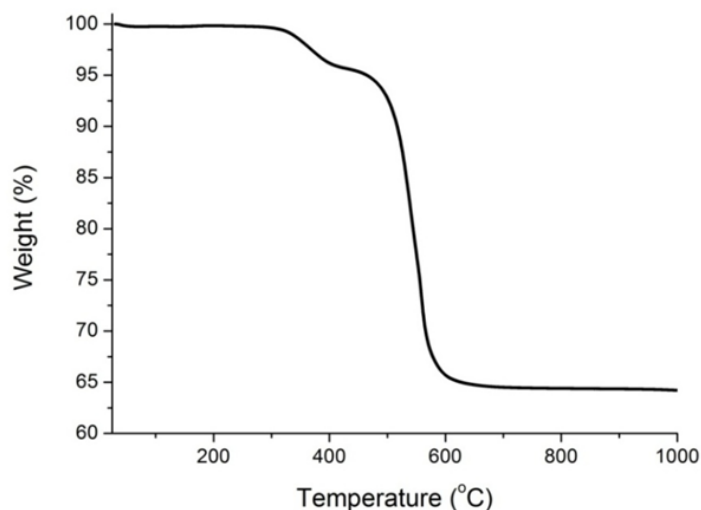


Figure 4.54. Thermogravimetric profiles of $[\text{Ba}(\text{H}_2\text{L}^2)]$ recorded under a flow of air at a heating rate of $5\text{ }^\circ\text{C min}^{-1}$.

Table 4.36. Analysis of the experimental TGA data for $[\text{Ba}(\text{H}_2\text{L}^2)]$.

MOF	Weight % organic moieties (C_{12}H_8)	Weight % metal phosphonate salts ($\text{P}_2\text{O}_6\text{BaH}_2$)
$[\text{Ba}(\text{H}_2\text{L}^2)]$	35.57	64.43

In situ high temperature powder X-ray diffraction measurements on $[\text{Ba}(\text{H}_2\text{L}^2)]$ under vacuum were carried out on Beamline I11 at Diamond Light Source, in order to further investigate its thermal stability. PXRD patterns were collected from room temperature up to $750\text{ }^\circ\text{C}$. The temperature was increased at a rate of $5\text{ }^\circ\text{C}$ per minute; once the desired temperature was reached it was held for 10 minutes and a collection scan of 15 minutes was recorded. This study showed that the crystallinity and the overall structure is perfectly retained up to $440\text{ }^\circ\text{C}$ in agreement with the TGA results. Partial decomposition of the framework is observed at $550\text{ }^\circ\text{C}$. The complete collapse of the framework occurs at $750\text{ }^\circ\text{C}$ (Figure 4.55).

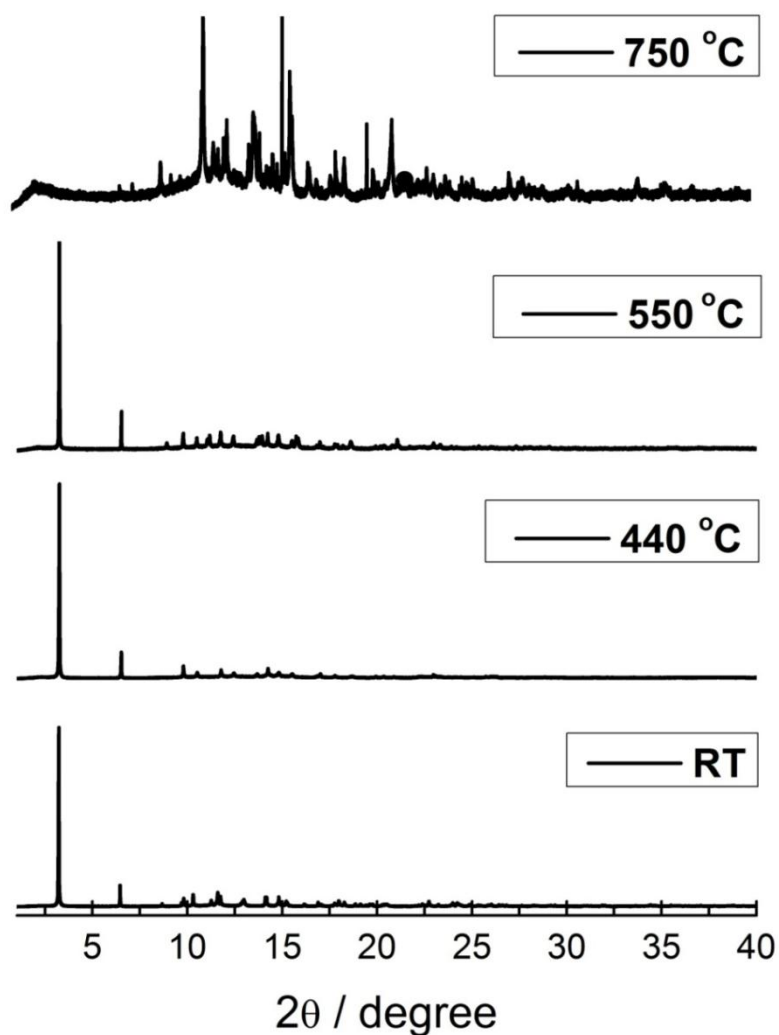


Figure 4.55. PXRD for $[\text{Ba}(\text{H}_2\text{L}^2)]$.

4.3.2.4 Infrared spectroscopy of $[\text{Ba}(\text{H}_2\text{L}^2)]$

Figure 4.56 shows the infrared spectra of H_4L^2 , $[\text{La}(\text{HL}^2)]$ and $[\text{Ba}(\text{H}_2\text{L}^2)]$ between 4000 cm^{-1} to 550 cm^{-1} ; the peaks were assigned according to literature.¹¹⁻¹³ The broad band centred around 2623 cm^{-1} is attributed to the stretching vibration of the O-H from the phosphonate group (P-OH). The drop in intensity of this band moving from $[\text{Ba}(\text{H}_2\text{L}^2)]$ to $[\text{M}(\text{HL}^2)]$ is consistent with the reduction in number of OH groups in the structure. The bands at 1138 cm^{-1} and 1087 cm^{-1} are typical of the stretching vibrations of the phosphonate P-O group. The signals at 1703 cm^{-1} and 893 cm^{-1} are respectively assigned to the stretching vibration of $\nu(\text{P}=\text{O})$ and $\nu(\text{P}-\text{C})$.

The bands centred at 1388 cm^{-1} and 716 cm^{-1} correspond to the C-C stretching vibrations of the phenylene group and in-plane deformation vibrations of para-disubstituted aromatic ring with identical groups. The band at 813 cm^{-1} arises from the C-H out-of-plane vibrations for para-disubstituted phenylene rings.

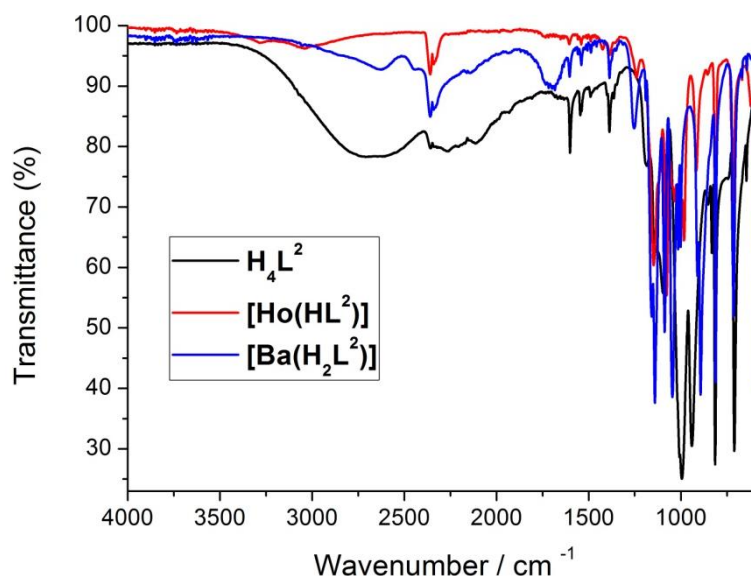


Figure 4.56. ATR infrared spectra of H_4L^2 (black), $[\text{Ho}(\text{HL}^2)]$ (red) and $[\text{Ba}(\text{H}_2\text{L}^2)]$ (blue).

4.3.2.5 Proton conductivity study of $[\text{Ba}(\text{H}_2\text{L}^2)]$

The proton conductivities of $[\text{Ba}(\text{H}_2\text{L}^2)]$ were studied by AC impedance spectroscopy on compact pellets using cell B (Section 2.2.3.2) at different values of % RH and temperatures. In order to compare the proton conductivities of $[\text{Ba}(\text{H}_2\text{L}^2)]$ with those previously reported for $[\text{M}(\text{HL}^2)]$ and $[\text{M}(\text{HL}^3)]$ (Sections 4.2.8 and 4.3.1.5) the samples were methodically prepared using the same procedure and the measurements were repeated under the same experimental conditions. This allows a direct comparison between the proton conductivities of all the materials discussed in this Chapter and to investigate if the use a 2+ metal instead of 3+ metals to increase

the concentration of protons in the framework improves the proton conductivity of the bulk material.

About 0.120 g of sample was ground into a fine powder using mortar and pestle and pressed for 5 minutes under a pressure of 5 tons using a die with 0.8 cm diameter. A silver paste was applied to either side of the sample to serve as electrode. The thickness and the diameter of the pellet were measured and used to calculate the proton conductivities of $[\text{Ba}(\text{H}_2\text{L}^2)]$ (Section 2.1.6, Equation 10). Measurements were repeated on two different batches; for each batch three measurements were collected at each temperature and relative humidity investigated. The data collected was used to calculate the mean value of the proton conductivity correspondent to the experimental conditions under study, together with the associated standard deviation.

Proton conductivity at different relative humidities:

Impedance measurements on $[\text{Ba}(\text{H}_2\text{L}^2)]$ were recorded at different % RH to investigate the relationship between their proton conductivity properties and the relative humidity. Measurements were collected between 99 % and 45 % at 20 °C. The dry pellet coated with silver paste was loaded inside the conductivity cell and exposed to 99 % RH humidity overnight to allow the sample compressed into the pellet to equilibrate under the desired conditions. After equilibration, three impedance measurements were recorded to ensure stable resistivity of the sample and reproducibility of the measurements. The % RH was then progressively decreased at 70 % and 45 % by regulating the flow of wet and dry gas inside the cell. For each % RH, measurements were collected every 45 minutes until the resistivity of the sample was stable over a period of 2 h suggesting the equilibration point had been reached.

Nyquist and Bode plots for each $[\text{Ba}(\text{H}_2\text{L}^2)]$ collected at 99 %, 70 % and 45 % RH at 20 °C are shown in Figure 4.57 together with the correspondent proton conductivity data (Table 4.37). The resistivity of $[\text{Ba}(\text{H}_2\text{L}^2)]$ at 70 % and 45 % RH was determined by fitting the well-defined semi-circle in the Nyquist plots, while in the case of 99 % RH the proton conductivity was calculated using the resistivity determined as the intercept with the real axis.

As for $[\text{M}(\text{HL}^2)]$ and $[\text{M}(\text{HL}^3)]$, the maximum conductivity was observed at 99 % RH followed by a progressive decrease of conductivity with decreasing the humidity. An increase of proton conductivity of one order of magnitude was measured for $[\text{Ba}(\text{H}_2\text{L}^2)]$ compared with $[\text{M}(\text{HL}^2)]$ (at 99 % RH and 20 °C). This proves the success of the suggested strategy. This represents the first time the proton conductivity of a MOF has been modulated by the use of a metal with different oxidation number without modifying the overall structure.

Proton conductivity at different temperatures:

The proton conductivity of $[\text{Ba}(\text{H}_2\text{L}^2)]$ at different temperatures was investigated in the range between 20 °C and 80 °C at 99 % RH (Figure 4.58, Table 4.38). The sample was equilibrated for 2 h at each chosen temperature and three measurements were collected to ensure the conductivity was stable and the measurement reproducible.

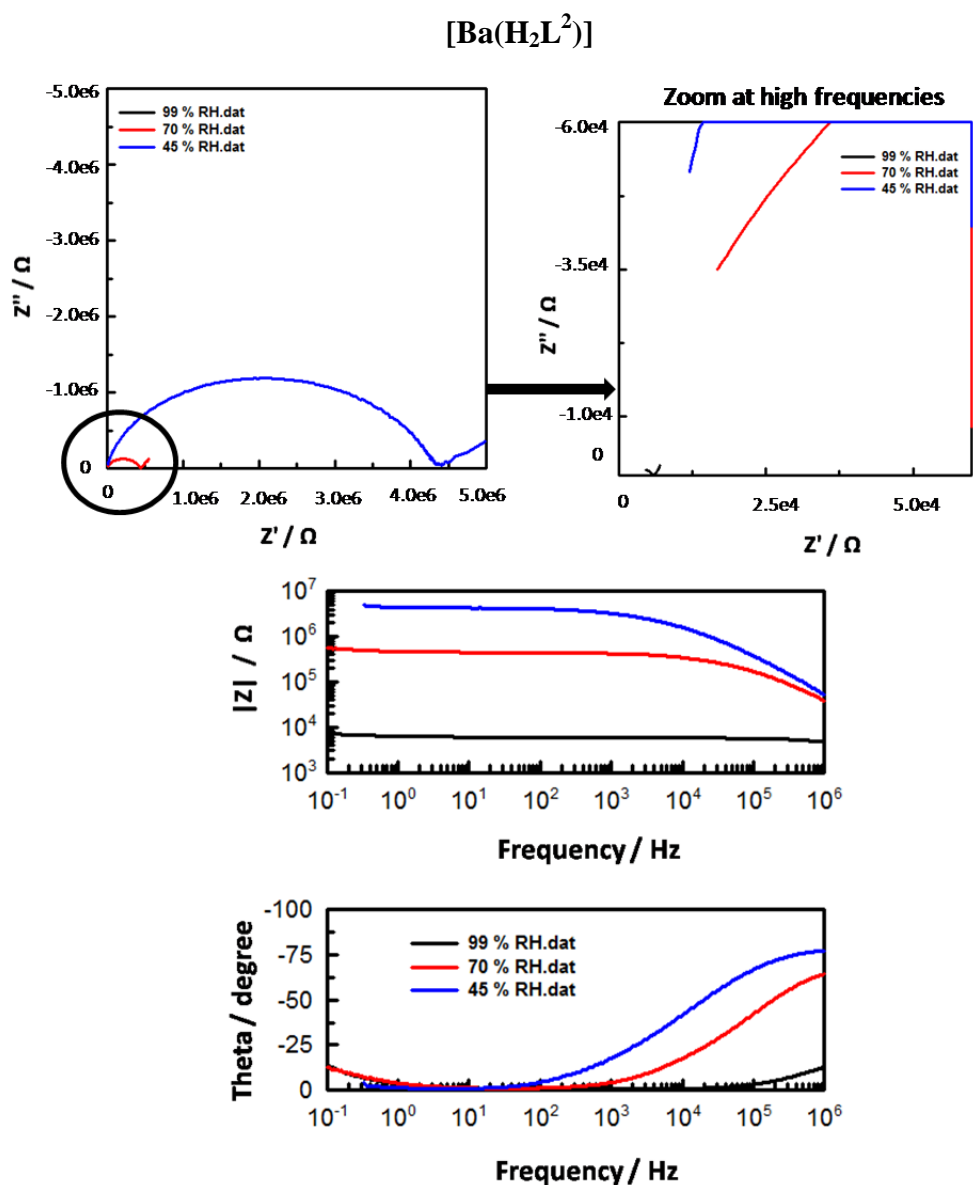


Figure 4.57. Nyquist and Bode plots for [Ba(H₂L²)] measured at different % RH and 20 °C.

Table 4.37. Proton conductivity (S cm⁻¹) for [Ba(H₂L²)] measured at different % RH and 20 °C.

[Ba(H ₂ L ²)]	σ at 99 % RH	σ at 70 % RH	σ at 45 % RH
σ	$4.12(12) \times 10^{-5}$	$5.37(09) \times 10^{-7}$	$5.49(14) \times 10^{-8}$

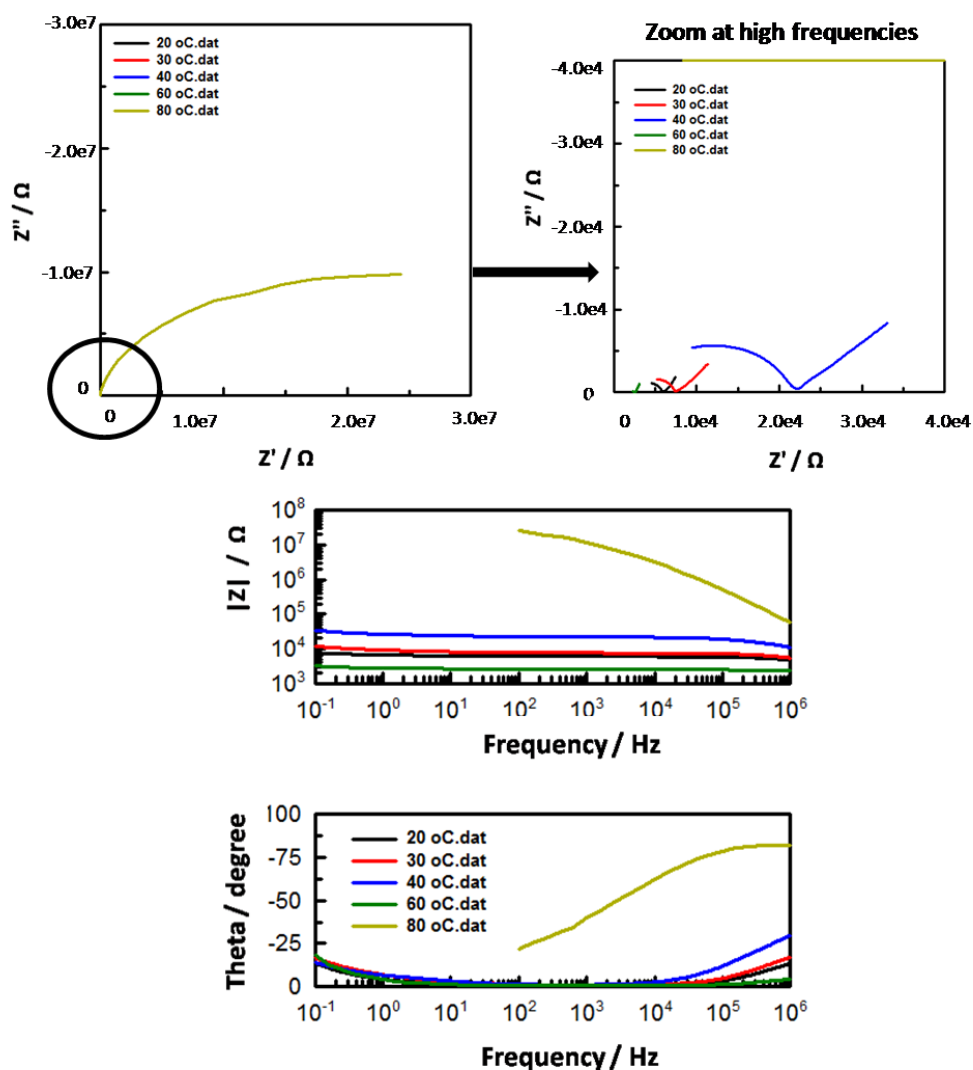
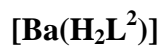


Figure 4.58. Nyquist and Bode plots for [Ba(H₂L²)] measured at different temperatures and 99 % RH.

Table 4.38. Proton conductivity (S cm⁻¹) for [Ba(H₂L²)] measured at different temperatures and 99 % RH.

[Ba(H ₂ L ²)]	σ at 20 °C	σ at 30 °C	σ at 40 °C	σ at 60 °C	σ at 80 °C
σ	4.12(12) x 10 ⁻⁵	3.20(10) x 10 ⁻⁵	1.09(14) x 10 ⁻⁵	9.53(09) x 10 ⁻⁵	9.31(13) x 10 ⁻⁹

4.4 Conclusions

New approaches to the preparation of MOFs with increased proton conductivity are currently of interest. In Chapter 4 were presented two novel strategies to increase the proton conductivity of MOFs.

A family of lanthanide MOFs, $[M(HL^2)]$ (H_4L^2 = biphenyl-4,4'-diphosphonic acid; M = La, Ce, Nd, Sm, Gd, Ho) was synthesised and used as starting point to describe and demonstrate the success of the two strategies proposed. Both approaches aim to enhance the concentration of protons in the framework to improve the proton conductivity of the bulk material without modifying the overall structure of the framework. This was achieved by changing first the length of the organic ligand and then substituting the metal ion with one with a lower oxidation number. To achieve these targets a second family of lanthanide MOFs $[M(HL^3)]$ (H_4L^3 = benzene-1,4-diphosphonic acid; M = La, Ce, Nd, Sm, Gd, Ho) and $[Ba(H_2L^2)]$ were synthesised. All the materials presented in this Chapter were fully characterised by X-ray diffraction and several spectroscopy techniques as discussed in the main text. Most relevant for the aim of this work are the impedance studies performed on these materials. Impedance measurements for $[M(HL^2)]$, $[M(HL^3)]$ and $[Ba(H_2L^2)]$ were performed as a function of different values of % RH and temperatures. Table 4.39, Table 4.40 and Figure 4.59 show the summary of the proton conductivity results. Both designed strategies were successful opening new approaches to create materials with improved conductivity.

Table 4.39. Summary of proton conductivity ($S\text{ cm}^{-1}$) for $[M(\text{HL}^2)]$, $[M(\text{HL}^3)]$ and $[\text{Ba}(\text{H}_2\text{L}^2)]$ measured at different % RH and 20 °C.

MOF	σ at 99 % RH	σ at 70 % RH	σ at 45 % RH
$[\text{La}(\text{HL}^2)]$	$4.00(15) \times 10^{-6}$	$6.09(11) \times 10^{-7}$	$1.24(10) \times 10^{-8}$
$[\text{Ce}(\text{HL}^2)]$	$1.46(11) \times 10^{-6}$	$5.05(12) \times 10^{-7}$	$1.82(09) \times 10^{-8}$
$[\text{Nd}(\text{HL}^2)]$	$7.85(09) \times 10^{-6}$	$2.47(10) \times 10^{-6}$	$2.86(12) \times 10^{-8}$
$[\text{Sm}(\text{HL}^2)]$	$3.83(11) \times 10^{-6}$	$9.22(08) \times 10^{-7}$	$4.47(10) \times 10^{-8}$
$[\text{Gd}(\text{HL}^2)]$	$1.87(08) \times 10^{-6}$	$5.63(11) \times 10^{-8}$	$7.38(13) \times 10^{-9}$
$[\text{Ho}(\text{HL}^2)]$	$5.22(13) \times 10^{-6}$	$7.52(10) \times 10^{-7}$	$1.53(09) \times 10^{-8}$
$[\text{La}(\text{HL}^3)]$	$1.00(12) \times 10^{-4}$	$2.14(14) \times 10^{-5}$	$7.37(10) \times 10^{-7}$
$[\text{Ce}(\text{HL}^3)]$	$1.62(10) \times 10^{-4}$	$4.74(11) \times 10^{-5}$	$3.84(15) \times 10^{-6}$
$[\text{Nd}(\text{HL}^3)]$	$2.91(13) \times 10^{-4}$	$5.08(08) \times 10^{-5}$	$7.15(11) \times 10^{-6}$
$[\text{Sm}(\text{HL}^3)]$	$2.89(09) \times 10^{-4}$	$5.48(14) \times 10^{-5}$	$3.79(10) \times 10^{-6}$
$[\text{Gd}(\text{HL}^3)]$	$2.97(06) \times 10^{-4}$	$4.64(09) \times 10^{-5}$	$5.56(11) \times 10^{-6}$
$[\text{Ho}(\text{HL}^3)]$	$2.51(05) \times 10^{-4}$	$7.72(11) \times 10^{-6}$	$7.11(13) \times 10^{-7}$
$[\text{Ba}(\text{H}_2\text{L}^2)]$	$4.12(12) \times 10^{-5}$	$5.37(09) \times 10^{-7}$	$5.49(14) \times 10^{-8}$

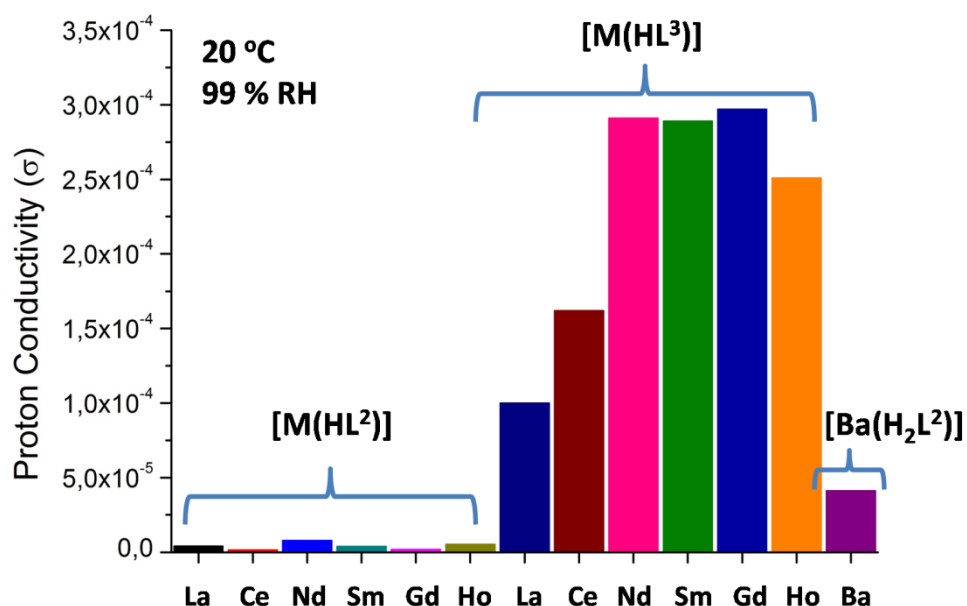


Figure 4.59. Comparison of proton conductivity ($S\text{ cm}^{-1}$) results for $[M(\text{HL}^2)]$, $[M(\text{HL}^3)]$ and $[\text{Ba}(\text{H}_2\text{L}^2)]$ at 20 °C and 99 % RH.

Table 4.40. Summary of proton conductivity (S cm^{-1}) for $[\text{M}(\text{HL}^2)]$, $[\text{M}(\text{HL}^3)]$ and $[\text{Ba}(\text{H}_2\text{L}^2)]$ measured at different temperatures and 99 % RH.

MOF	σ at 20 °C	σ at 30 °C	σ at 40 °C	σ at 60 °C	σ at 80 °C
$[\text{La}(\text{HL}^2)]$	$4.00(15) \times 10^{-6}$	$2.53(13) \times 10^{-6}$	$6.36(15) \times 10^{-7}$	$7.87(12) \times 10^{-8}$	$2.00(16) \times 10^{-7}$
$[\text{Ce}(\text{HL}^2)]$	$1.46(11) \times 10^{-6}$	$7.14(13) \times 10^{-7}$	$1.00(12) \times 10^{-7}$	$2.29(12) \times 10^{-8}$	$1.66(11) \times 10^{-7}$
$[\text{Nd}(\text{HL}^2)]$	$7.85(09) \times 10^{-6}$	$7.47(15) \times 10^{-6}$	$4.39(10) \times 10^{-6}$	$9.17(11) \times 10^{-7}$	$5.39(14) \times 10^{-6}$
$[\text{Sm}(\text{HL}^2)]$	$3.82(11) \times 10^{-6}$	$2.55(10) \times 10^{-6}$	$1.89(13) \times 10^{-6}$	$9.51(12) \times 10^{-6}$	$4.79(11) \times 10^{-6}$
$[\text{Gd}(\text{HL}^2)]$	$1.87(08) \times 10^{-6}$	$9.66(11) \times 10^{-6}$	$2.06(07) \times 10^{-7}$	$1.21(18) \times 10^{-8}$	$1.03(14) \times 10^{-7}$
$[\text{Ho}(\text{HL}^2)]$	$5.22(13) \times 10^{-6}$	$2.20(15) \times 10^{-6}$	$1.06(13) \times 10^{-6}$	$2.49(09) \times 10^{-7}$	$5.01(06) \times 10^{-7}$
$[\text{La}(\text{HL}^3)]$	$1.00(12) \times 10^{-4}$	$8.02(08) \times 10^{-5}$	$7.42(10) \times 10^{-5}$	$2.76(15) \times 10^{-5}$	$3.53(13) \times 10^{-4}$
$[\text{Ce}(\text{HL}^3)]$	$1.62(10) \times 10^{-4}$	$1.38(08) \times 10^{-4}$	$5.67(16) \times 10^{-5}$	$1.45(09) \times 10^{-5}$	$1.00(13) \times 10^{-4}$
$[\text{Nd}(\text{HL}^3)]$	$2.91(09) \times 10^{-4}$	$2.39(11) \times 10^{-4}$	$1.85(15) \times 10^{-4}$	$1.08(08) \times 10^{-4}$	$3.80(13) \times 10^{-4}$
$[\text{Sm}(\text{HL}^3)]$	$2.89(11) \times 10^{-4}$	$2.17(07) \times 10^{-4}$	$1.72(12) \times 10^{-4}$	$1.15(15) \times 10^{-4}$	$2.40(08) \times 10^{-4}$
$[\text{Gd}(\text{HL}^3)]$	$2.97(08) \times 10^{-4}$	$2.64(14) \times 10^{-4}$	$2.70(11) \times 10^{-4}$	$2.80(13) \times 10^{-4}$	$7.12(12) \times 10^{-4}$
$[\text{Ho}(\text{HL}^3)]$	$1.84(13) \times 10^{-4}$	$1.74(14) \times 10^{-4}$	$1.17(10) \times 10^{-4}$	$4.58(11) \times 10^{-3}$	$2.72(13) \times 10^{-4}$
$[\text{Ba}(\text{H}_2\text{L}^2)]$	$4.12(12) \times 10^{-5}$	$3.20(10) \times 10^{-5}$	$1.09(14) \times 10^{-5}$	$9.53(09) \times 10^{-5}$	$9.31(13) \times 10^{-9}$

For all the three types of materials a decrease in conductivity was observed with decreasing humidity and increasing the temperature, as typically observed for proton conductivity mediated by the presence of water. Interestingly, for $[\text{M}(\text{HL}^2)]$ and $[\text{M}(\text{HL}^3)]$, an increase in conductivity was observed around 80 °C at 99 % RH. This behaviour has been previously reported in only a handful of cases as most of the MOFs do not present high conductivity at high temperatures and high % RH (Table 1.3). Particularly high conductivity was found in the case of $[\text{M}(\text{HL}^3)]$ reaching values of $10^{-4} \text{ S cm}^{-1}$ at 80 °C and 99 % RH comparable with those reported in literature (Table 4.41).

Table 4.41. Proton conductivities of CPs and MOFs measured under hydrated conditions at about 80 °C reported in literature.

Compound	σ (S cm ⁻¹)	Temp. % RH	Ref.
UiO-66(SO ₃ H) ₂ ^[a]	8.4x10 ⁻²	80 °C 90 %	23
PCMOF-2½ ^[b]	2.1x10 ⁻²	85 °C 90 %	24
Cu-DSOA ^[c]	1.9x10 ⁻³	85 °C 98 %	25
[M(HL³)]^[d]	Range 7x10⁻⁴ 1x10⁻⁴	80 °C 99 %	This work
Zr-L _{lp} @H ^[e]	5.4x10 ⁻⁵	80 °C 95 %	26
[EuL(H ₂ O) ₃].2H ₂ O ^[f]	1.6x10 ⁻⁵	75 °C 97 %	27
[DyL(H ₂ O) ₃].2H ₂ O ^[f]	1.3x10 ⁻⁵	75 °C 97 %	27
Zr-L _{np} @H ^[e]	6.6x10 ⁻⁶	80 °C 95 %	26
MIL-53(Al)-OH ^[g]	1.9x10 ⁻⁶	80 °C 95 %	3

[a] UiO-66(Zr) = Zr₆O₄(OH)₄(CO)₁₂. [b] PCMOF-2½ = [Na₃L₁]_(0.66)[Na₃H₃L₂]_(0.34)(H₂O)_{1.2}; (Na₃L₁ = trisodium 2,4,6-trihydroxy-1,3,5-trisulfonate benzene; H₆L₂ = 1,3,5-benzenetriphosphonic acid). [c] Na₂H₃SODA = disodium-2,2'-disulfonate-4,4'-oxydibenzoic acid. [d] H₄L³ = benzene-1,4-diphosphonic acid; M = La, Ce, Nd, Sm, Gd, Ho. [e] H₈L = cyclohexyl,N,N,N',N'-diaminotetraphosphonate; *lp* = large pore; *np* = narrow pore. [f] L = N-phenyl-N'-phenyl bicyclo [2,2,2]-oct-7-ene-2,3,5,6-tetracarboxydiimide tetracarboxylic acid. [g] = MIL-53(M) = M(OH)(bdc-(COOH)₂); H₂bdc = 1,4-benzenedicarboxylic acid.

Attempts to synthesise [Ba(H₂L³)] with increased number of protons deriving from the combination of the two methodologies presented in this Chapter were performed. Unfortunately, such complex was not successfully synthesised and represents a promising target compound for the future.

4.5 Experimental Section

PXRD, TGA, solid-state UV-visible absorption spectra, solid-state NMR and impedance experimental details are fully discussed in the Experimental Section at the end of this Thesis.

4.5.1 Synthesis of biphenyl-4,4'-diphosphonic acid, H_4L^2

4,4'-Dibromobiphenyl (4.9943 g, 16.0 mmol), and tetrakis(triphenylphosphine) palladium (0) (0.0745 g, 0.065 mmol) as catalyst were mixed in triisopropyl phosphite (35 mL, 141.8 mmol) and heated for 2 h at 120 °C. The resultant mixture was cooled to 60 °C and tetrakis(triphenylphosphine) palladium (0) (0.0745 g, 0.065 mmol) together with triisopropyl phosphite (25 mL, 101.3 mmol) were added. The solution was stirred and heated using a sand bath at 200 °C for 3 days under an atmosphere of Ar. After cooling, the product 4,4'-[P(O)(OiPr)₂]biphenyl (2.5 g, 5.2 mmol) was isolated by filtration as a white powder and washed with large amount of hexane (60 mL). ¹H NMR (CDCl₃, 300 MHz): 1.35 (dd, 24H), 4.75 (m, 4H, OC-H), 7.68 (m, 4H, Ar-H), 7.92 (m, 4H, Ar-H). ³¹P NMR (DMSO, 400 MHz): 15.71. Mass (ESI) *m/z* (M-H⁺): 483.20. Elemental analysis (%): anal. calc. for C₂₄H₄₆O₆P₂: C 59.74, H 7.52, N 0; found: C 59.06, H 7.45, N 0.00. The ligand H_4L^2 was obtained as a white powder by acidification of 4,4'-[P(O)(OiPr)₂]biphenyl (2.5 g, 5.2 mmol) with a solution of HCl and H₂O (ratio 2:1) under stirring for 1 day at 90 °C. Yield: 1.29 g (4.1 mmol), 79 %. ¹H NMR (CDCl₃, 300 MHz) δ ppm: 7.78 (m, 8H, Ar-H). ³¹P NMR (DMSO, 400 MHz) δ ppm: 12.43 (s). ¹H MAS NMR (600 MHz) δ ppm: 7.10 (s, 8H, Ar-H), 12.78 (m, 4H, O-H). ³¹P{¹H} MAS NMR (600 MHz) δ ppm: 16.01. Mass (ESI) *m/z* (M-H⁺): 315.02. Elemental analysis (%): anal. calc. for C₁₂H₁₂O₆P₂: C 45.88, H 3.85, N 0.00; found: C 45.56, H 3.76, N 0.00. FTIR: ν (cm⁻¹) = 2681 (m),

2288 (m), 1596 (m), 1547 (w), 1489 (w), 1385 (m), 1103 (m), 995 (s), 939 (s), 834 (w), 814 (s), 709 (s).

4.5.2 Synthesis of La[C₁₂H₈P₂O₆H], [La(HL²)]

H₄L² (0.0450 g, 0.14 mmol) and LaCl₃·7H₂O (0.0531 g, 0.14 mmol) were suspended in water (6 mL). A 2.6 M solution of HNO₃ in H₂O (1.5 mL), and a 0.3 M solution of piperazine in H₂O (1.5 mL) were added to the ligand-metal mixture. The PARR pressure vessel was sealed, heated in the oven at 210 °C for 72 h and cooled to room temperature. The crystalline white powder obtained was washed first with DMF and water to eliminate the non reacted ligand and then with acetone. Yield: 0.05 g (0.11 mmol), 79 %. Elemental analysis (%): anal. calc. for C₁₂H₉O₆P₂La: C 32.03, H 2.02, N 0.00; found: C 32.12, H x1.99, N 0.00. FTIR: ν (cm⁻¹) = 3070 (w), 2358 (w), 1917 (w), 1604 (w), 1541 (w), 1482 (w), 1312 (m), 1138 (s), 1113 (s), 1055 (m), 968 (s), 807 (s), 720 (s), 703 (s), 645 (w), 629 (w). ¹H MAS NMR (600 MHz) δ ppm: 7.40 (s, 8H, Ar-H), 18.56 (w, 1H, O-H). ³¹P{¹H} MAS NMR (600 MHz) δ ppm: 10.67.

The same synthetic conditions described for [La(HL²)] were used to afford crystalline powders of [M(HL²)] (M = Ce, Nd, Sm, Gd and Ho). CeCl₃·7H₂O, Nd(NO₃)₃·6H₂O, Sm(NO₃)₃·6H₂O, GdCl₃·6H₂O and Ho(CH₃CO₂)₃·6H₂O were used as inorganic metal salts for the synthesis of the correspondent [M(HL²)].

4.5.3 Synthesis of Ce[C₁₂H₈P₂O₆H], [Ce(HL²)]

[Ce(HL²)] was obtained as a yellow crystalline powder. Yield: 0.047 g (0.10 mmol), 71 %. Elemental analysis (%): anal. calc. for C₁₂H₉O₆P₂Ce: C 31.94, H 2.01, N 0.00; found: C 31.90, H 1.86, N 0.00. FTIR: ν (cm⁻¹) = 3056 (w), 2362 (m), 1730 (w),

1605 (w), 1541 (w), 1488 (w), 1384 (m), 1326 (m), 1140 (s), 1116 (s), 985 (s), 811 (s), 718 (s), 703 (s), 606 (w), 563 (m).

4.5.4 Synthesis of Nd[C₁₂H₈P₂O₆H], [Nd(HL²)]

[Nd(HL²)] was obtained as a white crystalline powder. Yield: 0.052 g (0.11 mmol), 79 %. Elemental analysis (%): anal. calc. for C₁₂H₉O₆P₂Nd: C 31.65, H 1.99, N 0.00; found: C 31.61, H 1.91, N 0.00. FTIR: ν (cm⁻¹) = 3056 (w), 2360 (w), 2340 (w), 2162 (w), 1920 (w), 1605 (w), 1541 (w), 1489 (w), 1332 (m), 1141 (s), 1116 (s), 1055 (m), 973 (s), 807 (s), 720 (s), 701 (s), 648 (w), 560 (m).

4.5.5 Synthesis of Sm[C₁₂H₈P₂O₆H], [Sm(HL²)]

[Sm(HL²)] was obtained as a pale yellow crystalline powder. Yield: 0.050 g (0.11 mmol), 79 %. Elemental analysis (%): anal. calc. for C₁₂H₉O₆P₂Sm: C 31.23, H 1.97, N 0.00; found: C 31.11, H 1.87, N 0.00. FTIR: ν (cm⁻¹) = 3058 (w), 2356 (w), 2337 (w), 2164 (w), 1920 (w), 1602 (w), 1541 (w), 1489 (w), 1334 (m), 1141 (s), 1123 (s), 1061 (m), 976 (s), 807 (s), 720 (s), 702 (s), 648 (w), 561 (m).

4.5.6 Synthesis of Gd[C₁₂H₈P₂O₆H], [Gd(HL²)]

[Gd(HL²)] was obtained as a white crystalline powder. Yield: 0.054 g (0.11 mmol), 79 %. Elemental analysis (%): anal. calc. for C₁₂H₉O₆P₂Gd: C 30.77, H 1.94, N 0.00; found: C 30.81, H 1.93, N 0.00. FTIR: ν (cm⁻¹) = 3061 (w), 2354 (w), 2337 (w), 2158 (w), 1920 (w), 1607 (w), 1541 (w), 1488 (w), 1335 (m), 1139 (s), 1126 (s), 1066 (m), 980 (s), 806 (s), 723 (s), 704 (s), 647 (w), 561 (m).

4.5.7 Synthesis of $\text{Ho}[\text{C}_{12}\text{H}_8\text{P}_2\text{O}_6\text{H}]$, $[\text{Ho}(\text{HL}^2)]$

$[\text{Ho}(\text{HL}^2)]$ was obtained as a pale pink crystalline powder. Yield: 0.048 g (0.10 mmol), 71 %. Elemental analysis (%): anal. calc. for $\text{C}_{12}\text{H}_9\text{O}_6\text{P}_2\text{Ho}$: C 30.27, H 1.91, N 0.00; found: C 30.88, H 1.90, N 0.00. FTIR: ν (cm^{-1}) = 3282 (m), 3045 (m), 2360 (m), 1922 (w), 1737 (w), 1605 (w), 1539 (w), 1420 (w), 1385 (w), 1242 (w), 1148 (s), 1077 (s), 1032 (m), 1011 (m), 985 (m), 981 (s), 916 (s), 814 (s), 716 (s), 622 (w), 571 (m).

4.5.8 Synthesis of benzene-1,4-diphosphonic acid, H_4L^3

1,4-Dibromophenyl (5 g, 21.0 mmol) was suspended in triisopropyl phosphite (35 mL, 141.8 mmol) together with the catalyst tetrakis(triphenylphosphine) palladium (0) (0.0745 g, 0.065 mmol). After stirring under atmosphere of argon for 2 h at 120 °C, tetrakis(triphenylphosphine) palladium (0) (0.0745 g, 0.065 mmol) and triisopropyl phosphite (25 mL, 101.3 mmol) were added. The resultant solution with stirring was heated using a sand bath at 200 °C for 3 days under a flow of Ar. By cooling the mixture to room temperature, 1,4'-P(O)(OiPr)₂]phenyl (5.776 g, 18 mmol) precipitated as a white powder. The product was isolated by filtration and washed with large amount of hexane (60 mL). Yield: 5.78 g (18 mmol), 86 %. ¹H NMR (CDCl_3 , 300 MHz): 1.34 (dd, 24H), 4.68 (m, 4H, OC-H), 7.72 (m, 4H, Ar-H), 7.82 (m, 4H, Ar-H). ³¹P NMR (DMSO, 400 MHz): 15.69. Mass (ESI) m/z (M-H⁺): 407.40. The ligand H_4L^3 was obtained by acidification of 1,4-[P(O)(OiPr)₂]phenyl (5.776 g, 18 mmol) with a solution of HCl and H₂O (ratio 2:1) under stirring for 2 days at 90 °C. Yield: 3.3639 g (14 mmol), 90 %. ¹H NMR (CDCl_3 , 300 MHz) δ ppm: 7.92 (m, 8H, Ar-H). ³¹P NMR (DMSO, 400 MHz) δ ppm: 11.73 (s). Mass (ESI) m/z (M-H⁺): 239.08. Elemental analysis (%): anal. calc. for $\text{C}_6\text{H}_8\text{O}_6\text{P}_2$: C 30.27, H 3.39,

N 0.00; found: C 29.76, H 3.34, N 0.00. FTIR: ν (cm^{-1}) = 2626 (m), 2263 (m), 2099 (m), 1610 (w), 1384 (m), 1092 (s), 986 (s), 932 (s), 829 (s), 729 (m), 591 (s).

4.5.9 Synthesis of $\text{La}[\text{C}_6\text{H}_4\text{P}_2\text{O}_6\text{H}]$, $[\text{La}(\text{HL}^3)]$

One equivalent of H_4L^3 (0.0340 g, 0.14 mmol) and one equivalent of $\text{LaCl}_3 \cdot 7\text{H}_2\text{O}$ (0.0531 g, 0.14 mmol) were suspended in 6 mL of water. 1.5 mL of a 2.6 M solution of HNO_3 in H_2O , and 1.5 mL of a 0.3 M solution of piperazine in H_2O , were added to the ligand-metal mixture. The PARR pressure vessel was sealed and the reaction was carried out for 3 days at 210 °C. The white powder synthesised was washed first with DMF and water to eliminate the non-reacted ligand and then with acetone. Yield: 0.040 g (0.11 mmol), 78 %. Elemental analysis (%): anal. calc. for $\text{C}_6\text{H}_5\text{O}_6\text{P}_2\text{La}$: C 19.27, H 1.35, N 0.00; found: C 19.33, H 1.40, N 0.00. FTIR: ν (cm^{-1}) = 3024 (w), 2360 (w), 1736 (w), 1559 (w), 1539 (w), 1505 (w), 1470 (w), 1455 (w), 1384 (m), 1310 (m), 1129 (s), 1049 (m), 965 (s), 836 (s), 817 (s), 615 (m), 583 (s).

$[\text{M}(\text{HL}^3)]$ (M = Ce, Nd, Sm, Gd, Ho) where synthesised following the same method described for $[\text{La}(\text{HL}^3)]$. $\text{CeCl}_3 \cdot 7\text{H}_2\text{O}$, $\text{Nd}(\text{NO}_3)_3 \cdot 6\text{H}_2\text{O}$, $\text{Sm}(\text{NO}_3)_3 \cdot 6\text{H}_2\text{O}$, $\text{GdCl}_3 \cdot 6\text{H}_2\text{O}$ and $\text{Ho}(\text{CH}_3\text{CO}_2)_3 \cdot 6\text{H}_2\text{O}$ were used as metal sources.

4.5.10 Synthesis of $\text{Ce}[\text{C}_6\text{H}_4\text{P}_2\text{O}_6\text{H}]$, $[\text{Ce}(\text{HL}^3)]$

$[\text{Ce}(\text{HL}^3)]$ was synthesised as a white crystalline powder. Yield: 0.038 g (0.10 mmol), 71 %. Elemental analysis (%): anal. calc. for $\text{C}_6\text{H}_5\text{O}_6\text{P}_2\text{Ce}$: C 19.21, H 1.34, N 0.00; found: C 18.9, H 1.43, N 0.00. FTIR: ν (cm^{-1}) = 3375 (w), 3079 (w), 2364

(m), 1734 (w), 1558 (w), 1540 (w), 1506 (w), 1472 (w), 1456 (w), 1386 (m), 1318 (m), 1131 (s), 1053 (m), 966 (s), 833 (s), 820 (s), 654 (m), 583 (s).

4.5.11 Synthesis of Nd[C₆H₄P₂O₆H], [Nd(HL³)]

[Nd(HL³)] was synthesised as a white crystalline powder. Yield: 0.041 g (0.11 mmol), 78 %. Elemental analysis (%): anal. calc. for C₆H₅O₆P₂Nd: C 19.00, H 1.33, N 0.00; found: C 18.68, H 1.41, N 0.00. FTIR: ν (cm⁻¹) = 3436 (w), 3004 (w), 2357 (m), 1738 (w), 1386 (m), 1326 (m), 1131 (s), 1056 (m), 969 (s), 834 (s), 816 (s), 660 (m), 579 (s).

4.5.12 Synthesis of Sm[C₆H₄P₂O₆H], [Sm(HL³)]

[Sm(HL³)] was synthesised as a white crystalline powder. Yield: 0.045 g (0.12 mmol), 86 %. Elemental analysis (%): anal. calc. for C₆H₅O₆P₂Sm: C 18.80, H 1.31, N 0.00; found: C 18.05, H 1.36, N 0.00. FTIR: ν (cm⁻¹) = 3347 (w), 3023 (w), 2358 (m), 2337 (m), 1735 (w), 1559 (w), 1539 (w), 1505 (w), 1386 (m), 1332 (m), 1135 (s), 1059 (m), 972 (s), 836 (s), 819 (s), 661 (m), 583 (s).

4.5.13 Synthesis of Gd[C₆H₄P₂O₆H], [Gd(HL³)]

[Gd(HL³)] was synthesised as a white crystalline powder. Yield: 0.043 g (0.11 mmol), 78 %. Elemental analysis (%): anal. calc. for C₆H₅O₆P₂Gd: C 18.37, H 1.28, N 0.00; found: C 18.04, H 1.37, N 0.00. FTIR: ν (cm⁻¹) = 3370 (w), 2942 (w), 2368 (w), 1736 (w), 1387 (m), 1337 (m), 1134 (s), 1063 (m), 1031 (w), 977 (s), 839 (s), 820 (s), 663 (m), 583 (s).

4.5.14 Synthesis of $\text{Ho}[\text{C}_6\text{H}_4\text{P}_2\text{O}_6\text{H}]$, $[\text{Ho}(\text{HL}^3)]$

$[\text{Ho}(\text{HL}^3)]$ was synthesised as a pink crystalline powder. Yield: 0.041 g (0.10 mmol), 73 %. Elemental analysis (%): anal. calc. for $\text{C}_6\text{H}_5\text{O}_6\text{P}_2\text{Ho}$: C 18.02, H 1.26, N 0.00; found: C 17.88, H 1.34, N 0.00. FTIR: ν (cm^{-1}) = 3327 (w), 3084 (w), 2355 (m), 2339 (m), 1738 (w), 1557 (w), 1538 (w), 1505 (w), 1383 (m), 1133 (s), 1070 (m), 1032 (w), 982 (s), 839 (s), 824 (s), 669 (m), 580 (s).

4.5.15 Synthesis of $\text{Ba}[\text{C}_{12}\text{H}_8\text{P}_2\text{O}_6\text{H}_2]$, $[\text{Ba}(\text{H}_2\text{L}^2)]$

$[\text{Ba}(\text{H}_2\text{L}^2)]$ was synthesised from H_4L^2 and $\text{Ba}(\text{NO}_3)_2 \cdot 2\text{H}_2\text{O}$ (1:1 ratio) in a PARR pressure vessel at 210 °C for 3 days. The solvent mixture was prepared using the same conditions described for $[\text{La}(\text{HL}^2)]$. A off-white crystalline powder of $[\text{Ba}(\text{H}_2\text{L}^2)]$ was isolated by filtration, washed with DMF, H_2O and acetone, and dried in air. Yield: 0.046 g (0.10 mmol), 71 %. Elemental analysis (%): anal. calc. for $\text{C}_{12}\text{H}_{10}\text{O}_6\text{P}_2\text{Ba}$: C 32.07, H 2.24, N 0.00; found: C 32.4, H 2.19, N 0.00. FTIR: ν (cm^{-1}) = 2623 (w), 2360 (m), 1703 (w), 1602 (w), 1541 (w), 1483 (w), 1388 (m), 1253 (m), 1138 (s), 1087 (s), 1044 (s), 1014 (w), 1000 (w), 893 (s), 813 (s), 716 (s), 572 (s). ^1H MAS NMR (600 MHz) δ ppm: 7.09 (s, 8H, Ar-H), 13.24 (m, 2H, O-H). $^{31}\text{P}\{^1\text{H}\}$ MAS NMR (600 MHz) δ ppm: 10.67.

4.6 References

- (1) Sadakiyo, M.; Yamada, T.; Kitagawa, H. *J. Am. Chem. Soc.* **2009**, *789*, 9906–9907.
- (2) Sadakiyo, M.; Yamada, T.; Kitagawa, H. *J. Am. Chem. Soc.* **2014**, *136*, 13166–13169.
- (3) Shigematsu, A.; Yamada, T.; Kitagawa, H. *J. Am. Chem. Soc.* **2011**, *133*, 2034–2036.
- (4) Bureekaew, S.; Horike, S.; Higuchi, M.; Mizuno, M.; Kawamura, T.; Tanaka, D.; Yanai, N.; Kitagawa, S. *Nature Mater.* **2009**, *8*, 831–836.
- (5) Umeyama, D.; Horike, S.; Inukai, M.; Hijikata, Y.; Kitagawa, S. *Angew. Chem.* **2011**, *50*, 11706–11709.
- (6) Hurd, J.; Vaidhyanathan, R.; Thangadurai, V.; Ratcliffe, C. I.; Moudrakovski, I. L.; Shimizu, G. K. H. *Nature Chem.* **2009**, *1*, 705–710.
- (7) Ponomareva, V. G.; Kovalenko, K. A.; Chupakhin, A. P.; Dybtsev, D. N.; Shutova, E. S.; Fedin, V. P. *J. Am. Chem. Soc.* **2012**, *134*, 15640–15643.
- (8) Phang, W. J.; Lee, W. R.; Yoo, K.; Ryu, D. W.; Kim, B.; Hong, C. S. *Angew. Chem.* **2014**, *53*, 8383–8387.
- (9) Plabst, M.; Bein, T. *Inorg. Chem.* **2009**, *48*, 4331–4341.
- (10) Wharmby, M. T.; Miller, S. R.; Groves, J. A.; Margiolaki, I.; Ashbrook, S. E.; Wright, P. A. *Dalton Trans.* **2010**, 6389–6391.
- (11) Cabeza A., Aranda M., Bruque S., Poojary D., C. A. *Mater. Res. Bull.* **1998**, *33*, 1265–1274.
- (12) Amghouz, Z.; García-Granda, S.; García, J. R.; Clearfield, A.; Valiente, R. *Cryst. Growth Des.* **2011**, *11*, 5289–5297.

- (13) Demadis, K. D.; Katarachia, S. D. *Phosphorus. Sulfur. Silicon Relat. Elem.* **2004**, *179*, 627–648.
- (14) Adams J. *The American Mineralogist* **1965**, *50*, 356–366.
- (15) Bunzli J.C.; Eliseeva S.; “*Basics of Lanthanide Photophysics*” **2011**.
- (16) Binnemans, K.; Van Deun, R.; Görrler-Walrand, C.; Adam, J. L. *J. Non-Cryst. Solids* **1998**, *238*, 11–29.
- (17) Carnall, W. T.; Fields, P. R.; Rajnak, K. *J. Chem. Phys.* **1968**, *49*, 4424.
- (18) Pardo, E.; Train, C.; Gontard, G.; Boubekeur, K.; Fabelo, O.; Liu, H.; Dkhil, B.; Lloret, F.; Nakagawa, K.; Tokoro, H.; Ohkoshi, S. I.; Verdaguer, M. *J. Am. Chem. Soc.* **2011**, *133*, 15328–15331.
- (19) Dey, C.; Kundu, T.; Banerjee, R. *Chem. Commun.* **2012**, *48*, 266.
- (20) Okawa, H.; Sadakiyo, M.; Yamada, T.; Maesato, M.; Ohba, M.; Kitagawa, H. *J. Am. Chem. Soc.* **2013**, *135*, 2256–2262.
- (21) Aranda, M. A. G.; Leon-Reina, L.; Rius, J.; Demadis, K. D.; Moreau, B.; Villemin, D.; Palomino, M.; Rey, F.; Cabeza, A. *Inorg. Chem.* **2012**, *51*, 7689–7698.
- (22) Yoon, M.; Suh, K.; Natarajan, S.; Kim, K. *Angew. Chem.* **2013**, *52*, 2688–2700.
- (23) Phang, W. J.; Jo, H.; Lee, W. R.; Song, J. H.; Yoo, K.; Kim, B.; Hong, C. S. *Angew. Chem.* **2015**, *54*, 5142–5146.
- (24) Kim, S.; Dawson, K. W.; Gelfand, B. S.; Taylor, J. M.; Shimizu, G. K. H.; Gelfand, B. S. *J. Am. Chem. Soc.* **2013**, *135*, 963–966.
- (25) Dong, X.-Y.; Wang, R.; Li, J.-B.; Zang, S.-Q.; Hou, H.-W.; Mak, T. C. W. *Chem. Commun.* **2013**, *49*, 10590–10592.

- (26) Costantino, F.; Donnadio, A.; Casciola, M. *Inorg. Chem.* **2012**, *51*, 6992–7000.
- (27) Zhu, M.; Hao, Z.-M.; Song, X.-Z.; Meng, X.; Zhao, S.-N.; Song, S.-Y.; Zhang, H.-J. *Chem. Commun.* **2014**, *50*, 1912–1914.

Chapter 5

**Postsynthetic modification of NOTT-300(Al) and
proton conductivity studies**

List of Contents

5.1 Introduction	259
5.1.1 NOTT-300(Al) and postsynthetic modification	260
5.1.2 Aims of Chapter 5.....	262
5.2 Results and Discussion	263
5.2.1 Synthesis of Im@NOTT-300(Al) by vapour diffusion (d).....	263
5.2.2 Characterisation of Im@NOTT-300(Al)-(d)	266
5.2.3 Proton Conductivity study of NOTT-300(Al) and Im@NOTT-300(Al)-(d)	269
5.2.4 Synthesis of Im@NOTT-300(Al) by solvation (s)	272
5.2.5 Characterisation of Im@NOTT-300(Al)-(s)	275
5.2.6 Proton Conductivity study of NOTT-300(Al) and Im@NOTT-300(Al)-(s)	277
5.3 Conclusions and future perspectives	280
5.4 Experimental Section	282
5.4.1 Synthesis of the activated NOTT-300(Al).....	282
5.4.2 Synthesis of Im@NOTT-300(Al)-(d).....	283
5.4.3 Synthesis of Im@NOTT-300(Al)-(s)	283
5.5 References	284

5.1 Introduction

MOFs are promising candidates for the design of new ionic conductors. The proton conductivity of a material is predominantly determined by the proton concentration and mobility within the framework. In Chapter 4 (Section 4.1) the three main approaches available in the literature (Types I-III) to enhance proton conductivity of MOFs were introduced.^{1,2} Among them, promising results were found for the postsynthetic modification of MOFs by encapsulation of heterocycle proton-carrier guest molecules (e.g., triazole, imidazole, histamine) into the pores.³⁻⁶

In 2009 S. Kitagawa *et al.*, published one of the first examples of guest-dependent proton conduction.³ The encapsulation of imidazole into the channels of the Al-MOF, [Al(μ_2 -OH)(1,4-ndc)] (1,4-ndc²⁻ = 1,4-naphthalenedicarboxylate), resulted in a dramatic increase in proton conductivity highlighting the role of imidazole as proton-carrier. The MOF loaded with imidazole reached a proton conductivity of 2.20×10^{-5} S cm⁻¹ at 120 °C, eight orders of magnitude higher than the guest-free complex (10^{-13} S cm⁻¹).

Shimizu and co-workers reported a proton-conducting MOF with the channels occupied by triazole molecules loaded through a solvation method.⁵ Proton conduction in β -PCMOF-2 [Na₃(2,4,6-trihydroxy-1,3,5-benzenetrisulfonate)] was modulated by controlled loading of 1*H*-1,2,4-triazole within the pores and exhibited a proton conductivity of 5×10^{-4} S cm⁻¹ at 150 °C.

In 2015, Liu *et al.*, introduced imidazole into the channels of UiO-67, [Zr₆O₄(OH)₄(bpdc)₆] (bpdc²⁻ = biphenyldicarboxylate), by an evaporation method (Figure 5.1).⁶ Imidazole@UiO-67 showed a proton conductivity of 1.44×10^{-3} S cm⁻¹ at 120 °C under anhydrous conditions.

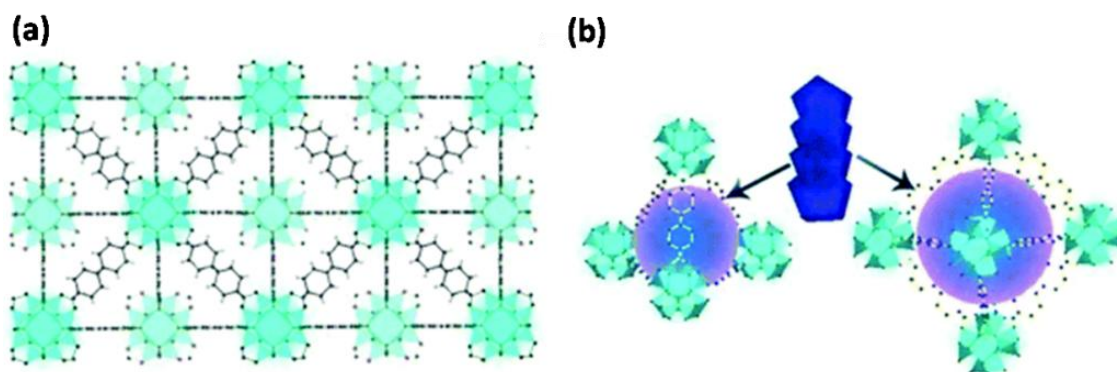


Figure 5.1 (a) Structure of UiO-67. (b) Schematic representation of loading imidazole molecules in the channels of UiO-67 (blue is the imidazole molecule).⁶

These findings demonstrate that guest molecules loaded into porous frameworks can result in significant enhancement of proton conductivity in low conducting MOFs. Moreover, non-volatile guest molecules can in principle replace the role of water (when it is needed to promote proton conduction and introduced through high % RH) allowing for operating temperatures above 80 °C and overcome one of the major problems faced with Nafion (Section 1.3.1). However, control and determine the number of guest molecules incorporated into the MOF, unequivocally localising their position inside the framework, identifying the interactions with the lattice and the resultant proton-hopping pathway still remain a challenge in the field.

5.1.1 NOTT-300(Al) and postsynthetic modification

NOTT-300(Al) is an extensively studied MOF through the Schröder group thanks to its high selectivity and uptake capacity for CO₂, SO₂ and hydrocarbons.^{7,8} It was chosen to investigate two guest-loading techniques and the effect of proton-carrier guest molecules encapsulated into the channels of the MOF on the proton conductivity.

NOTT-300(Al)-solvate has an open structure comprising chains of $[\text{AlO}_4(\text{OH})_2]$ moieties bridged by tetracarboxylate ligands. The Al(III) ion is six coordinated to oxygen atoms, with four from carboxylates O-donor $[\text{Al}-\text{O} = 1.935(1)$ and $1.929(2)$ Å] and the other two from bridging μ_2 -OH $[\text{Al}-\text{O} = 1.930(1)$ Å]. The overall connectivity affords a porous three-dimensional framework structure with square-shaped channels running through the *c*-axis with hydroxyl groups protruding into them, endowing the pore environment with free hydroxyl groups in four different directions (Figure 5.2). Taking into account the van der Waals radii of the surface atoms the channel window size is $\sim 6.5 \times 6.5$ Å.⁷

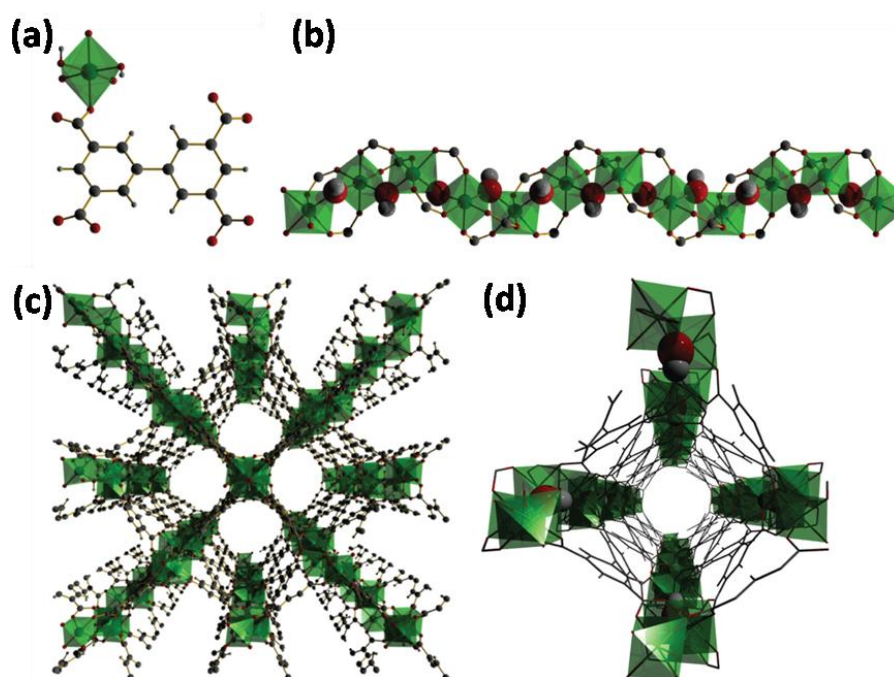


Figure 5.2 Structure of NOTT-300(Al)-solvate. (a) Coordination environment for the ligand (biphenyl-3,3',5,5'-tetracarboxylic acid) and the Al(III) centre. (b) View of the corner-sharing extended octahedral chain of $[\text{AlO}_4(\text{OH})_2]_\infty$. The μ_2 -(OH) groups are highlighted as a space-filling model. (c) View of the 3D framework structure with a channel formed along the *c*-axis. (d) View of the square-shaped channel. Aluminium (green); carbon (grey); oxygen (red); hydrogen (white).⁷

The porous nature of the MOF allows NOTT-300(Al) to be viewed as an ideal candidate for guest incorporation for proton conducting applications. In this work, imidazole was chosen as proton transfer agent for its available protons and amphiprotic nature, analogous to that of water. Superior to water media, imidazole with high melting and boiling point can potentially support stable proton transport pathways in a wide temperature range. With imidazole being much smaller (approx. 4.3 x 3.7 Å) compared to the channel window of the NOTT-300(Al) (6.5 x 6.5 Å), its introduction as a guest into the pores of the MOF is expected to be achieved.^{6,7,9} Two different approaches to incorporate guest molecules in NOTT-300(Al) were investigated; the vapour diffusion and solvation methods. In the vapour diffusion method guest molecules were loaded into the channels of the MOF by vaporisation under vacuum and high temperatures (90 °C). The solvation method involved addition of imidazole solutions in methanol to the MOF over a few days.

5.1.2 Aims of Chapter 5

Postsynthetic modification of MOFs through the insertion of proton-carrier guest molecules is a promising approach to access new materials with improved proton conductivity properties. The aim of this Chapter is to test this strategy and introduce a very preliminary study on this field which can offer the basis for new ideas and more extensive research in future.

In Chapter 5, NOTT-300(Al) was post-synthetically modified by the encapsulation of imidazole guest molecules into the channels of the MOF through vapour diffusion and solvation methods, leading to the synthesis of Im@NOTT-300(Al)-(d) and Im@NOTT-300(Al)-(s), respectively. The concentration of guest molecules in Im@NOTT-300(Al)-(d) and Im@NOTT-300(Al)-(s) was determined by CHN and

TGA analyses after carefully removing the imidazole accumulated on the surface and non-coordinated to the MOF. PXRD data revealed the structure of NOTT-300(Al) was retained in both complexes without any distortion due to the presence of imidazole in the channels. Impedance studies were performed at 20 °C and 99 % RH on Im@NOTT-300(Al)-(d) and Im@NOTT-300(Al)-(s) and compared with NOTT-300(Al) to investigate the effect induced by the presence of proton-carriers guest on the proton conductivity.

5.2 Results and Discussion

5.2.1 Synthesis of Im@NOTT-300(Al) by vapour diffusion (d)

NOTT-300(Al) was synthesised from biphenyl-3,3',5,5'-tetracarboxylic acid, H_4L^4 , and $Al(NO_3)_3 \cdot 9H_2O$ following the experimental conditions reported in the literature.⁷ Repeating the synthesis of the well-known H_4L^4 ligand was beyond the scope of this work and it was purchased. The solvated NOTT-300(Al) was synthesised as a microcrystalline powder by hydrothermal reaction of H_4L^4 and $Al(NO_3)_3 \cdot 9H_2O$ in water containing HNO_3 and piperazine, for 3 days at 210 °C. Removal of solvent molecules within the pores was achieved by suspending NOTT-300(Al) in acetone over a period of four days with fresh solvent exchanges three times per day. NOTT-300(Al) was then heated at 90 °C under vacuum.

Imidazole (Im) guest molecules were loaded into the activated NOTT-300(Al) by vapour diffusion technique. Imidazole and NOTT-300(Al) were placed in two different vials and enclosed inside a Schlenk flask under vacuum at 90 °C for three days. Imidazole (mp 89 °C) sublimates and diffuses over the gas phase into NOTT-300(Al) leading to Im@NOTT-300(Al)-(d). One of the aims of this work was to post-synthetically modify NOTT-300(Al) by insertion of non-volatile proton-carrier

guests confined in the channels and strongly interacting with the framework. Therefore, guest molecules weakly bound to the framework or deposited on the outer surface were removed. At this end, after vapour diffusion the MOF was repeatedly washed with methanol over the course of eight days to remove non-coordinated heterocycle molecules. Imidazole is highly soluble in methanol whilst NOTT-300(Al) is stable in such solvent. CHN analyses were recorded every 2 days to monitor the concentration of imidazole in NOTT-300(Al). Once a stable CHN was obtained, a timeframe was provided of when non-coordinated guest molecules are no longer removable by washing. The results indicated the washing of the loaded MOF can be stopped after 6 days. In Table 5.1 are summarised CHN results obtained after washing Im@NOTT-300(Al)-(d) for a certain number of days and the correspondent calculated molecular formulae. For direct comparison, the activated NOTT-300(Al) was also suspended in methanol for a few hours, dried in air and CHN was recorded.

Table 5.1 CHN analyses of NOTT-300(Al) and Im@NOTT-300(Al)-(d).

NOTT-300(Al) – MeOH			
Formula	$\{Al_2(OH)_2(C_{16}O_8H_6)(Al_2O_3)(CH_4O)_2\}_\infty$		
CHN	% C	% H	% N
	Calc.: 37.26	Calc.: 2.78	Calc.: 0
	Found: 37.04	Found: 2.90	Found: 0
Im@NOTT-300(Al)-(d) After washing for 2 days			
Formula	$\{Al_2(OH)_2(C_{16}O_8H_6)(Al_2O_3)(CH_4O)_2(C_3N_2H_4)_{0.80}\}_\infty$		
CHN	% C	% H	% N
	Calc.: 38.60	Calc.: 3.05	Calc.: 3.53
	Found: 38.42	Found: 3.15	Found: 3.51
Im@NOTT-300(Al)-(d) After washing for 4 days			
Formula	$\{Al_2(OH)_2(C_{16}O_8H_6)(Al_2O_3)(CH_4O)_2(C_3N_2H_4)_{0.65}\}_\infty$		
CHN	% C	% H	% N
	Calc.: 38.37	Calc.: 3.00	Calc.: 2.92
	Found: 37.90	Found: 3.12	Found: 2.80
Im@NOTT-300(Al)-(d) After washing for 6 days			
Formula	$\{Al_2(OH)_2(C_{16}O_8H_6)(Al_2O_3)(CH_4O)_2(C_3N_2H_4)_{0.61}\}_\infty$		
CHN	% C	% H	% N
	Calc.: 38.31	Calc.: 2.99	Calc.: 2.75
	Found: 38.20	Found: 3.01	Found: 2.69
Im@NOTT-300(Al)-(d) After washing for 8 days			
Formula	$\{Al_2(OH)_2(C_{16}O_8H_6)(Al_2O_3)(CH_4O)_2(C_3N_2H_4)_{0.60}\}_\infty$		
CHN	% C	% H	% N
	Calc.: 38.29	Calc.: 2.99	Calc.: 2.71
	Found: 38.25	Found: 3.04	Found: 2.67

The presence of nitrogen highlighted by elemental analyses suggests the incorporation of guest-heterocycle into the channels of NOTT-300(Al) and the successful synthesis of stable Im@NOTT-300(Al)-(d) after washing the MOF with methanol for 6 days. This study was initially performed on a small amount of sample

with intention of testing the guest loading methodology; the same procedure was subsequently repeated on larger scale of sample to allow for full characterisation and analysis. Evidences of the reproducibility of the method are highlighted in Table 5.2 which summarise the results obtained for the two different batches of samples.

Table 5.2 Comparison of CHN analyses of Im@NOTT-300(Al)-(d) (1st time) and Im@NOTT-300(Al)-(d) (2nd time).

Im@NOTT-300(Al)-(d) After washing for 6 days (1st time)			
Formula	$\{Al_2(OH)_2(C_{16}O_8H_6)(Al_2O_3)(CH_4O)_2(C_3N_2H_4)_{0.61}\}_\infty$		
CHN	% C	% H	% N
	Calc.: 38.31	Calc.: 2.99	Calc.: 2.75
	Found: 38.20	Found: 3.01	Found: 2.69
Im@NOTT-300(Al)-(d) After washing for 6 days (2nd time)			
Formula	$\{Al_2(OH)_2(C_{16}O_8H_6)(Al_2O_3)(CH_4O)_2(C_3N_2H_4)_{0.61}\}_\infty$		
CHN	% C	% H	% N
	Calc.: 38.31	Calc.: 2.99	Calc.: 2.75
	Found: 38.22	Found: 3.02	Found: 2.70

5.2.2 Characterisation of Im@NOTT-300(Al)-(d)

PXRD data of NOTT-300(Al) and Im@NOTT-300(Al)-(d) were recorded on a PANalytical X'Pert PRO diffractometer (Figure 5.3). After loading imidazole in NOTT-300(Al) by vapour diffusion technique, the MOF retained its structure without distortions. This suggests imidazole molecules are trapped into the pores of NOTT-300(Al) and likely interact with the channel walls of the MOF through intermolecular interactions to be strongly retained in the pores. Attempts to index the PXRD pattern and localised the imidazole trapped into the pores were not successful due to the low quality of the data. However, this is a promising approach to localise guest molecules into the pores in order to identify the proton-hopping pathway. This

would allow a better knowledge of the system and could represent a starting point for future investigation and design of new materials.

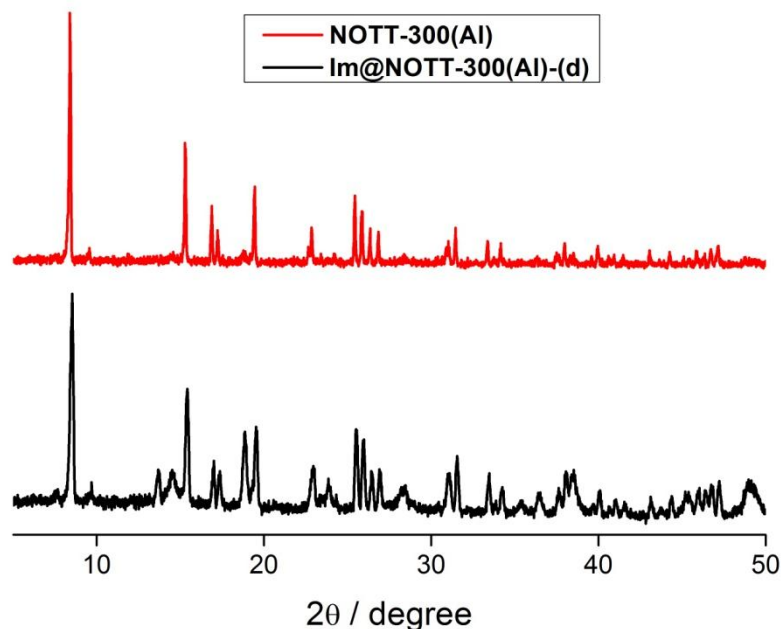


Figure 5.3 Comparison between PXRD patterns for NOTT-300(Al) (*red*) and Im@NOTT-300(Al)-(d) (*black*).

To further confirm the presence of imidazole into the pores of NOTT-300(Al), thermogravimetric analysis of Im@NOTT-300(Al)-(d) was recorded. For direct comparison, TGA of NOTT-300(Al) activated and subsequently suspended in methanol and dried in air (Section 5.2.1) was recorded. Thermal gravimetric analyses were performed from 25 to 800 °C with heating rate of 5 °C per minute at ambient pressure under a flow of air (Figure 5.4).

The TGA plot of NOTT-300(Al) shows an initial loss of solvent below 100 °C of ~10 % in mass which was assigned to two molecules of methanol. The MOF is stable up to 400 °C; above which temperature it starts to decompose. The TGA of Im@NOTT-300(Al)-(d) shows analogous loss of solvent molecules (about 10 % in

weight below 100 °C) compared with NOTT-300(Al). A second step of weight loss at about 200 °C was observed in the case of Im@NOTT-300(Al)-(d); this was assigned to the loss of imidazole incorporated into the channels of the MOF. According to the amphiphilic nature of the surface channel, the guest imidazole molecules likely interact with the hydrophilic sites of bridging μ_2 -OH or carboxylate group and are released at this higher temperature.

The findings from the TGA confirm that the vapour diffusion method of loading guest-molecules was successful; these results are in agreement with CHN elemental analysis confirming the proposed formula of Im@NOTT-300(Al)-(d) being $\{Al_2(OH)_2(C_{16}O_8H_6)(Al_2O_3)(CH_4O)_2(C_3N_2H_4)_{0.61}\}_\infty$. The presence of imidazole into the pores of NOTT-300(Al) has the potential to yield interesting results with regards to proton conductivity.

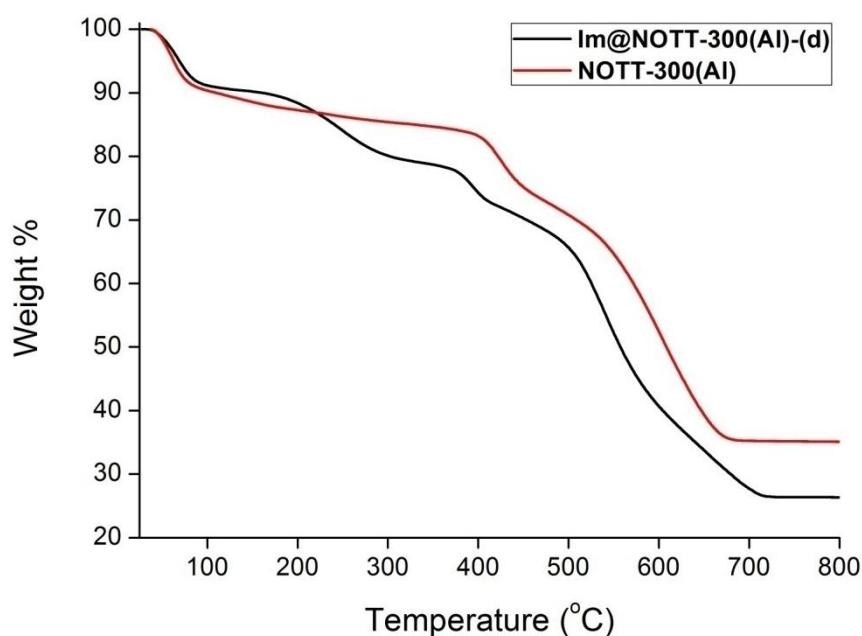


Figure 5.4 Thermogravimetric profiles of NOTT-300(Al) and Im@NOTT-300(Al)-(d) recorded under a flow of air at heating rate of 5 °C min⁻¹.

5.2.3 Proton Conductivity study of NOTT-300(Al) and Im@NOTT-300(Al)-(d)

The proton conductivity of NOTT-300(Al) and Im@NOTT-300(Al)-(d) was investigated by AC impedance spectroscopy on compact pellets using cell A (Section 2.2.3.1). For each MOF about 0.120 g of sample was ground into a fine powder using mortar and pestle, sandwiched between two discs of carbon film (Sigracet GDL, 10 BB) and pressed for 5 minutes under a pressure of 5 tons using a die with 0.8 cm diameter. The resulting thickness of each pellet was measured and, together with the diameter, was used to calculate the proton conductivity of the MOFs (Section 2.1.6, Equation 10). For each sample three measurements were collected at the investigated value of % RH and temperature and the standard deviation was calculated and indicated in brackets next to the proton conductivity value.

AC impedance measurements were performed for NOTT-300(Al) and Im@NOTT-300(Al)-(d) at 20 °C and 99 % RH (frequency range between 10 MHz to 0.1 Hz). In Figure 5.5 are shown Nyquist and Bode plots for NOTT-300(Al) and Im@NOTT-300(Al)-(d) together with the correspondent proton conductivity values calculated using the resistivity obtained by fitting the well defined semi-circles (Table 5.3).

Nyquist plots measured for the two MOFs are typical of materials with predominant ionic conductivity. Both contain a semi-circle plot in the high frequency region and a tail at low frequencies which indicates the blocking of protons at the electrode. The semi-circle plot in the high-frequency region represents the bulk resistance of the MOF.

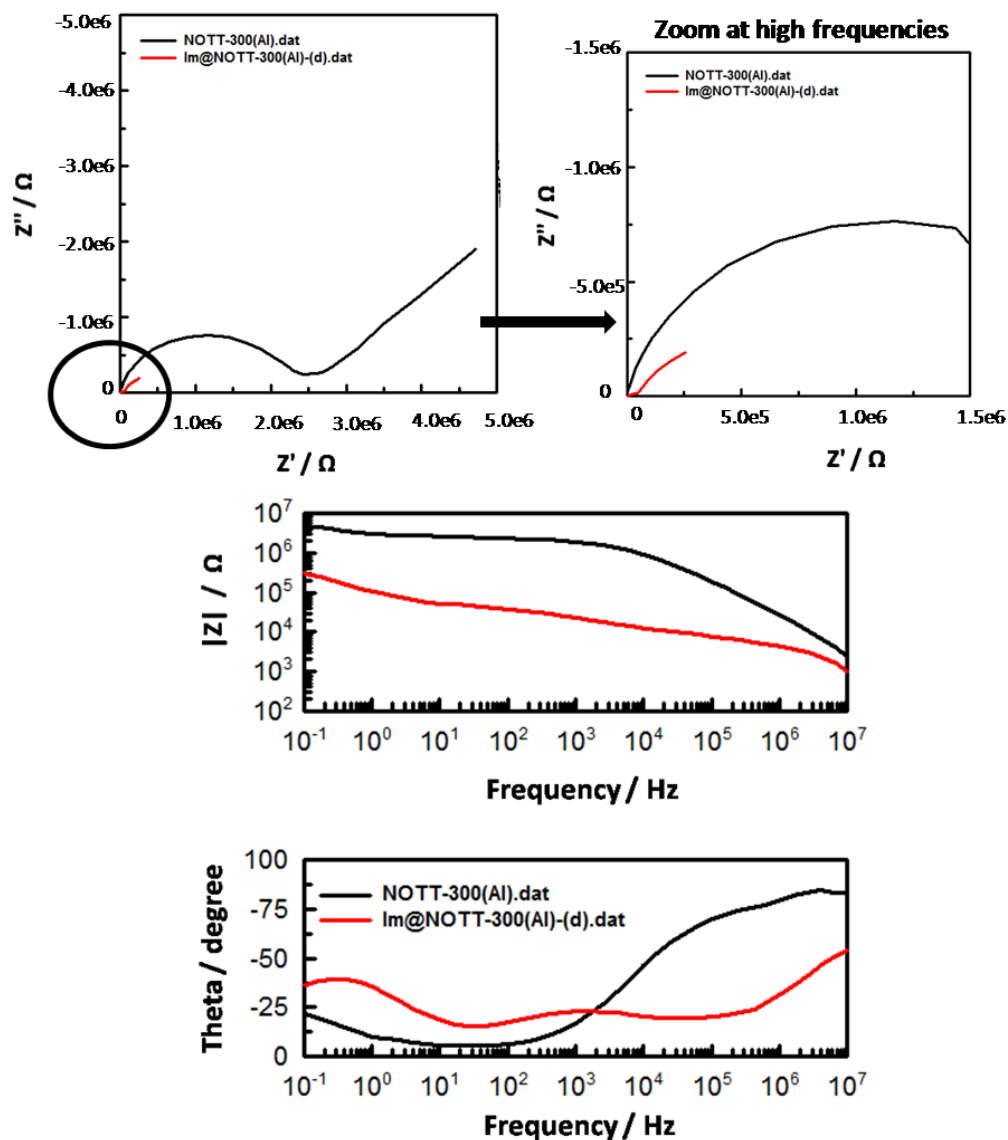


Figure 5.5 Nyquist and Bode plots for NOTT-300(Al) (*black*) and Im@NOTT-300(Al)-(d) (*red*) measured at 99 % RH and 20 °C.

Table 5.3 Proton conductivities (S cm^{-1}) for NOTT-300(Al) and Im@NOTT-300(Al)-(d) measured at 99 % RH and 20 °C.

	NOTT-300(Al)	Im@NOTT-300(Al)-(d)
Proton Conductivity	$1.00(10) \times 10^{-7}$	$2.00(11) \times 10^{-5}$

NOTT-300(Al) shows a proton conductivity of $1.08 \times 10^{-7} \text{ S cm}^{-1}$ at 99 % RH and 20 °C. The low conductivity of NOTT-300(Al) was expected and assigned to the presence of small concentration of protons located further apart to each other; the low conductivity mainly relies on the presence of water molecules deriving from the high humidity conditions interacting with the framework. The proton conductivity of Im@NOTT-300(Al)-(d) measured at 20 °C and 99 % RH is $2.39 \times 10^{-5} \text{ S cm}^{-1}$. The comparison between the proton conductivity of NOTT-300(Al) and Im@NOTT-300(Al)-(d) shows a remarkable increase of two orders of magnitude in the case of Im@NOTT-300(Al)-(d) confirming the role of imidazole as a proton-carrier which significantly increases the proton conductivity of the complex (Table 5.3). The increase in proton conductivity clearly proves the success of the strategy; loading proton-carrier guests into the pores of a MOF positively impacts the proton conducting property of a material.

Post-proton conductivity of NOTT-300(Al) and Im@NOTT-300(Al)-(d):

The retention of the structure after compressing the MOFs into pellets and during the analysis was investigated by PXRD analyses performed on the samples after the impedance experiments. In Figure 5.6 is shown the comparison between PXRD patterns of as-synthesised NOTT-300(Al) and NOTT-300(Al) and Im@NOTT-300(Al)-(d) after impedance measurements; experimental evidences show stability of the MOFs and retention of the structure.

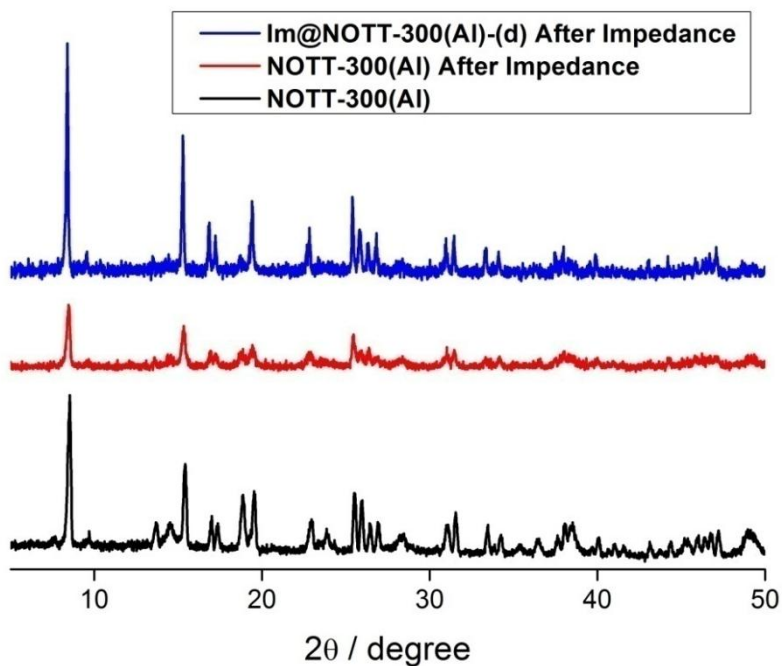


Figure 5.6 Comparison between PXRD patterns for as-synthesised NOTT-300(Al) (*black*) and NOTT-300(Al) (*red*) and Im@NOTT-300(Al)-(d) (*blue*) after impedance measurements.

5.2.4 Synthesis of Im@NOTT-300(Al) by solvation (s)

An alternative methodology of loading proton-carrier guests into the pores of a MOF is the solvation method (s). For direct comparison with the vapour diffusion approach, imidazole was loaded into the pores of NOTT-300(Al); characterisation of the resulting Im@NOTT-300(Al)-(s) and impedance studies were performed.

Activated NOTT-300(Al) was synthesised (Section 5.2.1) and imidazole was loaded into the channels of the framework by solvation method. Imidazole was dissolved in methanol and the solution was added to the activated NOTT-300(Al), with the mixture heated at 40 °C for 72 h. Fresh imidazole solutions were added once per day to ensure saturation. As for the diffusion method, the sample was then washed with methanol to ensure the imidazole molecules simply deposited on the surface of the MOF and non-coordinated were removed. CHN analysis were measured every two

days to monitor the concentration of the heterocycles loaded into the MOF and provide a period of time when a stable CHN was obtained. This would correspond with the maximum amount of imidazole coordinated with the MOF and non removable by washing.

In Table 5.4 are summarised CHN results obtained after washing Im@NOTT-300(Al)-*(s)* for eight days and the correspondent calculated molecular formulae. For direct comparison, the activated NOTT-300(Al) was also suspended in methanol for a few hours, dried in air and CHN was recorded. Similarly with the diffusion method, the results indicated the washing of the loaded MOF can be stopped after 6 days.

Table 5.4 CHN analyses of NOTT-300(Al) and Im@NOTT-300(Al)-(s).

NOTT-300(Al) - MeOH			
Formula	$\{Al_2(OH)_2(C_{16}O_8H_6)(Al_2O_3)(CH_4O)_2\}_\infty$		
CHN	% C	% H	% N
	Calc.: 37.26	Calc.: 2.78	Calc.: 0
	Found: 37.04	Found: 2.90	Found: 0
Im@NOTT-300(Al)-(s) After washing for 2 days			
Formula	$\{Al_2(OH)_2(C_{16}O_8H_6)(Al_2O_3)(CH_4O)_2(C_3N_2H_4)_{0.82}\}_\infty$		
CHN	% C	% H	% N
	Calc.: 38.64	Calc.: 3.06	Calc.: 3.61
	Found: 38.15	Found: 3.12	Found: 3.59
Im@NOTT-300(Al)-(s) After washing for 4 days			
Formula	$\{Al_2(OH)_2(C_{16}O_8H_6)(Al_2O_3)(CH_4O)_2(C_3N_2H_4)_{0.65}\}_\infty$		
CHN	% C	% H	% N
	Calc.: 38.37	Calc.: 3.00	Calc.: 2.92
	Found: 38.09	Found: 3.15	Found: 2.83
Im@NOTT-300(Al)-(s) After washing for 6 days			
Formula	$\{Al_2(OH)_2(C_{16}O_8H_6)(Al_2O_3)(CH_4O)_2(C_3N_2H_4)_{0.61}\}_\infty$		
CHN	% C	% H	% N
	Calc.: 38.31	Calc.: 2.99	Calc.: 2.75
	Found: 38.18	Found: 2.88	Found: 2.73
Im@NOTT-300(Al)-(s) After washing for 8 days			
Formula	$\{Al_2(OH)_2(C_{16}O_8H_6)(Al_2O_3)(CH_4O)_2(C_3N_2H_4)_{0.60}\}_\infty$		
CHN	% C	% H	% N
	Calc.: 38.29	Calc.: 2.99	Calc.: 2.71
	Found: 38.24	Found: 2.96	Found: 2.69

CHN elemental analyses of these materials revealed a significant enhancement in the composition of nitrogen in NOTT-300(Al) through guest loading. This suggests incorporation of guest-heterocycle into the channels of NOTT-300(Al) and the successful synthesis of stable Im@NOTT-300(Al)-(s) after washing the complex for

6 days. (Table 5.5). These results are also concurrent with the vapour diffusion method. Interesting, both methods shows concentration loading of guest molecules coordinated to the MOFs which suggests the maximum amount able to coordinate with the framework was loaded. This study was initially performed on a small amount of sample with intention of testing the guest loading methodology; same procedure was subsequently repeated on larger scale of sample to allow for complete characterisation and analysis. Evidences of the reproducibility of the method are shown in Table 5.5 which summarise the results obtained for the two different batches of samples.

Table 5.5 Comparison of CHN analyses of Im@NOTT-300(Al)-(s) (1st time) and Im@NOTT-300(Al)-(s) (2nd time).

Im@NOTT-300(Al)-(s) After washing for 6 days (1st time)			
Formula	$\{Al_2(OH)_2(C_{16}O_8H_6)(Al_2O_3)(CH_4O)_2(C_3N_2H_4)_{0.61}\}_\infty$		
CHN	% C	% H	% N
	Calc.: 38.31	Calc.: 2.99	Calc.: 2.75
	Found: 38.18	Found: 2.88	Found: 2.73
Im@NOTT-300(Al)-(s) After washing for 6 days (2nd time)			
Formula	$\{Al_2(OH)_2(C_{16}O_8H_6)(Al_2O_3)(CH_4O)_2(C_3N_2H_4)_{0.61}\}_\infty$		
CHN	% C	% H	% N
	Calc.: 38.31	Calc.: 2.99	Calc.: 2.75
	Found: 38.26	Found: 2.91	Found: 2.69

5.2.5 Characterisation of Im@NOTT-300(Al)-(s)

PXRD of NOTT-300(Al) and Im@NOTT-300(Al)-(s) exhibit the same pattern meaning that the structure of NOTT-300(Al) is intact after postsynthetic modification by loading guest molecules (Figure 5.7). As with what observed for Im@NOTT-300(Al)-(d), imidazole molecules are trapped into the pores of NOTT-

300(Al) and likely interact with the channel walls of the MOF through intermolecular interactions.

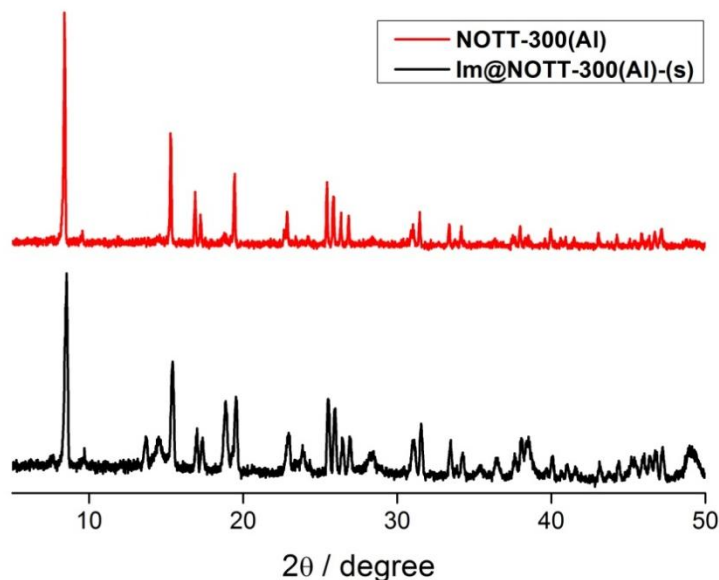


Figure 5.7 Comparison between PXRD patterns for NOTT-300(Al) (*red*) and Im@NOTT-300(Al)-(s) (*black*).

To confirm the presence of imidazole trapped into the pores of the MOF, thermogravimetric analysis were recorded for Im@NOTT-300(Al)-(s) and compared with NOTT-300(Al) activated and subsequently suspended in methanol and dried in air (Figure 5.8). Thermal gravimetric analyses were performed from 25 to 800 °C with heating rate of 5 °C per minute at ambient pressure under a flow of air. As previously discussed in Section 5.2.2, the TGA plot of NOTT-300(Al) shows an initial loss of solvent below 100 °C of ~10 % in mass which was assigned to two molecules of methanol. The MOF is stable up to 400 °C; above which temperature it starts to decompose. The TGA of Im@NOTT-300(Al)-(s) shows analogous loss of solvent molecules (about 10 % in weight below 100 °C) compared with NOTT-300(Al). Interestingly, the TGA profiles of Im@NOTT-300(Al)-(s) highlight a

significant step of decomposition around 200 °C which is not present in NOTT-300(Al); this was attributed to the release of accommodated guest-heterocycles trapped into the pores. The findings from the TGA confirm that the solvation method of loading guest-molecules was successful. By combining the CHN and TGA results it was possible to derive the formula of the guest loaded MOF being $\{Al_2(OH)_2(C_{16}O_8H_6)(Al_2O_3)(CH_4O)_2(C_3N_2H_4)_{0.61}\}_\infty$ for Im@NOTT-300(Al)-(s). The results are concurrent with the vapour diffusion method.

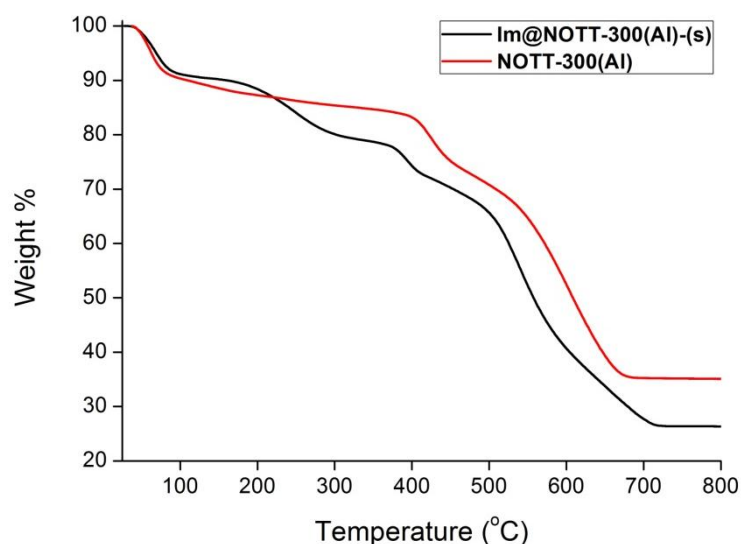


Figure 5.8 Thermogravimetric profiles of NOTT-300(Al) and Im@NOTT-300(Al)-(s).

5.2.6 Proton Conductivity study of NOTT-300(Al) and Im@NOTT-300(Al)-(s)

Proton conductivity of NOTT-300(Al) and Im@NOTT-300(Al)-(s) was investigated by AC impedance spectroscopy on compact pellets using cell A (Section 2.2.3.1). For each MOF about 0.120 g of sample was ground into a fine powder using mortar and pestle, sandwiched between two discs of carbon film (Sigracet GDL, 10 BB) and pressed for 5 minutes under a pressure of 5 tons using a die with 0.8 cm diameter.

For each sample three measurements were collected at the investigated value of % RH and temperature and the standard deviation was calculated and indicated in brackets next to the proton conductivity value. Measurements were repeated twice on different batch samples to ensure reproducibility of the data.

AC impedance measurements were performed for NOTT-300(Al) and Im@NOTT-300(Al)-(s) at 20 °C and 99 % RH (frequency range between 10 MHz and 0.1 Hz). Figure 5.9 depicts that both MOFs have plots characteristic of proton conducting materials; both contain a semi-circle in the high frequency region which represents the bulk resistance of the MOF and a tail at low frequencies indicating blocking of protons at the electrode. The proton conductivity data for each MOFs was calculated from the Nyquist plots and summarised in Table 5.6.

The low proton conductivity of NOTT-300(Al) ($1.00(12) \times 10^{-7} \text{ S cm}^{-1}$ at 20 °C and 99 % R) was discussed in Section 5.2.3. Im@NOTT-300(Al)-(s) shows a significant increase in proton conductivity of two orders of magnitude ($1.00(37) \times 10^{-5} \text{ S cm}^{-1}$ at 20 °C and 99 % R) compared with NOTT-300(Al). These results are concurrent with those obtained with the vapour diffusion method confirming the role of imidazole as proton-carrier in the channels of the MOF to assist proton conductivity.

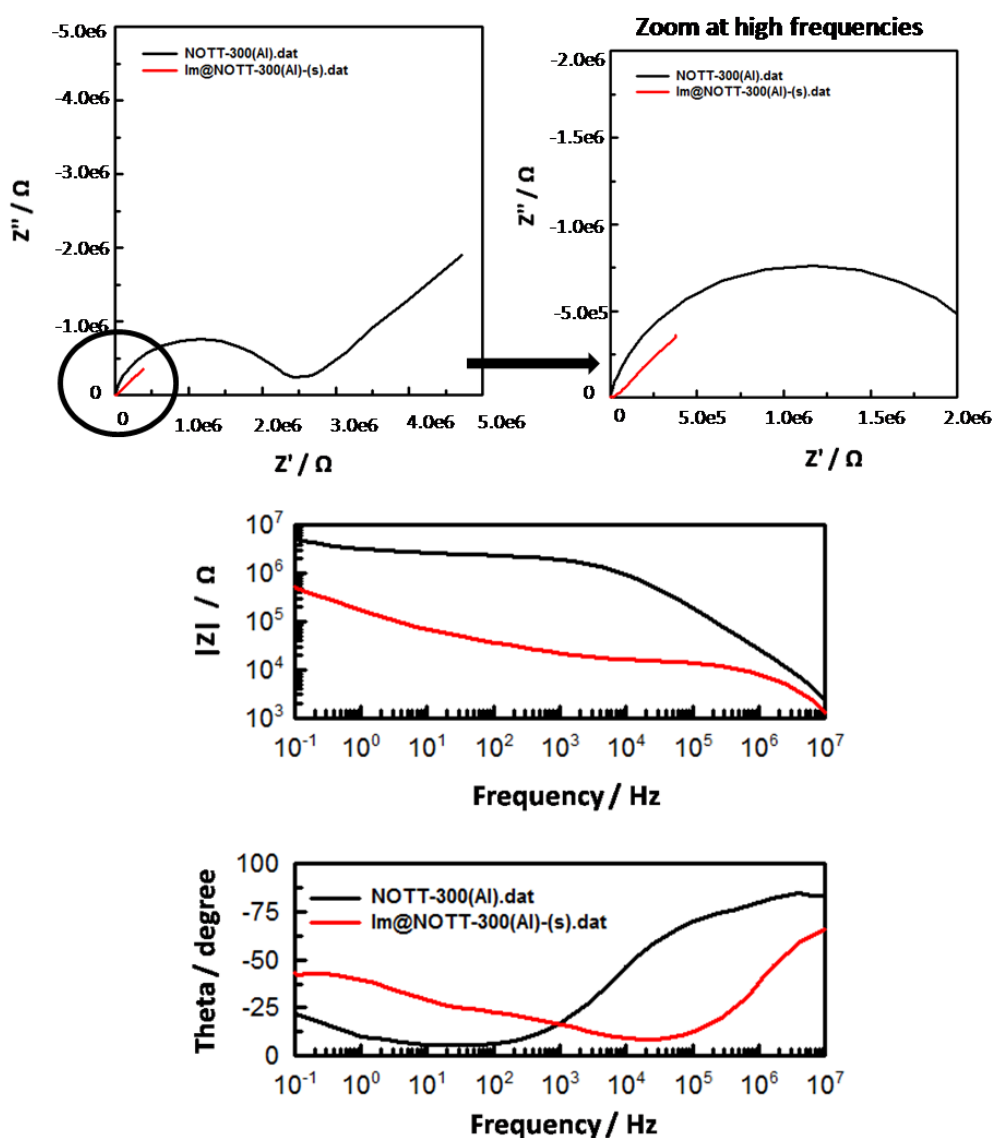


Figure 5.9 Nyquist and Bode plots for NOTT-300(Al) (*black*) and Im@NOTT-300(Al)-(s) (*red*) measured at 99 % RH and 20 °C.

Table 5.6 Proton conductivities (S cm^{-1}) for NOTT-300(Al) and Im@NOTT-300(Al)-(s) and measured at 99 % RH and 20 °C.

	NOTT-300(Al)	Im@NOTT-300(Al)-(s)
Proton Conductivity	$1.00(10) \times 10^{-7}$	$1.00(13) \times 10^{-5}$

Post proton conductivity of NOTT-300(Al) and Im@NOTT-300(Al)-(s):

PXRD analyses were performed to determine the stability of MOFs after being compressed into pellets and post impedance measurements. Figure 5.10 shows stability of NOTT-300(Al) and Im@NOTT-300(Al)-(d) after impedance analysis and retention of crystalline compared with as-synthesised NOTT-300(Al).

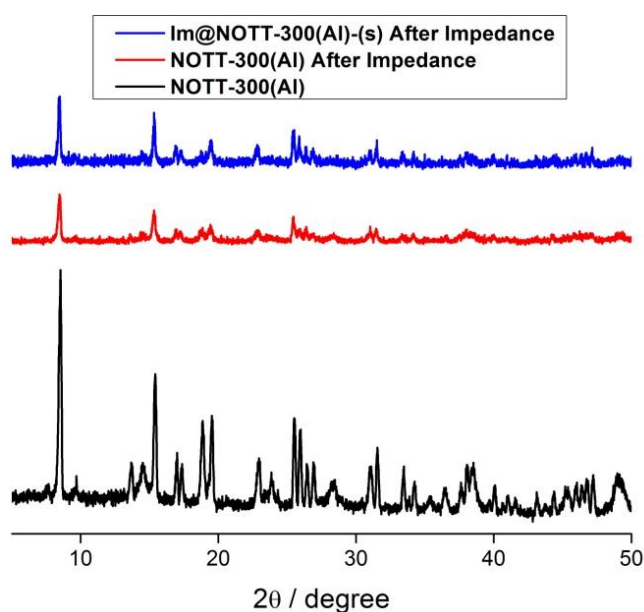


Figure 5.10 Comparison between PXRD patterns for as-synthesised NOTT-300(Al) (*black*) and NOTT-300(Al) (*red*) and Im@NOTT-300(Al)-(s) (*blue*) after impedance measurements.

5.3 Conclusions and future perspectives

Doping MOFs through post-synthetic insertion of proton-carrier guest molecules into the pores of the framework is a promising approach to enhance the proton conductivity properties of a material. In Chapter 5 were presented two different approaches to incorporate imidazole into the channels of NOTT-300(Al); vapour diffusion (d) and solvation (s) methods. Excess of imidazole non-coordinated or simply accumulated on the outer surface of the MOF was eliminated affording

Im@NOTT-300(Al)-(d) and Im@NOTT-300(Al)-(s). In both complexes a similar concentration of imidazole loaded inside the channels was determined. At 20 °C and 99 % RH, the proton conductivity of Im@NOTT-300(Al)-(d) and Im@NOTT-300(Al)-(s) was $2.00(11) \times 10^{-5} \text{ S cm}^{-1}$ and $1.00(13) \times 10^{-5} \text{ S cm}^{-1}$, respectively. These values are two order of magnitude higher compared with the proton conductivity of NOTT-300(Al) measured at the same experimental conditions ($1.00(10) \times 10^{-7} \text{ S cm}^{-1}$ at 20 °C and 99 % RH). Bulk imidazole has a known proton conductivity of $10^{-8} \text{ S cm}^{-1}$;^{3,6,9} the much higher proton conductivity in Im@NOTT-300(Al)-(d) and Im@NOTT-300(Al)-(s) is likely to be the result of the cooperation between the structure of NOTT-300(Al) and the heterocycle encapsulated into the channels. The similar results obtained after treating the MOF at different conditions (vapour diffusion and solvation) might suggest that the maximum concentration of imidazole bound into the channels was loaded.

These findings highlight that the idea of loading proton-carriers into the low conducting NOTT-300(Al) result in a vast improvement of the proton conduction which directly arise from the increased number of acidic protons in the channels of the MOF. The work presented in this Chapter only represents a preliminary stage of the research in this area; it provides a platform for more detailed studies and more work needs to be carried out in the future.

Future work on this area is suggested in three directions. Firstly, impedance analyses in a wide range of temperatures and % RH would be interesting to further investigate the proton conductivity properties of Im@NOTT-300(Al)-(d) and Im@NOTT-300(Al)-(s). Studies addressed to crystallographically determine the position of imidazole inside the channels of NOTT-300(Al) might give further insights on the proton-hopping pathway of the newly postsynthetic modified complexes. Finally,

attempts to encapsulate a variety of guests molecules into the frameworks, such as triazole and even more appealing proton-rich carrier guests based on phosphonate groups, are recommended.

5.4 Experimental Section

PXRD, TGA and impedance experimental details are fully discussed in the Experimental Section at the end of this Thesis.

5.4.1 Synthesis of the activated NOTT-300(Al)

Biphenyl-3,3',5,5'-tetracarboxylic acid, H_4L^4 , (0.0600 g, 0.182 mmol), $Al(NO_3)_3 \cdot 9H_2O$ (0.3400 g, 0.906 mmol) and piperazine (0.10 g, 1.26 mmol) were suspended in 10 mL of water. A 2.8 M solution of HNO_3 in H_2O (2.0 mL) was added to the ligand-metal mixture. The PARR pressure vessel was sealed, heated in the oven at 210 °C for 3 days and cooled to room temperature. The crystalline powder obtained was separated by filtration, washed with water and dried in air.⁷ The solvent exchanged material was prepared by suspending NOTT-300(Al) in acetone over a period of four days with fresh solvent exchanges three times per day. The acetone was removed by heating the sample at 90 °C for 24 h under reduced pressure in a Schlenk flask. For direct comparison with the postsynthetic modified MOFs, the activated NOTT-300(Al) was suspended in methanol for a few hours and dried in air before its characterisation leading to $\{Al_2(OH)_2(C_{16}O_8H_6)(Al_2O_3)(CH_4O)_2\}_\infty$. Elemental analysis (%): anal. calc. for $C_{18}H_{16}O_{15}Al_4$: C 37.26, H 2.78, N 0.00; found: C 37.04, H 2.90, N 0.00. FTIR: ν (cm^{-1}) = 3653 (w), 3298 (w), 3096 (w), 1703 (s), 1625 (m), 1569 (s), 1439 (s), 1390 (s), 1365 (m), 1317 (m), 1068 (s), 991 (m), 913 (s), 807 (m), 787 (s), 734 (m), 722 (m), 669 (m).

5.4.2 Synthesis of Im@NOTT-300(Al)-(d)

Imidazole (0.400 g, 5.876 mmol) and NOTT-300(Al) (0.250 g, 0.431 mmol) were placed in two different vials and enclosed inside a Schlenk flask at 90 °C under reduced pressure for 3 days. The product was repeatedly washed with methanol over the course of 6 days with regular exchange of fresh solvent twice a day to remove non-coordinated heterocycle molecules to yield Im@NOTT-300(Al)-(d), $\{\text{Al}_2(\text{OH})_2(\text{C}_{16}\text{O}_8\text{H}_6)(\text{Al}_2\text{O}_3)(\text{CH}_4\text{O})_2(\text{C}_3\text{N}_2\text{H}_4)_{0.61}\}_\infty$. Elemental analysis (%): anal. calc. for $\text{C}_{19.83}\text{H}_{18.44}\text{O}_{15}\text{Al}_4\text{N}_{1.22}$: C 38.31, H 2.99, N 2.75; found: C 38.22, H 3.02, N 2.70. FTIR: ν (cm^{-1}) = 3653 (m), 3282 (w), 3106 (w), 1710 (s), 1623 (m), 1564 (s), 1434 (s), 1388 (s), 1366 (s), 1314 (m), 1060 (m), 992 (m), 908 (s), 819 (m), 787 (s), 737 (m), 721 (s), 661 (m).

5.4.3 Synthesis of Im@NOTT-300(Al)-(s)

Imidazole (0.400 g, 5.876 mmol) was dissolved in MeOH (30 mL) and the solution was added to the activated NOTT-300(Al) (0.250 g, 0.431 mmol), with the mixture heated at 40 °C for 3 days. The mixture was exchanged once per day with fresh imidazole solutions. The product was isolated by filtration and repeatedly washed with methanol over the course of 6 days with regular exchange of fresh solvent twice a day to remove non-coordinated heterocycle molecules to yield Im@NOTT-300(Al)-(s) with molecular formula $\{\text{Al}_2(\text{OH})_2(\text{C}_{16}\text{O}_8\text{H}_6)(\text{Al}_2\text{O}_3)(\text{CH}_4\text{O})_2(\text{C}_3\text{N}_2\text{H}_4)_{0.61}\}_\infty$. Elemental analysis (%): anal. calc. for $\text{C}_{19.83}\text{H}_{18.44}\text{O}_{15}\text{Al}_4\text{N}_{1.22}$: C 38.31, H 2.99, N 2.75; found: C 38.26, H 2.91, N 2.69. FTIR: ν (cm^{-1}) = 3649 (w), 3291 (w), 3082 (w), 1714 (m), 1614 (m), 1566 (s), 1434 (s), 1386 (s), 1364 (w), 1319 (w), 1078 (m), 991 (s), 911 (s), 828 (w), 791 (s), 737 (m), 721 (s), 664 (s).

5.5 References

- (1) Sadakiyo, M.; Yamada, T.; Kitagawa, H. *J. Am. Chem. Soc.* **2009**, *789*, 9906–9907.
- (2) Sadakiyo, M.; Yamada, T.; Kitagawa, H. *J. Am. Chem. Soc.* **2014**, *136*, 13166–13169.
- (3) Bureekaew, S.; Horike, S.; Higuchi, M.; Mizuno, M.; Kawamura, T.; Tanaka, D.; Yanai, N.; Kitagawa, S. *Nature Mater.* **2009**, *8*, 831–836.
- (4) Umeyama, D.; Horike, S.; Inukai, M.; Hijikata, Y.; Kitagawa, S. *Angew. Chem.* **2011**, *50*, 11706–11709.
- (5) Hurd, J.; Vaidhyanathan, R.; Thangadurai, V.; Ratcliffe, C. I.; Moudrakovski, I. L.; Shimizu, G. K. H. *Nature Chem.* **2009**, *1*, 705–710.
- (6) Liu, S.; Yue, Z.; Liu, Y. *Dalton Trans.* **2015**, *44*, 12976–12980.
- (7) Yang, S.; Sun, J.; Ramirez-Cuesta, A. J.; Callear, S. K.; David, W. I. F.; Anderson, D. P.; Newby, R.; Blake, A. J.; Parker, J. E.; Tang, C. C.; Schröder, M. *Nature Chem.* **2012**, *4* (11), 887–894.
- (8) Yang, S.; Ramirez-Cuesta, A. J.; Newby, R.; Garcia-Sakai, V.; Manuel P.; Callear, S. K.; Campbell, S. I.; Tang, C. C.; Schröder M. *Nature Chem.* **2015**, *7*, 121–129.
- (9) Ye, Y.; Zhang, L.; Peng, Q.; Wang, G.-E.; Shen, Y.; Li, Z.; Wang, L.; Ma, X.; Chen, Q.-H.; Zhang, Z.; Xiang, S. *J. Am. Chem. Soc.* **2015**, *137*, 913–918.

Chapter 6

Conclusions and future perspectives

MOFs have been recently appointed as promising proton conducting materials for use as electrolytes in PEM-FCs. Their crystalline nature offers insights into better understanding the proton conductivity mechanism and the proton-hopping pathway can be modulated through careful design of their structure by choosing specific organic ligands and metal ions.

The study of proton conductivity in MOFs is a new research area through the Schröder group. The experimental set up for impedance measurements was designed and tested for the first time becoming a key aspect of the work presented in this Thesis. Imidazole was used as a reference to test the proton conductivity cell which allow to perform reproducible impedance measurements in a wide range of temperatures (from 25 °C to 80 °C) and relative humidities (from 0 % RH to 99 % RH).

Two new isostructural MOFs, NOTT-500(Ni, Co) were synthesised from organic ligands based upon phosphonate functional groups. Their structures showed an efficient proton-hopping pathway defined by the hydroxyl groups from the ligand (P-OH) and the water molecules bound to the metal ions (M-OH₂). NOTT-500(Ni, Co) were fully characterised and impedance measurements revealed proton conductivities of $1.11(03) \times 10^{-4} \text{ S cm}^{-1}$ and $4.42(06) \times 10^{-5} \text{ S cm}^{-1}$ at 25 °C and 99 % RH for NOTT-500(Ni) and NOTT-500(Co), respectively. Proton conductivity studies at different temperatures (from 18 °C to 31 °C at 99 % RH) were performed for NOTT-500(Ni) revealing activation energy of 0.46 eV; this indicates that the proton conduction mechanism derives from the cooperation of the Grotthuss and Vehicle mechanism. QENS studies carried out at 0 % RH gave insights into the intrinsic diffusion of protons in the hopping pathway, which was best described by the

“Spherical free diffusion” model over short distances (2.65 Å). The activation energy for this diffusion process was estimated from the QENS analysis to be 0.076 eV.

Two novel approaches to enhance the proton conductivity of MOFs were designed and tested using as a starting point to investigate the two methodologies proposed a new family of lanthanide MOFs, $[M(HL^2)]$ (H_4L^2 = biphenyl-4,4'-diphosphonic acid; $M = La, Ce, Nd, Sm, Gd, Ho$). The aim of both strategies was to increase the concentration of protons within the framework to consequently enhance the proton conductivity properties of the complexes. This was achieved firstly by using the shorter version of the organic ligand to increase the number of protons in a fixed volume of framework, and secondly by substituting a 3+ metal, $Ln(III)$, with a 2+ metal, $Ba(II)$, with resulting excess of protons in the structure for charge balance. In both cases the overall structure of $[M(HL^2)]$ was retained and $[M(HL^3)]$ (H_4L^3 = benzene-1,4-diphosphonic acid; $M = La, Ce, Nd, Sm, Gd, Ho$) and $[Ba(H_2L^2)]$ were synthesised. Impedance measurements revealed the success of the two newly designed strategies; proton conductivity at 20 °C and 99 % RH was 10^{-6} S cm^{-1} for $[M(HL^2)]$, 10^{-4} S cm^{-1} for $[M(HL^3)]$ and 10^{-5} S cm^{-1} for $[Ba(H_2L^2)]$.

Preliminary studies on a previously reported strategy to increase the proton conductivity of MOFs, which consists on loading proton carrier guest molecules into the porous of the framework, were performed on NOTT-300(Al). Imidazole molecules were encapsulated into the channels of NOTT-300(Al) through vapour diffusion and solvation methods leading to the synthesis of Im@NOTT-300(Al)-(d) and Im@NOTT-300(Al)-(s), respectively. Impedance studies performed at 20 °C and 99 % RH revealed a significant increase in proton conductivity of two orders of magnitude in the case of Im@NOTT-300(Al)-(d) ($2.39(11) \times 10^{-5}$ S cm^{-1}) and

$\text{Im}@N\text{OTT-300(Al)}-(s)$ ($1.37(13) \times 10^{-5} \text{ S cm}^{-1}$) compared with $N\text{OTT-300(Al)}$ ($1.08(10) \times 10^{-7} \text{ S cm}^{-1}$).

The findings in this Thesis offer a platform for further promising research in the future. Technical improvements on the conductivity cell would allow for impedance measurements on a wider temperature range (above 80 °C) and complete the characterisation of the complexes herein presented. Quasi-elastic neutron scattering studies have not been largely exploited to investigate the proton conductivity properties of MOFs and QENS measurements at different temperatures and % RH might give access to information about the mechanism of proton conductivity in the hopping-pathway. This would be of fundamental importance to design more efficient complexes for proton conductivity applications. Test the two new strategies proposed in Chapter 4 on different MOF systems to enhance their proton conductivity and verify if the methods can be successfully applied on more systems is also of interest. Finally, study the proton conductivity of porous MOFs loaded with several proton-rich carrier guests (such as compounds with free phosphonate functional groups) and attempts to crystallographically localised them are promising advises for the future.

Experimental part and details

Chemicals and solvents. All the chemical reagents and solvents were purchased from Sigma Aldrich, Fisher or Acros Organics and used without further purification.

Mass spectrometry. Mass spectrometry was performed on a Bruker Esquire electrospray (ESI) ion-trap spectrometer with samples dissolved in the appropriate solvent. Scanning was done in both positive and negative mode from m/z . Mass spectral data are reported as m/z values.

Elemental analysis. Elemental analysis for C, H, N of all ligands and complexes were performed on a Carlo Erba 440 Elemental analyser.

NMR spectroscopy. ^1H and ^{31}P NMR spectra were obtained on Bruker DPX 300 and DPX400 spectrometers.

FTIR spectroscopy. IR spectra were collected with a Thermo Scientific Nicolet iS5-IR spectrometer in ATR sampling mode. The spectra were recorded in the frequency range between 4000 cm^{-1} to 550 cm^{-1} .

Thermo gravimetric analysis (TGA). TGA were performed on a Pyris 1 thermogravimetric analyser (Perkin Elmer) under nitrogen or air atmosphere (60-100 ml/min). The temperature was increased from room temperature to a maximum of $1000\text{ }^\circ\text{C}$ (according to the sample) with a heating rate of $5\text{ }^\circ\text{C min}^{-1}$.

Single crystal X-ray crystallography. Single crystal X-ray diffraction data were collected at Diamond light source, (DLS), Beamline I19. Data refinement were done using OLEX2 crystallographic software and SHELXTL software package. Crystal structural pictures were generated using Diamond 3.2 or Mercury 2.4 crystallographic software.

Powder X-ray crystallography (PXRD). Powder X-ray diffraction measurements were performed on a PANalytical X'Pert PRO diffractometer with Cu-K α ($\lambda = 1.5406 \text{ \AA}$). The X-ray generator was set to 40 kV and 40 mA, with 0.02 step size and 2 s step time for values of 2θ between 4° and 50° . The high temperature (HT) PXRD data was collected on PANalytical X'Pert Pro diffractometer using Cu-K α_1 radiation ($\lambda = 1.5406 \text{ \AA}$). The measurements were performed by loading the sample in an alumina plate placed in a sealed furnace.

High resolution (HR) and *in situ* variable temperature (VT) synchrotron powder X-ray diffraction (PXRD) data were collected at Beamline I11 of Diamond Light Source using a multi-analysing crystal (MAC) detector and monochromated radiation ($\lambda = 0.826162 \text{ \AA}$, $\lambda = 0.825774 \text{ \AA}$ and $\lambda = 0.825690 \text{ \AA}$ according to the Beamline visit). For the measurements, the samples were loaded in a rotating borosilicate glass capillary of diameter of 0.5 mm. During the experiment, the sample was heated under vacuum in absence of any flow of air or inert gas in a selected temperature range. The temperature was increased at a rate of $5 \text{ }^\circ\text{C}$ per minute; once the desired temperature was reached it was held for 10 minutes and a collection scan of 15 minutes was recorded.

Solid state UV-visible.

Solid state UV-vis spectra were collected on an Ocean Optics USB2000+UV-VIS-ES spectrometer using a DT-MINI-2-GS light source and a R-400-7 fibre optic reflectance probe. Spectra were collected in reflectance (R) mode and converted to F(R) using the Kubelka-Munk function.¹

1. P. Kubelka, F. Munk, *Zeits. F. Tech. Physic* **1931**, 12, 589.

Solid state NMR

Magic angle spin (MAS) ¹H and ³¹P{¹H} NMR spectra were obtained on a Bruker Avance III spectrometer in the Centre of Biomolecular Science at University of Nottingham. Bruker Avance III operates at ¹H Larmor frequency of 600.13 MHz with a 14 T narrow bore magnet. The probe head spinning used was a 2.5 mm MAS probe with a maximum rate of 35 KHz. For the 1D experiments the sample was spinning at 15 kHz and for the 2D experiments at 20 kHz.

All of the samples were dry, packed in ZrO₂ rotors and tightly sealed. The measurements were performed at room temperature. [Relaxation time for protons; T1 = 45 seconds).

Neutron scattering

Incoherent neutron scattering measurements were carried out at ISIS pulsed neutron facility, Rutherford Appleton Laboratory, using IRIS backscattering neutron spectrometer with the (002) pyrolytic graphite crystal reflection configuration.

The dynamics of the protons were probed using the high resolution quasi-elastic and inelastic neutron spectrometer IRIS; a time-of-flight inverted-geometry crystal analyser spectrometer with diffraction capabilities. In the Quasi-Elastic Neutron

Scattering (QENS) measurements, neutrons scattered from the sample are energy-analysed by means of Bragg reflection from one of two large single crystal arrays (pyrolytic graphite and muscovite mica) in close to backscattering geometry ($2\theta_B = 175^\circ$ where θ_B is the Bragg angle of the analyser crystal) and are counted in the detector array ($27^\circ < 2\theta < 158^\circ$). IRIS was operated in the PG(002) configuration which provides an energy window of $-0.5 \text{ meV} < \hbar\omega < 0.5 \text{ meV}$ and an energy resolution ΔE_{res} of $17.5 \text{ } \mu\text{eV}$. The powdered sample was loaded into an annular aluminium container having a suitable sample thickness to minimise multiple scattering effects.

The QENS data were collected at 180 K (for resolution), 213 K, 250 K, 273 K, 300 K, 313 K, 333 K, 353 K, 373 K, 393 K and 423 K with counting time of 3 and 6 h. The diffraction patterns were simultaneously recorded at every measurement temperature.

Proton conductivity

The proton conductivities of the samples were examined by the AC impedance spectroscopy technique. Impedance analysis were performed with Solartron SI 1260 Impedance/Gain phase Analyser over a selected frequency range (maximum frequency range investigated between 0.1 Hz and 10 MHz) at signal voltage amplitude of 100 mV and 0 mV DC rest voltage. Temperature and humidity dependent conductivity was determined using an electrochemical homemade cell equipped with platinum current collectors. Conductivity measurements were carried out on pressed pellets of the finely ground powder samples. Samples for conductivity measurements were prepared by grinding the sample ($\sim 0.120 \text{ g}$) into a homogeneous powder with a mortar and pestle, added to a standard 8 mm die, sandwiched between

two porous carbon electrodes (Sigracet, GDL 10 BB) or coated with silver paste (Sigma Aldrich) electrode to improve contact with the platinum wires, and pressed at 5 tons for 5 minutes. Resultant pellets were placed into the electrochemical cell. Electrical measurements were taken at several temperatures and degree of relative humidity, which were obtained by a continuous flow of water-saturated N₂ through the cell. To ensure a fixed water content of the sample, all the conductivity values here reported refer to measurements carried out after equilibration for an overnight period; stable conductivity values were reached for at least 2 h to ensure full reproducibility. The temperature and relative humidity were recorded in close vicinity to the sample with a temperature and humidity sensor (Rotronic HC2-C04) in order to measure the temperature and humidity dependence of the conductivity. The proton conductivity (σ , S cm⁻¹) was calculated from the impedance data, using the following equation: $\sigma=l/RA$, where l and A are the thickness (cm) and cross-sectional area (cm²) of the pellet respectively, and R , which was extracted from the impedance plots, is the bulk resistance of the sample (Ω). SMaRT v. 3. 2. 1 and ZView software were used to fit the impedance data and obtain resistance values.